

---

# Thermal Behavior Impact on Electric Motor Sizing in Battery Electric Vehicles

---

Bicheng Chen



# **Thermal Behavior Impact on Electric Motor Sizing in Battery Electric Vehicles**

**Einfluss des thermischen Verhaltens auf die Dimensionierung von Elektromotoren in batterieelektrischen Elektrofahrzeugen**

Von der Fakultät für Maschinenwesen der Rheinisch-Westfälischen Technischen Hochschule Aachen zur Erlangung des akademischen Grades eines Doktors der Ingenieurwissenschaften genehmigte Dissertation

vorgelegt von

**Bicheng Chen**

Berichter: Univ.-Prof. Dr.-Ing. (USA) Stefan Pischinger  
Univ.-Prof. Dr.-Ing. Jakob Lukas Andert

Tag der mündlichen Prüfung: 23. Mai 2025

Diese Dissertation ist auf den Internetseiten der Universitätsbibliothek online verfügbar.



To my family



# Acknowledge

This dissertation was completed during my time as a Research Associate at the Chair of Thermodynamics of Mobile Energy Conversion Systems (TME), RWTH Aachen University. The research presented here was supported by funding from the European Union's Horizon 2020 research and innovation programme under Grant Agreement No. 824295 – CEVOLVER (Connected Electric Vehicle Optimized for Life, Value, Efficiency and Range). I am sincerely grateful for the financial support that enabled this work.

Foremost, A heartfelt thanks to Univ.-Prof. Dr.-Ing. (USA) Stefan Pischinger for his exceptional academic guidance, consistent support, and trust throughout the duration of this work. I am also grateful to Univ.-Prof. Dr.-Ing. Jakob Andert for kindly taking on the role of second examiner and agreeing to review this work.

In addition, I would like to sincerely thank Univ.-Prof. Dr.-Ing. Reinhold Kneer for chairing the examination committee, as well as Univ.-Prof. Dr.-Ing. Thomas Bergs for serving as a member of the committee.

Special thanks go to Dr.-Ing. Georg Birmes and Dr.-Ing. Rene Savelsberg for their continuous support, thoughtful suggestions, and fruitful discussions, which is invaluable in shaping the direction and the quality of this work. I am equally thankful to Marco Günther for his assistance with various organizational matters, which helped me stay focused on my research.

I am also deeply appreciative of all my colleagues at the Chair of Thermodynamics of Mobile Energy Conversion Systems and at FEV Europe GmbH. I would especially like to thank the team from BES-C, under the leadership of Dr.-Ing. Johannes Maiterth and Dr.-Ing. Feihong Xia, for creating a collaborative and motivating working environment and for their constant support. Furthermore, I would like to acknowledge the contributions of the student assistants, Bachelor's and Master's students who worked on different aspects of this work - your efforts were greatly appreciated.

On a more personal note, I would like to thank my parents for their steadfast support, encouragement, and belief in me throughout the entire PhD journey. Their faith in my abilities gave me strength, especially during challenging times.

Finally, my deepest and most heartfelt gratitude goes to my wife. Her love, patience, and unwavering support have been a constant source of strength and motivation. Her understanding and encouragement, even during the most difficult moments, have made this journey possible. I could not have done it without her.



# Abstract

The increasing popularity of electric vehicles (EVs) as eco-friendly alternatives in the automotive industry has been impeded by consumer apprehensions regarding limited driving range. This work addresses this challenge by focusing on two pivotal factors crucial for enhancing EV efficiency and extending driving range: accurate temperature monitoring and optimal sizing for electrical machines (EMs).

In response to the critical need for monitoring temperatures in electric drivetrain components, a centralized compact lumped parameter thermal network (LPTN) model is proposed. Departing from conventional distributed thermal models for each component, this thermal model considers the intricate thermal coupling between the inverter, EM and gearbox. Utilizing the measured and validated loss maps including the detailed losses distribution in the permanent magnet synchronous machine (PMSM), the model accurately calculates component losses. A global linear parameter-varying (LPV) identification approach is then applied to determine the parameters of the LPTN model. Cross-validation with independent experimental data of the US06 cycle on the chassis dynamometer yields a maximum estimation error of approximately 7 °C. Simulation results demonstrate the effectiveness of the centralized thermal model in estimating temperatures of critical parts while considering the thermal coupling between components.

Additionally, this work introduces a promising approach known as "right-sizing" for EMs. This involves an efficient scaling of thermal parameters in a low-order LPTN model, enabling the estimation of temperature for the scaled PMSM. The proposed scaling approach facilitates a preliminary evaluation of the thermal limits of the PMSM during the early stages of development. Validation for both axial and radial scaling, with scaling factors ranging from 0.8 to 1.2, is conducted on a previously validated Ansys Motor-CAD model for typical automotive driving cycles, revealing a maximum temperature scaling error of less than 3.5 °C.

The integration of the LPTN model and the scaling approach into a whole vehicle simulation model becomes instrumental in determining the optimal size of a specific EM for diverse driving scenarios, including urban and highway conditions. The pursuit of optimization is guided by considering critical factors such as the thermal constraints of the EM, the overall efficiency and performance of the EV. Employing the ant colony optimization (ACO) optimization algorithm results in the identification of a Pareto front for urban and highway scenarios. The optimization results suggest that a shorter motor length is advantageous in both urban and highway cycle scenarios. In urban scenarios, the optimized motor enhances acceleration performance while lowering energy consumption. However, in highway scenarios, there's a trade-off between energy consumption and acceleration, with the optimized motor leading to a 2.84% decrease in energy consumption.



# Kurzfassung

Die zunehmende Beliebtheit von Elektrofahrzeugen (EVs) als umweltfreundliche Alternativen in der Automobilindustrie wird durch Verbraucherbedenken bezüglich begrenzter Reichweite behindert. Diese Arbeit geht auf diese Herausforderung ein, indem sie sich auf zwei entscheidende Faktoren konzentriert, die für die Verbesserung der Effizienz von EVs und die Erweiterung der Reichweite entscheidend sind: genaue Temperaturüberwachung und optimale Dimensionierung der elektrischen Maschine (EM).

Zur Überwachung von Temperaturen in elektrischen Antriebsstrangkomponenten wird ein zentralisiertes kompaktes thermisches Netzwerk mit pauschalen Parametern (LPTN) vorgeschlagen. Abweichend von konventionellen verteilten thermischen Modellen für jede Komponente berücksichtigt dieses thermische Modell die komplexe thermische Kopplung zwischen dem Wechselrichter, der EM und dem Getriebe. Unter Verwendung der gemessenen und validierten Verlustkennfelder, einschließlich der detaillierten Verlustverteilung in der Permanentmagnet-Synchronmaschine (PMSM), berechnet das Modell präzise die Komponentenverluste. Ein globaler linear parameter-variabler (LPV) Identifikationsansatz wird dann angewendet, um die Parameter des LPTN-Modells zu bestimmen. Die Validierung mit unabhängigen experimentellen Daten auf dem Chassis-Dynamometer ergibt eine maximale Abweichung von etwa  $7^{\circ}\text{C}$ . Simulationsergebnisse zeigen die Wirksamkeit des zentralen thermischen Modells bei der Prädikation von Temperaturen kritischer Teile unter Berücksichtigung der thermischen Kopplung zwischen den Komponenten.

Zusätzlich stellt diese Arbeit einen vielversprechenden Ansatz namens "Optimierte Dimensionierung" für EM vor. Dies beinhaltet eine effiziente Skalierung thermischer Parameter in dem LPTN-Modell mit niedriger Ordnung, das die Schätzung der Temperatur für das skalierte PMSM ermöglicht. Der vorgeschlagene Skalierungsansatz erleichtert eine vorläufige Überprüfung der thermischen Einschränkungen des PMSMs in der frühen Entwicklungsphase. Die Validierung für sowohl axiale als auch radiale Skalierung mit Skalierungsfaktoren von 0.8 bis 1.2 wird an einem zuvor validierten Ansys MotorCAD-Modell für typische Fahrzyklen in der Automobilindustrie durchgeführt und zeigt eine maximale Temperaturabweichung für Skalierung von weniger als  $3.5^{\circ}\text{C}$ .

Die Integration des LPTN-Modells und des Skalierungsansatzes in ein Gesamtfahrzeug-Simulationsmodell wird entscheidend für die Bestimmung der optimalen Größe einer EM für verschiedene Fahrscenarien, einschließlich Stadt und Autobahn. Die Optimierung wird durch die Berücksichtigung von kritischen Faktoren wie thermischen Einschränkungen der EM, Gesamtwirkungsgrad und Performance des Fahrzeugs geleitet. Der Einsatz von Ameisenalgorithmen (ACO) führt zur Identifikation einer Pareto-Front für Stadt- und Autobahn-Szenarien. Die Optimierungsergebnisse legen nahe, dass eine kürzere Motorenlänge sowohl in Stadt- als auch in Autobahn-Szenarien vorteilhaft ist. In Stadt-Szenarien verbessert der optimierte Motor die Beschleunigungsleistung und senkt gleichzeitig den Energieverbrauch. In Autobahn-Szenarien besteht jedoch ein Kompromiss zwischen Energieverbrauch und Beschleunigung, wobei der optimierte Motor zu einer Senkung des Energieverbrauchs um 2.84 % führt.



# Contents

List of Figures	III
List of Tables	VII
Symbols	IX
Abbreviations	XVII
<b>1. Introduction</b>	<b>1</b>
1.1. Background and Motivation . . . . .	1
1.2. Outline of Thesis . . . . .	2
<b>2. Theoretical Background</b>	<b>3</b>
2.1. Components of Electric Drivetrain . . . . .	3
2.1.1. Inverter . . . . .	4
2.1.2. Electrical Machine . . . . .	5
2.1.3. Gearbox . . . . .	8
2.2. Heat Transfer . . . . .	9
2.3. Optimization Algorithms . . . . .	12
2.3.1. Evolutionary Algorithms . . . . .	13
2.3.2. Multi-objective Optimization Problem . . . . .	14
<b>3. State of the Research</b>	<b>15</b>
3.1. Thermal Analysis Methods . . . . .	15
3.1.1. Numerical Method . . . . .	15
3.1.2. Analytical Method . . . . .	16
3.1.3. Data-Driven Machine Learning Method . . . . .	17
3.2. Scaling of Electrical Machine . . . . .	19
<b>4. Thermal Modeling of Electric Drivetrain</b>	<b>23</b>
4.1. Lumped Parameter Thermal Network for Drivetrain . . . . .	23
4.1.1. Thermal Network for Coolant Outlet Temperature . . . . .	24
4.1.2. Thermal Network and Loss Model of Inverter . . . . .	28
4.1.3. Thermal Network and Loss Model of Electric Motor . . . . .	31
4.1.4. Thermal Network and Loss Model of Gearbox . . . . .	39
4.1.5. Thermal Network of the Whole Drivetrain . . . . .	42
4.2. Parametrization and Validation . . . . .	43
<b>5. Temperature Estimation of Scaled Permanent Magnet Synchronous Machines</b>	<b>49</b>
5.1. Calibration of the Thermal Behavior of the Motor-CAD Model for the Reference PMSM . . . . .	49

5.2. Scaling of Losses . . . . .	52
5.3. Scaling of Thermal Parameters of the LPTN . . . . .	55
5.3.1. Thermal Capacity . . . . .	55
5.3.2. Thermal Resistance . . . . .	56
5.4. Sensitivity Analysis Based on Validation Data of the Scaled Motor-CAD Model . . . . .	59
5.5. Validation Results . . . . .	61
5.5.1. Validation of the Losses of Scaled PMSMs . . . . .	61
5.5.2. Validation of the Temperatures of Scaled PMSMs . . . . .	64
5.6. Applicability of the Scaling Approach in PMSM Evaluation . . . . .	72
<b>6. Optimization of Electric Drivetrain with Scaled PMSM Model</b>	<b>73</b>
6.1. Modeling and Validation of a Battery Electric Vehicle . . . . .	73
6.1.1. Vehicle Model Overview . . . . .	74
6.1.2. Electric Motor Model . . . . .	76
6.1.3. Thermal Model . . . . .	83
6.1.4. Cooling System Model . . . . .	84
6.2. Optimization Problem Formulation . . . . .	88
6.3. Analysis of the Optimization Results . . . . .	91
6.4. Scope and Limitations of the Optimization . . . . .	97
<b>7. Conclusion and Outlook</b>	<b>99</b>
7.1. Conclusion . . . . .	99
7.2. Outlook . . . . .	100
<b>Bibliography</b>	<b>101</b>
<b>A. Appendix</b>	<b>109</b>
A.1. Loss Validation Between Motor-CAD and Measurements . . . . .	109
A.2. Detailed Representation of Matrices in State Space Model of the Drivetrain LPTN . . . . .	110
A.3. Parametrization and Validation of the LPTN for the Whole Drivetrain . . . . .	112
A.4. Loss Validation of the Scaled PMSM . . . . .	114
A.5. Cycle Profiles and Coolant Profiles for the Validation of the Reference PMSM . . . . .	116
A.6. Temperature Validation of the Reference PMSM . . . . .	118
A.7. Temperature Validation of the Scaled PMSM . . . . .	121

# List of Figures

2.1.	Key components of a front-wheel drive EV . . . . .	3
2.2.	Switching losses and conduction losses of an insulated-gate bipolar transistor (IGBT) . . . . .	4
2.3.	Magnitude of current density distribution for different types of alternating current (AC) losses in electrical machines. . . . .	6
2.4.	Hysteresis loop of a soft magnetic material at different temperatures . . . .	7
2.5.	EM cooling system in EVs . . . . .	8
2.6.	One-dimensional heat transfer by conduction . . . . .	10
2.7.	Enclosed channel forced convection heat transfer coefficient versus the fluid velocity . . . . .	11
2.8.	Illustration of multi-objective optimization process . . . . .	14
3.1.	A LPTN thermal network of a stator segment . . . . .	17
3.2.	Structure of the sequence learning with long short-term memory (LSTM) . .	18
3.3.	Scaling of PMSMs mainly based on axial scaling factor and radial scaling factor . . . . .	20
4.1.	Proposed heat transfer paths inside the whole drivetrain system . . . . .	24
4.2.	Conservation of energy for coolant in the control volume . . . . .	25
4.3.	Simplified representation of energy conservation for coolant in the control volume system . . . . .	26
4.4.	Proposed LPTN for the coolant outlet temperature . . . . .	27
4.5.	Thermal modeling of the inverter . . . . .	28
4.6.	Efficiency maps of inverter for different temperatures . . . . .	30
4.7.	Thermal modeling of the PMSM . . . . .	31
4.8.	Efficiency maps of PMSM for different temperatures . . . . .	34
4.9.	Initial design of the cross-section of the PMSM in Motor-CAD . . . . .	36
4.10.	Average loss difference between the measurement and the loss model at direct current (DC)-voltage of 350 V for the initial assumption . . . . .	37
4.11.	Final cross-section of the PMSM after adjustments to the slot and magnet .	38
4.12.	Average loss difference between the measurement and the loss model at DC-voltage of 350 V after fein tuning . . . . .	39
4.13.	Efficiency map comparison between Motor-CAD and measurements at DC-voltage of 350 V and temperature of 110 °C . . . . .	40
4.14.	Thermal modeling of the gearbox . . . . .	40
4.15.	Efficiency maps of gearbox for different temperatures . . . . .	42
4.16.	Structure of proposed LPTN for the whole drivetrain . . . . .	44
4.17.	Histogram of estimation errors based on worldwide harmonized light duty test cycle (WLTC) driving cycle . . . . .	46
4.18.	Histogram of estimation errors based on US06 driving cycle . . . . .	48
5.1.	Schematic and simplified overview of the LPTN model in Motor-CAD . . .	50

5.2.	Thermal modeling of the housing surface node in Motor-CAD . . . . .	51
5.3.	Temperature comparison of the simulation and the measurement for the extended WLTC cycle at ambient temperature of 20 °C . . . . .	52
5.4.	Calculation of the loss map for the scaled PMSM . . . . .	54
5.5.	Conductive thermal resistance between stator and end winding . . . . .	58
5.6.	Power share map of the scaled PMSM for the extended WLTC cycle at motor temperature of 110 °C . . . . .	60
5.7.	Temperatures and losses of the scaled PMSM for the extended WLTC at ambient temperature of 20 °C . . . . .	61
5.8.	Total losses validation for 0.8 axial scaling against the extended WLTC cycle at the ambient temperature of 20 °C . . . . .	62
5.9.	Related losses validation for 0.8 axial scaling against the extended WLTC cycle at the ambient temperature of 20 °C . . . . .	63
5.10.	Box-whisker charts for the total loss deviation in the axial scaling and radial scaling . . . . .	64
5.11.	Parametrization based on the extended WLTC cycle at an ambient temperature of 20 °C . . . . .	66
5.12.	Validation results of temperature estimation for 0.8 axial scaling against the extended WLTC cycle at an ambient temperature of 20 °C . . . . .	68
5.13.	Temperature deviation of axial scaling in comparison to Motor-CAD . . . . .	69
5.14.	Validation results of temperature estimation for 1.2 radial scaling against the extended WLTC cycle at an ambient temperature of 20 °C . . . . .	70
5.15.	Temperature deviation of radial scaling in comparison to Motor-CAD . . . . .	71
6.1.	Schematic block diagram of the battery electric vehicle (BEV) simulation . . . . .	73
6.2.	Motor mass and moment of inertia map for scaling from 0.8 to 1.2 . . . . .	76
6.3.	Schematic of the electric motor model based on dq-frame . . . . .	77
6.4.	Flux linkage map based on d and q component of phase current at motor temperature of 30 °C . . . . .	78
6.5.	Comparison of requested torque and actual torque in Simulink model . . . . .	79
6.6.	Peak torque comparison between scaling law and Motor-CAD . . . . .	80
6.7.	Phase current comparison between scaling law and Motor-CAD for 0.8 axial and 0.8 radial scaling . . . . .	81
6.8.	Copper losses, iron losses and magnet losses based on d and q component of phase current at speed of 3000 1/min and motor temperature of 30 °C . . . . .	82
6.9.	Efficiency map comparison between scaling law and Motor-CAD at motor temperature of 30 °C for 0.8 axial and 0.8 radial scaling . . . . .	82
6.10.	Centralized temperature simulation of powertrain . . . . .	83
6.11.	Layout of the cooling circuit including the coolant circuit and the refrigerant circuit . . . . .	85
6.12.	Block diagram of the thermal simulation including cooling system . . . . .	86
6.13.	Comparison of coolant outlet temperature of inverter and electric motor . . . . .	87
6.14.	Power of cooling system components . . . . .	88
6.15.	Driving cycles for optimization . . . . .	90
6.16.	Pareto front of the multi-objective optimization problem for the various scenarios . . . . .	92
6.17.	Supplementary plots of design variables and constraints for the Artemis urban cycle . . . . .	93

---

6.18.	Supplementary plots of design variables and constraints for the Artemis highway cycle . . . . .	94
6.19.	Relationship between acceleration time and motor peak torque and peak power . . . . .	95
6.20.	Power share plot maps of the reference and optimized motors for the urban cycle . . . . .	96
6.21.	Power share plot maps of the reference and optimized motors for the highway cycle . . . . .	97
A.1.	Validation result of the total loss against WLTC driving cycle at an ambient temperature of 20 °C . . . . .	109
A.2.	Validation result of the total loss against US06 driving cycle at an ambient temperature of 20 °C . . . . .	109
A.3.	Parametrization based on WLTC driving cycle with ambient temperature around 20 °C and varying coolant profiles . . . . .	112
A.4.	Cross-Validation against US06 driving cycle with ambient temperature around 20 °C and varying coolant profiles . . . . .	113
A.5.	Total losses validation for 1.2 radial scaling against the extended US06 cycle at the ambient temperature of 20 °C . . . . .	114
A.6.	Related losses validation for 1.2 radial scaling against the extended US06 cycle at the ambient temperature of 20 °C . . . . .	114
A.7.	Boundary condition for the extended US06 cycle at an ambient temperature of 20 °C . . . . .	116
A.8.	Boundary condition for the extended WLTC cycle at an ambient temperature of 35 °C and 50 °C . . . . .	117
A.9.	Validation against the extended US06 cycle at an ambient temperature of 20 °C . . . . .	118
A.10.	Validation against the extended WLTC cycle at an ambient temperature of 35 °C . . . . .	119
A.11.	Validation against the extended WLTC cycle at an ambient temperature of 50 °C . . . . .	120
A.12.	Validation results of temperature estimation for 0.8 axial scaling against the extended WLTC cycle at an ambient temperature of 35 °C . . . . .	121
A.13.	Validation results of temperature estimation for 0.8 axial scaling against the extended WLTC cycle at an ambient temperature of 50 °C . . . . .	122
A.14.	Validation results of temperature estimation for 0.8 axial scaling against the US06 cycle at an ambient temperature of 20 °C . . . . .	123
A.15.	Validation results of temperature estimation for 0.9 axial scaling against the extended WLTC cycle at an ambient temperature of 20 °C . . . . .	124
A.16.	Validation results of temperature estimation for 0.9 axial scaling against the extended WLTC cycle at an ambient temperature of 35 °C . . . . .	125
A.17.	Validation results of temperature estimation for 0.9 axial scaling against the extended WLTC cycle at an ambient temperature of 50 °C . . . . .	126
A.18.	Validation results of temperature estimation for 0.9 axial scaling against the US06 cycle at an ambient temperature of 20 °C . . . . .	127
A.19.	Validation results of temperature estimation for 1.1 axial scaling against the extended WLTC cycle at an ambient temperature of 20 °C . . . . .	128

---

A.20.	Validation results of temperature estimation for 1.1 axial scaling against the extended WLTC cycle at an ambient temperature of 35 °C . . . . .	129
A.21.	Validation results of temperature estimation for 1.1 axial scaling against the extended WLTC cycle at an ambient temperature of 50 °C . . . . .	130
A.22.	Validation results of temperature estimation for 1.1 axial scaling against the US06 cycle at an ambient temperature of 20 °C . . . . .	131
A.23.	Validation results of temperature estimation for 1.2 axial scaling against the extended WLTC cycle at an ambient temperature of 20 °C . . . . .	132
A.24.	Validation results of temperature estimation for 1.2 axial scaling against the extended WLTC cycle at an ambient temperature of 35 °C . . . . .	133
A.25.	Validation results of temperature estimation for 1.2 axial scaling against the extended WLTC cycle at an ambient temperature of 50 °C . . . . .	134
A.26.	Validation results of temperature estimation for 1.2 axial scaling against the US06 cycle at an ambient temperature of 20 °C . . . . .	135
A.27.	Validation results of temperature estimation for 0.8 radial scaling against the extended WLTC cycle at an ambient temperature of 20 °C . . . . .	136
A.28.	Validation results of temperature estimation for 0.8 radial scaling against the extended WLTC cycle at an ambient temperature of 35 °C . . . . .	137
A.29.	Validation results of temperature estimation for 0.8 radial scaling against the extended WLTC cycle at an ambient temperature of 50 °C . . . . .	138
A.30.	Validation results of temperature estimation for 0.8 radial scaling against the US06 cycle at an ambient temperature of 20 °C . . . . .	139
A.31.	Validation results of temperature estimation for 0.9 radial scaling against the extended WLTC cycle at an ambient temperature of 20 °C . . . . .	140
A.32.	Validation results of temperature estimation for 0.9 radial scaling against the extended WLTC cycle at an ambient temperature of 35 °C . . . . .	141
A.33.	Validation results of temperature estimation for 0.9 radial scaling against the extended WLTC cycle at an ambient temperature of 50 °C . . . . .	142
A.34.	Validation results of temperature estimation for 0.9 radial scaling against the US06 cycle at an ambient temperature of 20 °C . . . . .	143
A.35.	Validation results of temperature estimation for 1.1 radial scaling against the extended WLTC cycle at an ambient temperature of 20 °C . . . . .	144
A.36.	Validation results of temperature estimation for 1.1 radial scaling against the extended WLTC cycle at an ambient temperature of 35 °C . . . . .	145
A.37.	Validation results of temperature estimation for 1.1 radial scaling against the extended WLTC cycle at an ambient temperature of 50 °C . . . . .	146
A.38.	Validation results of temperature estimation for 1.1 radial scaling against the US06 cycle at an ambient temperature of 20 °C . . . . .	147
A.39.	Validation results of temperature estimation for 1.2 radial scaling against the extended WLTC cycle at an ambient temperature of 35 °C . . . . .	148
A.40.	Validation results of temperature estimation for 1.2 radial scaling against the extended WLTC cycle at an ambient temperature of 50 °C . . . . .	149
A.41.	Validation results of temperature estimation for 1.2 radial scaling against the US06 cycle at an ambient temperature of 20 °C . . . . .	150

# List of Tables

3.1. Analogy between heat transfer and electrical circuit . . . . .	16
4.1. Main parameters of the reference PMSM . . . . .	35
4.2. Model performance based on WLTC driving cycle . . . . .	46
4.3. Model performance based on US06 driving cycle . . . . .	47
5.1. DC-voltage for the reference PMSM and scaled PMSMs . . . . .	55
5.2. Thermal parameters of the reference PMSM . . . . .	65
5.3. Estimation of temperatures of scaled PMSMs at an ambient temperature of 20 °C considering measurement offset . . . . .	72
6.1. Objectives and constraints of the optimization problem . . . . .	88
6.2. Technical parameters of the reference vehicle for the simulation . . . . .	90
6.3. Optimization results of the PMSM for the "Urban Cycle" scenarios . . . . .	94
6.4. Optimization results of the PMSM for the "Highway Cycle" scenarios . . . . .	95
A.1. RMSE deviation of total loss for WLTC cycle . . . . .	115
A.2. RMSE deviation of total loss for US06 cycle . . . . .	115



# Symbols

## Greek characters

$\alpha$	Temperature coefficient of copper resistance
$\alpha_{\text{COE-HE}}$	Coefficient to characterize the temperature dependence of the fluid's flow rate on the convective thermal resistance between coolant and housing
$\alpha_{\text{CP-J}}$	Coefficient that accounts for the temperature-dependent behavior of the thermal resistance between cooling plate and junction
$\alpha_{\text{O}}$	Coefficient that accounts for the temperature-dependent behavior of the thermal capacity of lubricant oil
$\alpha_{\text{R-S}}$	Coefficient to characterize the temperature dependence of the fluid's flow rate on the convective thermal resistance between stator and rotor
$\alpha_{\text{th}}$	Coefficient to characterize the temperature dependence of the fluid's flow rate on the convective thermal resistance
$\beta$	Road incline angle in radians
$\eta_{\text{avg}}$	Average efficiency of the vehicle
$\lambda$	Solid thermal conductivity
$\nu_{\text{in}}$	Specific volume of the inlet fluid
$\nu_{\text{out}}$	Specific volume of the outlet fluid
$\omega$	Electrical frequency of the electric motor
$\Psi_{\text{d}}$	Direct magnetic flux linkage
$\Psi_{\text{Mag}}$	Magnetic flux linkage
$\Psi_{\text{Mag,scl}}$	Magnetic flux linkage of the scaled motor
$\Psi_{\text{q}}$	Quadrature magnetic flux linkage
$\sigma$	Stefan-Boltzmann constant
$\sigma_{\text{e}}$	Electrical conductivity of the conductor material
$\theta_{\text{em}}$	Moment of inertia of the electric motor
$\theta_{\text{red}}$	Reduced moment of inertia of the vehicle
$\theta_{\text{whl}}$	Moment of inertia of the wheels
$\varepsilon$	Emissivity for heat radiation

## Latin characters

$A$	Contact surface area
$a$	Constant in the convection correlation of Nusselt number

$a_{\text{COE-HE}}$	Coefficient to characterize the temperature dependence of the fluid's properties on the convective thermal resistance between coolant and housing
$A_{\text{Cu}}$	Cross-section of copper in the slot
$a_{\text{G-O}}$	Constant offset for the thermal resistance between gears and oil
$a_{\text{HG-O}}$	Constant offset for the thermal resistance between gearbox housing and oil
$a_{\text{R-S}}$	Coefficient to characterize the temperature dependence of the fluid's properties on the convective thermal resistance between stator and rotor
$a_{\text{th}}$	Coefficient to characterize the temperature dependence of the fluid's properties on the convective thermal resistance
$B$	Magnetic flux density
$b$	Exponent representing the dependence on the Reynolds number in the Nusselt number correlation
$b_{\text{COE-HE}}$	Exponent to approximate the flow rate dependence of the fluid on the convective thermal resistance between coolant and housing
$b_{\text{G-O}}$	Exponent that accounts for the temperature-dependent behavior of the thermal resistance between the gear and oil
$b_{\text{HG-O}}$	Exponent that accounts for the temperature-dependent behavior of the thermal resistance between the housing and the oil
$b_{\text{J}}$	Exponent that accounts for the temperature-dependent behavior of the thermal capacity of the junction
$B_{\text{R}}$	Magnetic remanence
$b_{\text{R-S}}$	Exponent to approximate the flow rate dependence of the fluid on the convective thermal resistance between stator and rotor
$b_{\text{th}}$	Exponent to approximate the flow rate dependence of the fluid on the convective thermal resistance
$c$	Exponent representing the dependence on the Prandtl number in the Nusselt number correlation
$C_{\text{c}}$	Equivalent thermal capacity of the coolant
$C_{\text{COE}}$	Thermal capacity of coolant outlet of the electric motor
$C_{\text{COE,scl}}$	Thermal capacity of coolant in the scaled motor
$C_{\text{COI}}$	Thermal capacity of coolant outlet of the inverter
$C_{\text{CP}}$	Thermal capacity of the cooling plate
$C_{\text{EW}}$	Thermal capacity of the end winding
$C_{\text{EW,scl}}$	Thermal capacity of the end winding of the scaled motor
$C_{\text{G}}$	Thermal capacity of the gear
$C_{\text{HE}}$	Thermal capacity of the electric motor housing
$C_{\text{HE,scl}}$	Thermal capacity of the housing of the scaled motor
$C_{\text{HG}}$	Thermal capacity of the gearbox housing
$C_{\text{HI}}$	Thermal capacity of the inverter housing

---

$C_J$	Thermal capacity of the junction
$C_{J,0}$	Thermal capacity of the junction at the reference temperature
$C_O$	Thermal capacity of the lubricant oil in the gearbox
$C_R$	Thermal capacity of the rotor
$C_{R,scl}$	Thermal capacity of the rotor of the scaled motor
$C_S$	Thermal capacity of the stator
$c_s$	Specific heat capacity
$c_{s,p}$	Specific heat capacity at constant pressure
$C_{S,scl}$	Thermal capacity of the stator of the scaled motor
$c_{s,v}$	Specific heat capacity at constant volume
$C_{th}$	Thermal capacity
$d_c$	Diameter of the circular conductor
$E_{in}$	Total energy flowing into the system
$E_{out}$	Total energy flowing out of the system
$\Delta E_{sys}$	Total energy change in the system
$f(\mathbf{x})$	Objective function in an optimization problem
$F_0$	Driveline and rolling resistance in $N$
$F_1$	Velocity dependent rolling resistance in $N/(km/h)$
$F_2$	Air-drag resistance in $N/(km/h)^2$
$F_{acc}$	Acceleration resistance
$F_{coast}$	Coast-down resistance
$F_{grade}$	Grade resistance
$\mathbf{F}(\mathbf{x}^*)$	Pareto front solutions
$F_{res}$	Total driving resistance of the vehicle
$\mathbf{F}(\mathbf{x})$	Set of objective functions in an optimization problem
$g$	Gravitational acceleration
$\mathbf{g}(\mathbf{x})$	Inequality constraints in an optimization problem
$H$	Magnetic field strength
$H_C$	Magnetic coercivity
$h_{conv}$	Convective heat transfer coefficient
$\mathbf{h}(\mathbf{x})$	Equality constraints in an optimization problem
$h_{rad}$	Radiative heat transfer coefficient
$I_{Batt}$	Battery current
$I_C$	Collector current
$I_d$	Direct component of phase current
$I_{d,scl}$	Direct component of phase current of the scaled motor
$i_{gear}$	Gear ratio of the reduction gear
$I_{max}$	Maximum available phase current
$I_q$	Quadrature component of phase current
$I_{q,scl}$	Quadrature component of phase current of the scaled motor
$k$	Fluid thermal conductivity
$k_A$	Axial scaling factor
$k_R$	Radial scaling factor
$L$	Characteristic length of the surface
$l$	Path length of heat transfer

$L_a$	Conductor active length
$l_{\text{core}}$	Length of the core region
$l_{\text{core,scl}}$	Length of the core region of the scaled motor
$l_{\text{EW}}$	Equivalent path length of the end winding
$l_{\text{EW,scl}}$	Equivalent path length of the end winding of the scaled motor
$l_{\text{H}}$	Length of the motor housing
$l_{\text{H,ext}}$	Length of motor housing out of the core region
$l_{\text{H,scl}}$	Length of the motor housing of the scaled motor
$l_{\text{scl}}$	Path length of heat transfer of the scaled motor
$M$	Torque of the reference electric motor
$m$	Mass of the material
$M_{\text{act}}$	Actual shaft torque of the electric motor
$\dot{m}_{\text{in}}$	Mass flow into the system
$\dot{m}_{\text{out}}$	Mass flow out of the system
$M_{\text{em}}$	Electromagnetic torque of electric motor
$m_{\text{em}}$	Mass of the electric motor
$m_{\text{eq}}$	Equivalent mass of the rotating components in the vehicle
$M_{\text{max,MotorCAD}}$	Peak torque of Motor-CAD Model
$M_{\text{peak}}$	Peak torque of the electric motor
$M_{\text{req}}$	Required torque of the electric motor
$M_{\text{scl}}$	Torque of the scaled electric motor
$m_{\text{veh}}$	Vehicle mass
$M_{\text{whl,act}}$	Actual wheel torque
$M_{\text{whl,req}}$	Required wheel torque
$n$	Rotational speed of the electric motor
$n_{\text{base}}$	Base speed of the electric motor
$n_{\text{Blower}}$	Blower speed
$n_{\text{Compressor}}$	Compressor speed
$n_{\text{Fan}}$	Fan speed
$n_{\text{Pump}}$	Pump speed
$Nu$	Nusselt number
$p$	Pole pair number
$P_{\text{Batt}}$	Battery losses
$P_{\text{Batt,elec}}$	Electrical power of battery
$P_c$	Equivalent power loss of the coolant
$P_{\text{Compressor}}$	Compressor power
$P_{\text{Cu}}$	Copper losses
$P_{\text{Cu,AC}}$	AC copper losses
$P_{\text{Cu,AC,scl}}$	AC copper losses of the scaled motor
$P_{\text{Cu,AC} T_{20}}$	AC copper losses at the temperature of $T_{20}$
$P_{\text{Cu,DC}}$	DC copper losses
$P_{\text{Cu,DC,scl}}$	DC copper losses of the scaled motor
$P_{\text{Cu,DC} T_{20}}$	DC copper losses at the temperature of $T_{20}$
$P_{\text{Cu,scl}}$	Copper losses of the scaled motor
$P_{\text{Cu} T}$	Total copper losses at a certain temperature of $T$
$P_{\text{EM}}$	Electric motor losses

---

$P_{EW}$	End winding losses
$P_{EW,scl}$	End winding losses of the scaled motor
$P_{Fric}$	Friction losses
$P_{GB}$	Gearbox losses
$p_{in}$	Pressure of the inlet fluid
$P_{INV}$	Inverter losses
$p_{out}$	Pressure of the outlet fluid
$P_{peak}$	Peak power of the electric motor
$P_{Pump}$	Pump power
$P_R$	Rotor losses
$P_{R,Fe}$	Rotor iron losses
$P_{R,Fe,scl}$	Rotor iron losses of the scaled motor
$P_{R,Mag}$	Rotor magnet losses
$P_{R,Mag,scl}$	Rotor magnet losses of the scaled motor
$P_{R,scl}$	Rotor losses of the scaled motor
$P_S$	Stator losses
$P_{S,Fe}$	Stator iron losses
$P_{S,Fe,scl}$	Stator iron losses of the scaled motor
$P_{S,scl}$	Stator losses of the scaled motor
$P_{total}$	Total losses of the electric motor
$P_V$	Switching and conduction losses
$Pr$	Prandtl number
$\dot{Q}_{comp}$	Heat flow rate from a component at system boundaries
$\dot{Q}$	Heat flow rate
$\dot{Q}_{ADC-A}$	Heat flow rate between the air in the drivetrain compartment and ambient
$\dot{Q}_{Batt-C}$	Heat flow rate between the battery and coolant
$\dot{Q}_{DCDC-C}$	Heat flow rate between the DCDC-converter and coolant
$\dot{Q}_{EM-C}$	Heat flow rate between the electric motor and coolant
$\dot{Q}_{GB-ADC}$	Heat flow rate between the gearbox and the air in the drivetrain compartment
$\dot{Q}_{INV-ADC}$	Heat flow rate between the inveter and the air in the drivetrain compartment
$\dot{Q}_{INV-C}$	Heat flow rate between the inverter and coolant
$\dot{Q}_{OBC-C}$	Heat flow rate between the on board charger and coolant
$\dot{Q}_{PMSM-ADC}$	Heat flow rate between the permanent magnet synchronous machine and the air in the drivetrain compartment
$\dot{Q}_{PMSM-C}$	Heat flow rate between the permanent magnet synchronous machine and coolant
$\dot{h}_{in}$	Rate of enthalpy into the control volume
$\dot{h}_{out}$	Rate of enthalpy out of the control volume
$R_{ADC-A}$	Thermal resistance between the air in the drivetrain compartment and ambient
$R_c$	Equivalent thermal resistance between coolant inlet and coolant outlet

$R_{C-HS}$	Thermal resistance between the coolant and housing surface
$R_{CIN-COE}$	Thermal resistance between coolant inlet and coolant outlet of the reference motor
$R_{CIN-COE,scl}$	Thermal resistance between the coolant inlet and coolant outlet of the scaled motor
$R_{CIN-COI}$	Equivalent thermal resistance between the coolant inlet and outlet of the inverter
$R_{COE-COI}$	Equivalent thermal resistance between the coolant outlet of the motor and the coolant outlet of the inverter
$R_{COE-HE}$	Thermal resistance between the electric motor housing and coolant
$R_{COE-HE,0}$	Thermal resistance between the coolant and housing at the reference condition
$R_{COE-HE,0,scl}$	Thermal resistance between the coolant and housing at the reference condition of the scaled motor
$R_{COI-CP}$	Thermal resistance between the cooling plate and coolant
$R_{COI-HI}$	Thermal resistance between the inverter housing and coolant
$R_{cond}$	Conductive thermal resistance
$R_{conv}$	Convective thermal resistance
$R_{conv,0}$	Reference convection resistance at the reference temperature $T_0$ and the reference volume flow rate $\dot{V}_0$
$R_{CP-J}$	Thermal resistance between the junction and cooling plate
$R_{CP-J,0}$	Thermal resistance between the cooling plate and junction at the reference temperature
$r_{dyn}$	Dynamic wheel radius
$r_{ew}$	Copper losses distribution ratio of the end winding
$r_{ew,scl}$	Copper losses distribution ratio of the end winding of the scaled motor
$R_{G-O}$	Thermal resistance between the gear and lubricant oil
$R_{G-O,0}$	Thermal resistance between the gear and oil at the reference temperature
$R_{HE-A}$	Thermal resistance between the electric motor housing and ambient
$R_{HE-A,scl}$	Thermal resistance between the housing and ambient of the scaled motor
$R_{HE-ADC}$	Thermal resistance between the electric motor housing and air in the drivetrain compartment
$R_{HE-S}$	Thermal resistance between the electric motor housing and stator
$R_{HE-S,scl}$	Thermal resistance between the housing and stator of the scaled motor
$R_{HG-A}$	Thermal resistance between the gearbox housing and ambient

$R_{\text{HG-ADC}}$	Thermal resistance between the gearbox housing and the air in the drivetrain compartment
$R_{\text{HG-G}}$	Thermal resistance between the gearbox housing and gear
$R_{\text{HG-O}}$	Thermal resistance between the gearbox housing and lubricant oil
$R_{\text{HG-O},0}$	Thermal resistance between the gearbox housing and oil at the reference temperature
$R_{\text{HI-A}}$	Thermal resistance between the inverter housing and ambient
$R_{\text{HI-ADC}}$	Thermal resistance between the inverter housing and the air in the drivetrain compartment
$R_{\text{HS-A}}$	Thermal resistance between the housing surface and ambient
$R_{\text{HS-IH}}$	Thermal resistance between the housing surface and inner housing
$R_{\text{IH-C}}$	Thermal resistance between the inner housing and coolant
$R_{\text{int}}$	Internal ohmic resistance
$R_{\text{R-A}}$	Thermal resistance between the rotor and ambient
$R_{\text{R-A,scl}}$	Thermal resistance between the rotor and ambient of the scaled motor
$R_{\text{R-G}}$	Thermal resistance between the rotor and gear
$R_{\text{rad}}$	Radiative thermal resistance
$R_{\text{s}}$	Stator phase resistance
$R_{\text{S-EW}}$	Thermal resistance between the stator and end winding
$R_{\text{S-EW,scl}}$	Thermal resistance between the stator and end winding of the scaled motor
$R_{\text{S-R}}$	Thermal resistance between the stator and rotor
$R_{\text{S-R},0}$	Thermal resistance between the stator and rotor at the reference condition
$R_{\text{S-R},0,\text{scl}}$	Thermal resistance between the stator and rotor at the reference condition of the scaled motor
$R_{\text{th}}$	Thermal resistance
$Re$	Reynolds number
$St_{\text{Valve}}$	Status of Valve
$T_{20}$	A constant temperature of 20 °C
$T_0$	Reference temperature
$T_A$	Ambient temperature
$T_{\text{ADC}}$	Temperature of the air in the drivetrain compartment
$T_{\text{Airgap}}$	Temperature of the air gap
$T_{\text{Batt}}$	Temperature of the battery
$T_{\text{EM}}$	Temperature of the electric motor
$T_{\text{CIN}}$	Coolant inlet temperature
$T_{\text{COE}}$	Temperature of the coolant outlet of the electric motor
$T_{\text{COI}}$	Temperature of the coolant outlet of the inverter
$T_{\text{CP}}$	Temperature of the cooling plate
$T_{\text{EW}}$	Temperature of the end winding
$T_{\text{G}}$	Temperature of the gear

$T_{GB}$	Temperature of the gearbox
$T_{HE}$	Temperature of the electric motor housing
$T_{HG}$	Temperature of the gearbox housing
$T_{HI}$	Temperature of the inverter housing
$T_{INV}$	Temperature of the inverter
$T_J$	Temperature of the junction
$T_{J,0}$	Reference temperature of the junction
$T_{LS}$	Left-side surface temperature
$T_O$	Temperature of the lubricant oil in gearbox
$T_{O,0}$	Reference temperature of the lubricant oil
$T_{O,max}$	Maximum temperature of the lubricant oil
$T_{PMSM}$	Temperature of the permanent magnet synchronous machine
$T_R$	Temperature of the rotor
$T_{Ref}$	Reference Temperature of the thermal network
$T_{RS}$	Right-side surface temperature
$T_S$	Temperature of the stator
$T_{SA}$	Surface area temperature
$U_{Batt}$	Battery voltage
$U_{CE}$	Voltage across the collector and emitter
$U_{d,scl}$	Direct component of the phase voltage of the scaled motor
$U_{pha,scl}$	Phase voltage of the scaled motor
$U_{max}$	Maximum voltage available from the inverter
$U_{OCV}$	Open circuit voltage
$U_{q,scl}$	Quadrature component of the phase voltage of the scaled motor
$v$	Vehicle velocity
$v_{act}$	Actual velocity of the vehicle
$\dot{V}_0$	The reference volume flow rate
$\dot{V}_{CIN}$	Coolant volume flow rate
$\dot{V}_p$	Volume flow rate of the pump
$v_f$	Velocity of the fluid
$V_p$	Displacement of the pump
$v_{req}$	Required velocity of the vehicle
$\mathbf{x}$	Set of optimal solutions in an optimization problem
$\mathbf{x}^*$	Set of optimal solutions in the Pareto front
$z_{in}$	Vertical coordinate of the inlet fluid
$z_{out}$	Vertical coordinate of the outlet fluid

# Abbreviations

<b>AC</b>	alternating current
<b>ACO</b>	ant colony optimization
<b>AUX</b>	auxiliaries
<b>AWD</b>	all-wheel drive
<b>BEV</b>	battery electric vehicle
<b>CAN</b>	controller area network
<b>CFD</b>	computational fluid dynamics
<b>CNN</b>	convolutional neural network
<b>DC</b>	direct current
<b>DE</b>	differential evolution
<b>DOE</b>	design of experiments
<b>EDU</b>	electric drive unit
<b>EESM</b>	electric excited synchronous machine
<b>EM</b>	electrical machine
<b>EV</b>	electric vehicle
<b>FEA</b>	finite element analysis
<b>GA</b>	genetic algorithm
<b>GB</b>	gearbox
<b>HPC</b>	high performance computing
<b>HV</b>	high voltage
<b>HVAC</b>	heating, ventilation and air conditioning
<b>IGBT</b>	insulated-gate bipolar transistor
<b>IM</b>	induction machine
<b>LPTN</b>	lumped parameter thermal network
<b>LPV</b>	linear parameter-varying

<b>LSTM</b>	long short-term memory
<b>MCU</b>	motor control unit
<b>MIDACO</b>	mixed integer distributed ant colony optimization
<b>MINLP</b>	mixed integer nonlinear programming
<b>MTPA</b>	maximum torque per ampere
<b>NTC</b>	negative temperature coefficient
<b>OBC</b>	on board charger
<b>OCV</b>	open circuit voltage
<b>ODE</b>	ordinary differential equation
<b>PDF</b>	probability density function
<b>PMSM</b>	permanent magnet synchronous machine
<b>PSO</b>	particle swarm optimization
<b>PTC</b>	positive temperature coefficient
<b>RMSE</b>	root mean square error
<b>RNN</b>	recurrent neural network
<b>SoC</b>	state of charge
<b>SynRM</b>	synchronous reluctance motor
<b>SiC</b>	Siliciumcarbid
<b>TCN</b>	temporal convolutional network
<b>WLTC</b>	worldwide harmonized light duty test cycle
<b>2D</b>	2-dimensional

# 1. Introduction

## 1.1. Background and Motivation

On December 12, 2015, a momentous event of great significance occurred in Paris, shaping the trajectory of worldwide endeavors aimed at addressing the challenges of climate change. Delegates from 195 nations convened to finalize the text of what would ultimately materialize into the preeminent global accord for climate action – the Paris Climate Agreement [1]. The focal objective of this accord was to reinforce the collective global response to the impending menace of climate change. The joint initiative aimed at curbing global temperature increases while encouraging collaborative efforts.

To avert the impending climate crisis, a united global endeavor to curtail carbon dioxide emissions from vehicles is imperative. Beyond its environmental implications, such an initiative holds the potential to mitigate the fossil energy crisis and combat air pollution in urban centers. In recent years, the market share of electric vehicles has witnessed a steady rise, indicating a positive shift towards sustainable transportation alternatives [2]. The escalating market share of electric vehicles stands as a testament to the growing consciousness surrounding environmental concerns. However, despite the strides made in this direction, a significant challenge persists: range anxiety [3]. This apprehension regarding the limited driving range of electric vehicles (EVs) remains a formidable obstacle in the widespread acceptance of these vehicles among consumers. Approaches such as intelligent control strategies with connectivity and fast charging of batteries are being researched to improve customer acceptance [4–7]. Besides that, two critical aspects in achieving these goals are accurate temperature estimation and optimizing the size of electrical machines (EMs).

In EVs, monitoring critical temperatures in the electric drivetrain components is becoming more and more crucial for operational safety and achieving better efficiency [8]. On one hand, accurate temperature estimation stands as a technological cornerstone that unlocks a multitude of benefits. By precisely gauging the temperature of critical components such as the power electronics and EM, operational parameters can be fine-tuned to achieve optimal efficiency. This, in turn, translates to reduced energy consumption and an increased driving range, key factors that influence the adoption of EVs on a global scale. Furthermore, maintaining appropriate temperatures within the electric drivetrain is essential to prevent the onset of stressful operational conditions. High temperatures can lead to accelerated aging of components, diminishing the overall lifespan of the vehicle and increasing maintenance costs. By incorporating an appropriate thermal model into the electric drivetrain’s design, the temperature fluctuations can be anticipated and strategies can be implemented to ensure a balance between performance, efficiency, and longevity.

On the other hand, the concept of right-sizing involves selecting an EM that aligns perfectly with the vehicle’s weight and performance goals. An overdimensioned EM may offer impressive acceleration and high-speed capabilities, but it could lead to excessive energy consumption during regular commuting scenarios. Conversely, an undersized EM

might compromise performance, diminishing the drive comfort. In order to addressing this challenge, one pivotal strategy is right-sizing of the electric drivetrain – encompassing components such as inverters, EMs, and transmissions. This approach holds the key to extending the driving range and enhancing the performance of electric vehicles, all while minimizing costs and maintaining a lightweight design. Among the components of the electric drivetrain, EMs play a crucial role. By implementing a scaling approach that considers variables like length, diameter, and turns per coil, EMs can be rapidly adapted to meet evolving requirements. This scaling approach proves to be more practical and efficient in comparison to the computationally intensive finite element analysis (FEA) calculations. The utilization of scaling laws for EMs presents a strategic advantage in the context of system-level drivetrain optimization at early development stage, particularly for driving cycles evaluation.

### 1.2. Outline of Thesis

The thesis consists of seven chapters. In Chapter 1, the background and motivation are introduced. The theoretical background of the electric drivetrain components, heat transfer and optimization algorithms are presented in Chapter 2. In Chapter 3, the state of the research, which covers the thermal analysis methods and the scaling approaches of EMs are reviewed. Chapter 4 focuses on the thermal modeling of the whole electric drivetrain. The thermal modeling of each component is addressed. Afterwards, the lumped parameter thermal network (LPTN) for the whole electric drivetrain regarding the thermal coupling between the components is presented. The parametrization and validation of the thermal model are demonstrated at the end. The scaling of losses and thermal parameters for permanent magnet synchronous machines (PMSMs) is proposed in Chapter 5. The calibration of the thermal behavior of the Ansys Motor-CAD model for the reference PMSM is explained at the beginning. Then, the scaling approach for losses and thermal parameters is presented and followed by the validation results and discussion. After the thermal models and the scaling approach are validated, the optimization of the electric drivetrain in a complete vehicle is carried out in Chapter 6. In the last chapter, a conclusion of this work is provided and an outlook for the further research possibilities is discussed.



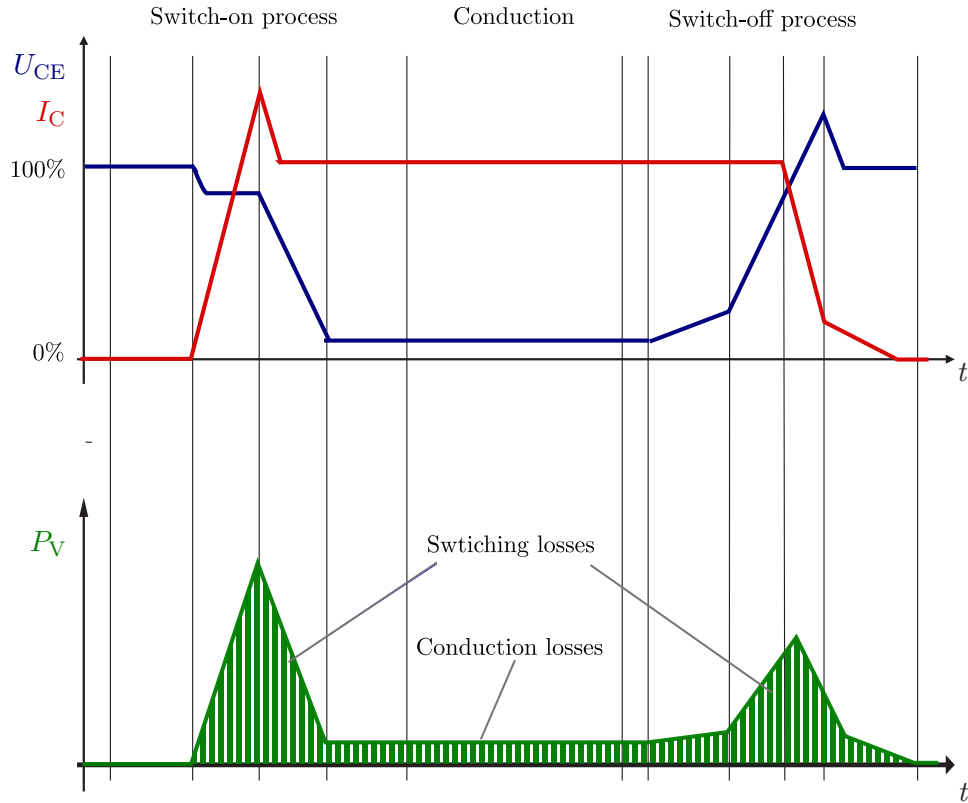


**Figure 2.2.** Switching losses and conduction losses of an IGBT

Adapted from "Modeling of Conduction and Switching Losses for IGBT and FWD Based on SVPWM in Automobile Electric Drives" by Y. Zhu, et al., 2020. Retrieved from <https://www.mdpi.com/2076-3417/10/13/4539>. Licensed under CC BY 4.0

role in managing torque and speed optimizing the efficiency of EM for different driving conditions.

### 2.1.1. Inverter

Inverter is a crucial component in various electrical systems, including those found in electric vehicles. Its primary function is to convert direct current (DC) into alternating current (AC), allowing the efficient operation of AC driven devices. The inverter's working principle involves the use of semiconductor switches, typically IGBT, to rapidly switch the DC voltage on and off [10]. This switching action generates an AC output waveform. As the inverter operates, it experiences power losses due to the inherent characteristics of the semiconductor devices and other components. These losses can be broadly categorized as conduction losses and switching losses, which are depicted in Fig. 2.2 . The upper diagram illustrates the voltage across the collector and emitter  $U_{CE}$  and the collector current  $I_C$ . The switching and conduction losses  $P_V$  are plotted below. Prior to the actual switching process initiation, the IGBT is in a high-resistance state, implying that the voltage  $U_{CE}$  equivalent to the battery DC-voltage. Since the

collector current  $I_C$  doesn't instantaneously jump to its final value during the switch-on process, switching losses occur in the IGBT throughout the switch-on and switch-off durations, respectively [10]. The conduction losses occur when IGBTs are in their "on" state, leading to resistive power losses.

The power losses of the inverter are influenced by the operating temperature. As the temperature increases, the conduction losses tend to rise due to the higher electrical resistance of the components [11, 12]. Besides that, at higher temperature the mobility of charge carriers in the semiconductor material decreases, leading to slower switching speeds. Slower switching speeds increase the time during which the IGBT is in its high-resistance state during transitions, resulting in higher switching losses [12, 13]. Additionally, higher temperatures may also increase the power required for gate drive circuits, contributing to increased switching losses.

To mitigate the adverse effects of temperature on the inverter's performance, proper thermal monitoring and cooling are essential. Efficient cooling methods, such as liquid cooling can help dissipate heat effectively and maintain the inverter's temperature within the temperature limit.

### **2.1.2. Electrical Machine**

The operation of an EM is based on the interaction between magnetic fields and electric currents, converting electrical energy into mechanical energy. Generally, EMs consist of a stator (stationary part) and a rotor (rotating part). When an electric current is supplied to the stator windings, it generates a magnetic field. The interaction between this magnetic field and the magnetic field induced by the rotor's permanent magnets or currents causes a rotational force, leading to the machine's mechanical motion [10, 14]. EVs utilize different types of EMs to drive their wheels efficiently. The most common types of EMs used in EVs are [10, 14]:

- Permanent magnet synchronous machine (PMSM): PMSMs are widely employed in electric vehicles due to their high power density, efficiency, and excellent torque characteristics. They have permanent magnets on the rotor, which interact with the stator's rotating magnetic field to produce torque. This characteristic allows for rapid torque response and enables precise control that is well-suited for various EV applications.
- Externally excited synchronous machine (EESM): EESMs allow for precise control of speed and torque due to the separate field winding in the rotor. Unlike PMSMs, EESMs offer increased robustness as they are not dependent on permanent magnets. This feature can be advantageous in scenarios where high temperatures might affect the performance of permanent magnets. However, it's important to note that EESMs are more complex than PMSMs, leading to potentially higher maintenance costs due to the additional field winding and related maintenance requirements.
- Induction machine (IM): IMs are another popular choice for EVs. They are robust, reliable, and relatively low-cost compared to other machine types. IMs operate based on electromagnetic induction, using a rotating magnetic field to induce currents in the rotor, generating torque and propelling the vehicle.
- Synchronous Reluctance Motor (SynRM): SynRMs are less common but an emerging magnet-free alternative gaining interest in EV applications. They operate on

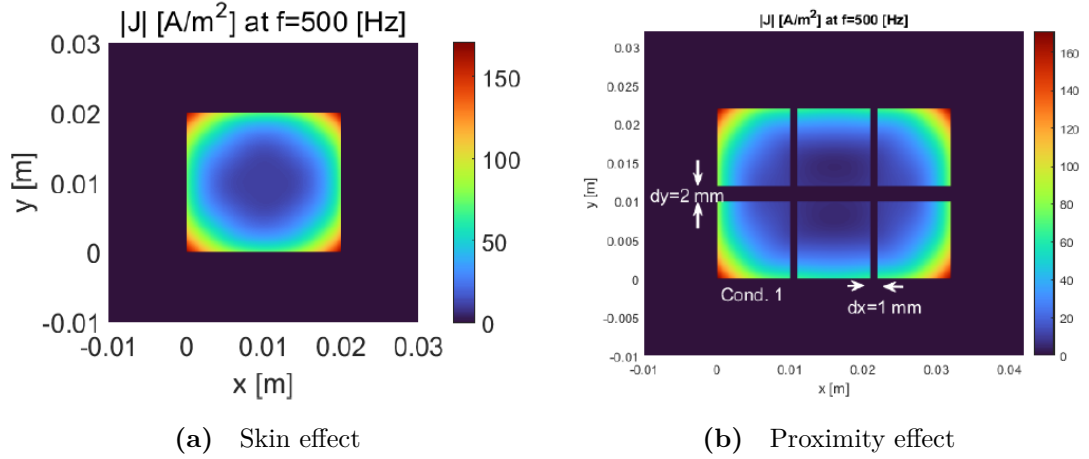


**Figure 2.3.** Magnitude of current density distribution for different types of AC losses in electrical machines

Adapted from "Skin and Proximity Effect Calculation of a System of Rectangular Conductors Using the Proper Generalized Decomposition Technique" by Tabei, B., Gole, A. M., and Kordi, B. (2024). *Energies*, 17(12), 2828. Source: <https://www.mdpi.com/1996-1073/17/12/2828>. Licensed under CC BY 4.0

magnetic reluctance and use a rotating stator field to pull a highly engineered rotor, causing it to spin in perfect synchrony. While their power density is typically lower than magnet-based motors, SynRMs combine high efficiency with the robustness of a magnet-less design, offering a compelling trade-off for next-generation EVs.

The performance and efficiency of EMs are influenced by temperature variations, as different types of losses within the machine exhibit temperature dependence. The major losses in EMs include copper losses, iron losses, magnet losses and mechanical losses. DC copper losses are the resistive losses in the windings. They are calculated using the RMS value of the AC current and the DC resistance of the copper windings. As the machine's temperature rises, the electrical resistance of the copper windings also increases leading to higher DC copper losses. Additionally, the high-frequency AC current leads to the generation of the AC copper losses in the windings. The reason behind this is an uneven current density distribution caused by eddy current-induced current displacement effects [15]. The skin effect and proximity effect are illustrated in Fig. 2.3.

The skin effect (Fig. 2.3a) occurs due to the presence of counter-directed eddy currents, which cause the charge carriers to be displaced towards the outer edge of the conductor. As a consequence, the local current density near the edge increases, creating an inhomogeneous distribution that increases the AC copper losses. The proximity effect (Fig. 2.3b) arises in addition to the skin effect when conductors are bundled together. In this scenario, the eddy current is induced by the alternating magnetic field of nearby conductors, resulting in another uneven distribution of current density. As the temperature increases, AC losses decrease in electrical conductors due to a decrease in electrical conductivity, resulting in a weakening of the movement of electrons along the edges of the conductors. As a result, the uneven distribution of current within the conductors is reduced, leading to a decrease in AC losses [15–17]. The calculation of total copper

losses has been established in (2.1).

$$P_{\text{Cu}}|_T = \frac{P_{\text{Cu,AC}}|_{T_{20}}}{\sqrt{1 + \alpha \cdot (T - T_{20})}} + P_{\text{Cu,DC}}|_{T_{20}} \cdot (1 + \alpha \cdot (T - T_{20})) \quad (2.1)$$

where  $P_{\text{Cu}}|_T$  denotes the total copper losses at the certain temperature of  $T$ .  $P_{\text{Cu,AC}}|_{T_{20}}$  and  $P_{\text{Cu,DC}}|_{T_{20}}$  are the AC and DC copper losses at the temperature of  $T_{20}$ , respectively. It should be noted that  $T_{20}$  always corresponds to 20 °C and the temperature coefficient of copper  $\alpha$  is 0.003 93 1/K.

Iron losses in EMs are primarily caused by magnetic hysteresis and eddy currents in the machine's iron core, which are reduced at rising temperatures. The hysteresis losses are proportional to the area inside the hysteresis loop as shown in Fig. 2.4. Where  $B$

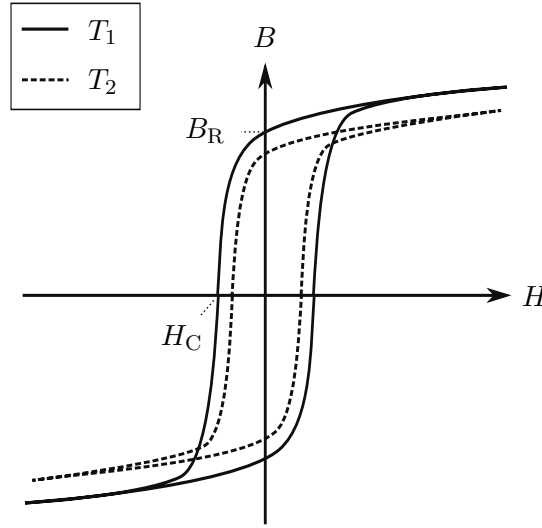


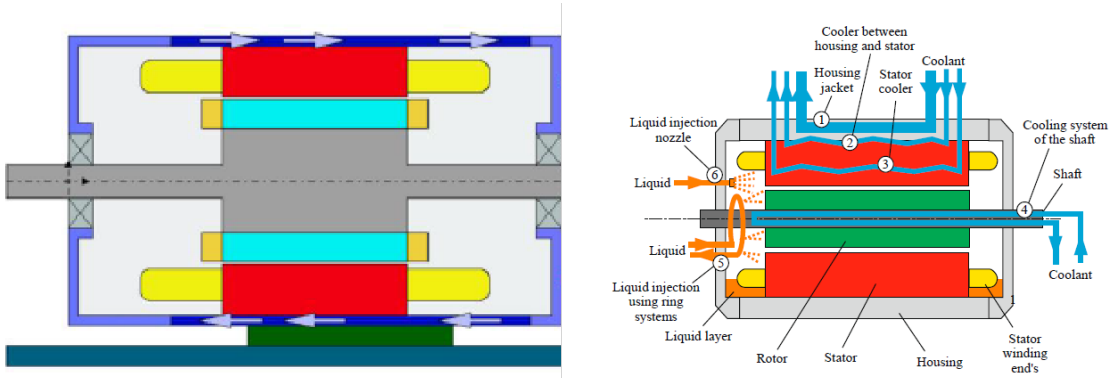
**Figure 2.4.** Hysteresis loop of a soft magnetic material at different temperatures [18]

is magnetic flux density,  $B_R$  represents remanence,  $H$  denotes field strength, and  $H_C$  indicates coercivity. At higher temperatures of  $T_2 > T_1$ , less polarization energy for the Weiss domains is needed due to increased atomic motion, resulting in lower hysteresis losses. Eddy current losses, on the other hand, are influenced by the resistivity of the iron material, which typically decreases with increasing temperature. As a result, the eddy current losses decrease with higher temperatures, contributing to a reduction in overall iron losses [18]. Magnet losses are primarily eddy current losses generated within the permanent magnets by magnetic field harmonics, which decrease as the magnet's temperature rises before irreversible demagnetization occurs. Additionally, mechanical losses also tend to reduce with increased temperature. These losses are attributed to bearing friction. As the temperature increases, the lubricant's viscosity decreases, leading to lower mechanical losses.

Therefore, effective cooling is crucial for maintaining temperatures within safe operating limits, ensuring high efficiency, reliability, and prolonging the lifespan of the EM. Liquid cooling and oil spray cooling are two effective methods used to manage the thermal challenges in EVs with powerful EMs [19,20]. Liquid cooling, as shown in Fig. 2.5a, involves circulating a coolant through the machine to absorb and dissipate the generated heat, preventing overheating and ensuring optimal performance. On the other hand, oil

## 2. Theoretical Background

spray cooling offers an alternative approach, particularly suited for high-performance EMs. In Fig. 2.5b, a fine mist of cooling oil is sprayed by injection nozzle directly onto the critical components of the EM, rapidly absorbing heat and providing targeted cooling. Both liquid cooling and oil spray cooling demonstrate their effectiveness in mitigating the thermal challenges associated with EMs in EVs. These innovative cooling solutions not only optimize the performance of the EM but also play a significant role in advancing the reliability and efficiency of EVs.



(a) Water jacket cooling

Adapted from "Modeling and Simulation of Electric Motors Using Lightweight Materials" by Boopathi, N. G., et al. (2022). Retrieved from <https://www.mdpi.com/1996-1073/15/14/5183>. Licensed under CC BY 4.0

(b) Oil spray cooling

Adapted from "Recent Developments in Cooling Systems and Cooling Management for Electric Motors" by Konovalov, D., et al. (2023). From <https://www.mdpi.com/1996-1073/16/19/7006>. Licensed under CC BY 4.0

**Figure 2.5.** EM cooling system in EVs

### 2.1.3. Gearbox

The power loss within a gearbox encompasses gear, bearing, seal, and auxiliary losses [21]. The losses in gears and bearings can be further categorized into two groups: no-load losses and load-dependent losses. Load-dependent losses consist of friction within the meshing teeth and in rolling element bearings, while no-load losses primarily arise from phenomena like oil churning, oil shearing, and windage losses [22]. The magnitude of no-load losses is chiefly influenced by lubricant properties such as density and viscosity, whereas load losses are contingent on factors like the load, coefficient of friction, and sliding velocity at the contact points between components. Under nominal gearbox conditions, load losses usually predominate, while under part-load and high-speed conditions, the total losses are primarily dictated by high no-load losses [23].

The performance and efficiency of a gearbox are significantly influenced by its operational temperature, as various losses within the gearbox exhibit temperature-dependent behavior. This phenomenon is intricate and multifaceted. Gear mesh losses arise due to the friction between interlocking gear teeth [22]. When the gear temperature rises, thermal expansion can cause changes in the contact geometry, resulting in increased mesh losses. Moreover, higher temperatures cause a reduction in lubricant viscosity, thinning the lubricating film and elevating mesh losses. Gear churning losses emanate from the viscous drag posed by the lubricant on rotating gears. These losses are directly

proportional to lubricant viscosity and the square of rotational speed [22, 24]. As the lubricant temperature increases, its viscosity declines, leading to reduced churning losses. Gear shearing losses occur when the lubricant film between mating gear teeth undergoes shearing. These losses are linked to lubricant viscosity and the sliding velocity between teeth [22, 24]. With increasing lubricant temperature, its viscosity decreases, causing a reduction in gear shearing losses. Bearing friction losses stem from the friction between rolling elements and bearing races. These losses correlate with the load and the rotational speed. In gearbox sealing, lip seals are the most common type employed [25]. These seals are typically made of elastomeric materials like rubber and rely on spring force to maintain contact with the rotating shaft [26]. When the seal temperature rises, the elastomeric material becomes softer, resulting in decreased spring force. This, in turn, can lead to heightened leakage and increased power losses. In general, when the temperature falls below freezing, the oil can gel due to a rapid increase in its viscosity, which can lead to a substantial reduction in gearbox efficiency [27–29]. Consequently, effective thermal management is imperative for the gearbox. It serves the purpose of cooling the gearbox during high-temperature operation, warming it in cold conditions to prevent lubricant oil from gelling and help to improve the efficiency of the gearbox.

## 2.2. Heat Transfer

The mechanisms of heat transfer can be categorized into the following: heat conduction, heat convection and heat radiation. Heat conduction describes the mechanism by which thermal energy is transferred from a region of higher temperature to a region of lower temperature through direct physical contact between neighboring particles or molecules. The rate of heat conduction is influenced by several factors, including the temperature difference between the two regions, the thermal conductivity of the material, and the cross-sectional area through which heat is conducted [30]. In the example of a one-dimensional plane wall, as illustrated in Fig. 2.6, the wall is under a steady-state condition with no internal heat generation. The left-side surface temperature is denoted as  $T_{LS}$ , while the right-side surface temperature is  $T_{RS}$ , and assuming that  $T_{LS}$  is higher than  $T_{RS}$ . The heat flow rate  $\dot{Q}$  across this wall, with a cross-area  $A$  and length  $L$  can be expressed as a function of the temperature gradient and thermal conductivity  $\lambda$ .

$$\dot{Q} = \lambda \cdot A \cdot \frac{T_{LS} - T_{RS}}{L} \quad (2.2)$$

Analogous to electrical resistance in electrical circuits, the thermal resistance  $R_{th}$  quantifies the extent to which heat energy encounters resistance while moving through a substance or from one point to another. This phenomenon is known as thermal resistance, and it can be defined mathematically as:

$$R_{th} = \frac{\Delta T}{\dot{Q}} \quad (2.3)$$

where  $\Delta T$  is the temperature difference between the two ends of the material and  $\dot{Q}$  is the heat flow rate passing through the material.

By combining equations (2.2) and (2.3), the conductive thermal resistance  $R_{cond}$  can be formulated in (2.4)

$$R_{cond} = \frac{T_{LS} - T_{RS}}{\dot{Q}} = \frac{L}{\lambda \cdot A} \quad (2.4)$$

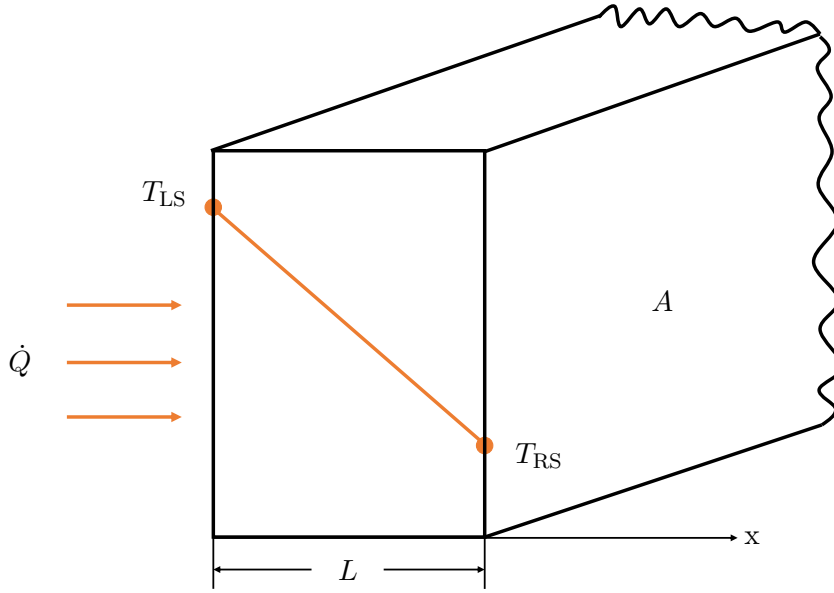


**Figure 2.6.** One-dimensional heat transfer by conduction

in general, the values for  $L$  and  $A$  in thermal resistance calculations can be obtained straightforwardly from the geometry of the components involved. However, the challenge lies in accurately determining the thermal conductivity  $\lambda$  for resistances due to the interface gaps between components. Many commercial software packages offer information on different types of materials with varying degrees of roughness and manufacturing methods to assist in setting thermal conductivity  $\lambda$ .

Heat convection is a heat transfer process that occurs when a fluid, which can be a liquid or a gas, is in motion and makes contact with a heated surface. When this happens, the fluid's movement facilitates the transfer of thermal energy from the warmer surface to the cooler one. As the fluid closer to the heated surface absorbs heat, it becomes less dense and expands, causing it to move upwards. This movement of the fluid is known as convection [31]. Convection can manifest in two primary modes: natural convection and forced convection. Natural convection is driven by buoyancy forces arising from temperature differences, resulting in fluid motion without any external mechanical intervention. In contrast, forced convection involves the use of an external force, like a fan or a pump, to actively propel the fluid. This external force accelerates the movement of the fluid, improving heat transfer efficiency by promoting more effective heat exchange between the fluid and the heated surface. In a highly simplified analysis of convection, the heat flow rate  $\dot{Q}$  depends on the convective heat transfer coefficient  $h_{\text{conv}}$  and the temperature difference between the surface  $T_{\text{SA}}$  and the surrounding ambient  $T_{\text{A}}$ .

$$\dot{Q} = h_{\text{conv}} \cdot A \cdot (T_{\text{SA}} - T_{\text{A}}) \quad (2.5)$$

Similarly, when combined with Equation (2.3), the convective thermal resistance  $R_{\text{conv}}$  can be represented as follows:

$$R_{\text{conv}} = \frac{T_{\text{SA}} - T_{\text{A}}}{\dot{Q}} = \frac{1}{h_{\text{conv}} \cdot A} \quad (2.6)$$

with

$$h_{\text{conv}} = \frac{Nu \cdot k}{L} \quad (2.7)$$

where  $L$  and  $k$  denote the characteristic length of the surface and fluid thermal conductivity, respectively. The convective heat transfer coefficient  $h_{\text{conv}}$  takes into account various factors such as fluid velocity, fluid properties, surface characteristics and the nature of the flow (whether laminar or turbulent). The Nusselt number  $Nu$  is a dimensionless parameter that gauges the efficiency of heat transfer during convection. In the context of laminar to turbulent flow transition, the Nusselt number becomes particularly relevant. In Fig. 2.7, the heat transfer coefficient  $h_{\text{conv}}$  from laminar flow to turbulent flow over the fluid velocity is shown.

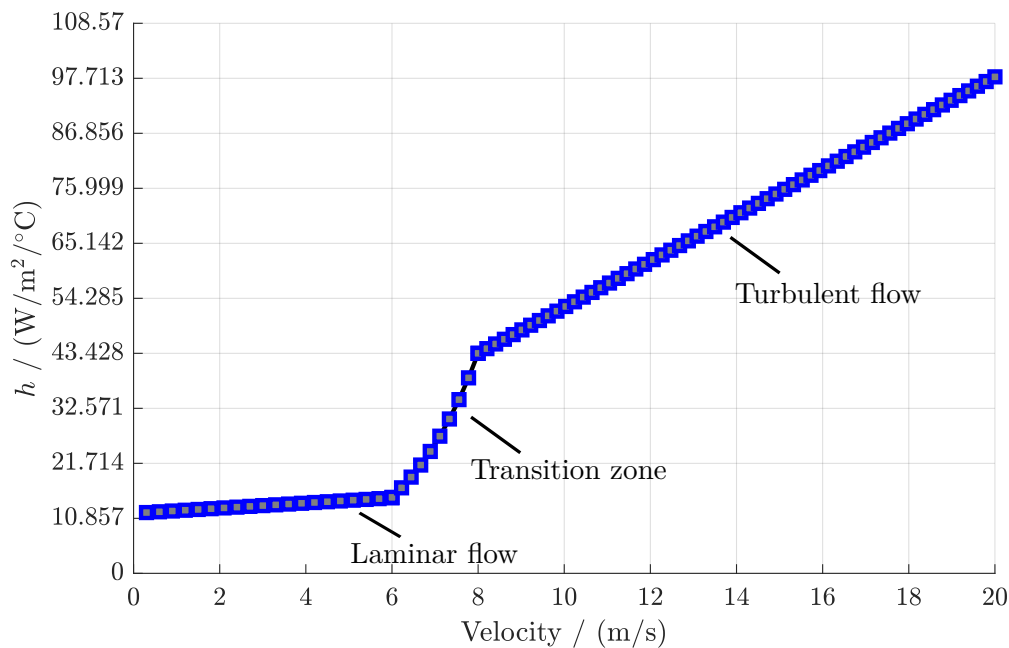


**Figure 2.7.** Enclosed channel forced convection heat transfer coefficient versus the fluid velocity [32]

As fluid flow transitions from laminar to turbulent, the Nusselt number experiences a distinct change. In laminar flow, characterized by smooth and orderly fluid motion, the Nusselt number follows an analytical relationship based on the geometry and fluid properties. However, as flow becomes more turbulent, marked by chaotic and irregular fluid motion, the Nusselt number increases due to enhanced mixing and increased contact between the fluid and the surface. Turbulent flow typically results in substantially higher heat transfer rates compared to laminar flow, making it advantageous for efficient heat exchange. Since the convection heat transfer coefficient and the Nusselt number  $Nu$  are positively correlated, it exhibits the same phenomenon.

Heat radiation refers to the energy released by substances with a temperature above absolute zero. This emission arises from changes in the arrangement of electrons in atoms or molecules that constitute the substance, regardless of its state. The energy of this emission is carried by electromagnetic waves or particles known as photons [30]. Unlike conduction or convection, radiation doesn't rely on a material medium to transmit

energy. In fact, it's most efficient in a vacuum. The heat flow rate  $\dot{Q}$  emitted by a real surface can be quantified by (2.8).

$$\dot{Q} = \sigma \cdot \varepsilon \cdot A \cdot (T^4 - T_A^4) \quad (2.8)$$

where  $\sigma$  is the Stefan-Boltzmann constant,  $\varepsilon$  is the emissivity.  $T$  and  $T_A$  are the temperatures of the surface and the ambient, respectively.

Employing a simplification in the same manner, the radiative thermal resistance  $R_{\text{rad}}$  can be represented mathematically by the surface area  $A$  and the radiative heat transfer coefficient  $h_{\text{rad}}$ :

$$R_{\text{rad}} = \frac{T - T_A}{\dot{Q}} = \frac{1}{h_{\text{rad}}A} \quad (2.9)$$

In most instances, heat transfer problems exhibit time-dependent scenarios, often associated with internal heat generation. To address these transient processes and determine temperature distribution over time within a solid, the concept of thermal capacity, also known as heat capacity, is introduced, which refers to the ability of a material or system to absorb and store thermal energy. Mathematically, thermal capacity  $C_{\text{th}}$  is expressed as:

$$C_{\text{th}} = c_s \cdot m \quad (2.10)$$

where  $m$  denotes the mass of the material and  $c_s$  is the specific heat capacity of the material that represents the amount of heat required to raise the temperature of one unit mass of a substance by one degree Celsius or Kelvin.

### 2.3. Optimization Algorithms

The use of optimization algorithms for solving electrical machine design is increasingly common, aimed at maximizing the performance and efficiency of electric vehicles. To account for component interactions, complex system-level models with several input parameters and constraints are needed, along with advanced optimization techniques.

Optimization algorithms are categorized into deterministic and stochastic. In deterministic algorithms, the optimization problem is systematically solved, whereas in stochastic algorithms, the exploration of the design space is random [33]. Deterministic optimization algorithm struggles with high computational cost when handling problems with multiple design variables using direct search methods. This is due to an inherent step-size challenge, often causing entrapment in local optima when utilizing solution gradients for faster convergence [34]. On the other hand, modern problems tend to exhibit complex and unknown functional relationships. Stochastic optimizations avoid the step-size problem and offer more detailed exploration in promising regions rather than in less promising ones. They operate without gradients and steer clear of local optima by employing random variables and a constantly evolving population. Among various stochastic algorithms evolutionary algorithms, inspired by nature, have gained significant attention. In addition, design of experiments (DOE), which is a systematic approach that plans and conducts experiments to obtain crucial insights into the relationships between input variables and output responses, could be commonly utilized as an initial stage during the optimization process to gather valuable information about the problem and to establish a feasible starting point for applying an optimization algorithm.

### 2.3.1. Evolutionary Algorithms

Evolutionary algorithms are a family of stochastic optimization techniques that mimic the natural selection and evolution process. By emulating the principles of natural selection and genetic inheritance, these algorithms aim to find the best possible solutions to complex problems. Several different types of evolutionary algorithms exist, each with its own characteristics and applications. Some of the most prominent ones include:

- Genetic algorithm (GA): GAs use the principles of selection, crossover, and mutation to evolve a population of potential solutions over generations. Solutions with better fitness values have a higher chance of being selected, and their genetic information is combined through crossover and mutation to generate new offspring, creating a process of optimization [35, 36].
- Particle swarm optimization (PSO): PSO is inspired by the social behavior of bird flocking or fish schooling. It involves particles moving through the solution space, adjusting their positions based on their own experience and the best solution found by the swarm. The particles' movements are guided by their own best-known position and the best-known position of the entire swarm [37, 38].
- Differential evolution (DE): DE is based on the concept of vector differences. It generates new candidate solutions by adding the scaled difference between two randomly selected solutions to a third solution. DE employs mutation and crossover operators to explore the solution space efficiently [39, 40].
- Ant colony optimization (ACO): ACO is inspired by the foraging behavior of ants. It uses pheromone trails left by ants to guide the search for optimal solutions. The algorithm simulates the movement of ants in the solution space and reinforces paths with higher pheromone levels, leading to the discovery of promising regions [41].

Within this work, the utilization of mixed integer distributed ant colony optimization (MIDACO) solver is employed to manage the intricacies of the optimization quandary. MIDACO represents a software utility geared towards numerical optimization, whose algorithm is devised as a versatile resolution mechanism catering to both single- and multi-objective optimization problems. A notable attribute of MIDACO lies in its adeptness in tackling constrained mixed integer nonlinear programming (MINLP) conundrums [41, 42]. To address the multi-objective MINLP problem, MIDACO employs a hybrid approach, which merges an extended evolutionary ACO algorithm with the oracle penalty method [43], designed to attain the global optimal solution while managing constraints through a parameter known as the oracle. The ACO algorithm utilized within MIDACO operates based on multi-kernel Gaussian probability density functions (PDFs) [42], which generate a series of iterations, also referred to as ants or individuals. In the MIDACO ACO algorithm, Gaussian PDFs are the core mechanism for generating new candidate solutions, or 'ants'. The framework adapts these functions to handle both continuous and integer variables, making it exceptionally effective for mixed-integer optimization problems. For continuous variables, a standard Gaussian PDF is used. It is defined by a mean, which represents the center of the search, and a standard deviation, which controls the exploration range. Sampling from this distribution generates new real-valued parameters. For integer variables, a discretized version of the Gaussian PDF is employed, where the continuous Gaussian curve is evaluated at discrete integer points.

After normalization, this process assigns a specific selection probability to each integer, allowing the same probabilistic sampling logic to apply. In tackling multi-objective optimization problems, MIDACO employs the Utopia-Nadir-Balance concept, which is effective across various types of Pareto fronts and offers an advantage by allowing faster and more thorough exploration of the most desirable section of the Pareto front [44].

### 2.3.2. Multi-objective Optimization Problem

Multi-objective optimization refers to the process of simultaneously optimizing multiple conflicting objectives in a problem. In various real-world scenarios, there are often multiple criteria or objectives that need to be considered. These objectives may be contradictory, meaning that improving one objective could lead to a deterioration in another. The goal of multi-objective optimization is to find a set of solutions that represents the best trade-offs among these conflicting objectives. Mathematically, it is written as

$$\begin{aligned} \min_{\mathbf{x}} \quad & \mathbf{F}(\mathbf{x}) = [f_1(\mathbf{x}), f_2(\mathbf{x}), \dots, f_n(\mathbf{x})] \\ \text{subject to} \quad & \mathbf{g}(\mathbf{x}) \leq 0 \\ & \mathbf{h}(\mathbf{x}) = 0 \end{aligned} \quad (2.11)$$

where input parameters  $\mathbf{x}$  which minimize a set of objective functions  $f(\mathbf{x})$ , subject to a number of inequality constraints  $\mathbf{g}(\mathbf{x})$  and equality constraints  $\mathbf{h}(\mathbf{x})$ .

A multi-objective optimization process is demonstrated in Fig. 2.8 as an instance. In this case, there are only two design variables and two objective functions. Since design variables have their own lower and upper bounds, all possible combinations of design variables fall within the design space.

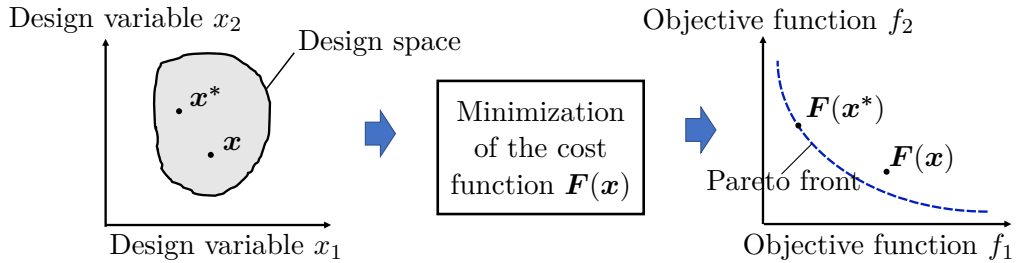


**Figure 2.8.** Illustration of multi-objective optimization process

These combinations are then mapped onto the performance space using an evaluation function  $\mathbf{F}(\mathbf{x})$  while adhering to certain constraints. For multi-objective optimizations, there is often not one unique solution, but rather a set of compromised solutions, which are commonly referred to as Pareto front. They are the set of solutions in multi-objective optimization where no other solution can improve any objective without degrading at least one other objective. The objective functions of solutions  $\mathbf{x}^*$  form the Pareto front  $\mathbf{F}(\mathbf{x}^*)$  in Fig. 2.8, representing the optimal compromise between the different objectives, offering decision-makers a range of solutions to choose.

## 3. State of the Research

This chapter provides a comprehensive overview of the thermal analysis techniques and motor scaling methods widely employed in both scientific research and industrial applications.

### 3.1. Thermal Analysis Methods

Thermal analysis of electrical machines (EMs) has not received as much attention as electromagnetic analysis in the past. This is clear from the number of technical papers published on each topic. This is especially true for small and medium-sized motors. Traditionally, motor designers have only considered thermal design aspects in a superficial way, such as specifying a limiting current density. However, this approach does not provide any indication of how the design can be improved to reduce temperatures. As the demand for miniaturization continues to grow, compact EM design requires intensive thermal investigation. Overheating is a critical concern that significantly contributes to the occurrence of failures in EMs. The excessive heat generated during operation can lead to various detrimental effects, including the thermal degradation of winding insulation and the thermal demagnetization of permanent magnets. When the temperature of the winding insulation rises beyond its rated limit, it can lead to accelerated aging, reduced mechanical strength, and eventually, insulation breakdown. This can result in short circuits, ground faults, and potential damage to the machine. Additionally, the thermal demagnetization of permanent magnets is another critical concern. In EMs that employ permanent magnets, the magnet's properties can be severely affected by elevated temperatures. High operating temperatures can result in complete demagnetization. In light of these challenges, proper thermal analysis and management are essential to estimate temperatures and prevent overheating in order to maintain the reliable operation of EMs. Over the past few decades, researchers have explored some approaches for thermal analysis, which involve current injection [45] or voltage injection [46] as well as using a flux-based temperature observer [47] in order to offer indirect insights into temperature-sensitive electrical model parameters. Despite their potential, these methods have a drawback: they are highly sensitive to electric model parameters and inaccuracies in modeling can result in significant estimation errors [48]. As a result, further methods for thermal analysis have been developed, which enhance their reliability in practical applications. The thermal analysis of EMs can be divided into three basic types: numerical method, analytical method and data-driven machine learning method.

#### 3.1.1. Numerical Method

Numerical analysis offers a significant advantage in its capability to model various device geometries. Nevertheless, it demands meticulous model setup and extensive computational time. Two primary types of numerical analysis, namely finite element analysis (FEA) and computational fluid dynamics (CFD) [49].

**Table 3.1.** Analogy between heat transfer and electrical circuit [50]

<b>Thermal properties</b>	<b>Electrical properties</b>
Temperature	Voltage
Power losses / Heat flow	Current
Thermal resistance	Resistance
Thermal capacity	Capacity

FEA plays a crucial role in the precise calculation of conduction heat transfer within intricate geometric shapes, making it particularly useful for analyzing heat transfer through strands of copper in a slot, among other scenarios. This approach enables the detailed evaluation of temperature distribution within the machine, making it ideal for detecting potential hot spots. The ability to accurately predict temperature distribution aids in identifying critical areas prone to overheating and allows for the optimization of thermal management strategies. Furthermore, it can be easily coupled with electromagnetic FEA, facilitating comprehensive loss calculations and providing a more holistic analysis of the machine’s thermal and electromagnetic behavior. This integration allows researchers and engineers to gain a comprehensive understanding of the machine’s performance, taking into account both electrical losses and thermal behavior. Ultimately, FEA serves as a powerful tool for accurately simulating and analyzing thermal aspects of electrical machines, aiding in their design, optimization, and reliability assessment.

CFD is utilized primarily to analyze and assess various aspects of coolant flow. This includes determining the flow rate, velocity, and pressure distribution within the cooling channels or water jacket around the machine, which are critical factors in ensuring efficient thermal management. Moreover, CFD is instrumental in evaluating surface heat transfer levels, enabling subsequent analysis of temperature distribution within the active material and other solid structures of the machine. By providing insights into the heat dissipation and cooling performance, CFD aids in identifying potential hot spots and optimizing the cooling system for improved thermal performance.

FEA and CFD are powerful tools commonly used for the design and validation of electrical machines. The integration of CFD with FEA, enables a comprehensive thermal analysis, where both thermal conduction and thermal convection are considered together. These numerical methods require detailed geometries and accurate materials information to provide accurate results. However, due to the complexity of the modeling process and the extensive computational resources, FEA and CFD are not well-suited for real-time or online applications.

### 3.1.2. Analytical Method

The Analytical Method in this subsection revolves around employing a lumped parameter thermal network (LPTN) analysis. This analysis technique draws parallels to electrical network analysis as shown in Table 3.1, where temperature takes the role of voltage, power losses mimic current, and thermal resistance resembles electrical resistance. A well-established practice in thermal network involves amalgamating components with

similar temperatures into distinct nodes [15]. The network then utilizes thermal resistances to depict the heat transfer taking place between these interconnected nodes. The thermal capacity provides valuable insights into how a system responds to changes in temperature over time. Fig. 3.1 presents an illustrative a simple LPTN thermal network of a stator segment. Where  $R$  symbolizes the thermal resistance between nodes,  $P$  represents the losses and  $T$  corresponds to the temperature. In this instance, the stator segment is divided into three nodes: winding, stator yoke and stator tooth, each with its distinct heat capacity and losses. These nodes are interconnected by thermal resistance, thereby forming a thermal network aimed at simulating the temperature at each individual node.

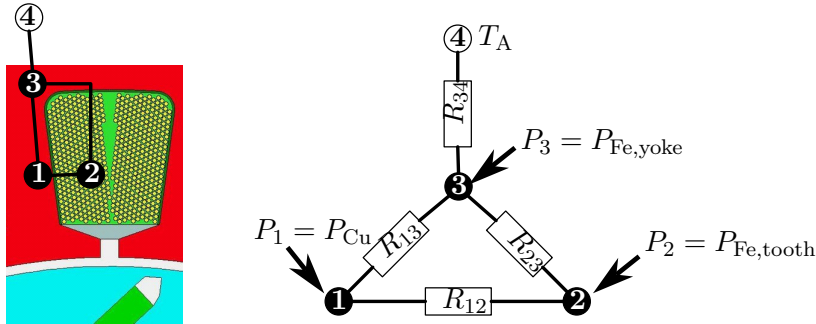


**Figure 3.1.** A simple LPTN thermal network of a stator segment in Ansys Motor-CAD

LPTNs can be acquired through two distinct methods: white-box approaches rely on the classical T-equivalent-circuit-method [51] or the k-shift-approach [52], producing complex differential-algebraic models [53]. These models require substantial computational resources, often exceeding the capabilities of industrial processing platforms when computed in real-time scenarios. In addition, complete material and geometric data must be accessible, which might not always be the situation, especially for older prototype motors. In contrast, grey-box LPTNs utilize empirical training data based on extensive motor measurements, leading to significantly reduced model complexity and greater system abstraction. Due to their limited model order, grey-box LPTNs can be effectively processed in real-time applications. However, the use of grey-box LPTNs exclusively focus on estimating the average temperature of components, leading to a lack of critical hot spot information [54]. As demonstrated in [55], this issue can be resolved by incorporating empirically obtained data that establish the relationship between average and hot spot temperatures of specific motor components. Otherwise, if only average temperatures are estimated, it is advisable to adopt more conservative safety margins concerning temperature limits during operation.

### 3.1.3. Data-Driven Machine Learning Method

Data-driven machine learning method is a novel approach for thermal modeling that relies on data rather than explicit motor sheet information. It operates as a blackbox model, enabling high estimation accuracy without requiring in-depth expertise in machine knowledge. The model parameters are solely derived from observational data,

minimizing the relevance of domain knowledge [56]. This broad applicability allows for easy transfer of insights from the application case of EMs to related fields of interest, such as power electronics overheating or battery state-of-health [57]. The current state-of-the-art leverages recurrent neural network (RNN) and convolutional neural network (CNN) architectures. RNN topologies are a suitable choice for the given application due to their well-established capability to model time dependencies. Additionally, the use of memory gate control, first introduced as long short-term memory (LSTM) in [58], can effectively solve the problems of gradient disappearance and explosion in order to enhance prediction accuracy. The structure of LSTM modeling the sequence learning is illustrated in Fig. 3.2. In contrast to RNN, which store all information at every moment without making any selection, LSTM is distinctive because it selectively stores information thanks to its control gates. The central memory cell is employed to retain all information, while the gates are responsible for governing the storage and deletion of information at each time step. The LSTM design is optimized for predicting time series data with diverse time scales, making it an ideal choice for numerous electric motor applications, especially in the automotive industry [59]. For many years, RNNs have been the dominant choice for sequential learning problems. However, CNNs, which have been widely used in image processing, have shown superior performance even in classic long-term memory sequential problems recently [60]. The possibility of achieving this architectural improvement was introduced in the work of Bai [60], which coined it as the temporal convolutional network (TCN). The TCN incorporates recent advancements in handling sequential data, such as causal and dilated convolutions, while being presented in a simplified form compared to previous approaches [56].

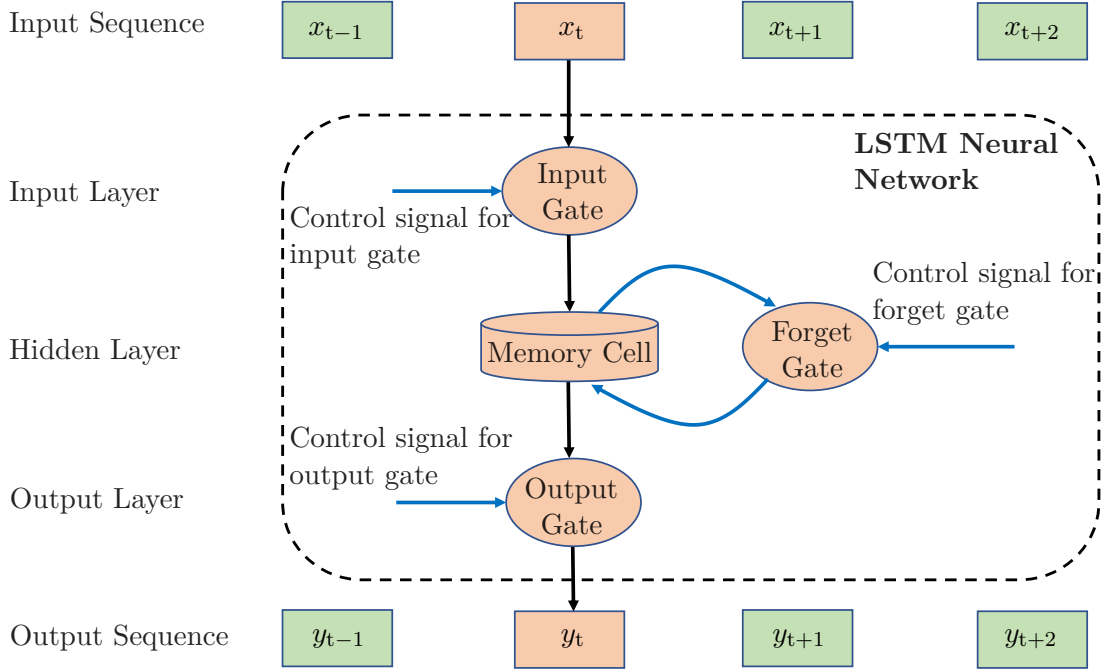


**Figure 3.2.** Structure of the sequence learning with LSTM

Training a machine learning model involves dealing with numerous hyperparameters. The initial step in model selection is to determine the weight parameters of a neural network through error backpropagation. At the second level of inference, careful con-

sideration is given to selecting the parameters that define the neural network's size, the optimization algorithms employed, precise weight initialization strategies, and other related factors. Given the extensive number of hyperparameters, an automated and structured approach for their selection holds great potential. During the third level of inference, model engineers are involved in selecting the parameters of the hyperparameters optimization [59].

Data-driven machine learning method also presents several challenges [56]:

1. **Interpretability:** Due to its data-driven nature, the model lacks clear physical meaning, making it difficult to interpret the underlying factors influencing the thermal behavior.
2. **Estimation accuracy vs. Real-time capability:** There exists a trade-off between achieving high estimation accuracy and maintaining real-time capability, as sophisticated data-driven models may be computationally intensive and challenging to apply in real-time scenarios.
3. **Initialization issues:** Black-box models do not allow for straightforward setting of initial values, potentially leading to issues during the initialization phase.
4. **Data availability:** Real-world data required for training such models can be limited, expensive, and time-consuming to acquire. The question of how much data is necessary to achieve reliable thermal estimations remains a crucial consideration.

## 3.2. Scaling of Electrical Machine

The topic of scaling laws for EM is of great importance in the field of electrical engineering. EMs are widely used in various industrial applications such as electric vehicles (EVs), wind turbines and robotics. Since FEA has been widely utilized in modeling of EMs, Domingues et al. [61] introduced an offline database approach to numerically generate various sizes of EMs using FEA. However, generating an accurate optimal efficiency map for a specific design using FEA becomes time-consuming due to the need to simulate a large number of current magnitudes and phase angles to maximize efficiency. This computational effort is further compounded when multiplied by the number of different machine designs. In order to efficiently explore a broad design space for various automotive applications within a shorter timeframe, scaling a reference machine to derive others with varying designs without reiterating intricate detailed design processes presents an intriguing strategy for system-level design. In this context, various scaling methodologies, such as map deforming [62], analytical calculation [63] and neural networks [64] have been addressed in the literature.

The most commonly employed methods for adjusting parameters are scaling laws of EM. W.L. Soong [65] discusses the relationship between torque capability and physical size in EMs. It highlights that torque is proportional to the product of rotor volume and shear stress, where shear stress depends on electric and magnetic loading. The rotor volume and design factors, such as rotor aspect ratio, stator slot diameter ratio, and the number of poles, play crucial roles in motor sizing. He delves into the practical considerations related to rotor volume, diameter, and stator slot diameter to optimize machine design, which offers valuable insights for machine design. Bone [66] established fundamental scaling laws for induction machines. His research reevaluated the classical

output equation's foundation and proposed an alternative equation based on conductor current density, suggesting the possibility of achieving output scaling with the cube of the diameter. Additionally, Binns and Shimmin [67] attempted to determine the scaling laws for permanent magnet synchronous machines (PMSMs). Their approach aimed to maintain equal current density for radially scaled machines, although this didn't preserve the same magnet flux density. Gu and Stiebler [68] addressed the scaling laws for switched reluctance machines using two-dimensional nonlinear field analysis, simplifying specific torque predictions during early design stages. Stipetic, Zarko, and Popescu [69, 70] expanded upon the work of Gu and Stiebler and derived analytical scaling laws for PMSMs based on axial scaling factor and radial scaling factor along with rewinding procedures as shown in Fig. 3.3. These factors are utilized to calculate torque, losses, and masses of scaled machines, aiming at rapidly and accurately recalculating parameters of PMSMs when geometrically scaled. The authors used Poisson's equations to derive the scaling law by maintaining the same magnetic flux density in the scaled machine. The scaling model includes adjustments for end-winding influence and three-dimensional permanent magnet loss effects. This is particularly valuable as it addresses the non-linear behavior and spatial challenges in the end-winding regions. The derived scaling laws are validated using FEA simulation, demonstrating that these analytical methods can closely match computationally expensive FEA results.

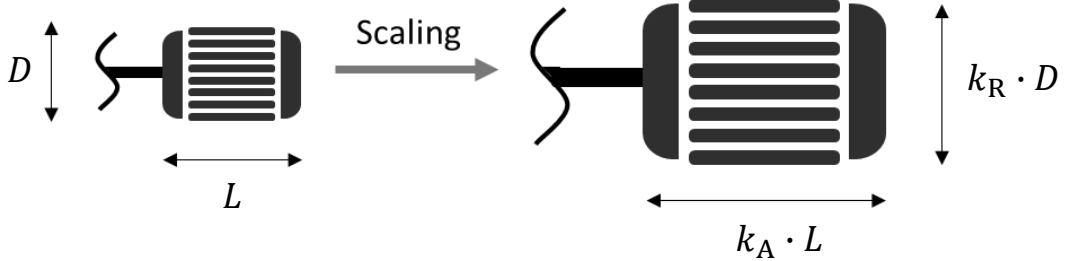


**Figure 3.3.** Scaling of PMSMs mainly based on axial scaling factor and radial scaling factor

The majority of scaling methods discussed in the literature primarily emphasize scaling the electromagnetic properties of the scaled machine, often overlooking the impact of scaling on thermal loading. The temperatures in the rotor magnets, for example, have a major influence on the transient performance and lifespan of EMs. Consequently, scaled machines may exceed the maximum permitted temperature or remain underutilized in their thermal potential, resulting in oversized configurations for the intended application. Therefore, it is essential to incorporate thermal effects into the scaling process.

Several efforts have been dedicated to tackling this issue. The work of Nell, Groschup and Hameyer [71] makes significant contributions to the field of electromagnetic-thermal modeling of induction machines (IMs) by introducing an efficient coupling approach using scaled FEA solutions. The key contribution is the development of a novel scaling procedure that allows updating temperature-dependent losses without performing repeated FEA simulations, significantly reducing computational costs while maintaining accuracy.

A scaling approach for FEA solutions that considers temperature variations in both stator and rotor, enabling quick updates of electromagnetic losses based on temperature changes. In their work, a three-node LPTN thermal model, combined with scaled FEA solutions, is applied. To validate this model, temperature measurements are collected from 10 IMs using multiple sensors. The comparison between scaled results and full FEA simulations demonstrates good agreement. This coupled electromagnetic-thermal model can be utilized for continuous operation conditions and powertrain optimization to verify temperature constraints. Although this work combines electromagnetic and thermal modeling and considers the impact of temperature on Ohmic losses, it does not address how the temperature model changes when the motor is scaled.

Stipetic, Zarko, and Popescu [69,70] examined the thermal effects associated with scaling and noted that, although thermal properties such as material conductivity and specific cooling techniques are not explicitly recalculated in this simplified scaling method, the proportional changes in cooling performance typically compensate for the thermal effects of scaling. In both radial and axial scaling, maintaining a constant specific electric load means that increasing the motor size results in reduced current density, which, in turn, decreases the temperature rise in the windings due to copper losses. Additionally, radial scaling aids in managing temperature by increasing the cooling surface area, which helps dissipate the heat generated from losses, thereby keeping thermal levels within acceptable limits. Furthermore, in some motor simulations, the average temperature throughout the motor cycle is utilized instead of a detailed temperature profile or distribution. This cycle-averaged approach simplifies the assessment of thermal impacts by concentrating on the overall thermal load rather than intricate thermal modeling, making it suitable for simulations that require quick evaluations, particularly in extensive optimization processes. Therefore, Stipetic, Zarko, and Popescu only analyzed the impact of temperature from a quantitative perspective. An accurate scalable thermal model is essential for more precise motor temperature estimation needed in powertrain optimization.

Pauli, Ruf, and Hameyer [72] proposed an approach to evaluate the thermal overload capability of scaled PMSMs under different load conditions. The authors considered the influence of temperature in the scaling of magnetic quantities and losses. The development of a scaled thermal model, employing the LPTN thermal model based on the stator geometry, allows for a rapid assessment of the thermal performance of PMSMs with different sizes and configurations. Using scaling laws, the authors present a method to predict thermal limits and optimize the design of PMSMs without extensive simulation or testing, which is often time-consuming and resource-intensive. While the developed thermal model offers practical insights, it has two limitations. Due to simplification, it is constrained by its focus solely on winding temperature and its applicability limited to steady-state conditions.

Künzler et al. [73] introduce a scalable thermal model specifically for evaluating thermal performance in PMSMs used in EVs. The model is focused on assessing how variations in motor dimensions affect the machine's thermal behavior under different driving conditions. The authors use a detailed LPTN thermal model to simulate heat distribution and temperature rise across different motor components. They examine a range of motor dimensions, varying parameters like length, diameter, and the number of turns per coil. This thermal model includes nodes that represent different sections of the motor, including the stator tooth, end windings, rotor iron, magnet, rotor shaft and cooling jacket, each connected by thermal resistances that reflect heat transfer through

conduction and convection. The thermal model helps determine how machine scaling impacts heat generation and dissipation, which is crucial for defining optimal motor designs that meet the thermal requirements of diverse driving scenarios, such as city driving or highway driving. By assessing the motor's thermal response early in the design phase, motor dimensions can be adapted more efficiently, preventing overheating in smaller and higher power density designs. Additionally, the study provides insight into the effect of use case-specific variables, like vehicle type (e.g., city cars versus highway cars) and driving cycle, on motor temperatures. Despite its innovations, the model has certain limitations. The model relies on certain design assumptions, such as specific material properties and detailed motor geometry, which may not be known at the early stage of system-level optimization. In addition, the scaled thermal model of PMSMs is neither validated with temperatures from FEA simulations nor with measurement data from a real PMSM.

The study conducted by Makowski and Helenbrook [74] primarily addresses thermal scaling in PMSMs, focusing on how these machines can maintain optimal temperatures across different sizes. The contribution of this research is its integration of thermal considerations into the scaling laws of PMSMs, which traditionally only focus on electromagnetic factors. By including temperature effects, the authors presented a more accurate LPTN thermal model with 13 nodes for predicting thermal behavior. The researchers explored both axial and radial scaling (increasing diameter) typically results in higher surface area but may not proportionally increase cooling capacity due to the reduced ratio of surface area to volume at larger scales. They also accounted for various cooling mechanisms, such as an impeller-driven cooling flow within the machine, simulating the cooling performance in different configurations. However, the scaled PMSMs are not validated using values from FEA simulations or real PMSM measurement data. Future research could focus on exploring this validation.

Therefore, one of the key focuses of this dissertation is to address this research gap by studying and improving the parameter scaling of the thermal model of EM at the system level, and by developing an efficient approach for scaling thermal parameters in a low-order LPTN model to estimate the temperature of the scaled PMSM for transient conditions, taking into account the temperature dependence of motor losses.

## 4. Thermal Modeling of Electric Drivetrain

Estimating component temperatures of electric drivetrain is vital for both efficiency improvement and the prevention of stressful operating conditions. Utilizing a model-based approach is the most effective method to obtain temperatures, even in case of sensor failures. To begin with, a centralized and compact thermal model for predicting the temperature of the electric drivetrain is introduced. Not only is the thermal modeling of each individual component addressed, but also the simulation of thermal coupling between the components is undertaken. The proposed thermal model is parameterized using the global identification approach, employing experimental measurements conducted at the vehicle level. Finally, the cross-validation results are presented and a discussion of potential improvements is initiated. The modeling method and analysis introduced in this chapter are based on a previously published IEEE paper [75].

### 4.1. Lumped Parameter Thermal Network for Drivetrain

The drivetrain system for an A-segment battery electric vehicle (BEV) consists of an inverter, a permanent magnet synchronous machine (PMSM) and a gearbox with a fixed gear ratio. Fig. 4.1 illustrates the proposed heat-transfer paths in the drivetrain system. The inverter and the PMSM are liquid-cooled, while the gearbox is passively cooled by the surrounding air.  $T_{INV}$ ,  $T_{PMSM}$  and  $T_{GB}$  denote the temperatures of inverter, PMSM and gearbox, respectively. The coolant inlet temperature and volume flow rate are represented by  $T_{CIN}$  and  $\dot{V}_{CIN}$ . The coolant flow passes through the inverter upstream of the PMSM.  $T_{COI}$  and  $T_{COE}$  are the coolant outlet temperature of the inverter and the PMSM. From the available measurement data it can be derived that in the inverter and the PMSM, most of the waste heat is taken away by the coolant, which are expressed as  $\dot{Q}_{INV-C}$  and  $\dot{Q}_{PMSM-C}$ . A small part of the heat from the inverter and PMSM entering into the air in the drivetrain compartment are  $\dot{Q}_{INV-ADC}$  and  $\dot{Q}_{PMSM-ADC}$ . Due to the lack of water cooling in the gearbox, most of the generated heat  $\dot{Q}_{GB-ADC}$  can only be dissipated into the surrounding air. Since the air in the drivetrain compartment absorbs the heat from the components, its temperature  $T_{ADC}$  is higher than the ambient temperature  $T_A$ , so there is a heat transfer from the compartment to the ambient  $\dot{Q}_{ADC-A}$ . It should be noted that the thermal conductive resistance between the inverter housing and the PMSM housing is neglected. Since the inverter and the motor use the same cooling duct, they have a stronger thermal coupling than housing. For the gearbox, it is assumed that the dominant thermal coupling exists only between the rotor of the PMSM and the gear of the gearbox. The thermal conductive resistance between the PMSM housing and gearbox housing is neglected as well.

In this work, the utilization of the lumped parameter thermal network (LPTN) provides a straightforward and practical means of determining critical component temperatures. This approach is quite abstract as only the most dominant heat paths are

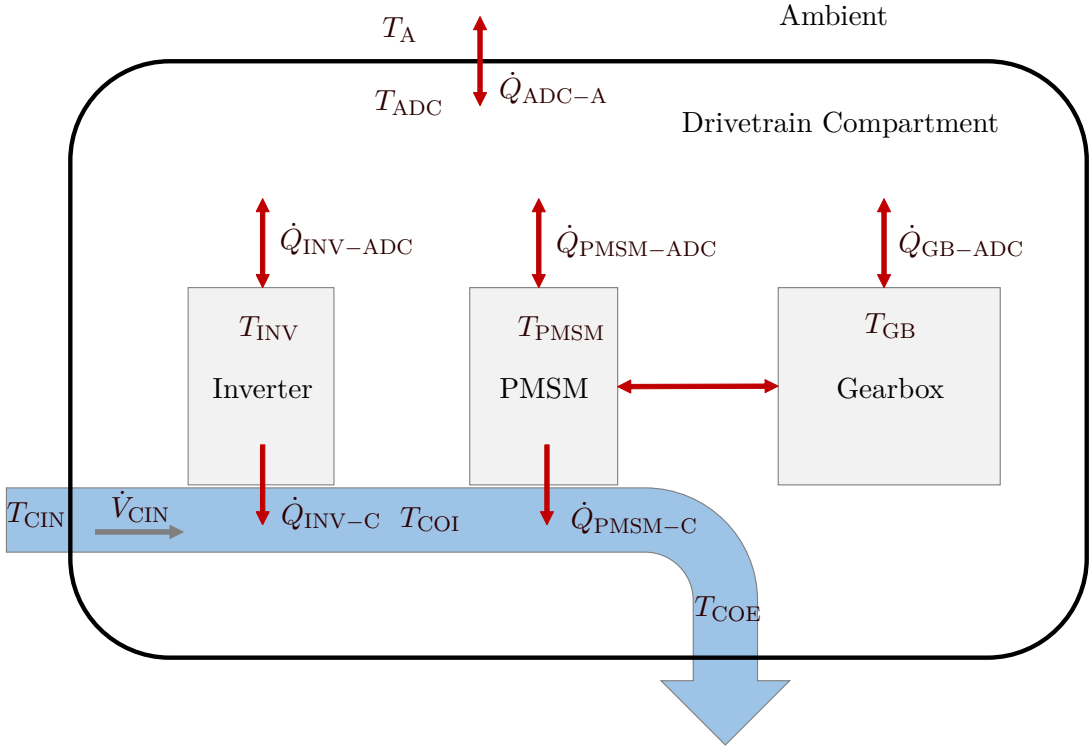


**Figure 4.1.** Proposed heat transfer paths inside the whole drivetrain system

© 2020 IEEE. Reprinted, with permission, from B. Chen et al., "A Comprehensive Thermal Model For System-Level Electric Drivetrain Simulation With Respect To Heat Exchange Between Components," 19th IEEE ITherm Conference, 2020, pp. 558-567

considered. Thus, this modeling is very beneficial to implement and the computation effort is minimal. In the LPTN model, heat transfer processes are abstracted by equivalent electric circuit diagrams [76]. The parts of a component that have similar temperatures are lumped together as a single node in the network, which is separated by thermal resistances to represent the heat transfer between different parts [49]. The thermal system dynamics are represented by thermal capacity. In the upcoming subsections, the focus is placed on the thermal modeling of each individual component.

#### 4.1.1. Thermal Network for Coolant Outlet Temperature

With a significantly enhanced level of integration, it is common practice to assemble the PMSM, inverter, and gearbox as a unified and compact unit. Given the close thermal interconnections between these components, it becomes essential to establish a system-level thermal model for the entire drivetrain. In this scenario, it is imperative to model the coolant outlet temperature, as the coolant outlet temperature of the inverter corresponds to the coolant inlet temperature of the electric motor, thus illustrating the thermal coupling between the inverter and the electric motor. In accordance with the first law of thermodynamics, the total energy within a system remains constant, thus the energy change in a system  $\Delta E_{\text{sys}}$  during a process is determined by taking the difference between the energy input  $E_{\text{in}}$  and the energy output  $E_{\text{out}}$  of the system [77]. Therefore,

the energy balance can be expressed as follows:

$$E_{\text{in}} - E_{\text{out}} = \Delta E_{\text{sys}} \quad (4.1)$$

Incompressible liquids have identical specific heats at constant volume  $c_{s,v}$  and constant pressure  $c_{s,p}$ . As a result,  $c_{s,v}$  and  $c_{s,p}$  can be omitted, and both specific heats are represented by a single symbol  $c_s$ . The specific heats of incompressible liquid depend solely on temperature, so the internal energy change in solids and liquids can be written as [77]

$$\Delta E_{\text{sys}} = m \cdot c_s \cdot \Delta T \quad (4.2)$$

Based on this, the differential equation of the temperature of incompressible liquid within the control volume can be derived from the energy balance:

$$c_s \cdot m \cdot \frac{dT}{dt} = \dot{h}_{\text{in}} + \dot{Q} - \dot{h}_{\text{out}} - \dot{W} \quad (4.3)$$

where  $c_s$  represents the specific heat,  $m$  signifies the liquid mass within the control volume, and  $T$  denotes the outlet temperature of the liquid. In Fig. 4.2, the conservation of energy for the incompressible liquid within the control volume is depicted. The figure illustrates the enthalpy inflow term  $\dot{h}_{\text{in}}$ , the enthalpy outflow term  $\dot{h}_{\text{out}}$ , as well as the heat transfer, including conduction and convection, at the system boundaries represented as  $\dot{Q}$ . Furthermore, it also includes the work term  $\dot{W}$  (excluding flow work).

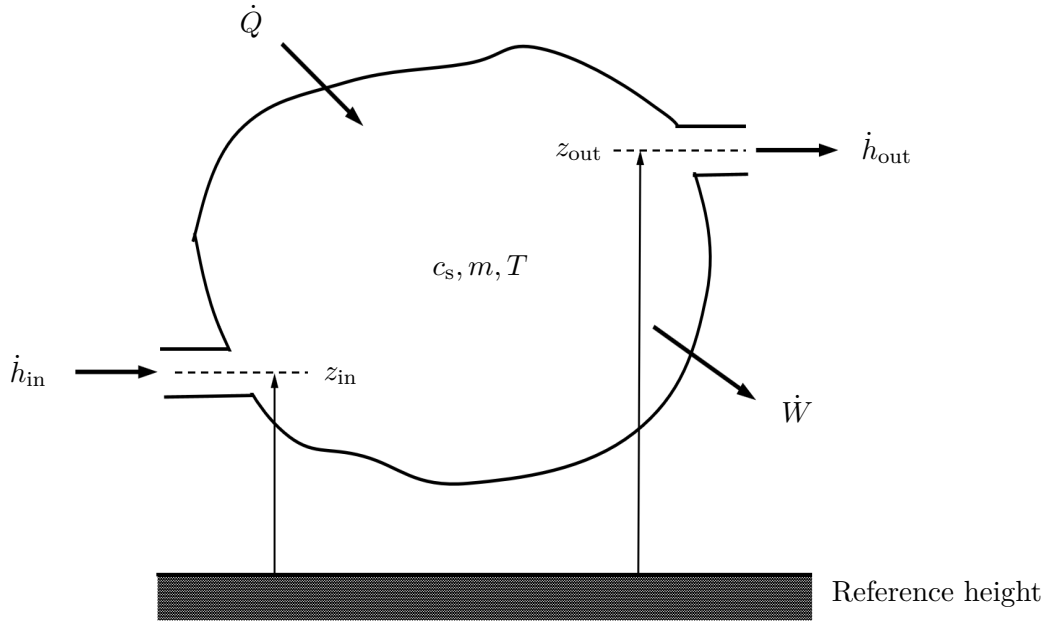


**Figure 4.2.** Conservation of energy for coolant in the control volume [30]

The energy transported by the mass entering or leaving the system is accounted for in the enthalpy inflow term  $\dot{h}_{\text{in}}$  and the enthalpy outflow term  $\dot{h}_{\text{out}}$ . These terms include the mass flow rate and the rates at which the respective types of energy (thermal energy, flow work energy, kinetic energy, and potential energy) are transported [30]. Thermal energy refers to the amount of energy stored in a fluid due to its temperature. Flow

work energy refers to the energy required to move a fluid from one location to another against a pressure gradient, which is relevant when considering the work done on or by the fluid, such as in pumps. Kinetic energy refers to the energy associated with the motion of the fluid, while the potential energy is the energy changed in gravitational potential. Therefore, the inflow and outflow energy flow of coolant can be expressed as in (4.4).

$$\begin{aligned} \dot{h}_{\text{in}} &= \dot{m}_{\text{in}}(c_s \cdot T_{\text{in}} + p_{\text{in}} \cdot \nu_{\text{in}} + \frac{1}{2}v_f^2 + g \cdot z_{\text{in}}) \\ \dot{h}_{\text{out}} &= \dot{m}_{\text{out}}(c_s \cdot T_{\text{out}} + p_{\text{out}} \cdot \nu_{\text{out}} + \frac{1}{2}v_f^2 + g \cdot z_{\text{out}}) \end{aligned} \quad (4.4)$$

where  $\dot{m}_{\text{in}}$  and  $\dot{m}_{\text{out}}$  are the mass flow into and out of the system.  $\nu_{\text{in}}$  and  $\nu_{\text{out}}$  represent the specific volume of the inlet and outlet fluid,  $v_f$  is the velocity of the fluid,  $g$  denotes the gravitational acceleration, and  $z_{\text{in}}$  and  $z_{\text{out}}$  signify the vertical coordinate of the inlet and outlet fluid.

It is assumed that the fluid functions as an incompressible liquid and there are no leaks, so its mass flow rates are equal at both the inlet and outlet of the control volume.

$$\dot{m}_{\text{in}} = \dot{m}_{\text{out}} = \dot{m} \quad (4.5)$$

Moreover, in heat transfer involving fluids, it is typically the case that changes in kinetic and potential energy are minimal and can be neglected. Consequently, the enthalpy flow of the inlet and outlet fluids can be simplified as

$$\begin{aligned} \dot{h}_{\text{in}} &= \dot{m}(c_s \cdot T_{\text{in}} + p_{\text{in}} \cdot \nu_{\text{in}}) \\ \dot{h}_{\text{out}} &= \dot{m}(c_s \cdot T_{\text{out}} + p_{\text{out}} \cdot \nu_{\text{out}}) \end{aligned} \quad (4.6)$$

Further simplification of the control volume system, as depicted in Fig. 4.2, is streamlined into Fig. 4.3. In the practical coolant system, there is an absence of the work term  $W$ , but instead, it features heat transfer from the component housing to coolant. It is also assumed that the coolant in the channel is a homogeneous mixture, so its temperature in the channel is the same as the coolant outlet temperature.

$$T = T_{\text{out}} \quad (4.7)$$

By merging equations (4.3), (4.6) and (4.7), the resulting differential equation for the coolant outlet temperature is formulated in (4.8):

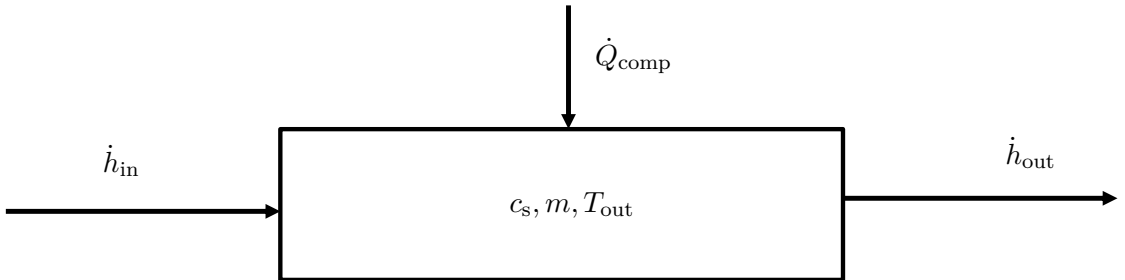


**Figure 4.3.** Simplified representation of energy conservation for coolant in the control volume system

$$\begin{aligned}
 c_s \cdot m \cdot \dot{T}_{\text{out}} &= \dot{h}_{\text{in}} + \dot{Q}_{\text{comp}} - \dot{h}_{\text{out}} \\
 c_s \cdot m \cdot \dot{T}_{\text{out}} &= \dot{m} \cdot c_s \cdot (T_{\text{in}} - T_{\text{out}}) + \frac{1}{R_{\text{th}}} \cdot (T_{\text{comp}} - T_{\text{out}}) + \dot{m} \cdot (p_{\text{in}} \cdot v_{\text{in}} - p_{\text{out}} \cdot v_{\text{out}}) \\
 c_s \cdot m \cdot \dot{T}_{\text{out}} &= \frac{1}{1/(\dot{m} \cdot c_s)} \cdot (T_{\text{in}} - T_{\text{out}}) + \frac{1}{R_{\text{th}}} \cdot (T_{\text{comp}} - T_{\text{out}}) + \dot{m} \cdot (p_{\text{in}} \cdot v_{\text{in}} - p_{\text{out}} \cdot v_{\text{out}})
 \end{aligned} \tag{4.8}$$

Thereby, the differential equation of the LPTN for the coolant outlet temperature, as shown in Fig. 4.4, can be derived in the following manner. The mathematical representation of the LPTN differential equation encapsulates the rate of change of the coolant outlet temperature with respect to time. Fig. 4.4 visually represents the components and interactions considered in the LPTN, providing a graphical insight into the thermal network's structure. The given set of equations provides a dynamic representation of

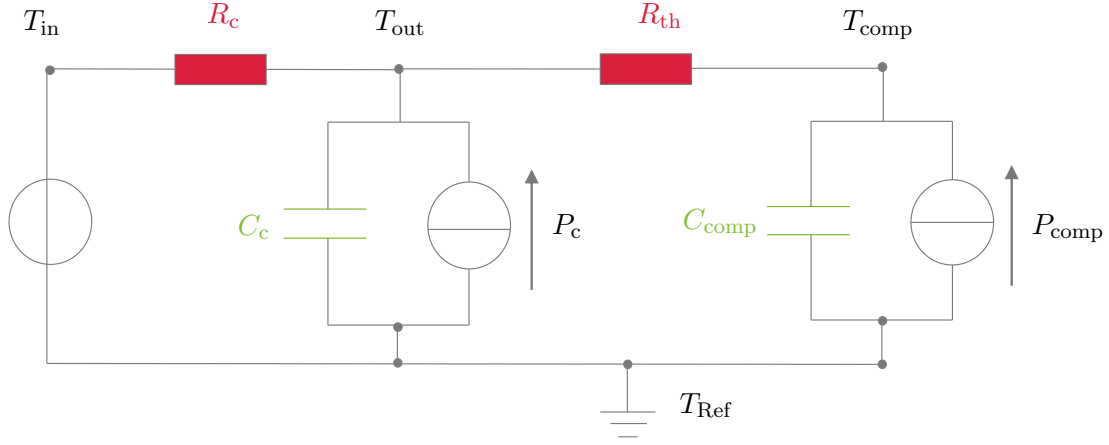


**Figure 4.4.** Proposed LPTN for the coolant outlet temperature

a thermal system, specifically focusing on the coolant temperature dynamics. The resulting differential equation forms a dynamic model that can be solved or simulated to predict the transient behavior of the coolant outlet temperature under different operating conditions.

$$C_c \cdot \dot{T}_{\text{out}} = \frac{1}{R_c} \cdot (T_{\text{in}} - T_{\text{out}}) + \frac{1}{R_{\text{th}}} \cdot (T_{\text{comp}} - T_{\text{out}}) + P_c \tag{4.9}$$

where

$$\begin{aligned}
 C_c &= c_s \cdot m \\
 R_c &= \frac{1}{\dot{m} \cdot c_s} \\
 P_c &= \dot{m} \cdot (p_{\text{in}} \cdot v_{\text{in}} - p_{\text{out}} \cdot v_{\text{out}})
 \end{aligned} \tag{4.10}$$

These equations collectively describe the energy balance and thermal dynamics within the system. Equation (4.9) expresses how the rate of change of coolant outlet temperature is influenced by thermal capacity, thermal resistances, and power input. Equations (4.10) provide specific definitions for the thermal capacity, thermal resistance, and power terms in the context of the coolant flow and component interactions. The thermal capacity of the coolant consists of the specific heat capacity  $c_s$  and the mass of the coolant in the channel  $m$ , which characterizes the system's ability to store thermal energy. The

thermal resistance of the coolant is the reciprocal of the product of mass flow rate  $\dot{m}$  and the specific heat capacity  $c_s$ . The power associated with the coolant, indicating the rate at which energy is either generated or absorbed by the coolant, is expressed in terms of the mass flow rate  $\dot{m}$  and the difference between the product of inlet pressure  $p_{in}$  and the specific volume of the inlet coolant  $\nu_{in}$  and the product of outlet pressure  $p_{out}$  and the specific volume of the outlet coolant  $\nu_{out}$ .

#### 4.1.2. Thermal Network and Loss Model of Inverter

The LPTN thermal modeling of an inverter involves constructing a network of thermal elements that represent the key components and their thermal interactions within the inverter. The goal is to create a mathematical model that can predict and analyze the temperature distribution and dynamics of the inverter under various operating conditions. Fig. 4.5a and Fig. 4.5b illustrate the diagram of the simplified inverter's structure and the corresponding LPTN model, respectively.

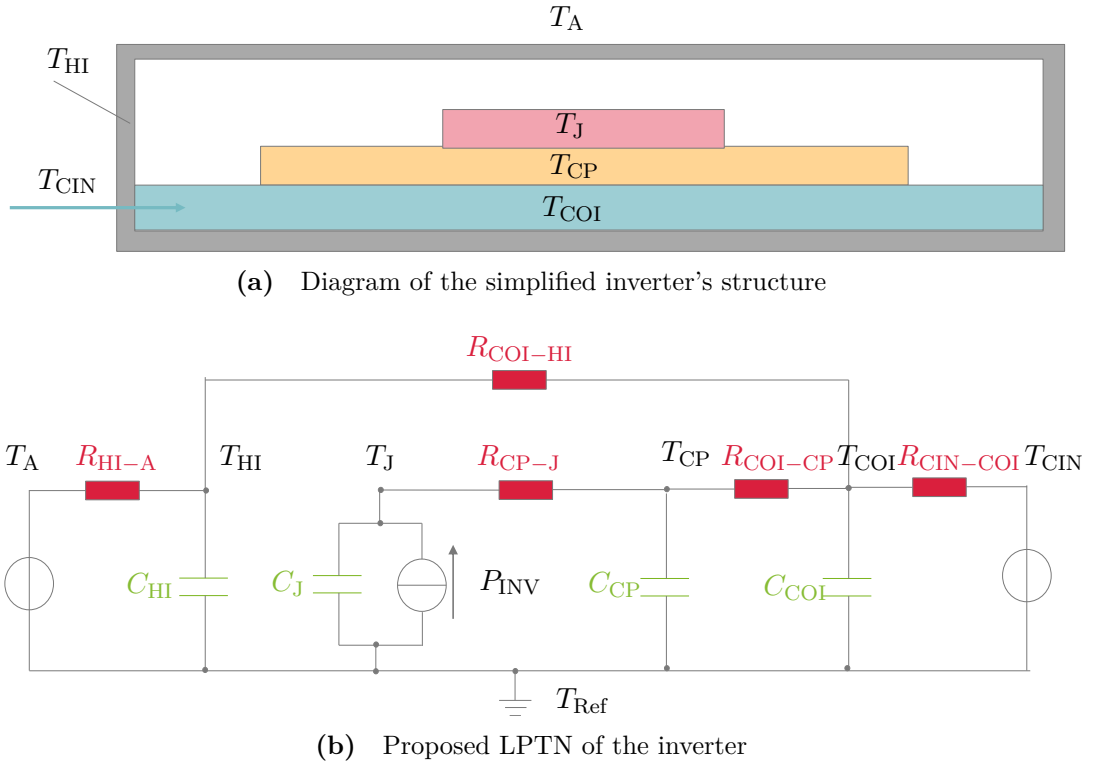


**Figure 4.5.** Thermal modeling of the inverter

In the context of thermal analysis, a Cauer thermal model based on the geometry is constructed for the LPTN model of the inverter, incorporating four nodes that represent the junction temperature  $T_J$ , cooling plate temperature  $T_{CP}$ , housing temperature  $T_{HI}$ , and coolant outlet temperature  $T_{COI}$ . The Cauer thermal model utilizes these nodes to establish a network that captures the thermal interactions and dynamics within the inverter. This model is particularly beneficial for predicting and analyzing temperature changes across different components and assessing the overall thermal performance of the inverter. The inlet coolant temperature  $T_{CIN}$  and ambient air temperature  $T_A$  serve as the boundary conditions for the thermal system. The temperature simulation in the

LPTN is based on the reference temperature  $T_{\text{Ref}}$ . The model assumes that the inverter losses  $P_{\text{INV}}$  are concentrated in the junction, which is representative for the average temperature of all IGBTs and diodes in the inverter.

The application of Kirchhoff's laws in the thermal domain ensures the conservation of energy within the network. For each thermal node in the LPTN of the inverter, the sum of heat inflows must be equivalent to the sum of heat outflows. The proposed LPTN of the inverter can be described in the form of the state space. The state space representation of the inverter LPTN model is expressed in (4.11).

$$\begin{aligned}\dot{\mathbf{x}} &= \mathbf{A}(T_J, T_{\text{CIN}}, \dot{V}_{\text{CIN}})\mathbf{x} + \mathbf{B}\mathbf{u} \\ \mathbf{y} &= \mathbf{C}\mathbf{x}\end{aligned}\quad (4.11)$$

where

$$\mathbf{A} = \begin{bmatrix} -\frac{1}{C_J R_{\text{CP-J}}} & \frac{1}{C_J R_{\text{CP-J}}} \\ \frac{1}{C_{\text{CP}} R_{\text{CP-J}}} & -\frac{1}{C_{\text{CP}}} \left( \frac{1}{R_{\text{CP-J}}} + \frac{1}{R_{\text{COI-CP}}} \right) \\ 0 & 0 \\ 0 & \frac{1}{C_{\text{COI}} R_{\text{COI-CP}}} \\ 0 & 0 \\ 0 & \frac{1}{C_{\text{CP}} R_{\text{COI-CP}}} \\ -\frac{1}{C_{\text{HI}}} \left( \frac{1}{R_{\text{COI-HI}}} + \frac{1}{R_{\text{HI-A}}} \right) & \frac{1}{C_{\text{HI}} R_{\text{COI-HI}}} \\ 0 & -\frac{1}{C_{\text{COI}}} \left( \frac{1}{R_{\text{COI-CP}}} + \frac{1}{R_{\text{CIN-COI}}} \right) \end{bmatrix}$$

$$\mathbf{B} = \begin{bmatrix} \frac{1}{C_J} & 0 & 0 \\ 0 & 0 & 0 \\ 0 & 0 & \frac{1}{C_{\text{HI}} R_{\text{HI-A}}} \\ 0 & \frac{1}{C_{\text{COI}} R_{\text{CIN-COI}}} & 0 \end{bmatrix}$$

$$\mathbf{C} = \begin{bmatrix} 1 & 0 & 0 & 0 \\ 0 & 1 & 0 & 0 \\ 0 & 0 & 1 & 0 \\ 0 & 0 & 0 & 1 \end{bmatrix}$$

$$\mathbf{y} = [T_J \ T_{\text{CP}} \ T_{\text{HI}} \ T_{\text{COI}}]$$

$$\mathbf{u} = [P_{\text{INV}} \ T_{\text{CIN}} \ T_{\text{A}}]$$

where, bold symbols denote vector or matrix quantities. The output vector  $\mathbf{y}$  contains the temperatures of the junction, cooling plate, housing and coolant. The input vector  $\mathbf{u}$  comprises the losses in the inverter, the coolant inlet temperature and the ambient temperature. (4.11) is a linear parameter-varying (LPV) system, because the thermal resistances in matrix  $\mathbf{A}$  are nonlinear and subject to variation with the scheduling variables [38], which include the junction temperature, the coolant inlet temperature and volume flow rate. This is because the thermal conductivity of silicon is highly temperature-sensitive [78] and the thermal resistance of fluid forced convection (laminar flow and turbulent flow) is dependent on the coolant inlet temperature and volume flow rate [79]. Therefore, the thermal resistance between junction and cooling plate  $R_{CP-J}$  in the temperature range from 20 °C to 200 °C can be approximated by

$$R_{CP-J} = R_{CP-J,0} \cdot [1 + \alpha_{CP-J} \cdot (T_J - T_{J,0})] \quad (4.12)$$

According to the IGBT materials thermal properties at different temperatures, the junction temperature is taken into account for the thermal parameter during the modeling to improve the accuracy of the estimation [78]. Thus, the thermal capacitance of the junction  $C_J$  can be derived as:

$$C_J = C_{J,0} \cdot T_J^{b_J} \quad (4.13)$$

where  $T_{J,0}$  denotes the reference temperature of junction.  $R_{CP-J,0}$  and  $C_{J,0}$  represent the thermal resistance and thermal capacity at the reference temperature, respectively.  $\alpha_{CP-J}$  and  $b_J$  are the coefficients that account for the temperature-dependent behavior.

To assess the total losses of the inverter, a comprehensive set of measurements is conducted on a test bench. The key parameters considered include input direct current (DC) power and output alternating current (AC) power, with measurements taken across different stator temperatures (-10 °C, 30 °C, 70 °C, and 110 °C). The inverter's internal temperature is monitored using negative temperature coefficient (NTC) sensors, which are integrated into the power electronics of the inverter for accurate temperature measurement [27]. The NTC sensor is a type of temperature sensor whose electrical resistance decreases as the temperature increases, which is commonly used for temperature measurement and control in various electronic and industrial applications. The efficiency of the inverter is evaluated through efficiency maps, representing the relationship between input power and output power at various temperatures. These maps, illustrated in Fig. 4.6, provide a visual representation of how the inverter's efficiency varies under different thermal conditions.

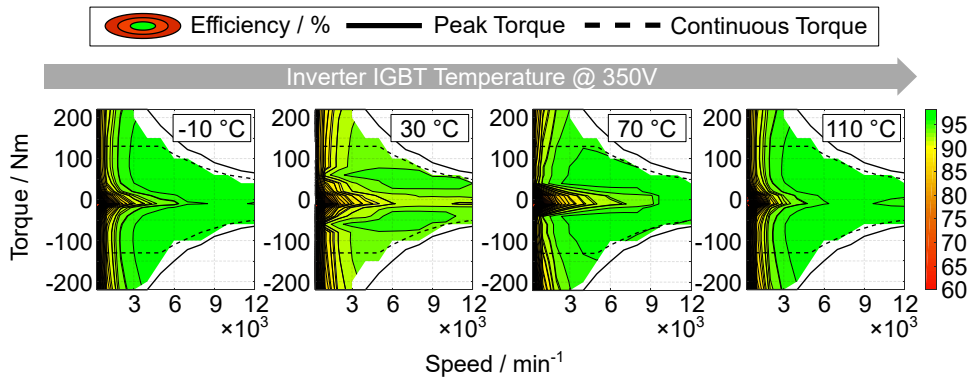
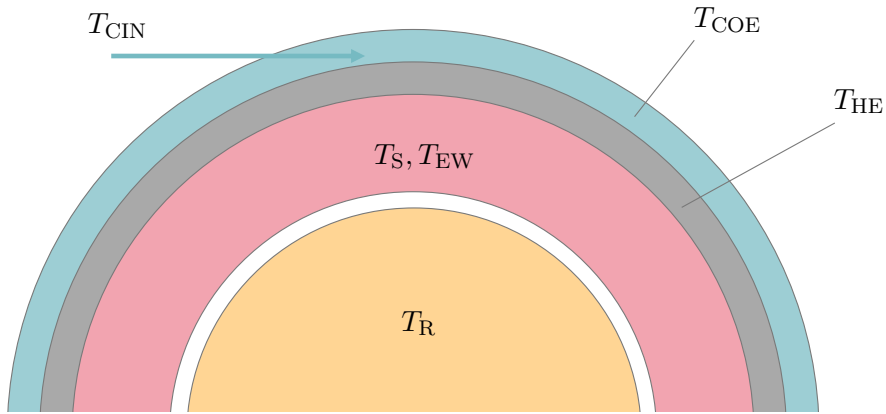


**Figure 4.6.** Efficiency maps of inverter for different temperatures [27]

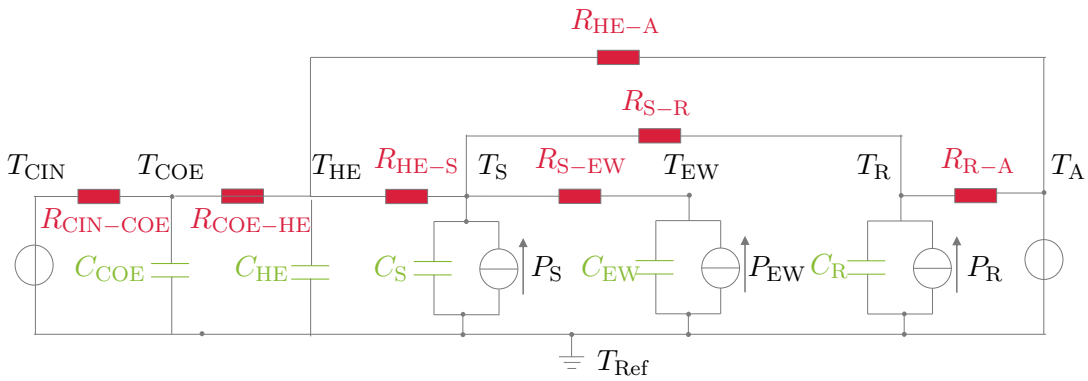
The efficiency maps of the inverter are related to speed, torque and temperature. In a general sense, rising temperature will increase the losses of the inverter and reduce efficiency. However, the actual measurement results show a less straightforward relationship due to variations in motor currents at different temperatures. To accurately capture the inverter losses within the LPTN, the speed and torque trajectories of the driving cycle are utilized. This involves tracking the changes in motor speed and torque over time during the driving cycle. By incorporating the losses map at different operating points and temperatures, the inverter losses within the LPTN can be precisely calculated.

### 4.1.3. Thermal Network and Loss Model of Electric Motor

With the intention of modeling the thermal behavior, the PMSM can be divided into five parts: the stator, rotor, end winding, housing and coolant as shown in Fig. 4.7a. The ambient is considered to be outside the PMSM. The PMSM generates heat during operation, attributed to electrical and mechanical losses. LPTN modeling is a commonly used approach for characterizing the thermal behavior of electric motors. This method simplifies the complex thermal interactions within the motor into a network of thermal elements, each of which represents a component with specific thermal properties. Through the application of the LPTN model, it becomes possible to accurately simulate the thermal behavior of each individual component.



(a) Diagram of the simplified structure of PMSM



(b) Proposed LPTN of the PMSM

**Figure 4.7.** Thermal modeling of the PMSM

The LPTN model for the PMSM is shown in Fig. 4.7b. The predicted temperatures for the PMSM are represented in five nodes corresponding to the stator  $T_S$ , end winding  $T_{EW}$ , rotor  $T_R$ , housing  $T_{HE}$  and coolant outlet temperature  $T_{COE}$ . The coolant inlet temperature  $T_{CIN}$  and the ambient temperature  $T_A$  are the boundary conditions for the thermal system. Moreover, the losses  $P$  in the stator, end winding and rotor are introduced as heat sources, which represent the inner heat generation in the system.

Like the inverter mathematical modeling, Kirchhoff's laws are used to derive the differential equations of the thermal dynamics of the system. For every thermal node within the LPTN of the PMSM, the total heat inflow must equal the total heat outflow. Therefore, the differential equations for each thermal node can be established and the proposed LPTN of PMSM can be described in the form of state-space form.

$$\begin{aligned}\dot{\mathbf{x}} &= \mathbf{A}(T_S, T_R, T_{CIN}, \dot{V}_{CIN}, n)\mathbf{x} + \mathbf{B}\mathbf{u} \\ \mathbf{y} &= \mathbf{C}\mathbf{x}\end{aligned}\quad (4.14)$$

where

$$\mathbf{A} = \begin{bmatrix} -\frac{1}{C_S} \left( \frac{1}{R_{HE-S}} + \frac{1}{R_{S-EW}} + \frac{1}{R_{S-R}} \right) & \frac{1}{C_S R_{S-EW}} & \frac{1}{C_S R_{S-R}} & 0 & 0 \\ \frac{1}{C_{EW} R_{S-EW}} & -\frac{1}{C_{EW} R_{S-EW}} & 0 & -\frac{1}{C_R} \left( \frac{1}{R_{S-R}} + \frac{1}{R_{R-A}} \right) & 0 \\ \frac{1}{C_R R_{S-R}} & 0 & 0 & 0 & 0 \\ \frac{1}{C_{HE} R_{HE-S}} & 0 & 0 & 0 & 0 \\ 0 & 0 & 0 & 0 & 0 \\ 0 & \frac{1}{C_S R_{HE-S}} & 0 & 0 & 0 \\ 0 & 0 & 0 & 0 & 0 \\ -\frac{1}{C_{HE}} \left( \frac{1}{R_{COE-HE}} + \frac{1}{R_{HE-S}} + \frac{1}{R_{HE-A}} \right) & \frac{1}{C_{COE} R_{COE-HE}} & -\frac{1}{C_{COE}} \left( \frac{1}{R_{COE-HE}} + \frac{1}{R_{CIN-COE}} \right) & 0 & 0 \end{bmatrix}$$

$$\mathbf{B} = \begin{bmatrix} \frac{1}{C_S} & 0 & 0 & 0 & 0 \\ 0 & \frac{1}{C_{EW}} & 0 & 0 & 0 \\ 0 & 0 & \frac{1}{C_R} & 0 & \frac{1}{C_R R_{R-A}} \\ 0 & 0 & 0 & 0 & \frac{1}{C_{HE} R_{HE-A}} \\ 0 & 0 & 0 & 1 & 0 \\ & & & C_{COE} R_{CIN-COE} & \end{bmatrix}$$

$$\mathbf{C} = \begin{bmatrix} 1 & 0 & 0 & 0 & 0 \\ 0 & 1 & 0 & 0 & 0 \\ 0 & 0 & 1 & 0 & 0 \\ 0 & 0 & 0 & 1 & 0 \\ 0 & 0 & 0 & 0 & 1 \end{bmatrix}$$

$$\mathbf{y} = [T_S \ T_{EW} \ T_R \ T_{HE} \ T_{COE}]$$

$$\mathbf{u} = [P_S \ P_{EW} \ P_R \ T_{CIN} \ T_A]$$

where the output vector  $\mathbf{y}$  contains the temperature of the stator, end winding, rotor, housing and the coolant outlet temperature. The input vector  $\mathbf{u}$  comprises the loss entries in the stator, end winding and rotor, along with the coolant inlet temperature and ambient temperature. The scheduling variables in (4.14) include the speed, stator temperature, rotor temperature of the PMSM, as well as the coolant inlet temperature and volume flow rate, due to the temperature and flow rate dependencies of the fluid in the air gap and cooling channel.

The thermal resistance  $R_{S-EW}$  between stator and end winding is modeled as a constant according to the conductive heat transfer, while the convection resistances, such as  $R_{C-HE}$  and  $R_{S-R}$ , depend on the fluid temperature  $T$  and the respective fluid volume flow rate  $\dot{V}$  for laminar and turbulent flows. The forced convection correlations for the Nusselt number  $Nu$  are given by:

$$Nu = a \cdot (Re)^b \cdot (Pr)^c \quad (4.15)$$

where  $a$ ,  $b$  and  $c$  are constants of the forced convection correlation.  $Nu$ ,  $Re$  and  $Pr$  denote Nusselt number, Reynolds number and Prandtl number respectively. Regarding the heat transfer fundamental formulas in (2.6) - (2.7), the convection resistance for a given contact surface area in the LPTN model are defined as (4.16) according to [79]

$$\begin{aligned} R_{\text{conv}} &\sim \frac{1}{h} \sim \frac{1}{Nu} \sim \frac{1}{a \cdot (Re(\dot{V}, T))^b \cdot (Pr(T))^c} \\ &= R_{\text{conv},0} \cdot \underbrace{\left(\frac{\dot{V}_0}{\dot{V}}\right)^{b_{\text{th}} - \alpha_{\text{th}} \cdot \left(1 - \frac{T_0}{T}\right)}}_{(Re(\dot{V}, T))^b} \cdot \underbrace{\left(\frac{T_0}{T}\right)^{a_{\text{th}}}}_{(Pr(T))^c} \end{aligned} \quad (4.16)$$

where  $R_{\text{conv},0}$  describes the reference convection resistance at the reference temperature  $T_0$  and the reference volume flow rate  $\dot{V}_0$ .  $b_{\text{th}}$ ,  $\alpha_{\text{th}}$  and  $a_{\text{th}}$  are the function coefficients to approximate the temperature and flow rate dependence of fluid, which are determined by the parameter identification.

The equation (4.16) represents the convective thermal resistance as a function of fluid flow parameters for Reynolds number, temperature-related parameters for Prandtl number, and their variations with respect to reference conditions. This kind of relationship is often encountered in convective heat transfer analysis, where the Nusselt number and convective heat transfer coefficient are crucial in understanding the heat transfer characteristics of a fluid. It's worth noting that this expression seems to be derived from a

correlation or empirical relation for convective heat transfer, and the specific values of the constants ( $b_{th}$ ,  $\alpha_{th}$  and  $a_{th}$ ) would typically be determined based on experimental data for a particular fluid flow.

With respect to the convection resistance of  $R_{S-R}$ , the temperature in the air gap  $T_{Airgap}$  is approximated by taking the average temperature of the stator and rotor. This simplification assumes that the temperature distribution within the air gap is relatively uniform and that taking the average temperature adequately represents the thermal conditions in this region. This is a simplification made to facilitate the analysis or modeling of the thermal behavior within the system. Mathematically, this approximation can be expressed as:

$$T_{Airgap} = (T_S + T_R)/2 \quad (4.17)$$

To simplify the analysis, the thermal resistance  $R_{R-A}$  is modeled as a constant in this work. It is assumed that only natural convection occurs between the rotor and the ambient through the shaft. Natural convection can usually dominate the cooling at low air speed [32]. Thermal capacity is mainly related to the geometry and the material property. Since the temperature has little impact on the motor materials, thermal capacity can be considered constant as well. This simplification is made to strike a balance between accuracy and computational complexity. However, it's essential to be aware of the assumptions and limitations introduced by such simplifications when interpreting the results.

In the LPTN temperature model, the loss estimation has a significant impact on the accuracy of the temperature prediction. The PMSM is measured on the test bench for the entire speed-torque-plane at the different average thermal conditions ( $-10^\circ\text{C}$ ,  $30^\circ\text{C}$ ,  $70^\circ\text{C}$  and  $110^\circ\text{C}$ ). The electrical power and the mechanical power of the PMSM are measured in order to derive the losses of the PMSM. The NTC sensors, which are built into the stator of PMSM, are used to measure the internal temperature of components. The internal temperatures are used as the target temperature for the conditioning system, which are communicated via CAN. The measurement setup is given in [80]. The calculated losses are implemented in three-dimensional maps and the calculated efficiency maps as shown in Fig. 4.8.

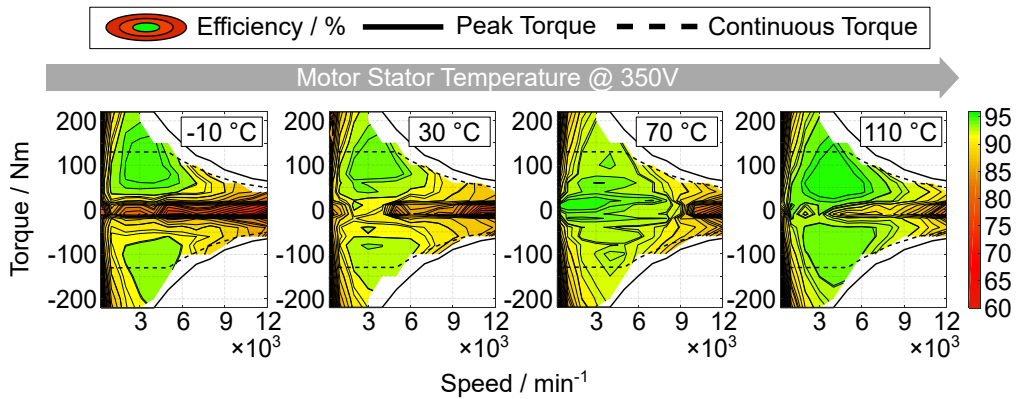


**Figure 4.8.** Efficiency maps of PMSM for different temperatures [27]

From Fig. 4.8, we can find that a rising temperature in the field-weakening range has a positive impact on the efficiency of PMSM, while increasing copper losses with temperature negatively affect efficiency at low speeds [81]. This is due to the weakening

of the fields of the permanent magnets in the rotor. The accuracy of the efficiency map at 70 °C shown in Fig. 4.8 is not plausible due to measurement errors in the low-speed, light-load region. As a result, only the efficiency maps at −10 °C, 30 °C and 110 °C are considered.

In order to simulate the temperature in LPTN, we employ a Motor-CAD model to reconstruct the loss distribution in the PMSM, namely the stator, rotor, and end winding losses. This reconstructed reference electric motor is a water jacket cooled axial channel PMSM designed for automotive applications with a housing diameter and length of 270 mm and 245 mm, respectively. The key parameters of the reference PMSM are listed in Table 4.1.

**Table 4.1.** Main parameters of the reference PMSM

Source: Chen et al. (2024). Reprinted with permission from SAGE Publications, Inc. doi:10.1177/09544070241254557

Discription	Value	Unit
No. pole pairs	3	-
No. slots	36	-
Nominal speed	4000	1/ min
Maximum speed	12000	1/ min
Peak torque	220	Nm
Peak power	97	kW
DC-Voltage	350	V
Housing diameter	270	mm
Housing length	245	mm
Stator bore diameter	240	mm
Stator outer diameter	240	mm
Core length	123	mm
Air gap	1	mm

With the aim of modeling the electromagnetic properties, a distributed winding scheme with 7 turns and 3 pole pairs was determined from the datasheet [82]. Additionally, the cross-sectional area  $A_{Cu}$  of the copper in each slot can be calculated based on a maximum effective current of 300 A and a given current density of 15.1 A/mm<sup>2</sup>.

$$A_{Cu} = \frac{300}{15.1} = 19.87 \text{ mm}^2$$

With the assumption of a wire slot fill factor of 0.84 and the number of strands of 40, the initial slot depth and tooth width were set to 27 mm and 5.5 mm respectively. Further modifications in the electromagnetic modeling were aimed at the position of the interior

permanent magnets and flux barriers in the rotor lamination as well as the magnet materials. The magnet type was set to N42SH with interior U-shape, since the remanent flux density of this type resulted in the highest agreement. The choice of materials for electrical steel was M300-35A. The initial design of the cross-section of the PMSM is shown in Fig. 4.9. The match between the modeled peak torque curve  $M_{\max, \text{MotorCAD}}$  and the measured peak torque curve is achieved through several modification iterations (see Fig. 4.10). The nominal speed is  $4000 \text{ min}^{-1}$ , which is mostly the same as in the datasheet.

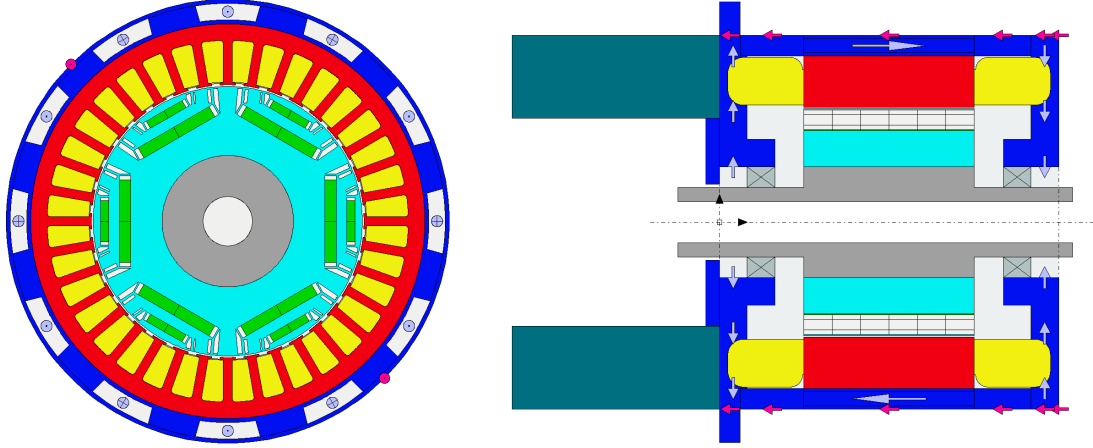


**Figure 4.9.** Initial design of the cross-section of the PMSM in Motor-CAD

An initial approximation of the losses was derived using the Motor-CAD LAB module with the control algorithms of maximum torque per ampere (MTPA). A production-related factor of 1.5 was used to subsequently analyze the iron loss in the stator and rotor, while hybrid finite element analysis (FEA) modeling with a default adjustment factor of 1 was used to estimate the AC copper loss based on the flux density levels in the slot [83,84]. AC copper losses are generated due to the proximity effect and skin effect. The proximity effect is the increase in ohmic loss due to high frequency currents in adjacent conductors. These give rise to eddy currents which cause a non uniform current distribution over the conductors cross-section. The skin effect leads to an increase in the AC resistance and thus an increase in the copper loss. The increase can be surprisingly large in high speed machines of e.g.  $12\,000 \text{ 1/min}$  and hairpin electrical machines (EMs) [85,86]. Apart from this, the friction loss was neglected in the initial assumption. The resulting deviation from the measured loss map is presented in Fig. 4.10. Negative values indicate higher losses in the model than in the measurement.

The losses agreed well with the measurements in the basic speed range. However, the field weakening range showed a dichotomy, with Motor-CAD overestimating the losses at high speeds and light loads but underestimating them at higher loads. As the mean loss deviation occasionally reached the kilowatt range, direct use of the losses for modeling was considered insufficiently accurate. By comparing the current value of operating points in the field weakening, we found that the simulated current value was larger than the measured current value, which leads to an overestimating of the DC copper loss at low loads. The reason may be that the magnet flux is too large and requires a larger reverse d-current to weaken the magnetic field. From this point, we can also conclude that there is an underestimating of the iron loss or AC copper loss in the field weakening

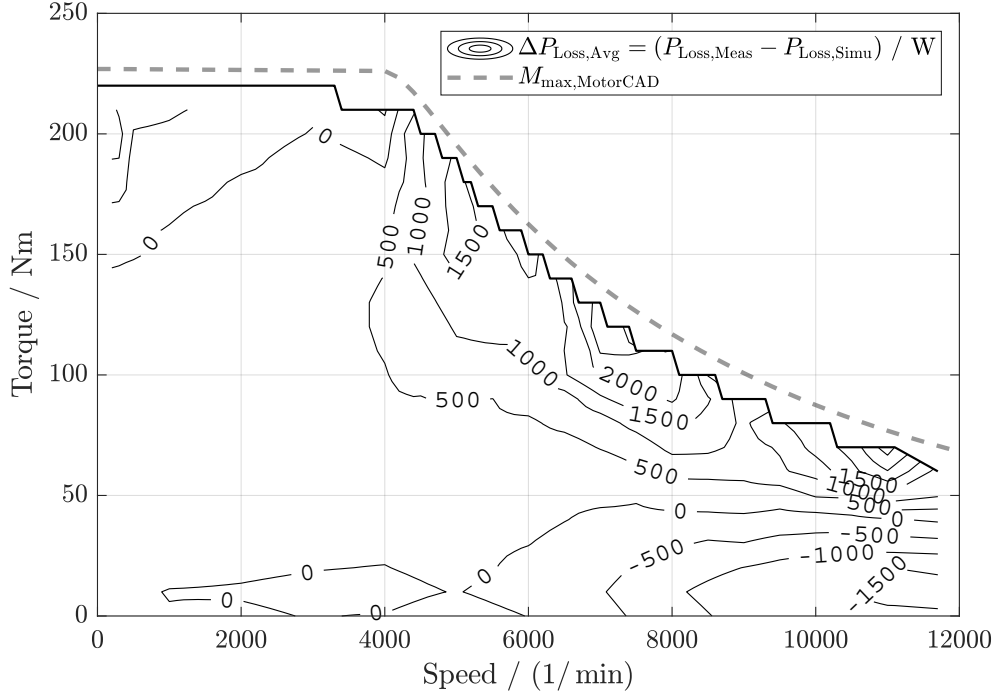


**Figure 4.10.** Average loss difference between the measurement and the loss model at DC-voltage of 350 V for the initial assumption

range at higher loads, in view of the fact that the DC copper loss (corresponding to the current value) is already too large, the simulation total loss is still relatively smaller than the measured value. For this reason, the following measures were conducted to fine-tune the Motor-CAD model [87]:

- Magnet remanence is the magnetic flux retained by the magnet field without magnetic field excitation, which is an important parameter affecting motor performance. This can reduce magnet flux saturation. Magnet remanence  $B_R$  and reversible temperature coefficient of induction  $\alpha_{B_R}$  are set to 1.31 T and  $-0.08\%/^{\circ}\text{C}$  respectively.
- Adjustment of slot depth and tooth width to change the magnet flux saturation in the stator, in order to adjust the magnetic field strength and iron loss distribution. Slot depth and tooth width are set to 24 mm and 7 mm respectively.
- Magnet shape has a significant impact on magnetic flux distribution and magnetic field strength. By optimizing the magnet shape, the magnetic flux distribution can be adjusted to reduce magnet flux. Meanwhile it increases the reluctance torque and reduces the current for torque generation, thereby reduce the DC copper loss.

The modified cross-section of the PMSM is illustrated in Fig. 4.11. The production-related factor of the iron loss in the stator and rotor was used to 1.9 and 1 respectively, while the friction loss was scaled linearly with speed. The friction loss of 150 W was set at speed of 6000 1/min. The average total loss deviation for different temperatures

between the measurements and the fine-tuned Motor-CAD model at temperatures of  $-10^{\circ}\text{C}$ ,  $30^{\circ}\text{C}$ , and  $110^{\circ}\text{C}$  as well as the peak torque curve of the Motor-CAD model are depicted in Fig. 4.12. The model exhibits higher losses than the actual measurements when negative values are present. A high level of match to the measured losses has been achieved across the most areas of the loss map. The primary discrepancies identified in the loss modeling are low torque readings in the high-speed range and high torque readings in the low-speed range. Measurement errors contributed to inaccuracies is particularly in the low-speed and low-torque regions, which can arise from various sources, including sensor calibration, data acquisition limitations, or inherent noise in the measurements. An absolute error of approximately 500 W was noted in the operating envelope. The operating envelope represents the motor's absolute peak power capability. This absolute error signifies a deviation between the model predictions and the actual measurements. The relative error of 500 W is deemed acceptable, when considering the context of the operating envelope as the absolute peak power is about 220 kW.

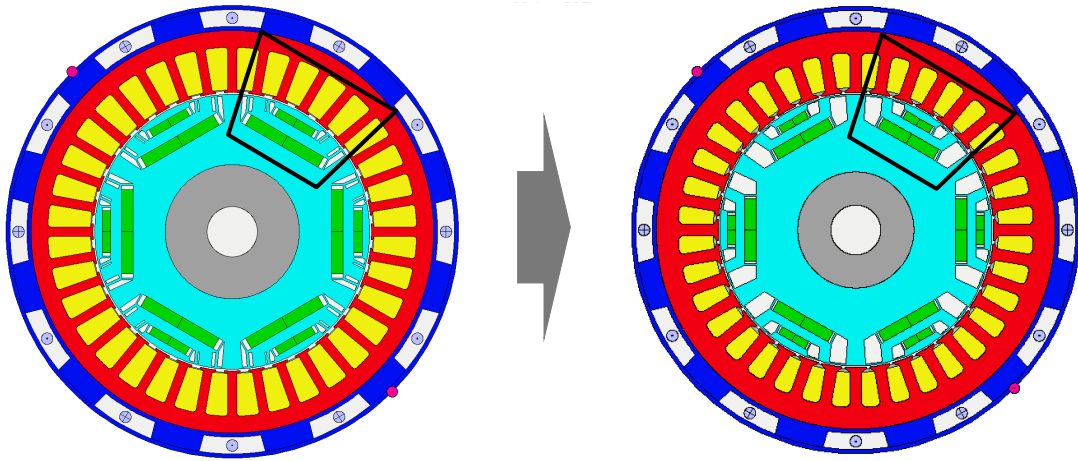


**Figure 4.11.** Final cross-section of the PMSM after adjustments to the slot and magnet

The efficiency map, generated through simulations using Motor-CAD, and the corresponding measured efficiency map at a stator temperature of  $110^{\circ}\text{C}$  are depicted in Fig. 4.13a and in Fig. 4.13b. The comparison reveals a commendable level of correlation between the simulated and measured efficiency maps, with only minimal distortion observed in the measured map across the entire operating envelope. Despite this slight distortion, the accuracy of the efficiency contours and magnitudes predicted by the simulation is noteworthy. It is important to note that the small amount of distortion observed in the measured map does not significantly impact the overall agreement between the simulated and measured efficiency maps. This distortion may be attributed to minor discrepancies between the simulation model and the actual experimental setup. Nevertheless, the fact that the efficiency contours and magnitudes are predicted very accurately by the simulation highlights the effectiveness of this modeling approach and analyzing the efficiency by using Motor-CAD.

The cross-validation of the loss maps determined by Motor-CAD was carried out against a worldwide harmonized light duty test cycle (WLTC) and a US06 driving cycle at an ambient temperature of  $20^{\circ}\text{C}$ . The close alignment between the estimated losses and the measured losses is evident from the data. The root mean square error (RMSE)

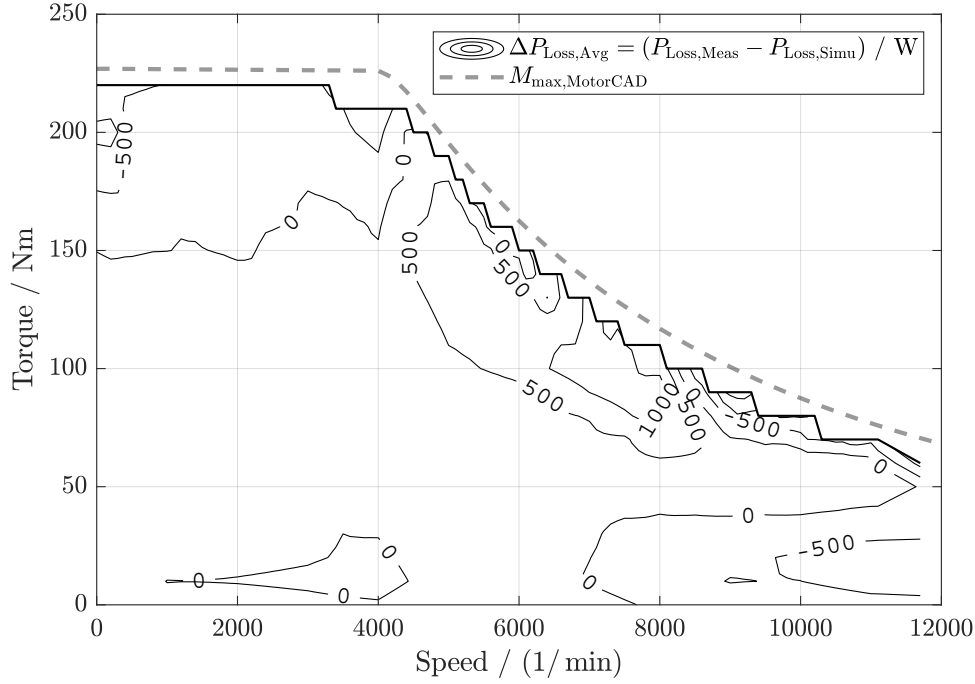
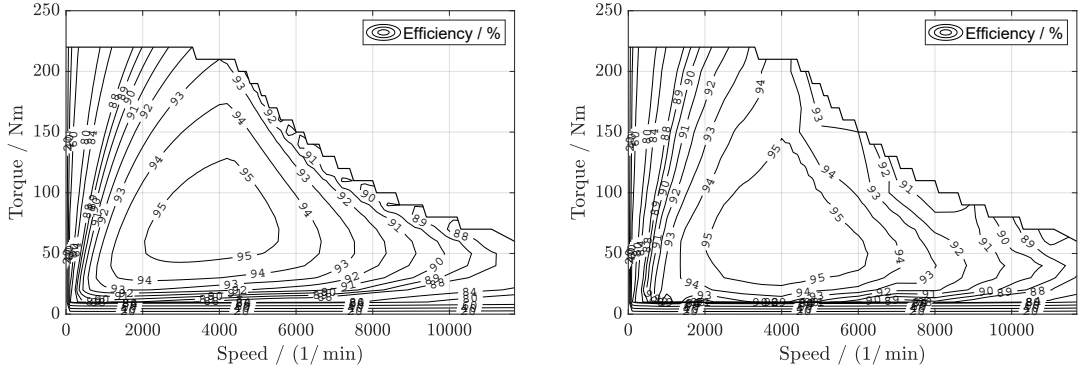


**Figure 4.12.** Average loss difference between the measurement and the loss model at DC-voltage of 350 V after fein tuning

of the total loss for WLTC and US06 cycle are 172 W and 374 W approximately. This level of proximity between estimated and measured losses underscores the accuracy and reliability of the estimation methods employed. The small RMSE values indicate that the estimated total losses closely track the actual losses during both the WLTC and US06 cycles. The significance of these results lies in the ability of the estimation methods to predict losses with a high degree of precision. From this we can conclude that the motor losses are well constructed and the loss model can be used to accurately estimate the motor losses under different operating points. Validation results are shown in Fig. A.1 and Fig. A.2 in appendix.

#### 4.1.4. Thermal Network and Loss Model of Gearbox

Thermal modeling using an LPTN for a gearbox involves representing the gearbox as a system of discrete thermal elements with associated thermal resistances and capacities. This approach simplifies the complex thermal behavior of the gearbox into a set of interconnected nodes, each characterized by its thermal properties. The LPTN model allows for an efficient analysis of temperature distribution and heat transfer within the gearbox. The simplified structural illustration of the gearbox, along with its corresponding representation using the LPTN is displayed in Fig. 4.14a and Fig. 4.14b, respectively. Within the LPTN model, three nodes are employed to simulate the temperatures of the gear  $T_G$ , lubricant oil  $T_O$ , and gearbox housing  $T_{HG}$ . This network structure effectively models the heat flow paths, where thermal resistances signify the opposition to heat transfer via conduction and convection, and thermal capacities represent each component's ability to store thermal energy. Additionally, the ambient temperature  $T_A$  functions as an external

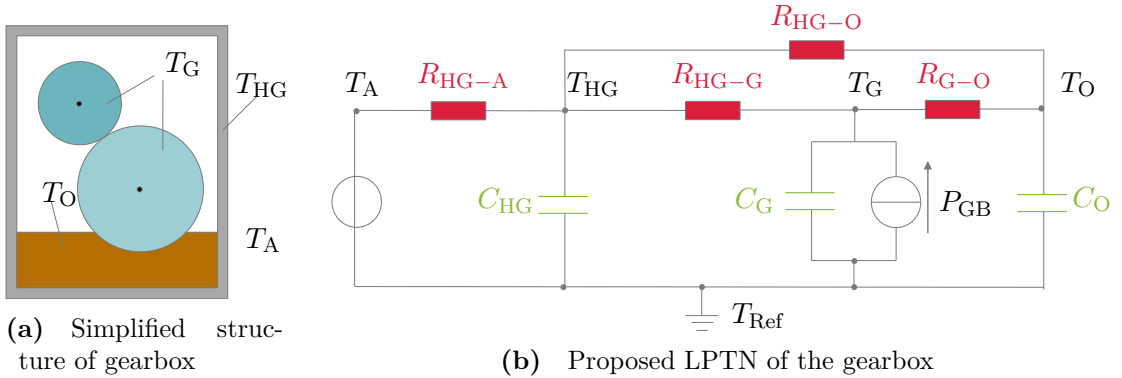


(a) Efficiency map simulated by Motor-CAD (b) Efficiency map from the measurements

**Figure 4.13.** Efficiency map comparison between Motor-CAD and measurements at DC-voltage of 350 V and temperature of 110 °C

Source: Chen et al. (2024). Reprinted with permission from SAGE Publications, Inc. doi:10.1177/09544070241254557

boundary condition for the thermal system. Furthermore, losses  $P_{GB}$  occurring in the gearbox, which, according to the assumption, are restricted to the gear, are integrated as heat sources, representing the internal heat generation within the system.



(a) Simplified structure of gearbox

(b) Proposed LPTN of the gearbox

**Figure 4.14.** Thermal modeling of the gearbox

The conservation of energy in the thermal network model is ensured through the Kirchhoff's laws. In the LPTN model of the gearbox, each thermal node adheres to the requirement that the sum of heat inflows equals the sum of heat outflows, which describes the differential equations for characterizing the thermal dynamics of the system. The proposed LPTN of the gearbox can be represented using the state space format, similar to that employed in the LPTN model of inverter and PMSM . In the state space representation, a mathematical structure is employed to describe and understand the behavior of the system, integrating its state variables, inputs, and outputs.

$$\begin{aligned} \dot{\mathbf{x}} &= \mathbf{A}(T_O)\mathbf{x} + \mathbf{B}\mathbf{u} \\ \mathbf{y} &= \mathbf{C}\mathbf{x} \end{aligned} \quad (4.18)$$

where

$$\mathbf{A} = \begin{bmatrix} -\frac{1}{C_G} \left( \frac{1}{R_{HG-G}} + \frac{1}{R_{G-O}} \right) & \frac{1}{C_G R_{G-O}} & \frac{1}{C_G R_{HG-G}} \\ \frac{1}{C_O R_{G-O}} & -\frac{1}{C_O} \left( \frac{1}{R_{G-O}} + \frac{1}{R_{HG-O}} \right) & \frac{1}{C_O R_{HG-O}} \\ \frac{1}{C_{HG} R_{HG-G}} & \frac{1}{C_{HG} R_{HG-O}} & -\frac{1}{C_{HG}} \left( \frac{1}{R_{HG-G}} + \frac{1}{R_{HG-O}} \right) \end{bmatrix}$$

$$\mathbf{B} = \begin{bmatrix} \frac{1}{C_G} & 0 \\ 0 & 0 \\ 0 & \frac{1}{C_{HG} R_{HG-A}} \end{bmatrix}$$

$$\mathbf{C} = \begin{bmatrix} 1 & 0 & 0 \\ 0 & 1 & 0 \\ 0 & 0 & 1 \end{bmatrix}$$

$$\mathbf{y} = [T_G \ T_O \ T_{HG}]$$

$$\mathbf{u} = [P_{GB} \ T_A]$$

The output vector  $\mathbf{y}$  contains the temperature of the gear, lubrication oil and housing. The input vector  $\mathbf{u}$  comprises the losses in the gearbox and the ambient temperature. The scheduling variable in (4.18) is the lubricant oil temperature, as its specific heat capacity increases and its thermal conductivity declines with an increase in temperature [88]. As a result, the thermal capacity of the lubricant oil  $C_O$  in the gearbox is given as:

$$C_O = C_{O,0} \cdot [1 + \alpha_O \cdot (T_O - T_{O,0})] \quad (4.19)$$

The natural exponential function is chosen to approximate the heat transfer in the oil. Therefore, the thermal resistances of the gearbox oil  $R_{HG-O}$  and  $R_{G-O}$  are defined as:

$$R_{HG-O} = R_{HG-O,0} \cdot e^{-\frac{T_O}{T_{O,max}} \cdot b_{HG-O}} + a_{HG-O} \quad (4.20)$$

and

$$R_{G-O} = R_{G-O,0} \cdot e^{-\frac{T_O}{T_{O,max}} \cdot b_{G-O}} + a_{G-O} \quad (4.21)$$

where  $T_{O,0}$  and  $T_{O,max}$  represent the reference temperature and the maximum temperature of the lubricant oil.  $R_{HG-O,0}$  and  $R_{G-O,0}$  denote the thermal resistance between the gearbox housing and the oil and between the gearbox and the oil at the reference temperature.  $\alpha_O$ ,  $b_{HG-O}$ ,  $b_{G-O}$ ,  $a_{HG-O}$  and  $a_{G-O}$  are parameters that reflect the influence of temperature variations on the heat transfer.

The loss map of the gearbox is already available from a project calibrated on the basis of the measurement data. The efficiency maps of the gearbox across varying temperatures of  $-20^\circ\text{C}$ ,  $20^\circ\text{C}$ ,  $60^\circ\text{C}$  and  $100^\circ\text{C}$  are illustrated in Fig. 4.15. The figure clearly

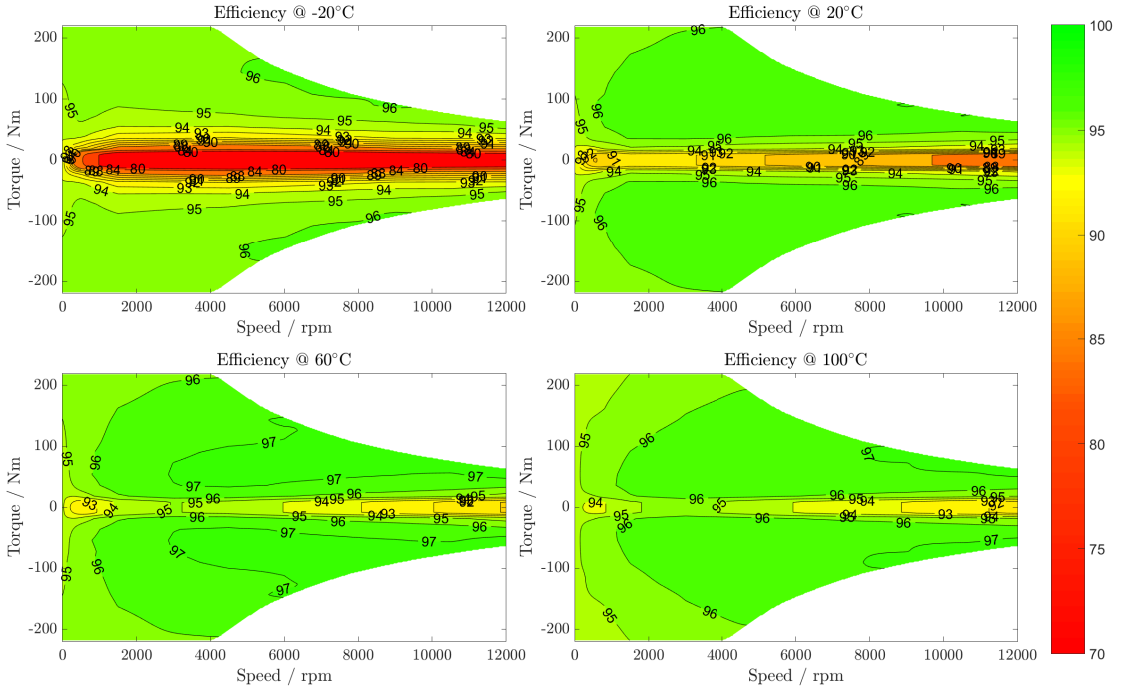


**Figure 4.15.** Efficiency maps of gearbox for different temperatures

depicts a strong correlation between gearbox efficiency and temperature. When the temperature falls below  $0^{\circ}\text{C}$ , the efficiency of the gearbox is notably reduced, particularly in the low-load region, where torques are below 50 Nm. Since gearbox temperature has a detrimental effect on the gearbox's performance, controlling the temperature within a suitable range is crucial to ensure that the gearbox can sustain its optimal efficiency. The losses calculation of the gearbox is analogous to that of the inverter, involving the interpolation of loss maps at different operating points and lubricant temperatures. The resulting losses serve as the heat source for the gear node in the LPTN.

#### 4.1.5. Thermal Network of the Whole Drivetrain

Upon integrating the LPTN thermal models of the aforementioned components, we establish an LPTN with a total of 13 nodes, enabling the estimation of the temperature for the entire drivetrain system, as depicted in Fig. 4.16. The LPTN of the drivetrain consists of three subordinate LPTNs: the LPTN of the inverter, the PMSM and the gearbox. The node  $T_{\text{ADC}}$  represents the air temperature in the drivetrain compartment. The three LPTNs are connected by thermal resistances to model the thermal coupling. The inverter and PMSM are coupled by the thermal resistance  $R_{\text{COE-COI}}$ , while the PMSM and the gearbox are connected by the thermal resistance  $R_{\text{R-G}}$ . The thermal resistance  $R_{\text{HI-ADC}}$ ,  $R_{\text{HE-ADC}}$  and  $R_{\text{HG-ADC}}$  represent the heat transfer resistance between the component housings and the air in the drivetrain compartment.  $R_{\text{ADC-A}}$  denotes the thermal resistance between the air in the drivetrain compartment and the ambient. Each node is connected to the thermal ground potential  $T_{\text{Ref}}$  via thermal capacitance in order to represent the heat-up and cool-down behavior. In the LPTN, the virtual nodes for the coolant with corresponding thermal capacities are added to simulate the coolant outlet

temperature. The coolant inlet temperature  $T_{\text{CIN}}$  and the ambient temperature  $T_{\text{A}}$  are the boundary conditions for the thermal system. Moreover, the losses  $P$  in the inverter, PMSM and gearbox represent the inner heat generation in the system.

In compliance with Kirchhoff's laws within every thermal node, the total heat inflow equals the total outflow. Consequently, the LPTN can be delineated through the formulation of differential equations, and these equations can then be transformed into the state space representation. The detailed representation of matrices  $\mathbf{A}$ ,  $\mathbf{B}$  and  $\mathbf{C}$  are in the appendix.

$$\begin{aligned}\dot{\mathbf{x}} &= \mathbf{A}(T_{\text{S}}, T_{\text{R}}, T_{\text{J}}, T_{\text{O}}, T_{\text{CIN}}, \dot{V}_{\text{CIN}}, n)\mathbf{x} + \mathbf{B}\mathbf{u} \\ \mathbf{y} &= \mathbf{C}\mathbf{x}\end{aligned}\tag{4.22}$$

where

$$\begin{aligned}\mathbf{y} &= [T_{\text{HI}} \ T_{\text{J}} \ T_{\text{COI}} \ T_{\text{COE}} \ T_{\text{HE}} \ T_{\text{S}} \ T_{\text{EW}} \ T_{\text{R}} \ T_{\text{O}} \ T_{\text{HG}}] \\ \mathbf{u} &= [P_{\text{INV}} \ P_{\text{S}} \ P_{\text{EW}} \ P_{\text{R}} \ P_{\text{GB}} \ T_{\text{CIN}} \ T_{\text{A}}]\end{aligned}$$

here, bold symbols denote vector or matrix quantities. The output vector  $\mathbf{y}$  contains the temperature nodes in the inverter housing, junction, inverter coolant outlet, PMSM coolant outlet, PMSM housing, winding, lubricant oil, gearbox housing as well as the air in the drivetrain compartment. The input vector  $\mathbf{u}$  comprises the loss entries in different components as well as the coolant inlet temperature and the ambient temperature. Compared to a linear time-invariant system, (4.22) is an LPV model. Because these scheduling variables in the matrix  $\mathbf{A}$  represent parameters or conditions that are time-varying, influencing the behavior of the system being modeled. In this LPTN model of the drivetrain, the scheduling variables are the speed of the PMSM, the torque of the PMSM, the winding temperature, the junction temperature of the inverter, the oil temperature in the gearbox as well as the coolant inlet temperature and the coolant volume flow rate, which are determined during the model identification process.

## 4.2. Parametrization and Validation

The objective of the parameter identification is to determine the model parameters that reduce the error between the model output and measurement results. This crucial process plays a pivotal role in enhancing the accuracy and reliability of dynamic system models. The cost function encapsulates the quantitative measure of the disparity between the simulated outputs of the model and the observed measurements. This is achieved by minimizing the cost function for multiple-input and multiple-output state-space models, which can be expressed as [38]:

$$J(\mathbf{x}) = \det \left( \sum_{i=1}^N \mathbf{e}(i, \mathbf{x}) \cdot \mathbf{e}(i, \mathbf{x})^T \right)\tag{4.23}$$

where  $i$  denotes the sampling index and  $\mathbf{x}$  contains all unknown model parameters.  $\mathbf{e}$  is the model output error given as

$$\mathbf{e} = \mathbf{y} - \hat{\mathbf{y}}\tag{4.24}$$

with  $\mathbf{y}$  and  $\hat{\mathbf{y}}$  as the measurement and the model output respectively. Therefore, the

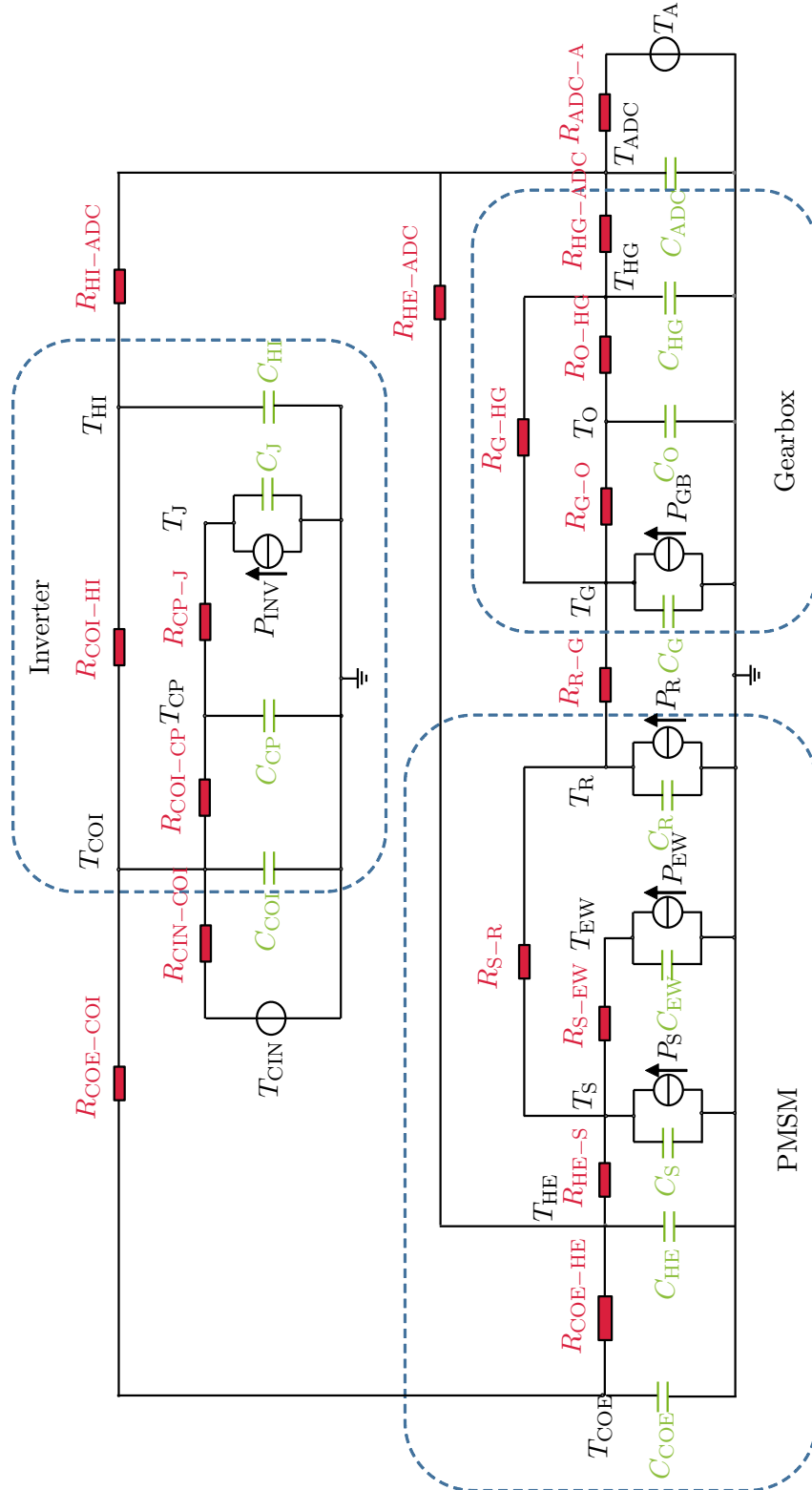


**Figure 4.16.** Structure of proposed LPTN for the whole drivetrain

© 2020 IEEE. Reprinted, with permission, from B. Chen et al., "A Comprehensive Thermal Model For System-Level Electric Drivetrain Simulation With Respect To Heat Exchange Between Components," 19th IEEE ITherm Conference, 2020, pp. 558-567

parameter identification can be interpreted as a constrained optimization problem

$$\begin{aligned} \min_{\mathbf{x}} \quad & J(\mathbf{x}) \\ \text{subject to} \quad & \mathbf{g}(\mathbf{x}) \leq 0 \\ & \mathbf{h}(\mathbf{x}) = 0 \end{aligned} \tag{4.25}$$

where  $J(\mathbf{x})$  is the cost function of the optimization problem.  $\mathbf{g}$  and  $\mathbf{h}$  are the equality and inequality constraints for the optimization problem. As the output error  $\mathbf{e}$  is nonlinearly dependent on the model parameters and the entries in matrix  $\mathbf{A}$  are nonlinearly dependent on the scheduling variables, (4.25) is a nonlinear, non-convex and multi-dimensional optimization problem [38]. In order to find the global optimum of (4.25) the ant colony optimization (ACO) algorithm with 'multi-start' approaches was applied to avoid the local optima [89, 90]. Since there are plenty of parameters to be optimized, well-known analytical formulations were used to roughly pre-calculate lower and upper bounds of the model parameters. The optimization was run with parallel computing on a high-performance computer, which speeds up the calculation and greatly reduces the computational time.

The LPTN parameters were determined using a global LPV approach based on measurements of the WLTC with a sampling time of 0.1 s. The reference vehicle was tested on a chassis dynamometer under controlled conditions, with actual power measurements of drivetrain components using a power analyzer for validation purposes. Various temperature measurements were also taken, including lubricant oil temperature of the gearbox, housing temperature of the inverter, PMSM and gearbox, coolant temperatures, and coolant volume flows. The inner temperatures of the inverter and PMSM were obtained via the controller area network (CAN) bus from the motor control unit (MCU) [80]. The maximum and average temperature deviations of key nodes for model identification, using the WLTC driving cycle, are detailed in Table 1. Across all nodes, predicted temperatures closely aligned with measured values, exhibiting a maximum estimation error of approximately 5.45 °C. This indicated strong agreement between predicted and actual temperatures, confirming the accuracy of the model in simulating thermal behavior under WLTC conditions.

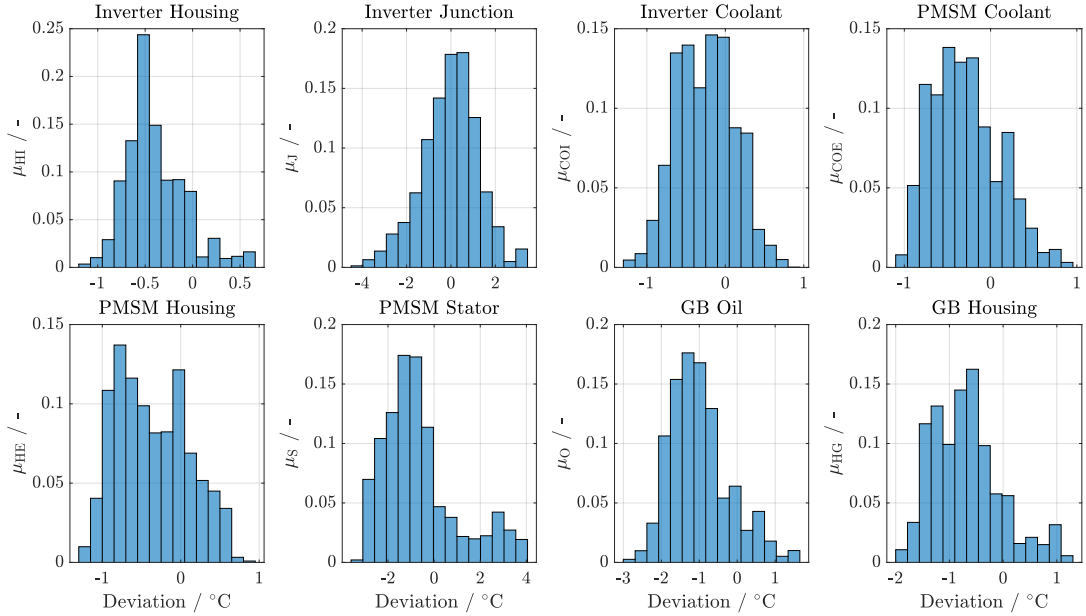
The distribution of estimation errors is illustrated through a histogram, providing a comprehensive view of the accuracy and robustness of the identification results. This visualization serves as a powerful tool for assessing the reliability and precision of the identification process. The histogram, as shown in Fig. 4.17, highlights the relationship between the estimation deviation and the occurrence probability of this deviation. A well-behaved histogram, resembling a white-noise pattern, signifies that the estimation errors are evenly distributed across various magnitudes, showcasing the model's robustness in diverse operating conditions [91]. As observed in Fig. 4.17, the distributions of inverter junction temperatures closely resemble an ideal white-noise form, indicating robust estimation results. Conversely, the distributions of other nodes exhibit a biased form of quasi-white-noise, suggesting some degree of systematic error in the estimation process. In addition to the histogram, detailed simulation results over time are provided in Fig. A.3 in the appendix. These results offer a more granular understanding of the system's thermal behavior throughout the simulation period.

The parametrized thermal model was cross-validated using a load profile based on US06 driving cycles, with measurements sampled at a rate of 0.1 s. The coolant inlet temperature and volume flow rate exhibited variability, while the ambient temperature

**Table 4.2.** Model performance based on WLTC driving cycle

© 2020 IEEE. Reprinted, with permission, from B. Chen et al., "A Comprehensive Thermal Model For System-Level Electric Drivetrain Simulation With Respect To Heat Exchange Between Components," 19th IEEE ITherm Conference, 2020, pp. 558-567

Nodes	Max. Deviation	Avg. Deviation
Inverter Housing	1.13 °C	0.47 °C
Inverter Junction	5.45 °C	0.45 °C
Inverter Coolant	1.55 °C	0.40 °C
PMSM Coolant	1.28 °C	0.48 °C
PMSM Housing	1.34 °C	0.65 °C
PMSM Stator	4.19 °C	0.42 °C
Gearbox Oil	1.57 °C	0.32 °C
Gearbox Housing	1.65 °C	0.29 °C

**Figure 4.17.** Histogram of estimation errors based on WLTC driving cycle

© 2020 IEEE. Reprinted, with permission, from B. Chen et al., "A Comprehensive Thermal Model For System-Level Electric Drivetrain Simulation With Respect To Heat Exchange Between Components," 19th IEEE ITherm Conference, 2020, pp. 558-567

remained relatively stable around 20 °C. Once again, a comprehensive assessment of temperature deviations for key thermal nodes is presented in Table 4.3. Across various critical points within the system, the estimated temperatures closely mirror the measured values, with temperature discrepancies typically below 7 °C. These validation results underscore the effectiveness of the identified thermal model in accurately predicting thermal behavior under the US06 driving cycle conditions. For detailed simulation results, please refer to Fig. A.4 in the appendix.

**Table 4.3.** Model performance based on US06 driving cycle

© 2020 IEEE. Reprinted, with permission, from B. Chen et al., "A Comprehensive Thermal Model For System-Level Electric Drivetrain Simulation With Respect To Heat Exchange Between Components," 19th IEEE ITherm Conference, 2020, pp. 558-567

Nodes	Max. Deviation	Avg. Deviation
Inverter Housing	1.41 °C	0.43 °C
Inverter Junction	6.64 °C	0.17 °C
Inverter Coolant	1.88 °C	0.11 °C
PMSM Coolant	1.42 °C	0.13 °C
PMSM Housing	1.57 °C	0.30 °C
PMSM Stator	6.37 °C	0.22 °C
Gearbox Oil	2.76 °C	0.47 °C
Gearbox Housing	1.61 °C	0.61 °C

The histogram Fig. 4.18 illustrates the distribution of errors across various components, providing insights into the accuracy and robustness of the thermal model. Upon examination of the histograms, it is observed that the estimation errors for certain components, such as the inverter junction, inverter coolant, gearbox oil, and gearbox housing, closely resemble a quasi-Gaussian distribution. This suggests that the errors associated with these components exhibit a symmetrical pattern around the mean, indicating a balanced distribution of overestimations and underestimations. Conversely, the estimation errors for the PMSM exhibit deviations from a normalized distribution. This deviation suggests that the errors associated with the PMSM are skewed or asymmetric, potentially indicating systematic biases or inaccuracies in the thermal model's predictions for this component. These findings highlight areas where further improvements may be necessary to enhance the accuracy and reliability of the thermal model, particularly in relation to the PMSM.

One potential approach is to enhance the LPTN by incorporating additional nodes into the PMSM. Currently, the thermal modeling within the LPTN is relatively simplistic, treating the entire stator as a thermal mass and only connecting the rotor shaft thermally to the gearbox gear via a mechanical coupling. However, the rotor shaft is also thermally linked to the end-cap air within the motor housing and the bearings. Devel-

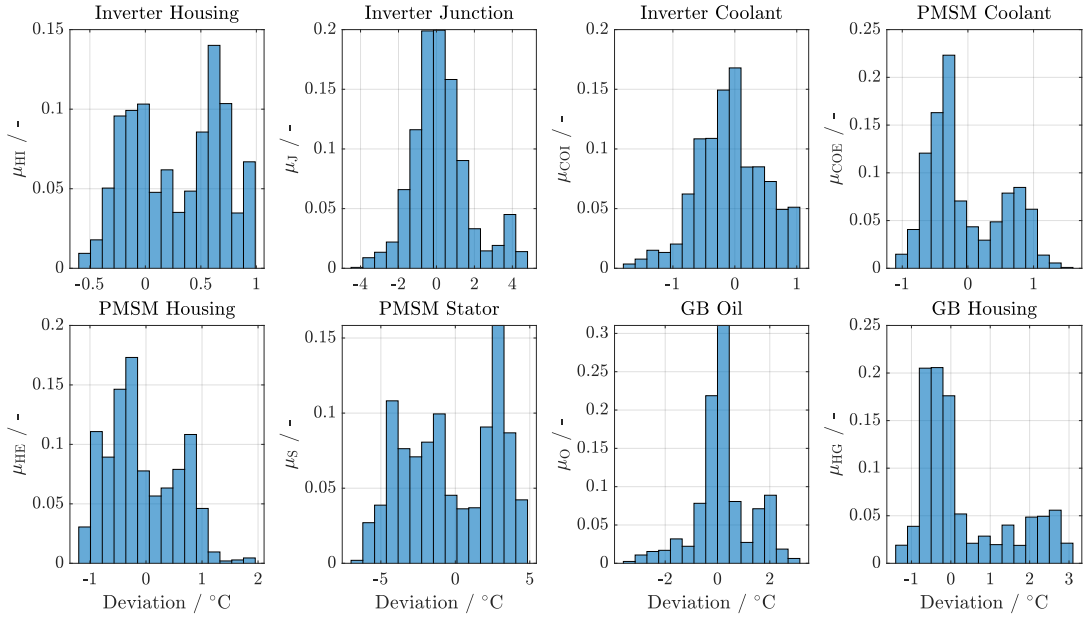


**Figure 4.18.** Histogram of estimation errors based on US06 driving cycle  
 © 2020 IEEE. Reprinted, with permission, from B. Chen et al., "A Comprehensive Thermal Model For System-Level Electric Drivetrain Simulation With Respect To Heat Exchange Between Components," 19th IEEE ITherm Conference, 2020, pp. 558-567

oping separate models for these components could improve estimation accuracy, albeit at the expense of increased computational complexity required to execute the resulting model. Additionally, it's essential to consider the trade-off between model flexibility and robustness, as augmenting the number of nodes and parameters may exacerbate identification challenges.

Furthermore, the validation results reveal that the junction temperature exhibited the maximum temperature deviation, which was attributed to the limited bandwidth and slower transient response of the first-order thermal impedance between junction and cooling plate [92, 93]. However, the steady-state average temperature estimation matched the measurement quite well. To improve the junction temperature estimation, the inverter model can be extended with a higher-order thermal impedance, although this would increase the calculation effort. The proposed thermal model and parameter identification method offer a convenient solution that can be readily applied with vehicle-level measurements. This approach circumvents the need for time-consuming and costly thermal measurements conducted on individual components at test benches. By leveraging vehicle-level measurements, which provide comprehensive data on the thermal behavior of the entire system, this method streamlines the process of thermal analysis and parameter identification. This is particularly advantageous in the automotive industry, where rapid development cycles and cost pressures necessitate efficient testing and validation processes. By employing vehicle-level measurements, engineers can expedite the thermal analysis process and accelerate the development of thermal management strategies.

# 5. Temperature Estimation of Scaled Permanent Magnet Synchronous Machines

In this chapter, the necessary steps to estimate the temperature of a scaled permanent magnet synchronous machine (PMSM) are outlined. Firstly, a thermal model in Ansys Motor-CAD is to be built and validated through measurements, as the electromagnetic modeling has been completed in the previous chapter. This Motor-CAD model is utilized for the generation of validation data for the scaled PMSMs. Subsequently, the low-order lumped parameter thermal network (LPTN) model of the reference PMSM is described, serving as the foundational model for the application of the scaling approach. The chapter then addresses the scaling approach for losses and the derivation of the scaling approach for thermal parameters. Following this, the validation results are presented. Finally, the conclusions are drawn and subjected to a comprehensive discussion.

## 5.1. Calibration of the Thermal Behavior of the Motor-CAD Model for the Reference PMSM

Due to the restrictions in production and laboratory resources, it is challenging to acquire measurement data for electrical machines (EMs) that have varying geometries but the same design. Therefore, we propose to utilize a validated Motor-CAD model based on the measurements of the reference EM to generate validation data for the scaled EM. Ansys Motor-CAD is a widely accepted industry standard tool for electromagnetic thermal, and mechanical analysis of EMs, which has been validated by various EM technologies and cooling topologies. It is assumed that a good agreement between the model and experimental measurements indicates a reliable representation of the real EM by the model. When the scaling approach demonstrates a comparable level of agreement with the model results, its effectiveness is verified.

To reconstruct the reference EM, we create a Motor-CAD model that represents both the electromagnetic and thermal behaviors of the EM. The electromagnetic behavior has been validated in Section 4.1.3. Temperatures of the reference PMSM, which is modeled by a detailed LPTN model with 106 thermal nodes in Motor-CAD, are validated by the driving cycle measurements in this section. A schematic and simplified overview of the LPTN model of the reference PMSM in Motor-CAD is given in Fig. 5.1:

In order to match the temperature measurements, the thermal parameters in the thermal model are calibrated based on the heat transfer fundamentals, which are the axial and radial conduction resistance  $R_{\text{cond}}$  of an object and the convection resistance

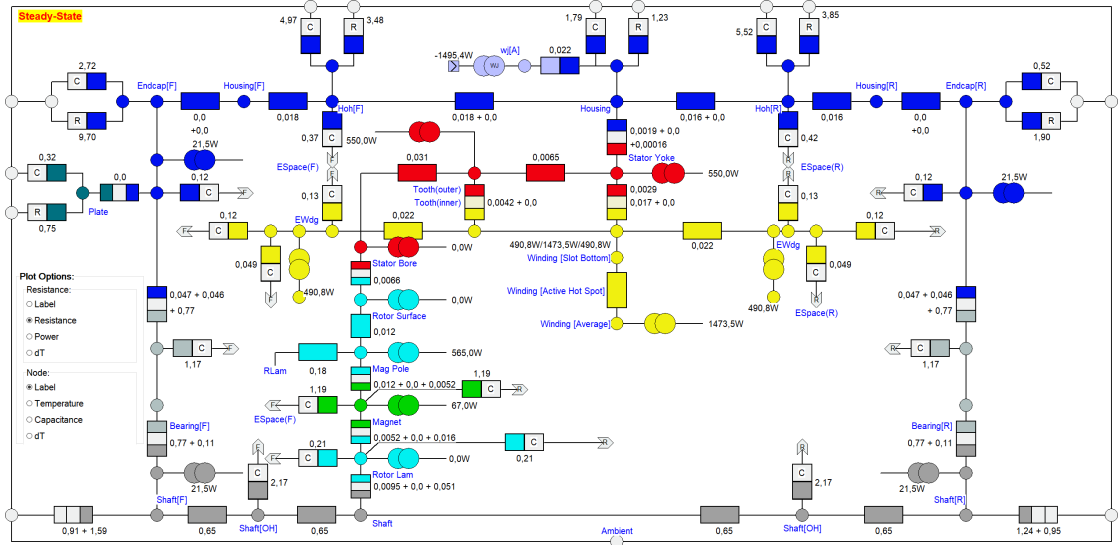


**Figure 5.1.** Schematic and simplified overview of the LPTN model in Motor-CAD

$R_{\text{conv}}$  due to fluid movement [49]:

$$R_{\text{cond}} = \frac{L}{\lambda \cdot A} \quad (5.1)$$

$$R_{\text{conv}} = \frac{1}{h_{\text{conv}} \cdot A} \quad (5.2)$$

The geometric parameters for path length  $L$  and contact surface area  $A$  are derived from the geometry of the Motor-CAD model automatically. By selecting the material data that corresponds to the machine datasheet and defining the thermal boundaries, such as the fluid volume flow rate, the values of the thermal conductivity  $\lambda$  and the heat convection coefficient  $h_{\text{conv}}$  are determined. In the given example of a steady-state thermal simulation of the PMSM shown in Fig. 5.1, the inlet coolant temperature of  $60^\circ\text{C}$  and the volume flow rate of  $6\text{L}/\text{min}$  are the thermal boundaries for the water jacket cooling. Motor-CAD calculates the heat transfer coefficient accordingly, which is in this case based on the laminar correlation depending on the Reynolds number and Prandtl number, resulting in a convection coefficient of  $h_{\text{conv}}$  for water jacket cooling of  $328\text{W}/(\text{m}^2\text{C})$ . With consideration of the housing water jacket surface area  $A$  of  $0.1377\text{m}^2$ , the thermal resistance  $R_{\text{conv}}$  of  $0.022^\circ\text{C}/\text{W}$  is determined.

To simulate the coolant outlet temperature, heat transfer from the housing to the coolant is considered with the coolant inlet temperature being taken as a boundary condition. The comparison of the stator temperature takes place close to the end winding, where a thermocouple is placed. So one of the winding nodes in that position in the Motor-CAD model is chosen. An additional node in the LPTN model of Motor-CAD is created to simulate the temperature of the housing surface as only the temperature of the inner housing is provided by Motor-CAD. Derived from the observation of the measurement setup, it can be assumed that the additional node is connected to the node of the inner housing, the ambient and the coolant, as illustrated in Fig. 5.2. The nodes and thermal resistances marked in black have already existed in the Motor-CAD model, whereas the gray nodes and thermal resistances are additionally modeled.

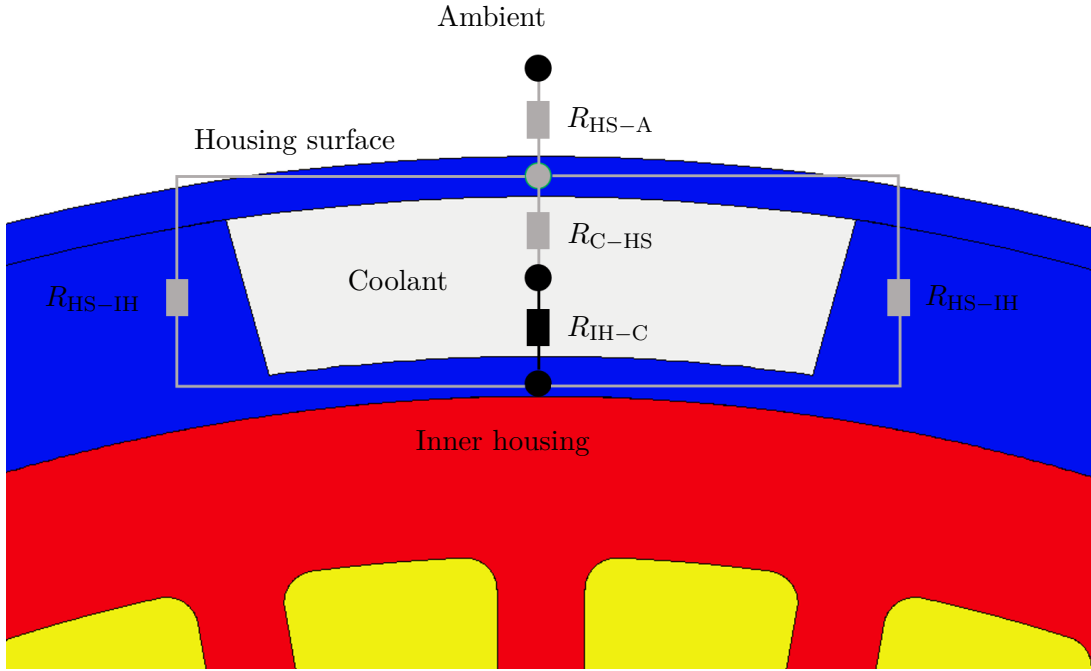


**Figure 5.2.** Thermal modeling of the housing surface node in Motor-CAD

Source: Chen et al. (2024). Reprinted with permission from SAGE Publications, Inc. doi:10.1177/09544070241254557

The thermal resistance  $R_{C-HS}$  between the coolant and the housing surface could be the same as the resistance  $R_{IH-C}$  between the inner housing and the coolant due to the symmetrical arrangement to the coolant channel. The conduction resistance  $R_{HS-IH}$  between the housing surface and the inner housing can be calculated by (5.1) as the thermal conductivity of the aluminum housing, the path length and the average contact surface area are known. The convection resistance  $R_{HS-A}$  from the housing surface to ambient is calculated according to the heat transfer fundamental formula (5.2) with the general formula of the convective coefficient (2.7) and the forced convection correlations as follows [32].

$$Nu = a \cdot (Re)^b (Pr)^c$$

where  $a$ ,  $b$  and  $c$  are constants in the convection correlation.  $Nu$ ,  $Re$  and  $Pr$  denote the Nusselt number, the Reynolds number and the Prandtl number respectively. With the assumption of the reference temperature of  $20^\circ\text{C}$  and the laminar air flow, the following Nusselt number correlation is applied for the calculation of the convection resistance from the housing surface to the ambient, which is suitable for the laminar flow over a flat plate [32].

$$Nu = 0.664 \cdot (Re)^{0.5} (Pr)^{0.33} \quad (5.3)$$

The loss distribution of the PMSM for the thermal model is determined by the interpolation of the loss maps. For each sampling time step, the temperatures from the thermal model in Motor-CAD are fed back to the loss maps to calculate the temperature-dependent losses iteratively. The temperature comparison between the simulation and

the measurement for the extended worldwide harmonized light duty test cycle (WLTC) with an additional low and medium WLTC section at an ambient temperature of 20 °C is shown in Fig. 5.3. The stator temperature differs by a root mean square error (RMSE)

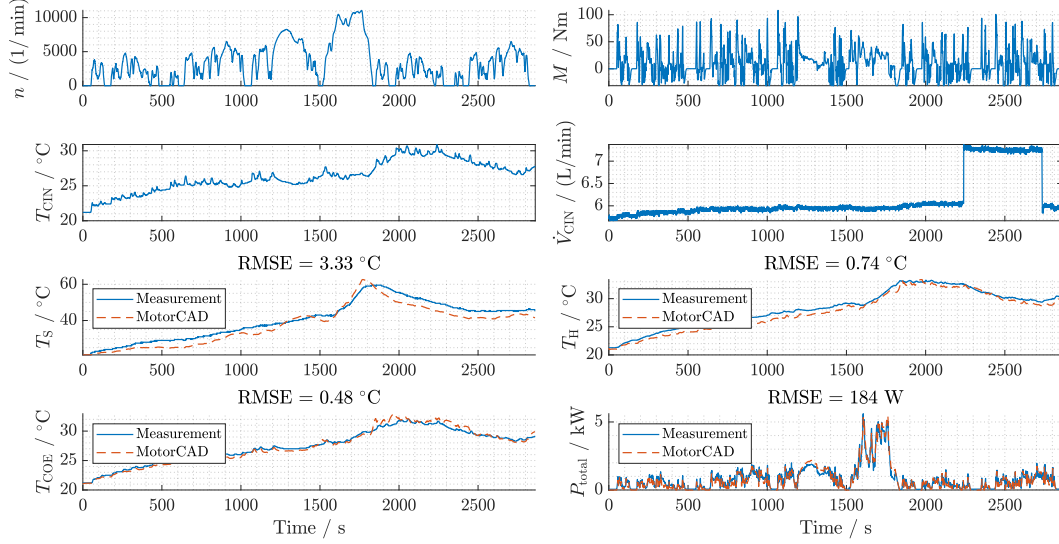


**Figure 5.3.** Temperature comparison of the simulation and the measurement for the extended WLTC cycle at ambient temperature of 20 °C

Source: Chen et al. (2024). Reprinted with permission from SAGE Publications, Inc. doi:10.1177/09544070241254557

of 3.33 °C, while the housing and coolant outlet temperatures are very similar with an RMSE of 0.74 °C and 0.48 °C respectively. The temperature deviation in the winding can either be due to the deviation of losses or an increased contact resistance to the temperature sensor.

## 5.2. Scaling of Losses

The losses in the PMSM can be categorized into copper losses, iron losses and magnet losses. Specifically, copper losses consist of direct current (DC) copper losses and alternating current (AC) copper losses. Additionally, the losses of the reference PMSM are further broken down into more detailed sections, including the copper losses in the core region and end winding, as well as the iron losses in the stator and rotor, and the magnet losses. Hence, the losses for each thermal node can be specified in (5.4) - (5.6):

$$P_S = (1 - r_{ew}) \cdot P_{Cu} + P_{S,Fe} \quad (5.4)$$

$$P_{EW} = r_{ew} \cdot P_{Cu} \quad (5.5)$$

$$P_R = P_{R,Mag} + P_{R,Fe} \quad (5.6)$$

where

$$P_{Cu} = P_{Cu,DC} + P_{Cu,AC} \quad (5.7)$$

and  $r_{ew}$  denotes the copper loss distribution ratio for the end winding.

Axial scaling factor  $k_A$  and radial scaling factor  $k_R$  are applied independently to scale the PMSM. During axial scaling, only the length in the core region is altered by  $k_A$ . The scaling of AC copper losses can be expressed by

$$P_{\text{Cu,AC,scl}}(n, M_{\text{scl}}) = k_A k_R^4 \cdot P_{\text{Cu,AC}}(n, M) \quad (5.8)$$

due to its direct correlation with the dimensions of the conductor arrangement and the skin depth for a round winding as described in (5.9) [83].

$$P_{\text{Cu,AC}} = L_a \frac{\pi d_c^4 \sigma_e (\omega B)^2}{128} \quad (5.9)$$

where  $L_a$  is the conductor active length and  $B$  is the magnitude (peak) of the sinusoidal external field.  $d_c$  denotes the diameter of the circular conductor.  $\omega$  and  $\sigma_e$  are the electrical frequency and the electrical conductivity of the conductor material, respectively.

The scaling laws developed by Stipetic et al. are used to determine the rest of the losses of the scaled PMSM [69, 70]. In order to use the scaling laws, it is essential to maintain a consistent magnetic flux density across all scaled variations. As shown in Fig. 5.4, the losses of each operating point  $(n_i, M_i)$  in the reference loss map, which are scaled by using the formula in (5.8) and (5.10) - (5.13), associate with the losses of each operating point  $(n_i, M_{i,\text{scl}})$  in the scaled loss map [96].

$$P_{\text{Cu,DC,scl}}(n, M_{\text{scl}}) = k_A \cdot P_{\text{Cu,DC}}(n, M) \quad (5.10)$$

$$P_{\text{S,Fe,scl}}(n, M_{\text{scl}}) = k_A k_R^2 \cdot P_{\text{S,Fe}}(n, M) \quad (5.11)$$

$$P_{\text{R,Fe,scl}}(n, M_{\text{scl}}) = k_A k_R^2 \cdot P_{\text{R,Fe}}(n, M) \quad (5.12)$$

$$P_{\text{R,Mag,scl}}(n, M_{\text{scl}}) = k_A k_R^2 \cdot P_{\text{R,Mag}}(n, M) \quad (5.13)$$

As the identical magnetic flux density and saturation in the scaled PMSM are preserved, the scaled torque is derived in (5.14) based on the dq-frame linked to the rotor flux linkage vector [69, 70, 94].

$$\begin{aligned} M_{\text{scl}} &= \frac{3}{2} p (\Psi_{\text{Mag,scl}} I_{\text{q,scl}} + I_{\text{d,scl}} I_{\text{q,scl}} (L_{\text{d,scl}} - L_{\text{q,scl}})) \\ &= \frac{3}{2} p (k_A k_R \Psi_{\text{Mag}} \cdot k_R I_{\text{q}} + k_R I_{\text{d}} \cdot k_R I_{\text{q}} \cdot (k_A L_{\text{d}} \\ &\quad - k_A L_{\text{q}})) \\ &= k_A k_R^2 \cdot \frac{3}{2} p (\Psi_{\text{Mag}} I_{\text{q}} + I_{\text{d}} I_{\text{q}} (L_{\text{d}} - L_{\text{q}})) \\ &= k_A k_R^2 \cdot M \end{aligned} \quad (5.14)$$

In general, the motor's peak torque curve is determined by analyzing flux linkage and phase current using a specific control algorithm like maximum torque per ampere (MTPA). The utilization of the scaling law [69, 70] for flux linkage and phase current, which evident from the Poisson's equation, enables the calculation of the peak torque and nominal speed for the scaled motor. This approach will be verified in Chapter 6 and implemented into the Simulink model of the vehicle. It's essential to note that this approach is derived in the dq-frame. It requires detailed motor parameters, including dq-axis flux linkage. However, not all of these parameters are obtainable, leading to a

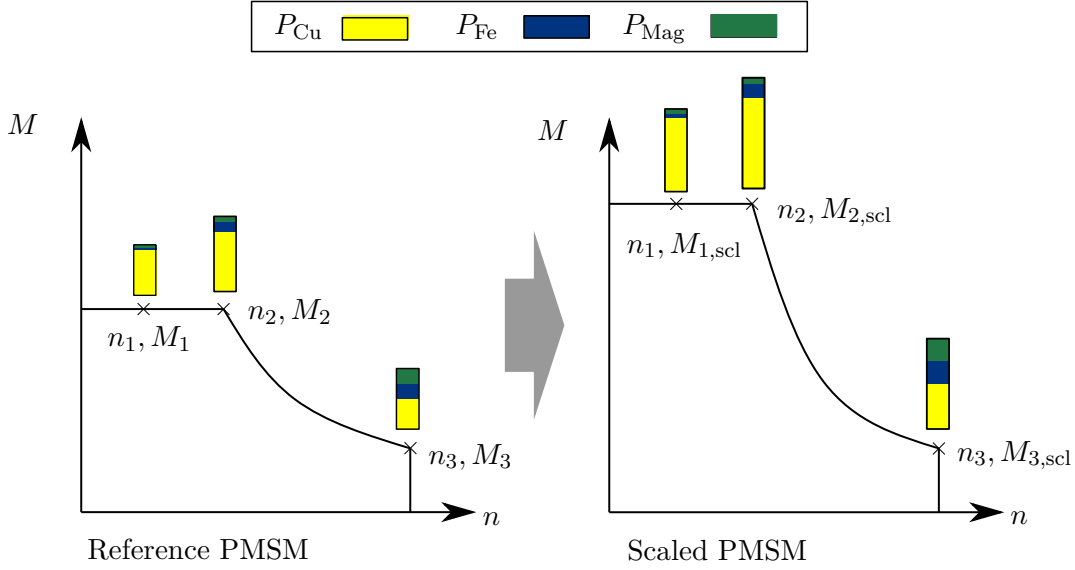


**Figure 5.4.** Calculation of the loss map for the scaled PMSM

Source: Chen et al. (2024). Reprinted with permission from SAGE Publications, Inc. doi:10.1177/09544070241254557

more general scenario where we can generally access only the total motor loss map and its peak torque curve at a fixed nominal speed from the test bench. Consequently, we consider that the nominal speed of the scaled PMSM remains the same as the reference PMSM to demonstrate a case study in this chapter. Since the phase voltage of the scaled PMSM will be changed as in (5.15) to (5.17) [69, 70], the DC-voltage for the scaled PMSM must be adjusted consequently to provide sufficient phase voltage for the motor at the operating point with nominal speed and maximum torque [87]. An overview of the DC-voltage supply for the reference PMSM and scaled PMSMs is shown in the Table 5.1.

$$U_{d,scl} = \frac{k_A}{k_R} R_s I_d + \omega k_A k_R L_q I_q \quad (5.15)$$

$$U_{q,scl} = \frac{k_A}{k_R} R_s I_q + \omega k_A k_R L_d I_d + k_A k_R \omega \Psi_{Mag} \quad (5.16)$$

$$U_{pha,scl} = \sqrt{U_{d,scl}^2 + U_{q,scl}^2} \quad (5.17)$$

The copper loss distribution ratio for the end winding  $r_{ew}$  is derived from the volume ratio. When it comes to axial scaling, only the volume in the core region is scaled by  $k_A$ , whereas for radial scaling, the winding in the core region is scaled by  $k_R^2$  and the end winding is scaled by  $k_R^3$ . Thus, the loss distribution ratio for the end winding in the scaled PMSM  $r_{ew,scl}$  can be calculated as follows:

$$r_{ew,scl} = \frac{k_R \cdot r_{ew}}{k_R \cdot r_{ew} + k_A \cdot (1 - r_{ew})} \quad (5.18)$$

Therefore, the loss maps for the stator, end winding and rotor of the scaled PMSM can be determined by the scaled copper losses, iron losses and magnet losses as well as

**Table 5.1.** DC-voltage for the reference PMSM and scaled PMSMs  
 Source: Chen et al. (2024). Reprinted with permission from SAGE Publications, Inc. doi:10.1177/09544070241254557

PMSM Scaling	DC-Voltage
Reference	350 V
$k_A = 0.8; k_R = 1$	278 V
$k_A = 0.9; k_R = 1$	315 V
$k_A = 1.1; k_R = 1$	385 V
$k_A = 1.2; k_R = 1$	420 V
$k_A = 1; k_R = 0.8$	280 V
$k_A = 1; k_R = 0.9$	315 V
$k_A = 1; k_R = 1.1$	385 V
$k_A = 1; k_R = 1.2$	420 V

the scaled loss distribution ratio for the end winding:

$$P_{S,scl} = (1 - r_{ew,scl}) \cdot P_{Cu,scl} + P_{S,Fe,scl} \quad (5.19)$$

$$P_{EW,scl} = r_{ew,scl} \cdot P_{Cu,scl} \quad (5.20)$$

$$P_{R,scl} = P_{R,Mag,scl} + P_{R,Fe,scl} \quad (5.21)$$

$$(5.22)$$

where

$$P_{Cu,scl} = P_{Cu,DC,scl} + P_{Cu,AC,scl} \quad (5.23)$$

By interpolating the operating points of the driving cycle on these loss maps of the scaled PMSM, the associated losses for the thermal model are computed.

### 5.3. Scaling of Thermal Parameters of the LPTN

The LPTN model for the reference PMSM, developed in Section 4.1.3, necessitates adaptation to simulate the temperature of the scaled PMSM. The adaptation process involves the scaling of thermal capacities and thermal resistances. The proof-of-concept for the proposed scaling approach for a PMSM for fixed operating points was first introduced in [95] and now further developed for the transient operating points [96]. The proposed scaling approach for thermal parameters are described as follows:

#### 5.3.1. Thermal Capacity

The scaling of thermal capacity is consistent with the approach in [95, 96]. The thermal capacities of the stator, rotor and housing in the scaled PMSM, determined by (5.24)

- (5.26), are scaled proportionally to the mass of the scaled PMSM by neglecting the temperature influence on the specific heat capacity:

$$C_{S,\text{scl}} = k_{\text{R}}^2 k_{\text{A}} \cdot C_{\text{S}} \quad (5.24)$$

$$C_{\text{R},\text{scl}} = k_{\text{R}}^2 k_{\text{A}} \cdot C_{\text{R}} \quad (5.25)$$

$$C_{\text{HE},\text{scl}} = k_{\text{R}}^2 k_{\text{A}} \cdot C_{\text{HE}} \quad (5.26)$$

The axial scaling has no impact on the thermal capacity of the end winding, as it solely alters the length in the core region. In radial scaling, the thermal capacity of the end winding is scaled by  $k_{\text{R}}^3$ , as it involves resizing the end coil in both axial and circumferential directions to form a circumferential coil loop in the end region [70]. Consequently, the thermal capacity of the end winding is scaled according to (5.27):

$$C_{\text{EW},\text{scl}} = k_{\text{R}}^3 \cdot C_{\text{EW}} \quad (5.27)$$

The thermal capacity of coolant presented in Section 4.1.1 shows a direct linear relationship with the mass of the coolant in the cooling channel. Therefore, the thermal capacity of the coolant for the scaled PMSM is expressed as in (5.28)

$$C_{\text{COE},\text{scl}} = k_{\text{R}}^2 k_{\text{A}} \cdot C_{\text{COE}} \quad (5.28)$$

By adopting this approach, the thermal model gathers all the entire thermal capacities essential for the scaled PMSM. Subsequently, the next step involves establishing the requisite thermal resistances within the scaled thermal model.

### 5.3.2. Thermal Resistance

Heat transfer is, as is known, classified into three mechanisms: conduction, convection and radiation. The thermal resistance of heat convection can be expressed by the contact surface and the heat convection coefficient, which is mostly determined by dimensionless empirical heat transfer correlations [49]. In the proposed LPTN, the convection resistance is represented by (4.16), where  $R_{\text{conv},0}$  includes the geometry information of the contact surface.

The primary mechanism for heat transfer between the housing and water jacket coolant is heat convection. To reduce complexity, it is assumed that the convection coefficient for the scaled PMSM is identical to that of the reference PMSM, as both have the same coolant inlet temperature and volume flow rate. Consequently, the convection resistance is influenced solely by the inner surface of the housing, where the coolant flows through. The width of the contact surface, which is equivalent to the perimeter of the radial cross-section, can be directly scaled by  $k_{\text{R}}$ , whereas the length of the contact surface  $l_{\text{H},\text{scl}}$  is the sum of the unchanged length out of the core region  $l_{\text{H},\text{ext}}$  and the scaled length in the core region  $l_{\text{core},\text{scl}}$  by the axial scaling. The calculation of the scaled thermal resistance  $R_{\text{COE-HE},0,\text{scl}}$  is as follows:

$$l_{\text{H},\text{ext}} = l_{\text{H}} - l_{\text{core}} \quad (5.29)$$

$$l_{\text{core},\text{scl}} = k_{\text{A}} \cdot l_{\text{core}} \quad (5.30)$$

$$l_{\text{H},\text{scl}} = l_{\text{core},\text{scl}} + l_{\text{H},\text{ext}} \quad (5.31)$$

$$R_{\text{COE-HE},0,\text{scl}} = \frac{l_{\text{H}}}{k_{\text{R}} \cdot l_{\text{H},\text{scl}}} \cdot R_{\text{COE-HE},0} \quad (5.32)$$

The set of equations (5.29) - (5.32) delineates the interrelation of parameters in the thermal model, specifically addressing the length and width of the contact surface in the context of a scaled PMSM. The unchanged length out of the core region  $l_{H,\text{ext}}$  is the difference between the total length  $l_H$  and the length within the core  $l_{\text{core}}$ . As only the length in the core region is scaled, the length  $l_{\text{core}}$  is influenced by an axial scaling factor  $k_A$ . The scaled equivalent path length of the end winding  $l_{\text{EW},\text{scl}}$  is proportional to the original path length  $l_{\text{EW}}$  with  $k_R$ . The total length of the contact surface  $l_{H,\text{scl}}$  can be expressed as the combination of two components: the unaltered length beyond the core region  $l_{H,\text{ext}}$  and the length within the core region that has been scaled  $l_{\text{core},\text{scl}}$ . The width of the contact area is proportional to the scaling factor  $k_R$ , as the radial scaling factor influences the diameter of the PMSM by  $k_R$ . Therefore, the final scaling formula for  $R_{\text{COE-HE},0,\text{scl}}$  is obtained as (5.32).

The thermal resistance between the housing and stator is primarily governed by heat conduction, which is influenced by factors such as path length, contact area, and thermal conductivity of the material [49]. Similar to how thermal resistance is scaled between the housing and the water jacket coolant, the contact surface length is divided by axial scaling into an unchanged part outside the core region and a proportionally adjusted length in the core region. The width of the contact area is directly scaled by the radial scaling factor  $k_R$ . Therefore, assuming negligible temperature effects on the thermal conductivity of the material, the scaled thermal resistance  $R_{\text{HE-S},\text{scl}}$  can be expressed as shown in (5.33) - (5.35).

$$l_{\text{core},\text{scl}} = k_A \cdot l_{\text{core}} \quad (5.33)$$

$$l_{H,\text{scl}} = l_{\text{core},\text{scl}} + l_{H,\text{ext}} \quad (5.34)$$

$$R_{\text{HE-S},\text{scl}} = \frac{l_H}{k_R \cdot l_{H,\text{scl}}} \cdot R_{\text{HE-S}} \quad (5.35)$$

The thermal resistance between the stator and rotor is generally not only dependent on the geometric dimensions, but also related to the rotational speed of the rotor and temperature. At different rotational speeds, the dominant convection in the air gap is different, resulting in different heat transfer such as laminar flow, Taylor vortices and turbulent flow. Since the operating points of the driving cycle and transmission ratio are unchanged, the rotational speed of the rotor is identical to that of the reference PMSM. Moreover, the change in air gap temperature from 50 °C to 200 °C does not have a considerable impact on the convection resistance as shown in [95]. Therefore, the influence of the temperature in the air gap can be neglected. Given this assumption, the convection coefficient remains unchanged from the reference PMSM, meaning that the scaling of thermal resistance  $R_{\text{S-R},0}$  is determined solely by the contact surface and expressed in (5.36).

$$R_{\text{S-R},0,\text{scl}} = \frac{1}{k_R k_A} \cdot R_{\text{S-R},0} \quad (5.36)$$

The thermal resistance between the stator and the end winding plays a crucial role in the thermal management of electric motors. The thermal resistance between the stator and the end winding is characterized by heat conduction as well, a fundamental process in which heat energy transfers through materials due to a temperature gradient. As depicted in Fig. 5.5, the path length  $l$  is the distance between the average temperature point of the winding in the core region and the average temperature point of the end winding, which consists of the equivalent path length in the core region  $l_{\text{core}}$  and the

equivalent path length of the end winding  $l_{EW}$ . The contact area  $A$  only changes due to the change in the cross-sectional area of the winding by  $k_R$ . Thus, the thermal resistance  $R_{S-EW,scl}$  for the scaled PMSM is outlined by (5.37) - (5.41).

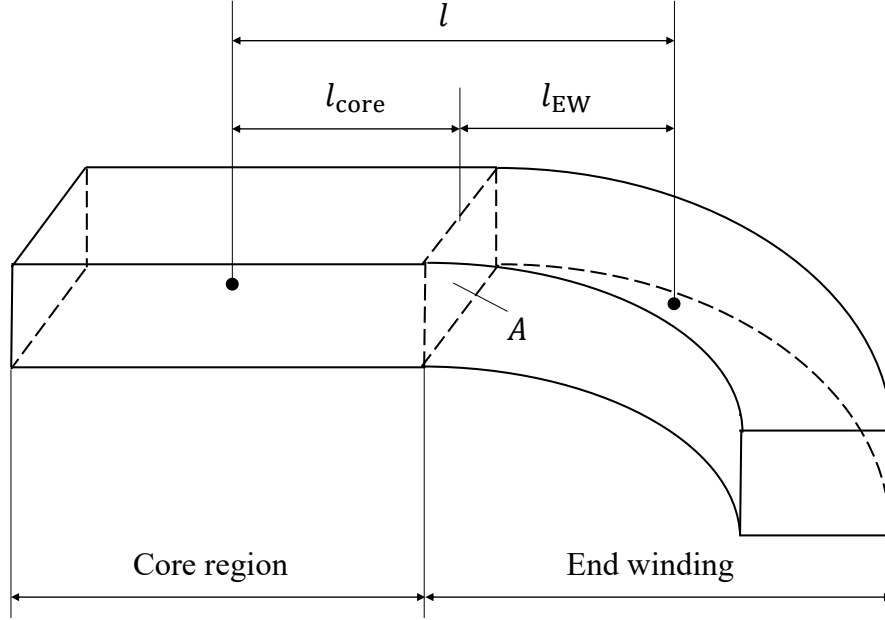


**Figure 5.5.** Conductive thermal resistance between stator and end winding  
 Source: Chen et al. (2024). Reprinted with permission from SAGE Publications, Inc. doi:10.1177/09544070241254557

$$l_{core,scl} = k_A \cdot l_{core} \quad (5.37)$$

$$l_{EW,scl} = k_R \cdot l_{EW} \quad (5.38)$$

$$l_{scl} = l_{core,scl} + l_{EW,scl} \quad (5.39)$$

$$A_{scl} = k_R^2 \cdot A \quad (5.40)$$

$$R_{S-EW,scl} = \frac{l_{scl}}{k_R^2 \cdot l} \cdot R_{S-EW} \quad (5.41)$$

The scaled equivalent path length  $l_{core,scl}$  is directly proportional to the original path length in the core region  $l_{core}$  with the scaling factor  $k_A$ . Similar to the core region, this path length is influenced by a scaling factor  $k_R$ . The scaled equivalent path length of the end winding  $l_{EW,scl}$  is proportional to the original path length  $l_{EW}$  with  $k_R$ . The overall scaled path length  $l_{scl}$  is the sum of the scaled equivalent path lengths in the core region  $l_{core,scl}$  and the end winding  $l_{EW,scl}$ . Moving on to (5.40), the scaled contact area  $A_{scl}$  is determined by scaling the original contact area  $A$  by the square of the scaling factor  $k_R$ . Since conduction resistance is directly proportional to the length and inversely proportional to the contact area, the final scaling formula is obtained as (5.41).

As outlined in the LPTN model, the consideration primarily revolves around the circumferential contact area with the ambient environment. This means that the contact area is intricately linked to the product of the scaling factors of  $k_A$  and  $k_R$ . Thus, the

scaled thermal resistance between the housing and the ambient environment, indicated as  $R_{R-A,scl}$ , is approximated as follows.

$$R_{HE-A,scl} = \frac{1}{k_A k_R} \cdot R_{HE-A} \quad (5.42)$$

In the proposed LPTN model, the thermal resistance  $R_{R-A}$  represents a strong abstract heat dissipation from the rotor to the ambient. This representation significantly simplifies the physical and thermal conditions, as other heat paths e.g., through the bearing or end space are only indirectly taken into account. As a result, we consider the thermal resistance between the rotor and ambient for the scaled PMSM, denoted as  $R_{R-A,scl}$ , to remain unchanged.

$$R_{R-A,scl} = R_{R-A} \quad (5.43)$$

The formula of the thermal resistance between the coolant inlet and the coolant outlet is shown in Section 4.1.1. Since the volume flow rate of the coolant is unchanged, under the assumption of constant coolant density, we can infer that the mass flow rate of the coolant remains constant as well. This constancy in mass flow rate results in a consistent thermal resistance between the coolant inlet and outlet.

$$R_{CIN-COE,scl} = R_{CIN-COE} \quad (5.44)$$

Using this approach, thermal resistances for the scaled PMSM are calculated. These determined thermal parameters enable the simulation of the thermal behavior of the scaled PMSM, when incorporated into the LPTN thermal model.

## 5.4. Sensitivity Analysis Based on Validation Data of the Scaled Motor-CAD Model

The validated Motor-CAD model in Section 5.1 is utilized to generate the temperature of the coolant, stator, end winding and rotor for the reference PMSM and the scaled PMSM to verify the scaling approach. Since the losses are the heat sources of the thermal model for temperature estimation, the scaling approach for losses explained in the Section 5.2 is employed to determine the losses for the scaled Motor-CAD model. Differently scaled Motor-CAD models are implemented to get the required validation data for the scaled PMSMs. The design space for the reference PMSM is restricted due to the manufacturing and technological limitations, e.g. the stiffness of the shaft restricts the maximum length of the PMSM [72]. Furthermore, 25% change in the axial and radial directions of the PMSM can result in an almost 200% change in the output torque [97,98]. So in this dissertation the scaling range is limited by 0.8 to 1.2. Besides that, the optimal split ratio, which reflects the ratio between the stator's inner and outer diameters, generally alters depending on whether the machine is small, medium, or large in size.

With the comparison of the power share map between the scaled PMSM in Fig. 5.6, which indicates the locations the PMSM visited most frequently, we can gain insight into the changes in losses of the scaled PMSM. Axial scaling has an impact on the peak torque of the PMSM but does not substantially affect the efficiency distribution in the map. Although most losses, with the exception of friction losses, will increase or decrease

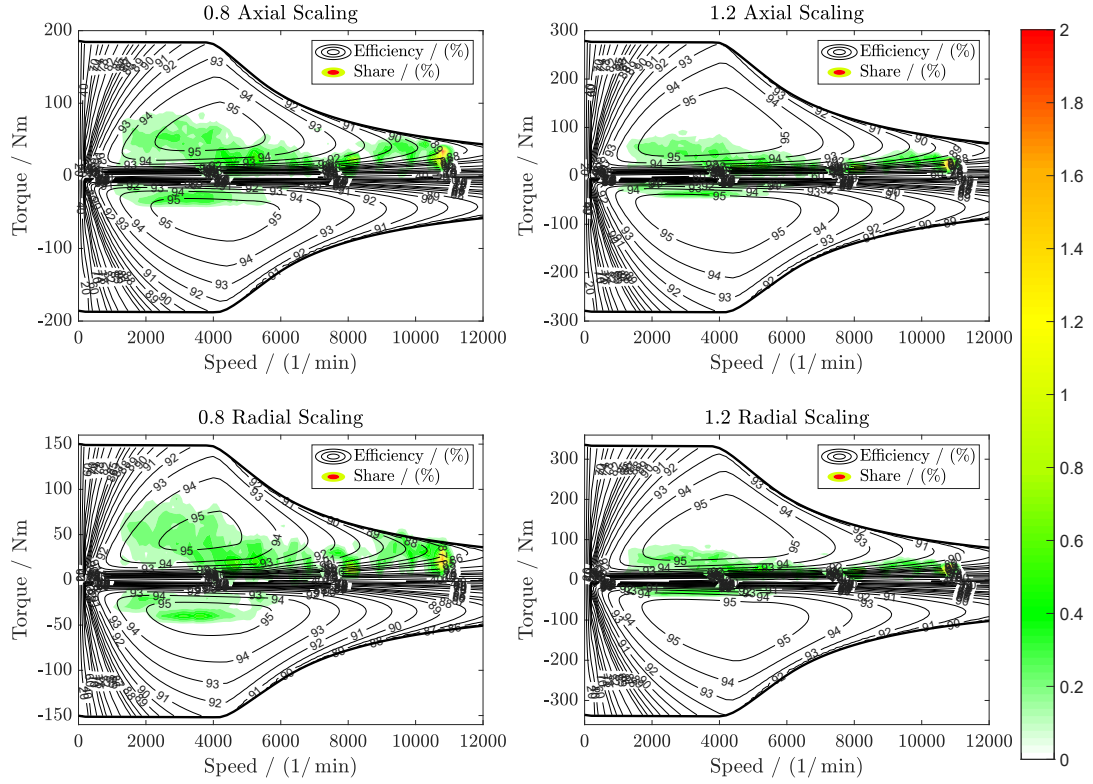


**Figure 5.6.** Power share map of the scaled PMSM for the extended WLTC cycle at motor temperature of  $110^{\circ}\text{C}$

with axial scaling, the corresponding output power increases or decreases proportionally. Running the same operating points, the PMSM with an axial scaling of 0.8 has more operating points in the high-efficiency region than the PMSM with an axial scaling of 1.2, resulting in reduced losses. When applying radial scaling, the AC copper losses, the iron losses, and the magnetic losses are affected, while DC copper losses in the core region are only impacted by axial scaling. In the case of 0.8 radial scaling, the efficiency of the PMSM declines in the base speed region due to a reduction in output power. Conversely, for 1.2 radial scaling, the output power increases, resulting in a slight improvement in efficiency to some extent across the base speed region. However, the operating points are far away from the high-efficiency region. The total loss resulting from scaling can be observed in the last subplot of Fig. 5.7.

The results of the sensitivity analysis for various axial and radial scaling factors in Fig. 5.7 demonstrate that the temperature of the PMSM is substantially impacted by radial scaling in geometric dimensions. The reason for this is that the increase in loss is balanced by a corresponding increase in contact surface with the coolant, as the axial length of the PMSM is increased, leading to only slight changes in temperature. Conversely, when the radial diameter of the PMSM is decreased, the contact surface with the coolant decreases, causing the temperature to rise more significantly. The influence of motor scaling on coolant output temperature is marginal since the heat generated by the motor constitutes a small fraction of the total cooling power. The dominant factors

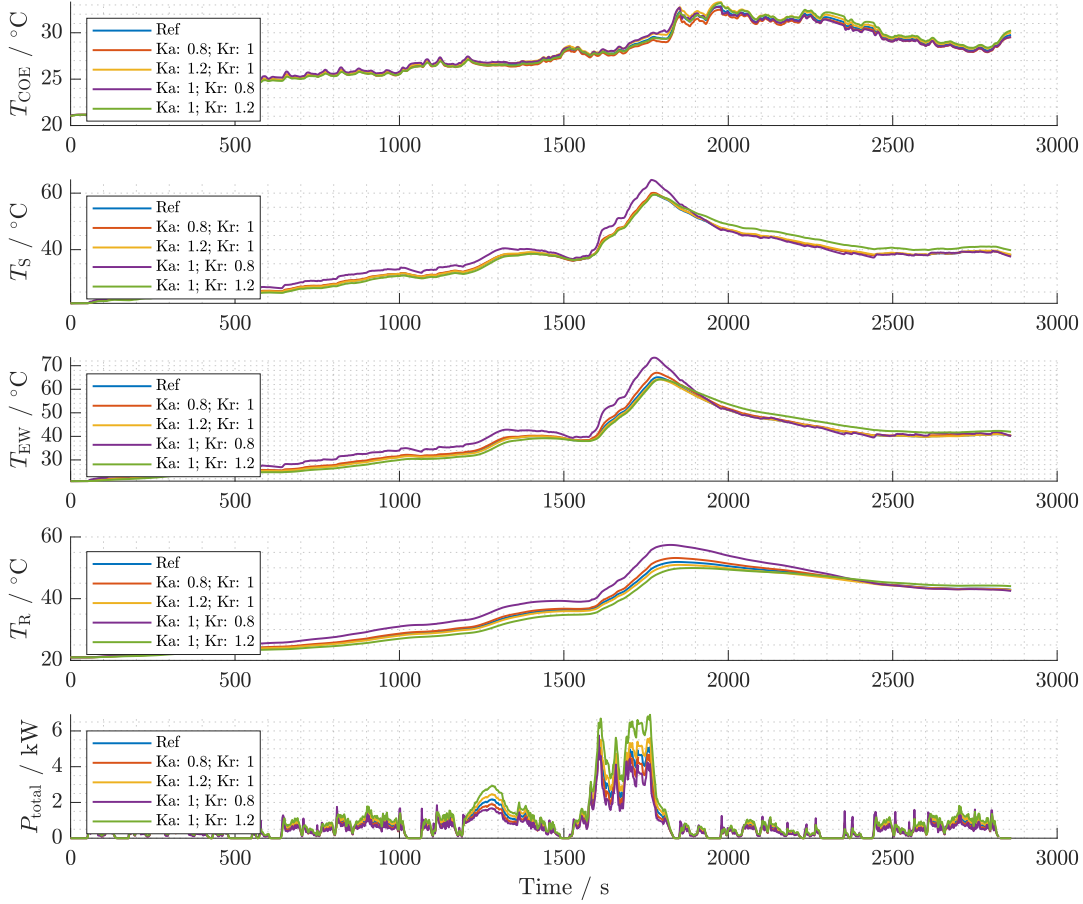


**Figure 5.7.** Temperatures and losses of the scaled PMSM for the extended WLTC at ambient temperature of 20°C

governing the cooling process, such as coolant flow rate and heat exchange efficiency, are largely unaffected by changes in motor scaling.

## 5.5. Validation Results

In this chapter, the accuracy of the losses and temperatures attributed to the scaled PMSMs are substantiated through a comprehensive validation process against the outcomes obtained from Motor-CAD simulations. This validation step is crucial for ensuring the reliability and the predictive capabilities of the scaling approach.

### 5.5.1. Validation of the Losses of Scaled PMSMs

The losses of the reference PMSM are adjusted using the methodology outlined in Section 5.2 and compared to the outcomes of the scaled Motor-CAD model. The validation, is conducted based on the total losses, particularly focusing on a scenario where the axial scaling factor is set to 0.8. This validation is performed against the extended WLTC under ambient temperature conditions of 20°C. The comparison is visualized in Fig. 5.8,

where the red line corresponding to the total losses calculated using the scaling law methodology and the blue line depicting the total losses determined by Motor-CAD based on finite element analysis (FEA). Upon examining the plot, it becomes apparent that throughout the entire WLTC cycle, including low, medium, high and extra high phases, the total losses derived from the scaling law closely match those obtained from the Motor-CAD analysis. This alignment between the two methods indicates a high degree of consistency and accuracy in the modeling and prediction of losses. The RMSE associated with this comparison is reported to be 34 W, which indicates the average deviation between the predicted and actual losses across the entire WLTC cycle. Additionally, the maximum loss error observed is 230.2 W, representing the highest deviation recorded between the two methods at any point within the cycle.

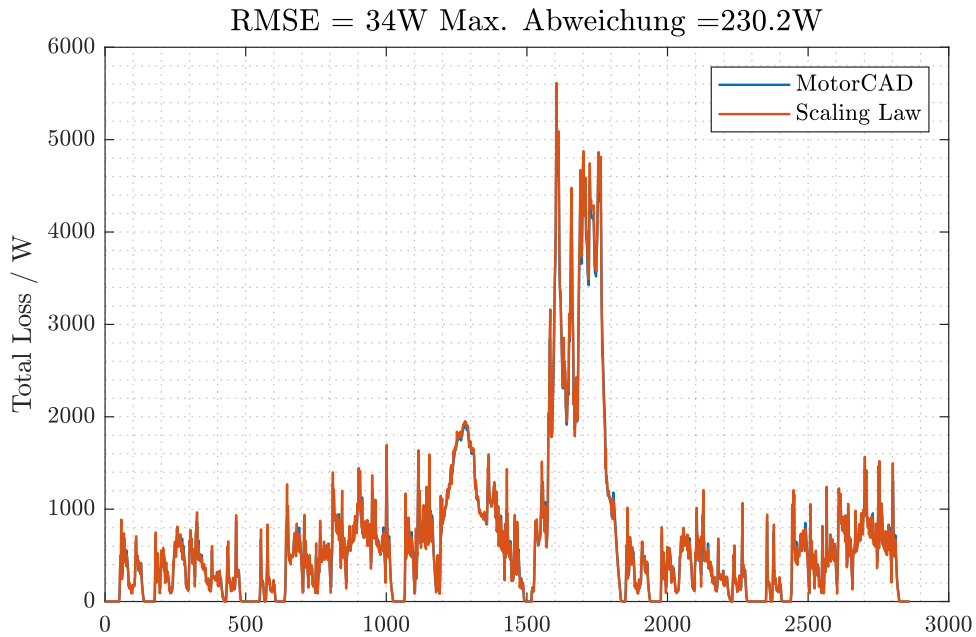


**Figure 5.8.** Total losses validation for 0.8 axial scaling against the extended WLTC cycle at the ambient temperature of 20 °C  
 Source: Chen et al. (2024). Reprinted with permission from SAGE Publications, Inc. doi:10.1177/09544070241254557

Fig. 5.9 provides a detailed breakdown of various components contributing to the total losses in the motor system. This breakdown includes DC copper loss, AC copper loss, stator iron loss, rotor iron loss, magnet loss, and friction loss. Analyzing Fig. 5.9 offers a means to assess the accuracy of the scaling methodology for each loss component individually. By comparing the results obtained from the scaling approach with those from Motor-CAD, discrepancies or errors specific to certain loss components can be identified. For instance, the figure reveals that DC copper loss and magnet loss exhibit discrepancies, particularly in the high-speed region. While DC copper loss appears disproportionately large, magnet loss conversely appears diminished. Within this complex interplay of electromagnetic phenomena, two primary factors emerge as potential contributors to these observed errors: the consistency of magnet flux density between the reference PMSM and the scaled PMSM, and the nonlinearity of ferromagnetic materials,

especially within the high-frequency domain. However, other loss components, such as AC copper loss, stator iron loss, rotor iron loss, and friction loss, show close agreement between the scaling approach and Motor-CAD results across various operating conditions. This indicates that the scaling methodology is effective in modeling these loss components accurately. In the appendix, a validation of total losses and related losses for a radial scaling factor of 1.2 for the US06 cycle is presented in Fig. A.5 and Fig. A.6.

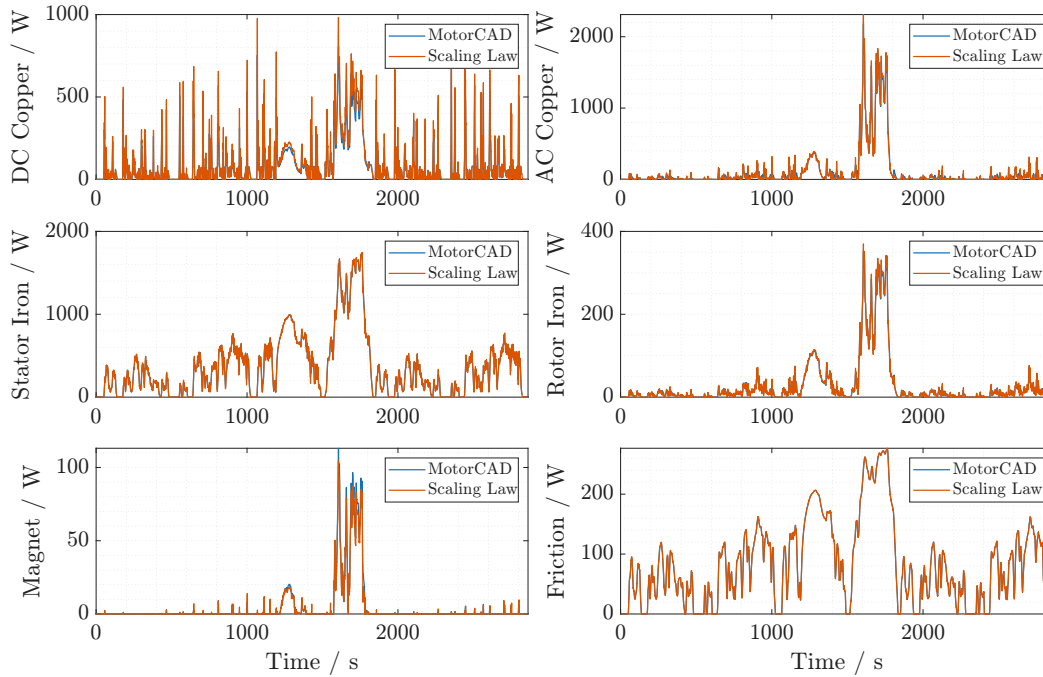


**Figure 5.9.** Related losses validation for 0.8 axial scaling against the extended WLTC cycle at the ambient temperature of 20 °C

Fig. 5.10 illustrates a comprehensive visualization of the total loss deviation for both axial and radial scaling scenarios, employing box-whisker charts to elucidate the comparative analysis. The blue box signifies data derived from the WLTC at an ambient temperature of 20 °C, while the red box represents results obtained from the US06 cycle under the same ambient conditions. These box-whisker charts offer a succinct representation of the distribution of total loss deviation, capturing key statistical measures such as the median, interquartile range, and the range of variability. The central tendency of the data is encapsulated by the median, situated within the confines of each box. A notably diminutive median deviation is evident in both charts, underscoring a remarkable concordance between the Motor-CAD simulation results and the outcomes derived from the scaling approach. Such consistency is indicative of the reliability and accuracy of the scaling approach in approximating motor losses across diverse operational conditions. The interquartile range, delineated by the extent of the box, encompasses the middle 50% of the total loss deviation. Extending beyond the confines of the box, the whiskers of the charts delineate the minimum and maximum values of the total loss deviation. Notably, the interquartile range and whiskers in the US06 cycle exhibit a broader span compared to those of the WLTC cycle, indicative of a greater degree of dispersion and

variability in total loss deviation. This variance is attributed to the dynamic nature of the US06 cycle, characterized by higher load driving conditions and more aggressive acceleration profiles that impose higher demands on the motor. Additionally, the summaries of the deviations in total loss between the scaling approach and the Motor-CAD results for both the WLTC and the US06 cycle for various axial scaling factors and radial scaling factors are listed in the appendix in Table A.1 and Table A.2, providing a concise overview of the performance of the scaling approach under varied operating conditions.

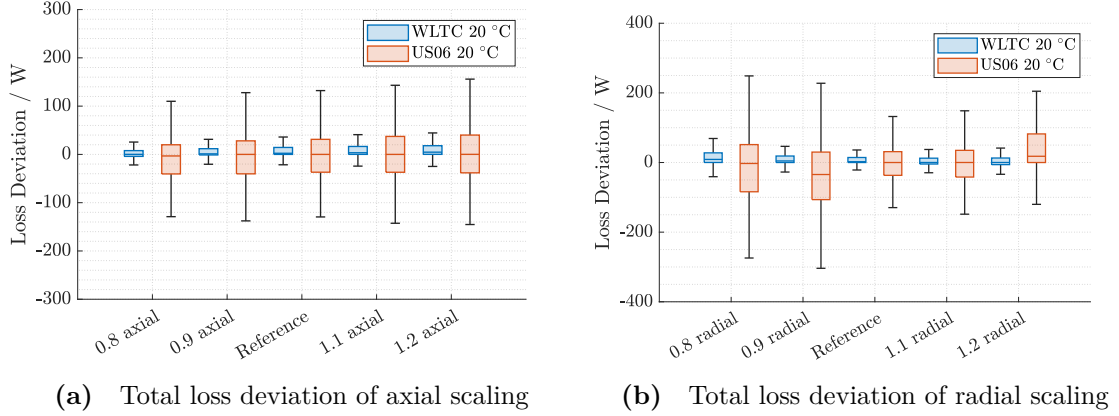


**Figure 5.10.** Box-whisker charts for the total loss deviation in the axial scaling and radial scaling

Source: Chen et al. (2024). Reprinted with permission from SAGE Publications, Inc. doi:10.1177/09544070241254557

### 5.5.2. Validation of the Temperatures of Scaled PMSMs

Based on the resulting temperature profiles of Motor-CAD in Section 5.4, the thermal parameters of the reference PMSM in the low-order LPTN can be firstly identified, which are the basic parameters for applying the scaling approach. The parameter identification can be interpreted as a constrained optimization problem in order to reduce the error between the model output and the measurements simultaneously. The optimization problem can be generally formulated as in (4.25). The simulation of the validated Motor-CAD model for the extended WLTC cycle with the realistic coolant profile shown in Fig. 5.3 are used to identify the thermal parameters of the proposed LPTN. The thermal parameters of a reference PMSM are crucial for understanding its thermal behavior and optimizing its performance. These parameters, delineated in detail within Table 5.2, are divided into two primary categories: Scaling-related parameters and Fluid-related parameters. Scaling-related parameters play a pivotal role in adapting the motor's thermal characteristics to variations in its geometric volume. Among these parameters are thermal capacity and thermal resistance. In contrast, Fluid-related parameters are primarily concerned with the properties of the fluid used for cooling purposes within the motor. These parameters typically encompass temperature and flow rate, both of which significantly influence the effectiveness of fluid-based heat transfer mechanisms.

The simulation results of the identified LPTN model are plotted in Fig. 5.11. The alignment between the estimated temperatures and the values derived from the Motor-CAD model is evident, demonstrating a high degree of consistency across various op-

**Table 5.2.** Thermal parameters of the reference PMSM

Symbol	Value	Comments
$C_{\text{COE}}$	367 J/K	Scaling-related
$C_{\text{S}}$	10 821 J/K	Scaling-related
$C_{\text{EW}}$	3664 J/K	Scaling-related
$C_{\text{R}}$	11 511 J/K	Scaling-related
$C_{\text{HE}}$	10 997 J/K	Scaling-related
$R_{\text{CIN-COE}}$	0.003 K/W	Scaling-related
$R_{\text{COE-HE},0}$	0.0006 K/W	Scaling-related
$b_{\text{COE-HE}}$	1.58	Fluid-related
$\alpha_{\text{COE-HE}}$	0.0213	Fluid-related
$a_{\text{COE-HE}}$	0.0981	Fluid-related
$R_{\text{S-R},0}$	0.0505 K/W	Scaling-related
$b_{\text{R-S}}$	0.0398	Fluid-related
$\alpha_{\text{R-S}}$	2.151	Fluid-related
$a_{\text{R-S}}$	1.808	Fluid-related
$R_{\text{HE-S}}$	0.0146 K/W	Scaling-related
$R_{\text{S-EW}}$	0.0244 K/W	Scaling-related
$R_{\text{HE-A}}$	0.1267 K/W	Scaling-related
$R_{\text{R-A}}$	795 K/W	Scaling-related

erating conditions. Upon scrutinizing the temperature deviations, it becomes apparent that the stator temperature, end winding temperature, and rotor temperature exhibit a remarkable alignment with the results generated by Motor-CAD right from the outset. Their trajectories closely mirror each other, suggesting a near-perfect correspondence between the predicted and observed temperatures. This high degree of agreement underscores the accuracy of the modeling process employed. Conversely, while the temperatures of the housing and coolant generally track the trends observed in the Motor-CAD results, there are discernible deviations present from the initial stages. These variations, albeit minor, indicate some level of discrepancy between the predicted and observed temperatures for these components. It is worth noting that despite these deviations, the overall trends remain consistent. Interestingly, upon closer inspection, the validation data pertaining to the housing and coolant temperatures exhibits a degree of fluctuation, particularly when compared to the smoother temperature profiles generated by the LPTN model. This implies that the identified thermal capacity can be further reduced.

The stator temperature boasts the lowest RMSE, registering at approximately  $0.48\text{ }^{\circ}\text{C}$ . This minimal RMSE value reflects a high level of agreement between the predicted and actual stator temperatures, affirming the fidelity of the modeling approach in capturing the thermal behavior. The maximum temperature error is identified in the rotor temperature, amounting to  $1.71\text{ }^{\circ}\text{C}$ , which seems relatively modest in relation to the overall temperature range.

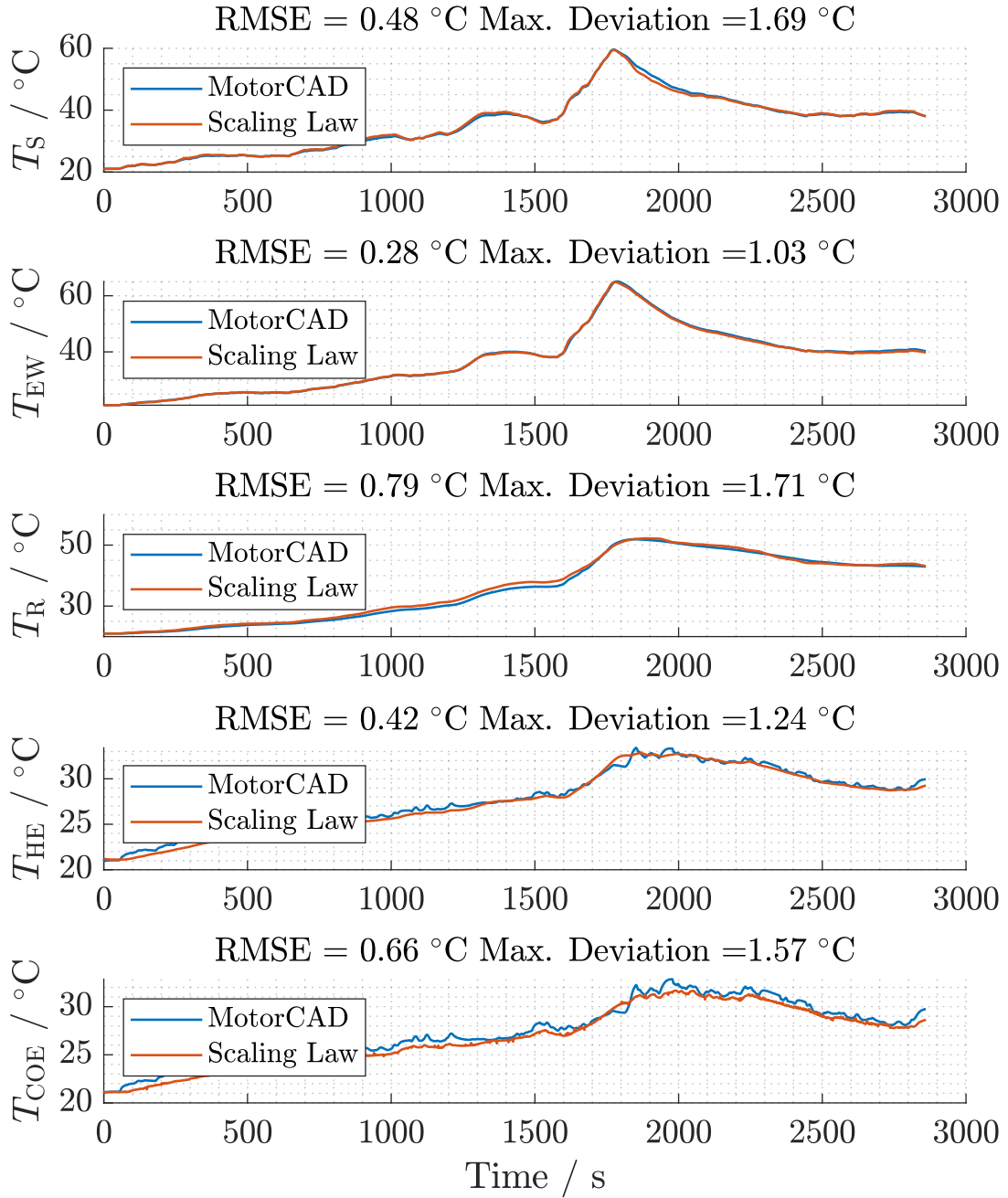


**Figure 5.11.** Parametrization based on the extended WLTC cycle at an ambient temperature of  $20\text{ }^{\circ}\text{C}$

To evaluate the accuracy of the identified LPTN, comprehensive validation against real-world conditions is imperative. In this evaluation, the LPTN model undergoes validation against two distinct driving cycles: the extended WLTC at ambient temperatures of 35 °C and 50 °C, and the extended US06 cycle at an ambient temperature of 20 °C. It's noteworthy that the extended US06 cycle comprises two sequential US06 cycles. For a detailed understanding, the cycle and coolant profiles utilized in the validation process are provided in the appendix. Upon analysis of the validation results, it is obvious that all estimated temperatures are very close to the values of the Motor-CAD model. Despite the overall satisfactory performance, the validation results reveal a maximum temperature deviation during the extended WLTC cycle at an ambient temperature of 35 °C. The RMSE of the stator temperature for this scenario is calculated to be 1.3 °C, with the maximum temperature error reaching 2.82 °C. For a more detailed insight into the validation results of the reference PMSM, the temperature profiles for the extended WLTC cycle at an ambient temperature of 35 °C and 50 °C as well as the extended US06 cycle at an ambient temperature of 20 °C are provided in the appendix.

Following the identification of the LPTN model for the reference PMSM, a scaling procedure outlined in Section 5.3 is applied to the LPTN. Subsequently, the scaled LPTN model is compared against the results obtained from the scaled Motor-CAD model. This comparison is particularly focused on an axial scaling factor of 0.8 and is conducted against the extended WLTC at an ambient temperature of 20 °C, as illustrated in Fig. 5.12. In Fig. 5.12, the red line represents the simulated temperatures derived from the scaled PMSM using the scaling approach, while the blue line depicts the validation results obtained from the Motor-CAD model. This graphical representation offers a visual assessment of the agreement between the simulated temperatures of the stator, end winding, rotor, housing, and coolant derived from the scaling approach and the corresponding values obtained from the Motor-CAD model. Upon scrutiny of the validation outcomes, it becomes apparent that the scaling approach yields simulated temperatures that closely resemble the values obtained from the Motor-CAD model across various components of the PMSM. Specifically, the validation results pertaining to the housing and coolant outlet temperature for the scaled PMSM closely align with the values obtained from the Motor-CAD model. However, it is observed that these temperatures exhibit a relatively flatter profile, which can be attributed to the larger thermal capacity resulting from the reference LPTN model. Upon evaluation of the validation results, it is determined that the RMSE reaches 1.32 °C, with the maximum temperature error amounting to 2.61 °C.

The temperature deviations of the stator, end winding, rotor, and coolant between the scaling approach and the Motor-CAD model for all validation cases with axial scaling are summarized in Fig. 5.13. This comprehensive overview provides insights into the discrepancies across different cycle profiles and ambient conditions. Upon analysis of the overview results, several key observations can be made. Firstly, it is evident that, apart from the coolant temperature, the errors in the stator, end winding, and rotor temperature models tend to increase with rising temperatures, with the largest errors observed during the WLTC at 50 °C. This trend suggests that higher ambient temperatures pose greater challenges in accurately predicting temperatures across various components of the PMSM. The maximum RMSE observed across all validation cases is less than 3 °C. On average, the RMSE is calculated to be 0.73 °C in comparison to Motor-CAD results, confirming the accuracy of this approach. Furthermore, the error between the rotor and coolant temperatures appears to be less significant across varying

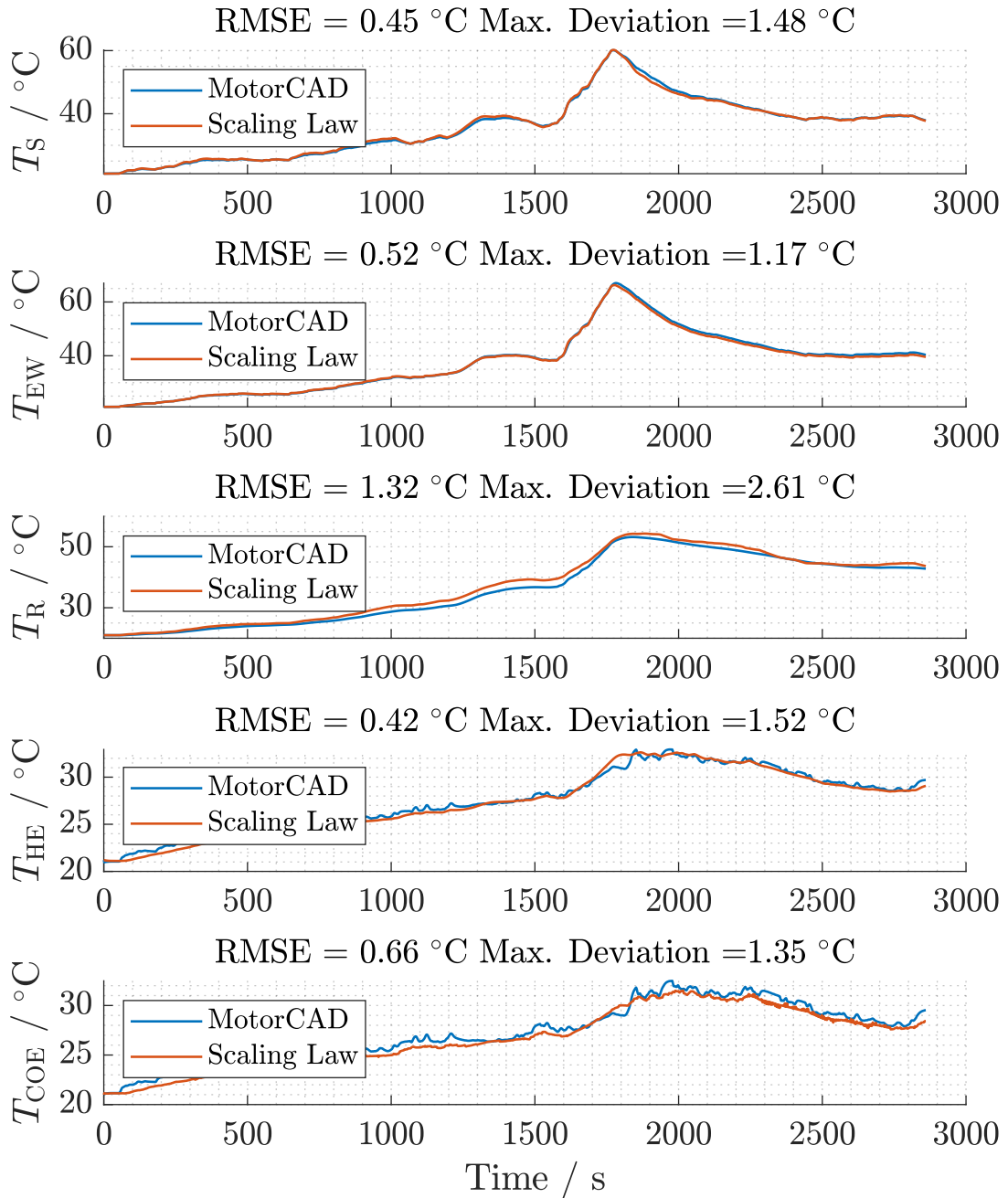


**Figure 5.12.** Validation results of temperature estimation for 0.8 axial scaling against the extended WLTC cycle at an ambient temperature of 20 °C

ambient temperatures compared to the stator and end winding temperatures. It is notable that the temperature errors of the stator and end winding are greatly influenced by the ambient temperature.

In Fig. 5.14, the validation results for a radial scaling factor of 1.2 are presented. The red line represents the temperatures simulated by the scaled PMSM using the scaling approach, while the blue line depicts the validation results obtained from Motor-CAD.

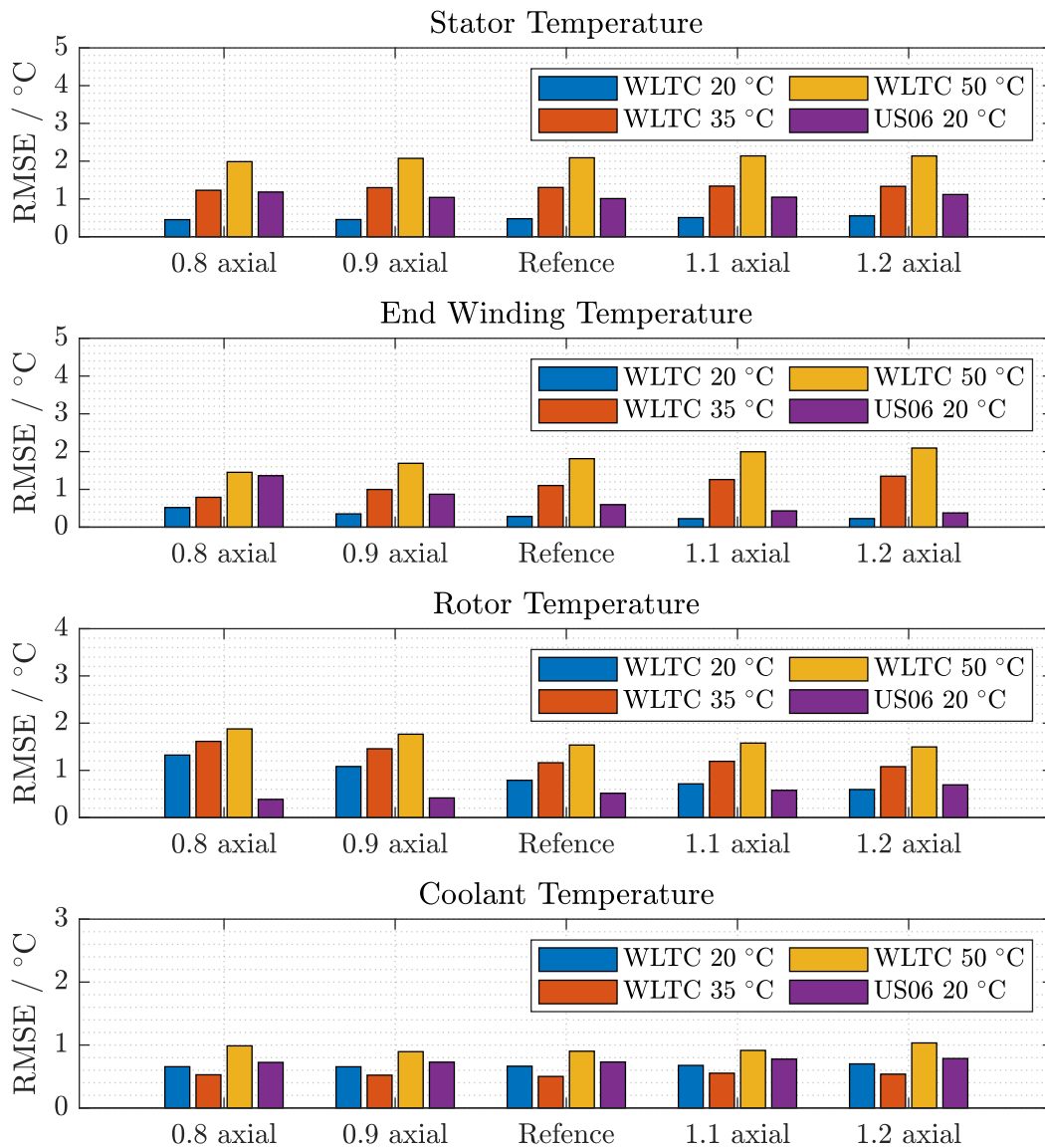


**Figure 5.13.** Temperature deviation of axial scaling in comparison to Motor-CAD

Similar to the previous results for axial scaling of 0.8, the temperature profiles of the stator and rotor obtained from the scaling approach closely match those predicted by the Motor-CAD model. However, it is observed that the rotor temperature is slightly overestimated for a radial scaling factor of 1.2. This deviation may arise due to factors such as the omission of heat exchange between the rotor and end space in the thermal modeling process, which could lead to an inaccurate representation of the thermal behavior in this region. The maximum deviation in the rotor temperature for a radial scaling of 0.8 can reach up to 2.61 °C. By incorporating the heat exchange between the rotor and end space into the modeling, it may be possible to improve the accuracy of temperature predictions and reduce deviations observed in the scaled PMSM simulations.

The comparison of stator, end winding, and rotor temperatures between the scaling

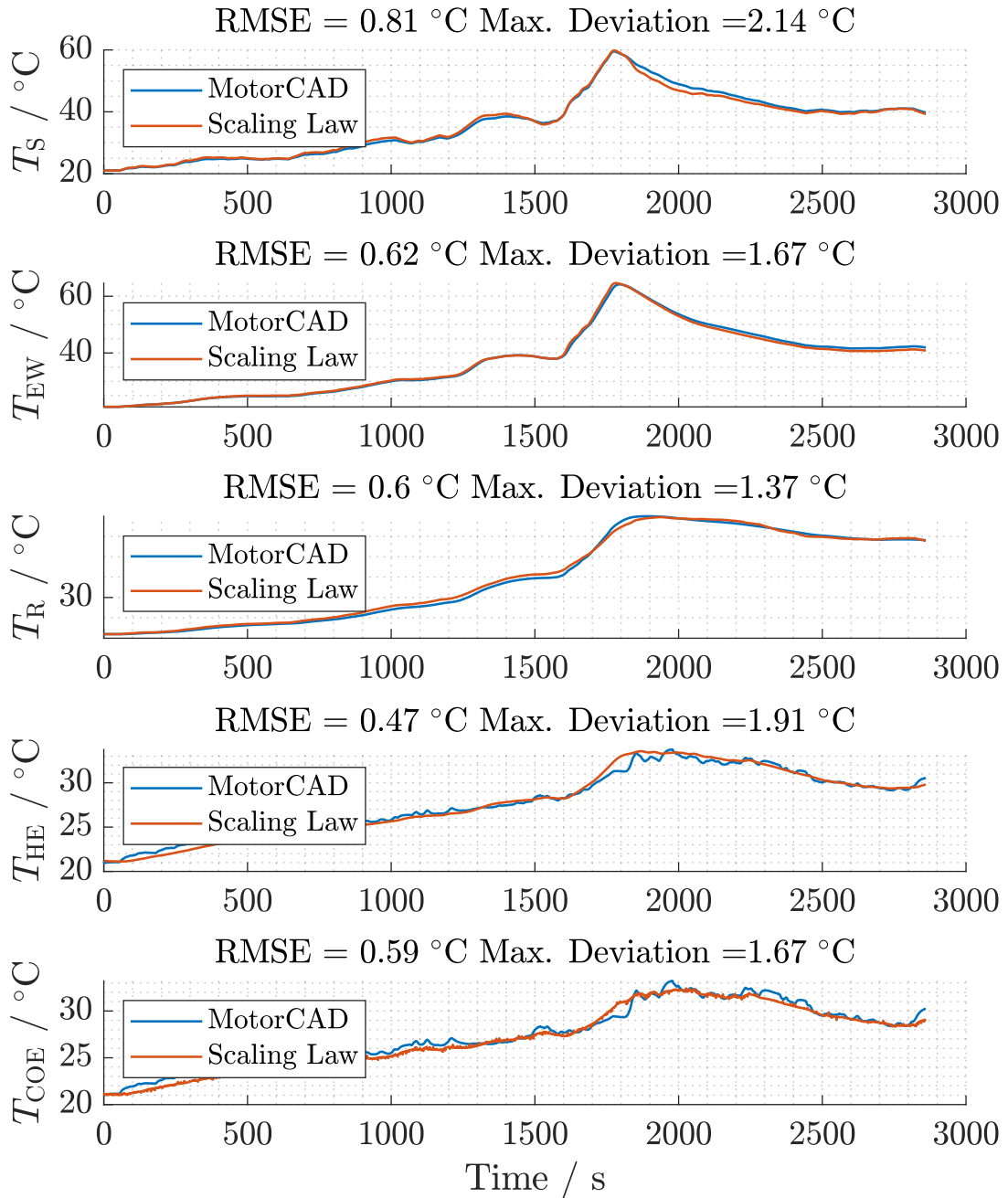


**Figure 5.14.** Validation results of temperature estimation for 1.2 radial scaling against the extended WLTC cycle at an ambient temperature of 20 °C

approach and the Motor-CAD model for all radial scaling validation cases is illustrated in Fig. 5.15. This comprehensive overview allows for a detailed analysis of temperature errors across different cycles and ambient conditions for radial scaling. Similar to the overview results for axial scaling, all temperature errors tend to increase with rising temperatures, with the largest errors observed during the WLTC at 50 °C. The RMSE of 2.92 °C is observed in the end winding temperature for the extended WLTC at an

ambient temperature of 50 °C. Despite the maximum deviation, the average RMSE of all temperatures is calculated to be 1.22 °C, indicating a strong level of agreement between the temperatures calculated by the scaling approach and the observed temperatures from Motor-CAD. Moreover, the error between the rotor and coolant temperatures appears to be relatively stable across different ambient temperatures compared to the stator and end winding temperatures.

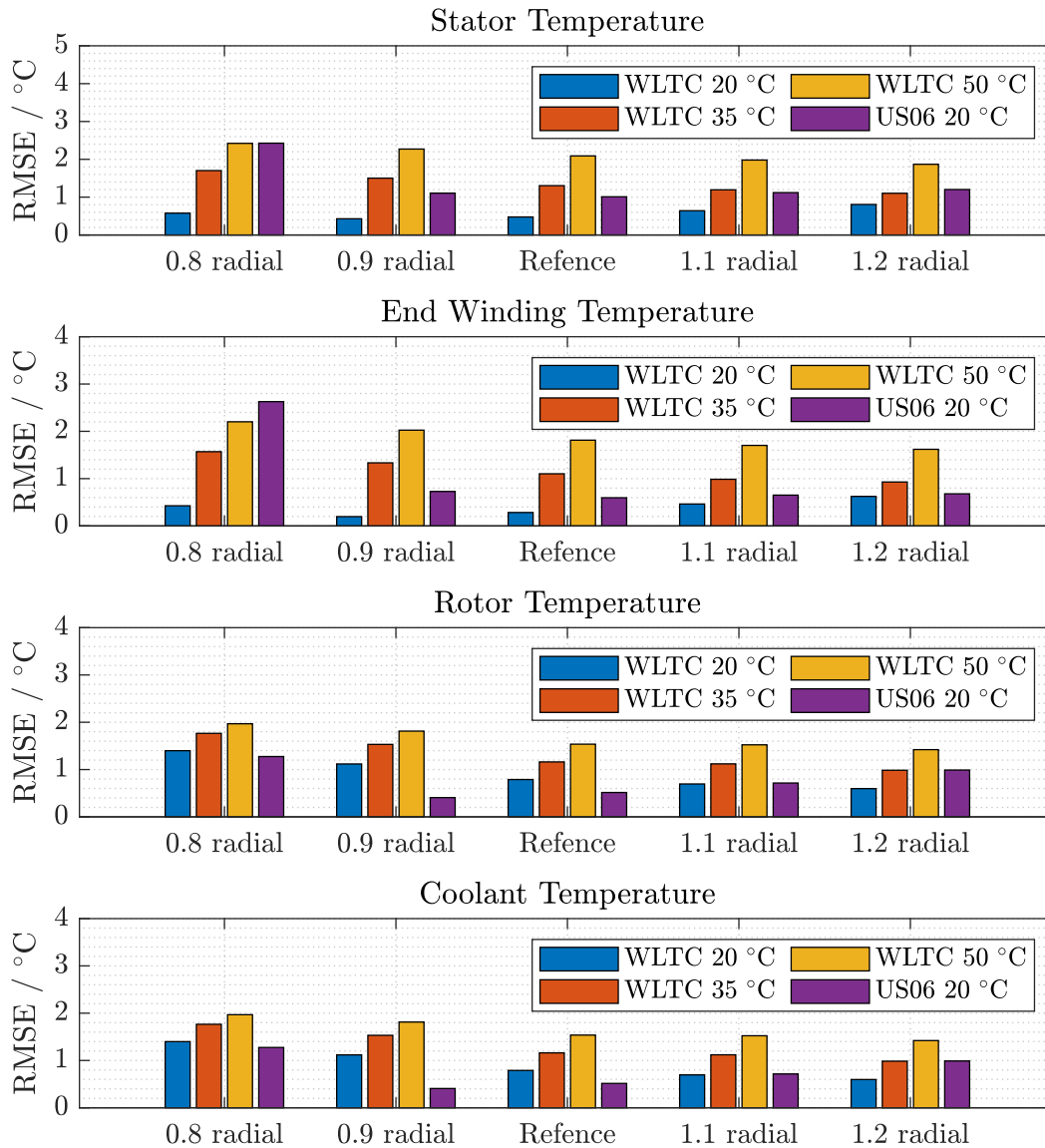


**Figure 5.15.** Temperature deviation of radial scaling in comparison to Motor-CAD

Based on the observations from Fig. 5.3, where the maximum deviation between the simulated stator temperature via Motor-CAD and the actual measured stator temperature is 5 °C, it is prudent to incorporate this offset of 5 °C when assessing differences between the actual measured temperature and the scaled temperatures of the stator,

end winding, and rotor. This approach ensures a conservative estimate of temperature deviations, allowing for a more comprehensive evaluation of thermal performance. The conservative estimates of deviations between actual measured temperature and scaled temperatures of the stator, end winding, and rotor are summarized in Table 5.3. By considering this 5 °C offset, the maximum temperature deviations for most of the components are less than 8 °C, enabling a more robust assessment of thermal behavior in the scaled PMSM.

**Table 5.3.** Estimation of temperatures of scaled PMSMs at an ambient temperature of 20 °C considering measurement offset

		Stator	End Winding	Rotor
Axial Scaling	Max. RMSE	3.8 °C	3.7 °C	4.4 °C
	Max.Deviation	6.9 °C	6.3 °C	7.9 °C
Radial Scaling	Max. RMSE	4.1 °C	5.7 °C	4.5 °C
	Max.Deviation	7.3 °C	13.2 °C	7.8 °C

## 5.6. Applicability of the Scaling Approach in PMSM Evaluation

To investigate the influence of length and diameter variations on the thermal behavior of the reference PMSM, a scaling approach is employed to modify the thermal parameters in a low-order LPTN model, which is identified solely by the measurements. The scaling approach is validated with the results from a validated Ansys Motor-CAD model by considering the temperature-dependent losses. The maximum RMSE of temperatures between the scaling approach and the Motor-CAD model is 3.21 °C. By employing the proposed scaling approach, a preliminary estimation of the PMSM’s thermal overload capacity could be achieved as part of the system-level optimization of the electric powertrain.

Of course, the presented scaling approach has its own limitations. The scaling approach offers only limited flexibility, as it requires magnetic flux density and saturation to be identical in both the reference and scaled machines. Due to its reliance on simplified assumptions and reduced model complexity, the scaling approach is better suited for estimating the average thermal behavior of components rather than precisely detecting hotspot temperatures. To perform more comprehensive thermomechanical analyses at the machine level, computationally intensive FEA or computational fluid dynamics (CFD) simulations may still be required.

The proposed scaling approach has been verified at an extremely hot ambient condition of 50 °C. However, the –20 °C extreme cold climate condition was not simulated due to the absence of a loss map at that temperature, making it impossible to calculate the corresponding loss. Furthermore, the low ambient temperature is generally beneficial to the electric motor, as it helps prevent thermal overload.

## 6. Optimization of Electric Drivetrain with Scaled PMSM Model

Upon the successful development of the lumped parameter thermal network (LPTN) model for the drivetrain and the validation of the scaling approach for the permanent magnet synchronous machine (PMSM), we integrate them into a comprehensive vehicle simulation framework. This integration enables a preliminary evaluation of the thermal limit of the PMSM within the optimization of the electric powertrain at an early stage of development. In the subsequent steps, the focus will first be on the modeling and validation of a battery electric vehicle (BEV) model. Importantly, this includes the incorporation of the standard cooling system into the model. Subsequently, the optimization problem is defined, considering the vehicle parameters and the boundary conditions for optimization. To conduct the optimization, both an urban cycle and a highway cycle are selected. After the optimization algorithm is implemented and executed, the results will be subjected to a thorough analysis, followed by an in-depth discussion of the optimization outcomes.

### 6.1. Modeling and Validation of a Battery Electric Vehicle

The simulation model can be divided into four main subsystems: Cycle, Driver, Controller and Physical. To have a better understanding of how this model works, a simplified block diagram of the BEV with its main blocks is shown in the Fig. 6.1.

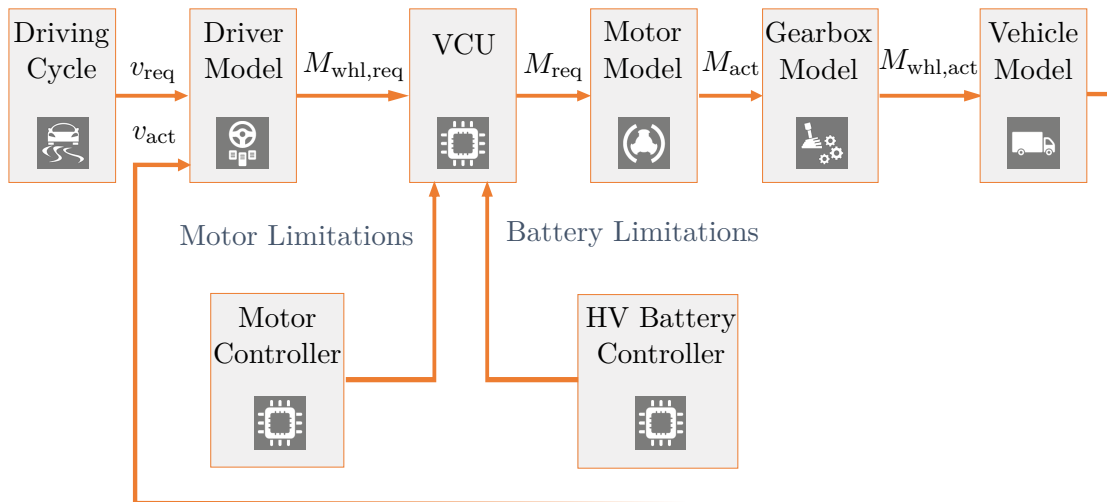


**Figure 6.1.** Schematic block diagram of the BEV simulation

The Cycle located in the Environmental Model will state the target velocity that the vehicle should reach at specific times. The driver model chooses whether to brake or

accelerate according to the desired vehicle velocity  $v_{\text{req}}$  and the actual vehicle velocity  $v_{\text{act}}$  and depending on the requirements of the cycle. The controller uses the input required torque at the wheel  $M_{\text{whl,req}}$  and calculates the required torque for the electric motor  $M_{\text{req}}$ , considering the motor torque limits. Lastly, the Physical model takes the motor model, the transmission model and the vehicle model into account. The actual torque of the electric motor  $M_{\text{act}}$  is calculated considering the losses in the motor model. Subsequently, the actual torque at the front wheels  $M_{\text{whl,act}}$  is calculated considering the gear ratio in the transmission model to determine the actual vehicle velocity taking into account the total inertia of the vehicle.

### 6.1.1. Vehicle Model Overview

In this subsection, we'll start with a general description of the components in the BEV with the exception of the motor model, thermal model and cooling system model. They are introduced in detail in the next separate subsections. It's important to emphasize that the motor, thermal model and cooling system models are particularly significant within the context of this work.

Physical part mainly contains the following components:

- Driver model
- Gearbox model
- High-voltage (HV) battery model
- DC/DC converter model
- Vehicle dynamics model

The driver model houses a predefined driving profile that acts as an input for the simulation. Additionally, it conducts various calculations related to the drive cycle, including determining the necessary vehicle acceleration to adhere to the cycle's specifications and analyzing the cycle's gradient profile. These calculations are vital for pre-control purposes within the driver model. Furthermore, the model encapsulates the physical behavior of the driver, specifically in terms of accelerator and brake torque requests at the wheels. These requests are based on the desired velocity and real-time feedback regarding the vehicle's velocity.

The gearbox model is a physical representation of the vehicle's gearbox, which includes details about gear ratios, the differential, and mechanical efficiency. By using map-based modeling, the total losses in the gearbox can be calculated based on factors like input torque, speed and oil temperature. The output torque and speed of the gearbox are determined using the fixed gear ratio.

A HV battery is an energy storage, which transforms stored chemical energy directly into electrical energy. To model the electrical behavior of a battery cell, a simple equivalent circuit model with internal ohmic resistance has been utilized. The voltage of the battery cell can be expressed based on the open circuit voltage (OCV) and internal resistance as in equation (6.1) :

$$U_{\text{Batt}} = U_{\text{OCV}} - I_{\text{Batt}} \cdot R_{\text{int}} \quad (6.1)$$

The actual battery current is calculated using OCV, internal resistance and battery power:

$$I_{Batt} = \frac{U_{OCV} - \sqrt{U_{OCV}^2 - 4 \cdot P_{Batt,elec} \cdot R_{int}}}{2 \cdot R_{int}} \quad (6.2)$$

Based on the battery capacity and the calculated battery current, the state of charge (SoC) can be determined.

The DC/DC converter model accounts for the power losses during the conversion of power from the HV battery to the 12V battery. These losses are quantified by a parameter known as efficiency.

The vehicle dynamics model represents the physical characteristics of the vehicle's chassis and tires, including how weight shifts between the front and rear axles as the vehicle moves (known as longitudinal dynamics). The forces that propel the vehicle forward consist of a combination of factors such as aerodynamic drag, rolling resistance, uphill resistance, and acceleration. In this model, the total resistance opposing the vehicle's motion is determined by (6.3) that considers coast down resistance, grade resistance, and acceleration resistance.

$$F_{res} = F_{coast} + F_{grade} + F_{acc} \quad (6.3)$$

Coast down resistance  $F_{coast}$  depends on velocity and certain coefficients, which are determined by the velocity  $v$  as well as the coast down coefficients  $F_0$ ,  $F_1$  and  $F_2$ . Grade resistance  $F_{grade}$  is influenced by the vehicle's mass  $m_{veh}$ , gravitational acceleration  $g$  and the road incline angle  $\beta$ ,

$$F_{grade} = m_{veh} \cdot g \cdot \sin(\beta) \quad (6.4)$$

while acceleration resistance  $F_{acc}$  is calculated by multiplying the acceleration of the vehicle  $a$  by the sum of the vehicle's mass  $m_{veh}$  and the equivalent mass of its rotating components  $m_{eq}$ . Considering that in this work, there is just a reduction gear in the battery electric vehicle, and only the moments of inertia of the motor and the wheels are of concern. Therefore, the acceleration resistance can be calculated as follows:

$$\begin{aligned} F_{acc} &= a \cdot (m_{veh} + m_{eq}) \\ &= a \cdot (m_{veh} + \theta_{red}/r_{dyn}^2) \\ &= a \cdot (m_{veh} + (4 \cdot \theta_{whl} + \theta_{em} \cdot i_{gear}^2)/r_{dyn}^2) \end{aligned} \quad (6.5)$$

where  $\theta_{red}$  is the reduced moment of inertia of the vehicle,  $r_{dyn}$  is the dynamic wheel radius,  $i_{gear}$  denotes the gear ratio of the reduction gear,  $\theta_{whl}$  and  $\theta_{em}$  are the moment of inertia of wheels and electric motor, respectively.

As we alter the size of the electric motor, both its mass  $m_{em}$  and inertia  $\theta_{em}$  undergo changes. We've collected motor mass and inertia data for sizes ranging from 0.8 to 1.2, with increments of 0.1. These data points, extracted from Motor-CAD, have been synthesized into a scaling factor map, displayed in Fig. 6.2. By utilizing interpolation techniques, we can readily determine the mass and moment of inertia for motors of various sizes. Combined with (6.5), the acceleration resistance  $F_{acc}$  for a scaled motor can be determined. In addition, the wheel torque, or the rotational force applied to the wheels, is usually limited by the maximum amount of torque that can be effectively transmitted to the road surface, determined by the static normal force and the friction coefficient.

Controller part mainly contains the following components:

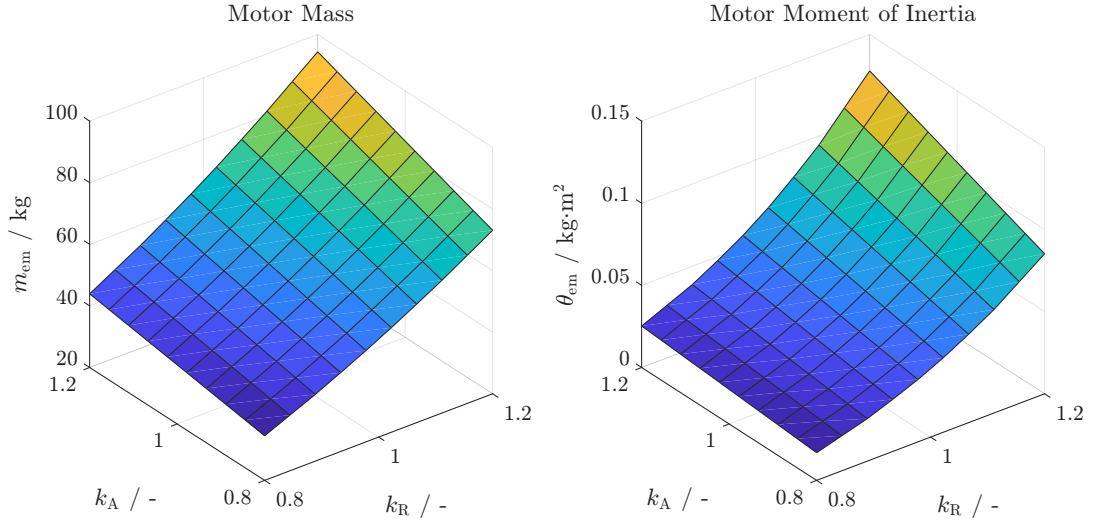


**Figure 6.2.** Motor mass and moment of inertia map for scaling from 0.8 to 1.2

- Vehicle controller
- DC/DC converter controller
- HV battery controller

The vehicle controller is responsible for several key functions. It determines the limits for wheel torque and system power within the vehicle. Additionally, it manages the distribution of torque between the front and rear wheels for all-wheel drive (all-wheel drive (AWD)) configurations. Moreover, it evaluates the negative torque required at the electrical machines, specifically at the wheel level. Meanwhile, the DC/DC converter controller plays a pivotal role in monitoring the SoC of the 12V battery. It takes actions to control and maintain this SoC by requesting power from the High-Voltage (HV) battery. Simultaneously, the HV battery controller calculates the power limits of the battery and determines a strategy for battery derating, ensuring the safe and efficient operation of the battery.

### 6.1.2. Electric Motor Model

In short, the motor model simulates the dynamic behavior of the electric motor. It generates the actual torque  $M_{act}$  as well as the total losses  $P_{total}$  and the corresponding losses in rotor  $P_{R,Fe}$ ,  $P_{R,Mag}$ ,  $P_{Fric}$  based on the actual speed  $n$ , required torque  $M_{req}$  and the temperature of the electric motor  $T_{EM}$ . The schematic of the motor model is shown in the Fig. 6.3.

With a specified speed and requested torque, the motor controller employs the maximum torque per ampere (MTPA) algorithm to calculate the necessary  $I_d$  and  $I_q$  currents. The motor's losses are determined based on the  $I_d$ ,  $I_q$ , speed, and temperature, relying on a predefined loss map embedded within the "Losses Calculation" block. This map serves as a reference guide, incorporating a comprehensive understanding of how losses vary with different operating conditions. The next step involves determining the Flux linkage within the motor, denoted as  $\Psi_d$  and  $\Psi_q$ . Flux linkage represents the magnetic

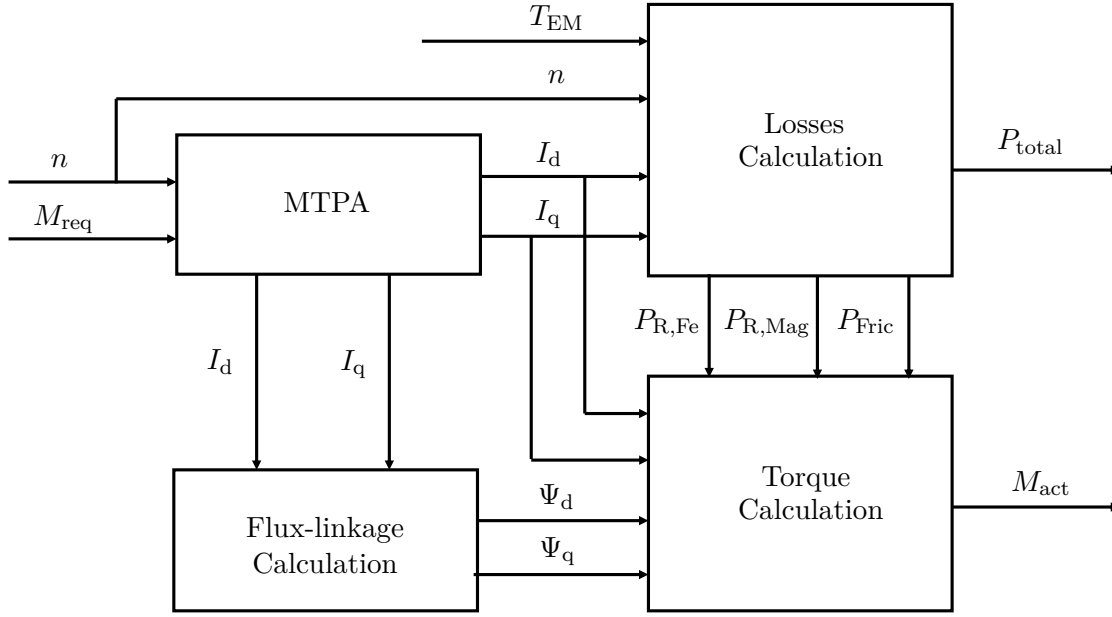


**Figure 6.3.** Schematic of the electric motor model based on dq-frame

linkage between the stator and rotor windings and is vital for understanding the electromagnetic characteristics of the motor. To calculate  $\Psi_d$  and  $\Psi_q$ , the motor controller refers to a predetermined Flux linkage map that correlates these values with the corresponding  $I_d$  and  $I_q$  parameters. By establishing the currents and Flux linkage, the electromagnetic torque is calculated. However, the calculated electromagnetic torque is not the final output torque experienced by the motor. Subtracting rotor losses and friction loss torque from the electromagnetic torque yields the actual torque.

### Saturated flux-linkage model

The saturated flux-linkage model is designed to account for the effects of saturation on the direct (d) and quadrature (q) flux-linkages, which are mathematically represented as  $\Psi_d = f(I_d, I_q)$  and  $\Psi_q = f(I_d, I_q)$ , where  $I_d$  and  $I_q$  are the d and q components of the phase current. To ensure the model's accuracy across a broad operational spectrum in the  $(I_d, I_q)$  space, finite element analysis (FEA) results from 30 different load conditions, computed using Ansys Motor-CAD, are taken into consideration. These mathematical functions are independent of frequency and are used to compute the electromagnetic torque generated by the motor based on specific  $(I_d, I_q)$  pairs. Fig. 6.4 displays the d and q flux linkage map based on the d and q components of the phase current for the reference PMSM.

In this context, the saturated flux linkage map illustrates how the flux linkages change concerning variations in the  $I_d$  and  $I_q$  currents. The  $I_d$  current represents the direct current component aligned with the rotor magnetic field, while the  $I_q$  current represents the quadrature current component perpendicular to the rotor magnetic field. The nonlinearity of the saturated flux linkage map stems from the inherent magnetic characteristics of the motor. The flux linkage  $\Psi_q$  is directly proportional to the quadrature current  $I_q$ . This relationship signifies that increasing the  $I_q$  current results in a proportional increase in the flux linkage  $\Psi_q$ . As  $I_q$  continues to increase, the flux linkage  $\Psi_q$  obviously

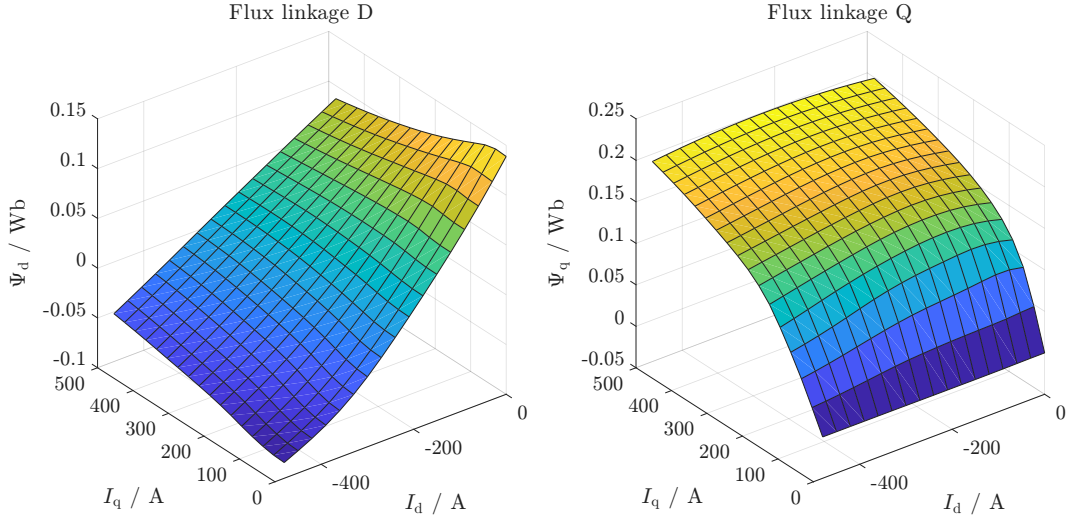


**Figure 6.4.** Flux linkage map based on d and q component of phase current at motor temperature of 30 °C

becomes saturated. This behavior is consistent with the principle that the quadrature current influences the magnetic field orientation and, consequently, the flux linkage in the quadrature axis. On the other hand, the flux linkage  $\Psi_d$  is related to both the  $I_d$  and  $I_q$  currents. This introduces a level of complexity, as changes in both direct and quadrature currents contribute to variations in the flux linkage  $\Psi_d$ . The flux linkage  $\Psi_d$  does not appear to be saturated.

### Actual Torque Calculation

In a three-phase PMSM, the electromagnetic torque  $M_{em}$  depends on the flux linkage and phase current. This relationship is expressed in the dq-frame:

$$M_{em} = \frac{3}{2} \cdot p \cdot (\Psi_d I_q - \Psi_q I_d) \quad (6.6)$$

where  $p$  denotes the number of pole pairs,  $\Psi_d$  and  $\Psi_q$  are the d and q flux linkages,  $I_d$  and  $I_q$  represent the d and q components of the phase current.

The actual shaft torque  $M_{act}$  is determined by subtracting the loss torque on the rotor from the electromagnetic torque, which captures the net mechanical torque delivered by the motor

$$\begin{aligned} M_{act} &= M_{em} - \frac{P_R}{\Omega} \\ &= M_{em} - \frac{P_{R,Fe} + P_{R,Mag} + P_{Fric}}{\Omega} \end{aligned} \quad (6.7)$$

where  $P_R$  denotes the losses on the rotor and  $\Omega$  is the mechanical rotational speed in radians.

Fig. 6.5 illustrates the comparison between the requested torque and actual torque within the Simulink model. As we delve into the figure, a striking observation emerges: the actual torque closely tracks the trajectory of the requested torque. This alignment is indicative of an effective and responsive torque control mechanism within the system.

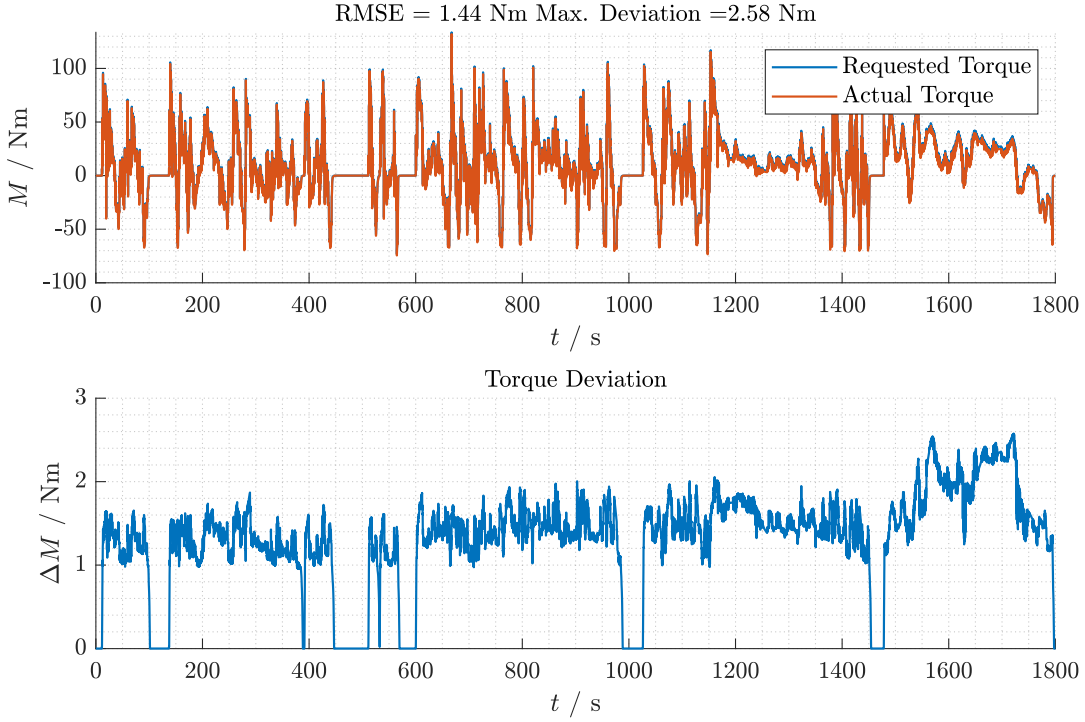


**Figure 6.5.** Comparison of requested torque and actual torque in Simulink model

However, a discerning eye may notice a slight deviation between the requested torque and the actual torque at certain points in the figure. The maximum deviation, signifying the greatest absolute difference observed between the requested and actual torque values during the monitored period, quantifies at 2.58 Nm, while the root mean square error (RMSE) error is measured at 1.44 Nm. This variance is not arbitrary; rather, it can be attributed to the presence of loss torque on the rotor. Loss torque in the rotor, stemming from various sources such as magnet losses, eddy current losses and mechanical friction, introduces a dynamic element into the system's torque response.

### Maximum Torque Calculation

The maximum torque at any given speed should be calculated, so that the required torque does not exceed the capability of the motor. Maximum torque calculation based on MTPA is a control strategy that aims to maximize the torque output of the motor while maintaining the voltage and current limits, which can be described as an optimization problem:

$$\begin{aligned}
 \max_{I_d, I_q} \quad & M_{em} = \frac{3}{2} \cdot p \cdot (\Psi_d I_q - \Psi_q I_d) \\
 \text{subject to} \quad & \sqrt{I_d^2 + I_q^2} \leq I_{max} \\
 & \omega \sqrt{\Psi_d^2 + \Psi_q^2} \leq U_{max}
 \end{aligned} \tag{6.8}$$

where  $U_{max}$  is the maximum voltage available from the inverter and  $I_{max}$  is the maximum available phase current. The terminal voltage's determination relies on the flux linkage and the electrical rotational speed based on the phasor diagram.

The maximum torque of the motor  $M_{\text{peak}}$  undergoes a validation process using the outcomes generated by Motor-CAD. This validation process is crucial to ensure the accuracy and reliability of the Simulink model in representing the behavior of the PMSM. Fig. 6.6 provides a comparison of the peak torque curve between the scaling law and Motor-CAD. By examining the Fig. 6.6, it becomes evident that the peak torque curve

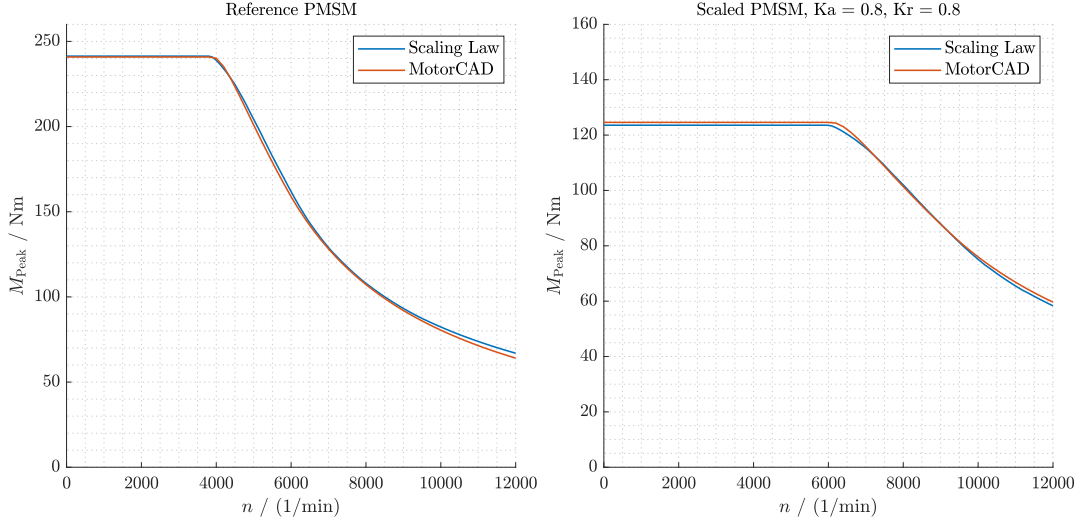


**Figure 6.6.** Peak torque comparison between scaling law and Motor-CAD

exhibits remarkable consistency, whether it pertains to the reference motor or the scaled motor.

### Current Components Calculation

To calculate the actual output torque of the motor, the current component values for the entire operational range are required. The current components  $I_d$  and  $I_q$  needed to meet the demands of the drive cycle, which are determined point by point using the MTPA control algorithm as shown in (6.9). The d and q components are crucial for achieving precise control of motor torque. Accurate modeling of these components ensures that the actual torque and losses can be accurately determined.

$$\begin{aligned}
 \min_{I_d, I_q} \quad & I_{\max} = \sqrt{I_d^2 + I_q^2} \\
 \text{subject to} \quad & M_{\text{em}} = \frac{3}{2} \cdot p \cdot (\Psi_d I_q - \Psi_q I_d) \\
 & \omega \sqrt{\Psi_d^2 + \Psi_q^2} \leq U_{\max}
 \end{aligned} \tag{6.9}$$

For each size of the motor, the maximum phase current and the maximum torque are changed, which can be determined by the scaling approach. Therefore, the d and q component phase current maps must be generated for every motor size in the Simulink model.

The current component maps in the Simulink model are validated by the outcomes from Motor-CAD for their ability to accurately predict the d and q components of phase current based on MTPA control algorithms. Fig. 6.7 shows a comparison between the

d- and q-current obtained using the scaling law and those obtained using Motor-CAD for 0.8 axial and 0.8 radial scaling. It can be found that the  $I_d$  and  $I_q$  map calculated

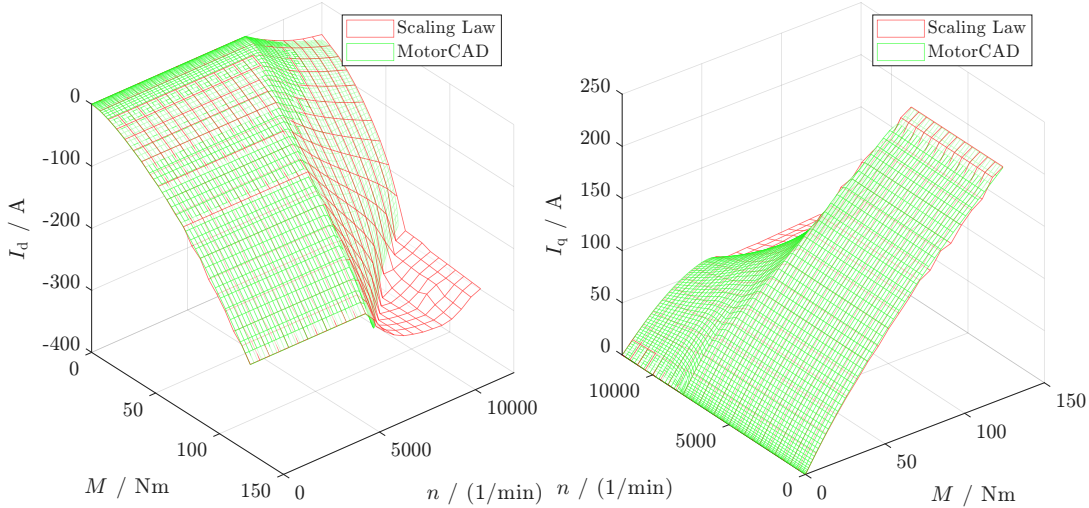


**Figure 6.7.** Phase current comparison between scaling law and Motor-CAD for 0.8 axial and 0.8 radial scaling

based on the scaling approach matches the results of Motor-CAD very well within the maximum torque range. In the area of large torque, the error will increase to a certain extent. The possible reason is that high torque corresponds to large current. When the current increases, the flux linkage easily enters the saturation region, which reduces the accuracy of the calculation.

### Saturated Losses Modeling

To calculate the energy consumption of an electrical machine (EM) in a specific driving scenario, it is essential to accurately determine the losses in the motor model. The saturated loss model, developed from a series of 30 FEA calculations conducted under various load conditions, estimates several types of losses in a motor: DC copper losses, AC copper losses, iron losses, magnet losses, and friction losses. These losses depend on the motor's current components  $I_d$  and  $I_q$ , speed and temperature. The model's primary purpose is to calculate the total losses subject to specific electrical loads and operating conditions. It should be noted that only the temperature dependent DC copper losses are considered in the modeling. Fig. 6.8 provides an example of loss maps, including copper losses, iron losses, and magnet losses, based on  $I_d$  and  $I_q$  at a speed of 3000 1/min and motor temperature of 30 °C. As can be seen from the picture, copper loss is primarily associated with resistive losses in the motor windings. It is proportional to the square of the currents flowing through the windings. Iron losses involve complex interactions influenced by magnetic field strength and frequency. Magnet losses are tied to magnetization effects. Therefore, iron losses and magnet losses introduce nonlinearities into the relationship.

The losses can be transferred into the efficiency map, which provides insights into how efficiently the motor converts electrical energy into mechanical power across its entire operating range. For the validation of the losses of the motor, a reliable loss model should

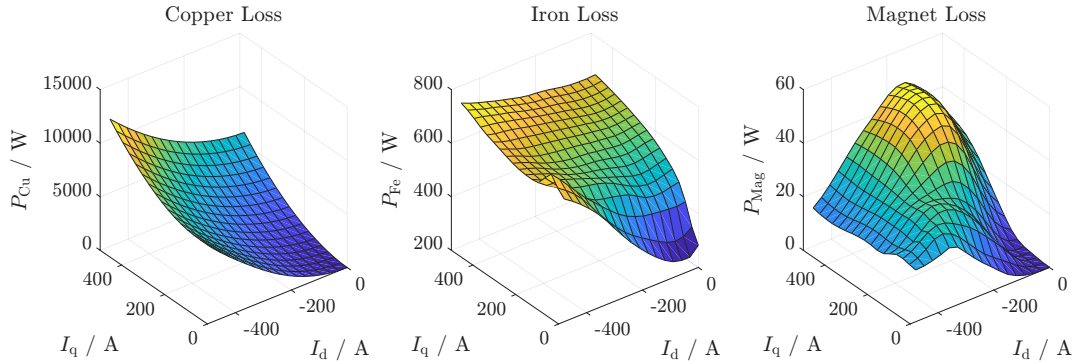


**Figure 6.8.** Copper losses, iron losses and magnet losses based on d and q component of phase current at speed of 3000 1/min and motor temperature of 30°C

closely match the efficiency characteristics observed in the motor. This validation ensures that the model can be used for later sizing optimization based on energy consumption. The efficiency map for the scaling law and Motor-CAD at motor temperature of 30°C for 0.8 axial and 0.8 radial scaling are depicted in Fig. 6.9 respectively. A high level of matching with the measured efficiency has been achieved over most areas of the map.

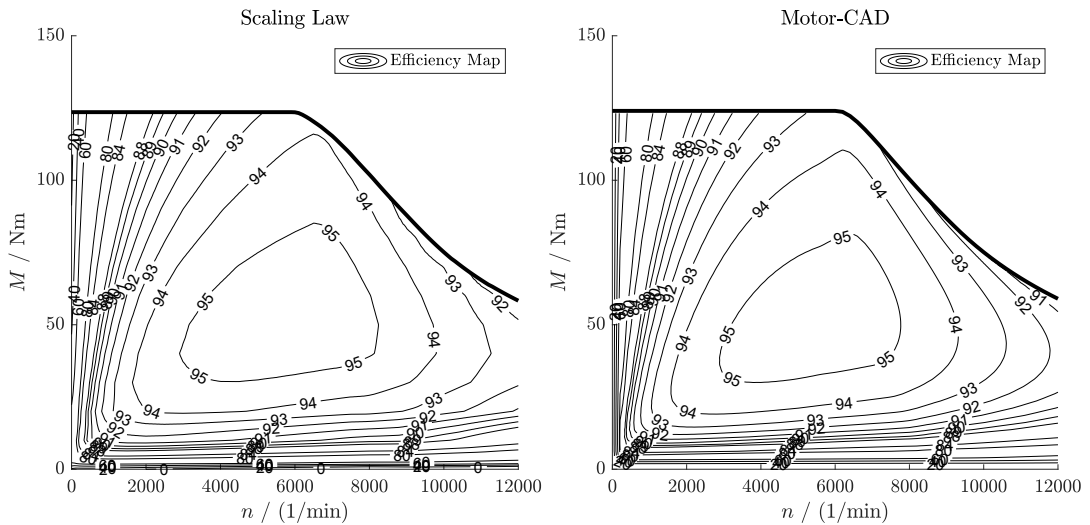


**Figure 6.9.** Efficiency map comparison between scaling law and Motor-CAD at motor temperature of 30°C for 0.8 axial and 0.8 radial scaling

The saturated flux-linkage and loss models can be adjusted in size using a geometric scaling approach. This approach allows for effective adaptation of the flux-linkage and loss model to motors of different sizes. It's essential to emphasize that FEA is used only for the initial calculations of the saturated reference motor model, while all subsequent calculations for scaled motors are based on the scaling approach.

### 6.1.3. Thermal Model

The main purpose of the component thermal model is to determine the temperature of the components of the powertrain, including the coolant outlet temperature. The schematic can be found in Fig. 6.10.

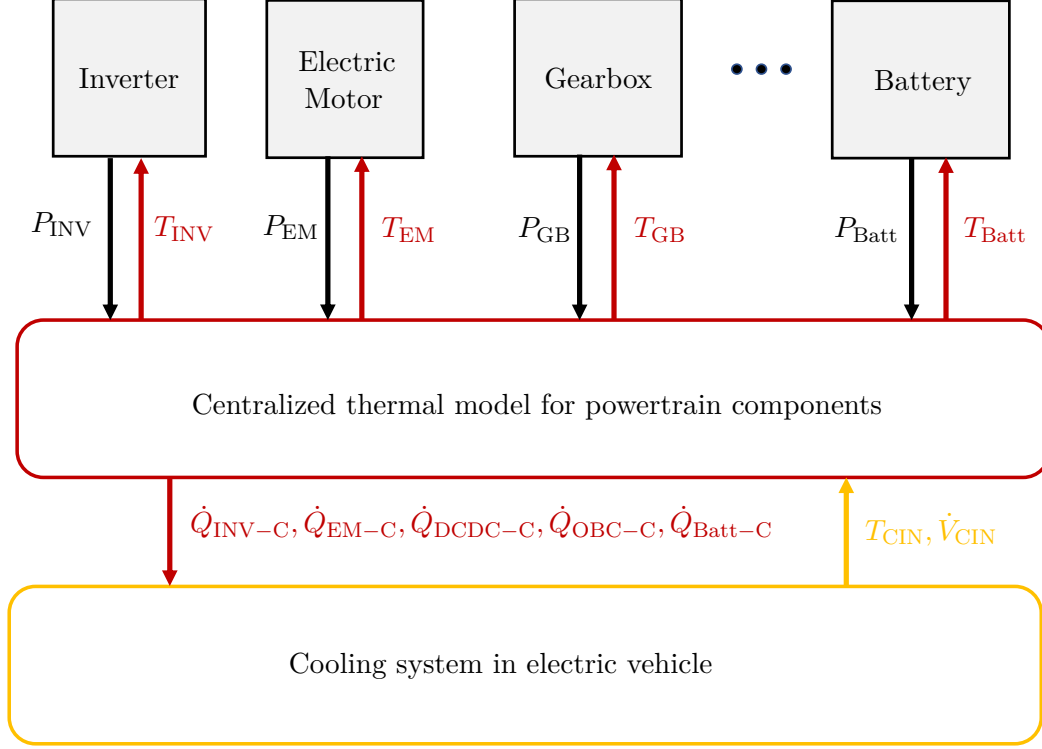


**Figure 6.10.** Centralized temperature simulation of powertrain

For powertrain thermal modeling, the centralized temperature simulation instead of the distributed one is conducted. This centralized approach allows for the consideration of temperature interactions, which enables a more comprehensive understanding of the interplay between components in the system. To simulate temperature, the losses of individual components ( $P_{INV}$ ,  $P_{EM}$ ,  $P_{GB}$ ,  $P_{Batt}$ , etc.) are derived from their respective physics modules. Subsequently, the simulated temperatures ( $T_{INV}$ ,  $T_{EM}$ ,  $T_{GB}$ ,  $T_{Batt}$ , etc.) are fed back into the physics modules to calculate temperature-related losses. The LPTN method in chapter 4 is used to build the thermal model. The ordinary differential equation (ODE) of each temperature node can be formed by the integrator block to represent the integration of temperature over time.

The ambient temperature and the initial coolant temperature for the powertrain are pre-defined as boundary conditions, whereas the coolant temperature during simulations is obtained from the cooling system model, which will be explained in detail in the following section.

To simulate coolant temperature, it's essential to consider the heat transfer from the components to the coolant. In particular, the heat flow from the motor into the coolant  $\dot{Q}_{EM-C}$  can be quantified as follows.

$$\dot{Q}_{EM-C} = \dot{m}_{cout,em} \cdot c_{s,coolant} \cdot T_{COE} - \dot{m}_{cin,em} \cdot c_{s,coolant} \cdot T_{COI} \quad (6.10)$$

where  $c_{s,coolant}$  denotes the coolant specific heat capacity,  $T_{COI}$ ,  $T_{COE}$  and  $\dot{m}_{cin/cout,em}$  are the coolant inlet/outlet temperatures and mass flow rate through the motor, respectively.

The coolant specific heat capacity is related to its temperature. Here, the temperature-relevant heat capacity function is presented as a look-up table in the Simulink model. The average temperature of the coolant inlet and outlet is used to define the heat capacity. Assuming that the mass flow rate of coolant  $\dot{m}$  entering and exiting the motor is equal, the following equation holds:

$$\dot{Q}_{EM-C} = \dot{m} \cdot c_{s,coolant} \cdot (T_{COE} - T_{COI}) \quad (6.11)$$

Applying the same methodology, the heat flow from the inverter into the coolant can be obtained:

$$\dot{Q}_{INV-C} = \dot{m} \cdot c_{s,coolant} \cdot (T_{COI} - T_{CIN}) \quad (6.12)$$

where  $\dot{m}$  denotes the average mass flow rate of coolant and  $T_{COI}$  and  $T_{CIN}$  are the coolant outlet/inlet temperatures through the inverter.

Similarly, the heat dissipation into the coolant from the battery  $\dot{Q}_{Batt-C}$ , DCDC converter  $\dot{Q}_{DCDC-C}$ , and on board charger (OBC)  $\dot{Q}_{OBC-C}$  can be obtained from their respective thermal models.

The thermal model for the entire powertrain addressing the thermal coupling of components and the associated scaling approach outlined in chapter 5 are seamlessly integrated into the vehicle model platform for further optimization tasks. This integration allows us to take temperature limits into account during the optimization process.

#### 6.1.4. Cooling System Model

To keep the powertrain component temperatures within a reasonable range, as well as taking the cabin air conditioning into account, a cooling system is integrated into the vehicle model. Additionally, the power consumption of the overall vehicle cooling system is considered.

The cooling system implemented in this particular vehicle model plays a fundamental role in maintaining optimal temperature conditions for both the powertrain components and the cabin. This cooling circuit, illustrated in Fig. 6.11, comprises two primary loops: the coolant circuit and the refrigerant circuit, interconnected through a 4-way valve and two bypass valves. It represents the thermal management in the powertrain and cabin.

The refrigerant circuit is shown in blue in the schematic, representing the air conditioning function of the model. It is composed of a compressor, a condenser, a chiller, an evaporator and two expansion valves, controlling the heat flow through the chiller and evaporator, respectively. As it can be seen, the chiller is interconnected with the battery circuit and the evaporator with the cabin circuit, allowing the coolant in the battery circuit and the cabin air to be cooled using additional cooling power.

The coolant circuit in the schematic is colored by red and yellow, divided by the “Parallel-Serial Mode Valve” into two sub-circuits, namely the motor circuit and the battery circuit. This valve has two active modes, the parallel and serial modes. In the serial mode, both sub-circuits are connected, and the coolant flows first through the battery circuit and then to the motor circuit. On the other hand, the two circuits work separately, making the battery cooled solely by the chiller. The valve is by default in serial mode, it switches to parallel mode if either one of the environmental or the

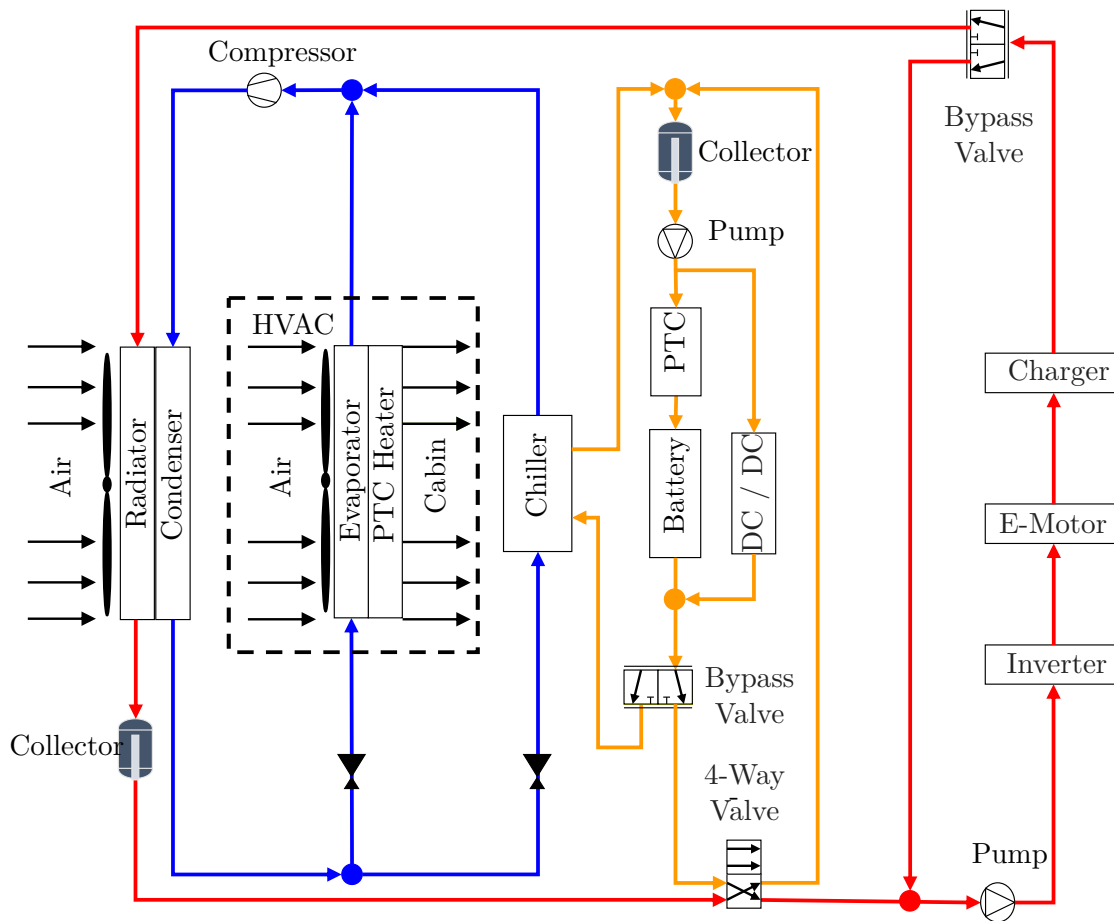


**Figure 6.11.** Layout of the cooling circuit including the coolant circuit and the refrigerant circuit

coolant temperature is beyond  $35^{\circ}\text{C}$ ., and it will be switched back to serial mode if both temperatures are lower than  $30^{\circ}\text{C}$ .

In the motor circuit, the coolant is pressurized by the pump and flows past the inverter, motor and charger, successively. Followed by a radiator bypass valve, the coolant flow can be controlled to pass through the radiator and be cooled by the fan when required. The radiator engages when the coolant temperature is higher than  $25^{\circ}\text{C}$  and disengages when the coolant temperature is already lower than  $20^{\circ}\text{C}$ . In the battery circuit, there is also a pump cooling the DCDC converter and the battery pack. In contrast to the motor circuit, there is a positive temperature coefficient (PTC) heater and a chiller in the battery circuit. The PTC is actuated if the environmental and the coolant temperature fall under  $5^{\circ}\text{C}$  and the chiller, controlled by the chiller bypass valve, cools down the coolant if the coolant temperature exceeds a temperature of  $35^{\circ}\text{C}$ . This function prevents extreme cold from negatively affecting the battery's performance. The dotted box indicates the heating, ventilation and air conditioning (HVAC) for the cabin. A desired temperature is maintained by the air conditioner and PTC heater and the moist-air flow rate is controlled by a blower.

To accurately simulate the cooling system model, the cooling system should be interconnected with the entire vehicle simulation model. The structure of the cooling system

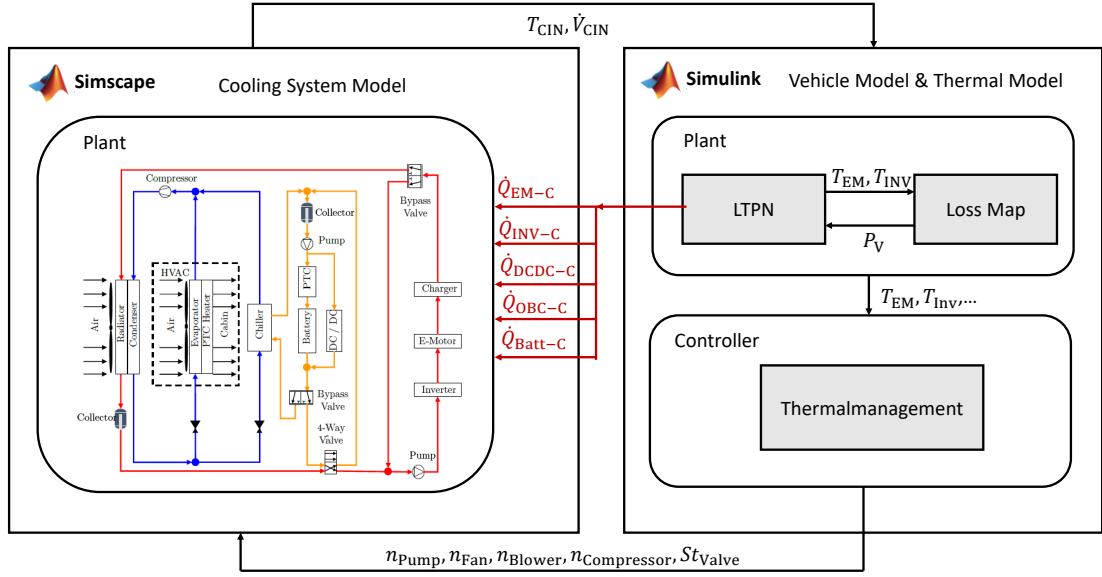


**Figure 6.12.** Block diagram of the thermal simulation including cooling system

considered in this work is shown in Fig. 6.12, which is separated into the Simulink and Simscape sub-models.

In the Simulink submodel, it calculates the power losses  $P_V$  of the electrical components based on the loss maps. The Simulink submodel also contains the LPTN models of all electrical components, which determine the distribution of temperatures and the heat flows that flow from components into the coolant for each electrical component as mentioned in the thermal model. Since the power losses also depend on component temperatures, an interaction is formed between power losses and component temperatures. This means that the power losses can influence the component temperature and the variation of the component temperature in turn leads to a change in the power losses. The heat dissipation into the coolant is realized by the “Coolant Jacket” block in the Simscape model, which simulates the heat transfer process between the components and the coolant, so that the coolant temperatures in the cooling circuit are simulated. Based on the operating states and ambient conditions, the coolant temperatures  $T_{CIN}$  and volume flow rate  $\dot{V}_{CIN}$  are calculated by the Simscape model and sent back as inputs for the Simulink model. The actuators in the cooling system such as pump  $n_{Pump}$ , fan  $n_{Fan}$ , blower  $n_{Blower}$ , compressor  $n_{Compressor}$  and valve  $St_{Valve}$  are controlled by a thermal management controller built in the Simulink model in order to generate a desired cooling performance while taking into account the electrical consumption of the entire system.

A validation is performed to check if the result from the LPTN thermal model matches the simulation result from the Simscape model in the cooling system. As shown in Fig. 6.13, only a minor deviation for inverter and motor coolant outlet temperatures can be observed during the simulation between the LPTN and Simscape models.

Within the cooling system model, the components demanding energy include the motor/battery pump, compressor, fan and cabin blower. These elements are regarded as ideal, and their power can be determined using the following equations.

The power of an ideal pump  $P_{Pump}$  is calculated with its volumetric flow rate  $\dot{V}_p$  and

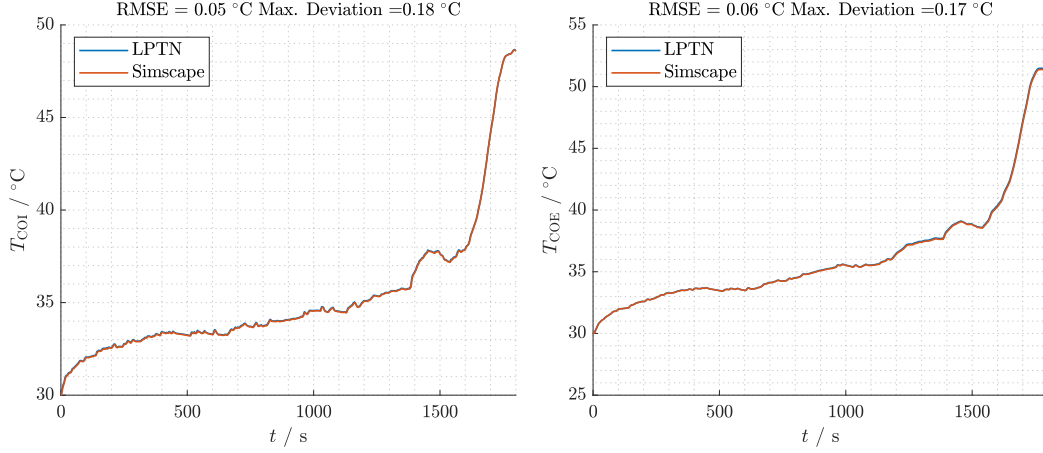


**Figure 6.13.** Comparison of coolant outlet temperature of inverter and electric motor

the pressure drop  $\Delta p$  between the inlet and outlet by considering of 100% volumetric efficiency, as shown in (6.13).

$$\begin{aligned} P_{\text{Pump}} &= \dot{V}_p \cdot \Delta p \\ &= n_{\text{Pump}} \cdot V_p \cdot \Delta p \end{aligned} \quad (6.13)$$

where the flow rate  $\dot{V}_p$  is the product of the rotational speed  $n_{\text{Pump}}$  and the displacement  $V_p$  of the pump.

The compressor work is calculated by multiplying the mass flow rate  $\dot{m}$  and the specific total enthalpy difference  $\Delta h$  between the inlet and outlet of the compressor by neglecting mechanical losses within the compressor.

$$P_{\text{Compressor}} = \dot{m} \cdot \Delta h \quad (6.14)$$

The power consumption of the blower can be calculated using the same equation as in (6.14). Whereas the fan has its own characteristic power map, which is a function of volume flow rate of the air into the radiator. By connecting a volumetric flow rate sensor to the fan in the Simscape model, its power can be identified from the map.

The graphical representation in Fig. 6.14 provides a comprehensive insight into the various power components of the cooling system. This illustration serves as an invaluable tool to assess the system's performance, as it offers a detailed overview of the power levels associated with different components. Examining the power levels depicted in the figure, it is evident that all values fall within the acceptable range. One notable observation in the graphical representation is the sudden and significant change in battery pump power around the 1400s. This abrupt fluctuation can be attributed to the rapid rebalancing of pressure within the system. This phenomenon occurs when the 4-way valve undergoes a swift transition from serial mode to parallel mode. The 4-way valve plays a crucial role in regulating the flow of coolant within the system. The transition from serial to parallel mode involves a strategic redirection of the coolant flow, impacting the pressure dynamics within the system.

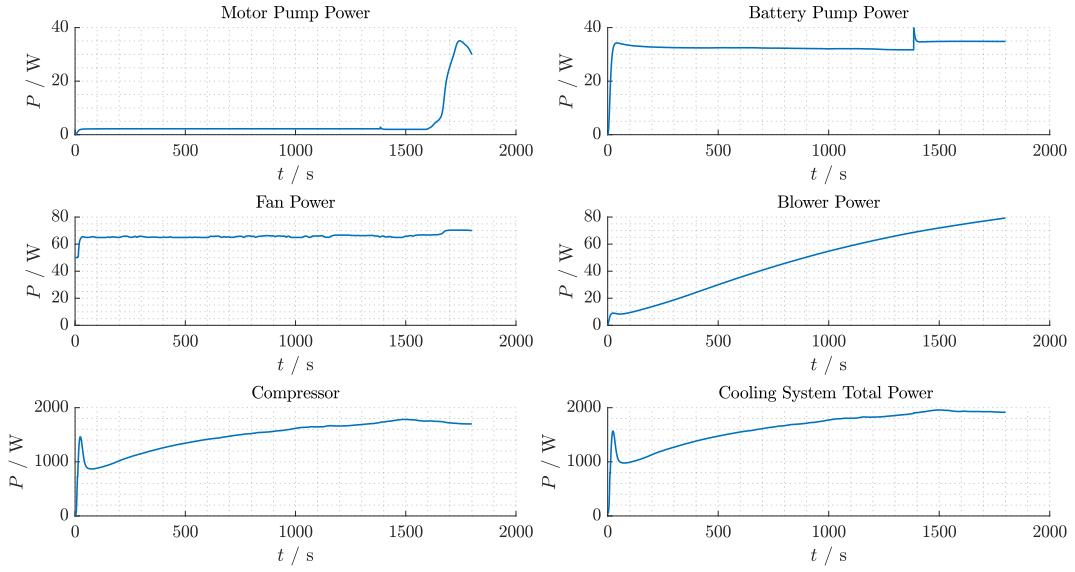


**Figure 6.14.** Power of cooling system components

## 6.2. Optimization Problem Formulation

The vehicle model presented in Section 6.1 serves as the foundation for an extensive exploration into the optimal sizing of the motor, undertaken through a global optimization approach. This optimization unfolds at the comprehensive level of the entire vehicle system, reflecting a holistic approach to enhance overall performance. Importantly, this systematic investigation aims to identify the most suitable motor size across various scenarios, with a keen consideration of the thermal limits imposed on powertrain components. This inclusion is essential to ensure the selected motor size meets performance criteria and temperature limits. The optimization problem at the vehicle system level is characterized by a set of defined objectives and constraints, encapsulated in Table 6.1.

**Table 6.1.** Objectives and constraints of the optimization problem

Objectives	Minimum of energy consumption
	Minimum of acceleration time for 0 – 100 km/h
Optimization variables	Motor scaling factor in the axial direction $k_A$
	Motor scaling factor in the radial direction $k_R$
Constraints	follow the cycle profile $ v_{\text{act}} - v_{\text{req}}  < 2$ km/h
	Maximum end winding temperature $T_{\text{EW}} < 120$ °C
	Maximum magnet temperature $T_{\text{R}} < 100$ °C
	Axial scaling range $0.8 \leq k_A \leq 1.2$
	Radial scaling range $0.8 \leq k_R \leq 1.2$

These objectives delineate the desired outcomes that the optimization seeks to minimize, while the constraints outline the limitations or conditions that must be satisfied throughout the optimization process. In the optimization problem, we take into account two pivotal cost functions. First, we evaluate the total energy consumption, a critical factor in the context of energy-efficient powertrain systems. The second cost function focuses on the acceleration time from 0 to 100 km/h. This metric directly impacts vehicle performance, as it relates to the peak wheel torque and peak wheel power that the powertrain can provide. By optimizing acceleration time, the vehicle's responsiveness and overall driving experience can be improved. The design variables  $k_A$  and  $k_R$  are chosen in order to scale the motor in the axial and radial directions, respectively. In parallel, the optimization process incorporates five essential design constraints to guarantee the feasibility of design solutions and compliance with performance requirements. These constraints serve to maintain the system within operational boundaries and ensure that it meets specific criteria. Firstly, the vehicle must closely follow the prescribed cycle, with a deviation between the requested velocity and the actual velocity staying below 2 km/h. Next, motor temperature limits are strictly adhered to, preventing the risk of damage by avoiding temperature exceedances. Additionally, both scaling factors are confined within a range of 0.8 to 1.2, ensuring that they do not fall outside these specified limits.

The realistic technical data for the vehicle and components are used in the optimization. The vehicle specifications outlined in the Table 6.2. provide a comprehensive overview of key parameters influencing its performance and operational characteristics. The vehicle, with a weight of 1580 kg, features a -PMSM. The coast-down factors, including  $F_0$  at 110.8 N,  $F_1$  at 0.6537 N/(km/h), and  $F_2$  at 0.0311 N/(km/h)<sup>2</sup>, shed light on the vehicle's driving resistance characteristics. In terms of the motor specifications, the reference configuration includes a motor with a mass of 59.08 kg, inertia of 0.0552 kg · m<sup>2</sup>, peak power output of 97 kW, and peak torque of 220 Nm. The motor mass and inertia, however, vary during the optimization process, according to Fig. 6.2. The vehicle's transmission system is characterized by a gear ratio of 8.17, indicating the relationship between the motor's rotational speed and that of the wheels. The HV-battery powering the vehicle is of NMC chemistry, with a substantial energy capacity of 42 kWh. The individual cell capacity is specified as 53 Ah, and the battery configuration includes 108 cells in series and 2 cells in parallel. The operational parameters include a maximum speed of 12 000 1/min for the motor, a DC voltage of 350 V, and an ambient temperature of 30 °C. These parameters contribute to defining the vehicle's speed capabilities, electrical requirements, and the environmental boundary conditions under the optimization process.

Two different driving cycles were investigated in the optimization, namely the Artemis urban cycle, and the Artemis highway cycle. The velocity profiles can be seen in Fig. 6.15. The Artemis urban cycle is designed to replicate the dynamics of urban road segments where vehicles typically operate at speeds below 60 km/h. This simulation captures the stop-and-go traffic patterns, frequent intersections, and lower speed limits commonly encountered in city environments. On the other hand, the Artemis highway cycle is tailored for emulating highway conditions, where vehicles tend to maintain higher speeds, generally around 130 km/h. It reflects the smooth and continuous flow of traffic found on highways. The Artemis urban cycle and the Artemis highway cycle are two real-world driving cycles, which are derived from measurements taken during real test drives, which provide a better understanding of real driving conditions and real performance.

**Table 6.2.** Technical parameters of the reference vehicle for the simulation

Parameter	Value / Description
Vehicle weight	1580 kg
Dynamic wheel radius	0.2731 m
Coast down factor $F_0$	110.8 N
Coast down factor $F_1$	0.6537 N/(km/h)
Coast down factor $F_2$	0.0311 N/(km/h) <sup>2</sup>
Motor Type	PMSM
Mass (Reference)	59.08 kg
Inertia (Reference)	0.0552 kg · m <sup>2</sup>
Peak power (Reference)	97 kW
Peak torque (Reference)	220 Nm
Max. speed	12 000 1/min
DC Voltage	350 V
Gear ratio	8.17
HV battery type	Nickel-Mangan-Cobalt (NMC)
Battery energy	42 kWh
Cell capacity	53 Ah
Number of cell in series	108
Number of cell in parallel	2
Ambient temperature	30 °C

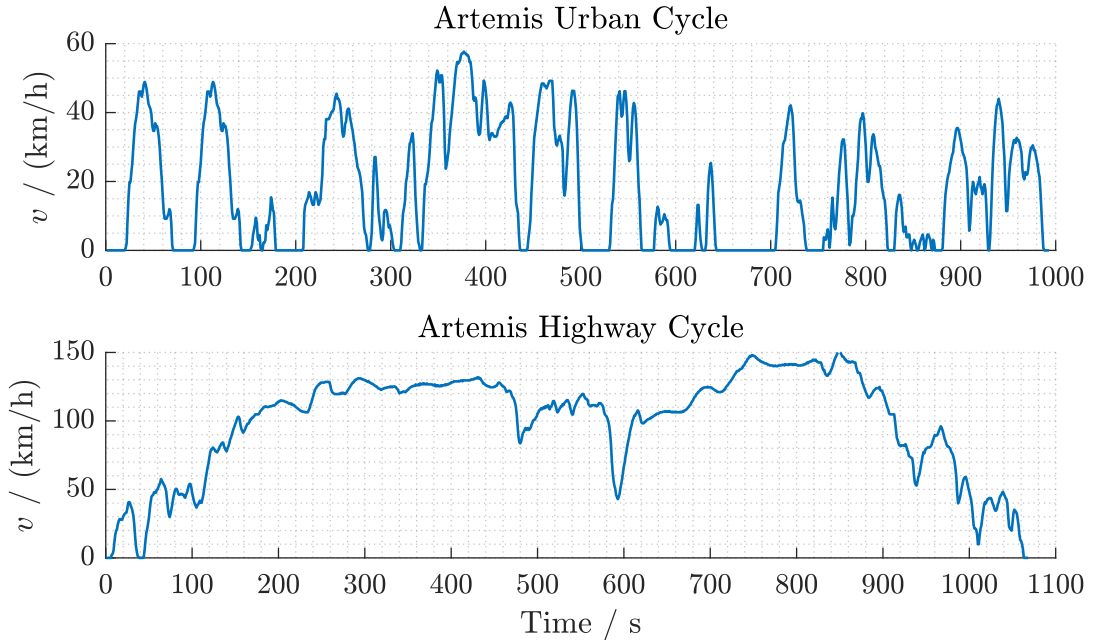


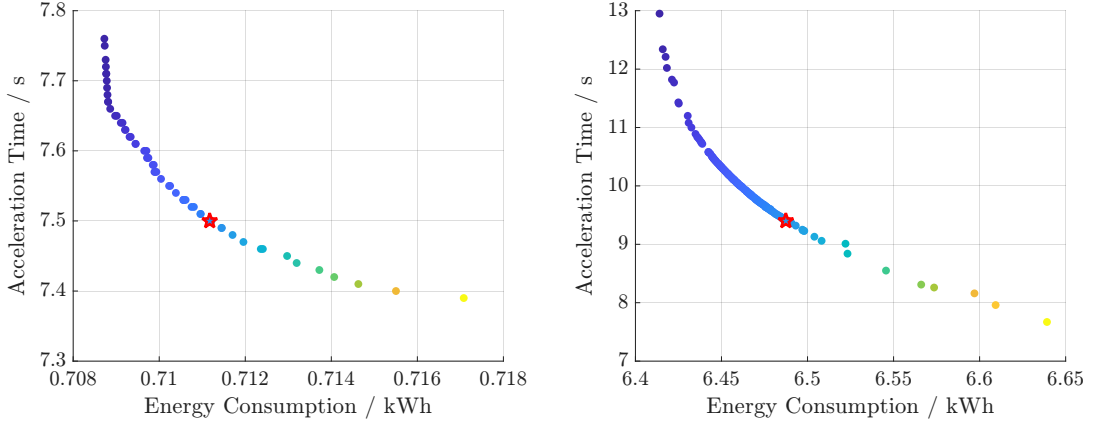
**Figure 6.15.** Driving cycles for optimization

The mixed integer distributed ant colony optimization (MIDACO) software, used in this work, treats the optimization problem as "black-box" functions. This implies that only the resulting objective and constraint values are accessible to MIDACO for a given input vector. MIDACO does not require specific knowledge about how these functions are calculated. The parameters "Ant" and "Kernel" in MIDACO are set at 30 and 5, which are chosen based on recommendations for CPU-time expensive problems from [89, 90]. While other combinations of ant and kernel parameters have been tested, it's worth noting that the optimal values for these parameters can vary significantly depending on the specific problem. Nevertheless, this work does not delve into the detailed tuning of these parameters, as it is outside the scope of this work. While there are alternative stopping criteria, one of which involves an adaptive approach that ends the optimization when no more improvements are detected, this work exclusively utilizes the criterion of a maximum runtime of 120 hours. Furthermore, the MATLAB Parallel Computing Toolbox enables the utilization of multi-core desktops, leading to a remarkable acceleration of the evaluation process. The calculations for this work are conducted using the high performance computing (HPC) infrastructure at RWTH Aachen University.

### 6.3. Analysis of the Optimization Results

The Pareto front results for the optimization process of the Artemis urban cycle and the Artemis highway cycle are illustrated in Fig. 6.16a and Fig. 6.16b with more than 50 Pareto front solutions, respectively. These results reveal a wide spectrum of design solutions, all of which offer notable improvements in terms of energy consumption and acceleration time over the reference design. The Pareto front shows a trade-off between these two key performance metrics. Each Pareto solution is represented by a different color. The bluer the point, the lower the energy consumption but the poorer the acceleration performance. Conversely, the yellower the point, the better the acceleration performance but the higher the energy consumption. This methodology provides the flexibility to choose the most suitable solution. The red pentagram symbol marks our chosen solution, which achieves the most balanced outcome between the two objectives.

To extract valuable engineering insights from these designs, the supplementary plots are depicted in Fig. 6.17. The first row is the design variable plots. From left to right are the average efficiency of the vehicle  $\eta_{avg}$ , motor peak torque  $M_{peak}$ , motor peak power  $P_{peak}$  and motor base speed  $n_{base}$ , respectively. These plots display the design variables for the Pareto front solutions within the upper and lower limits of their respective search space. The constraints plots, which from left to right show the axial scaling factor  $k_A$ , radial scaling factor  $k_R$ , maximum temperature of end winding  $T_{EW}$  and maximum temperature of rotor  $T_R$ , are in the second row and showcase the constrained performance outputs for the Pareto front solutions. In both of these plots, the design solutions with lower energy consumption are positioned towards the left side, while those with lower acceleration time are found on the right. It is worth noting, as demonstrated in the constraint plot, that all Pareto front solutions successfully satisfy the imposed constraints. In the context of Fig. 6.17, the motor's diameter predominantly increases up to the maximum scaling factor of 1.2. This extension is not only aimed at enhancing the efficiency of the base speed range but also improving acceleration performance. Meanwhile, the motor's length undergoes significant variations, ranging from 0.8 to 1.05. As the



(a) Pareto front for the Artemis urban cycle (b) Pareto front for the Artemis highway cycle

**Figure 6.16.** Pareto front of the multi-objective optimization problem for the various scenarios

motor's diameter grows, its maximum torque increases proportionally. However, the elongation of the motor contributes to an elevated voltage drop, subsequently leading to a decrease in the motor's base speed for a given direct current (DC) terminal voltage. Consequently, the peak power remains relatively constant at 130.9 kW. This analysis indicates a reduction in the required acceleration time from 0 to 100 km/h. The increasing of the motor length beyond optimal levels results in overdesign, causing a subsequent decrease in the average efficiency. Owing to the operating point characteristics of the urban cycle, the motor operates within moderate speed and torque ranges, preventing a rapid temperature rise in the motor. The maximum temperatures recorded for the end winding and rotor stand at 39.3 °C and 36.1 °C, respectively, both well below their respective maximum temperature limits of 120 °C and 100 °C.

To derive valuable engineering insights for the optimization of the highway cycle, additional plots are presented in Fig. 6.18. Differing from the results obtained in the Artemis urban cycle, the motor's length experiences a substantial reduction to 0.8, whereas the motor's diameter undergoes an increment from 0.85 to 1.2. Despite the fact that a motor diameter scaling factor less than 0.85 can contribute to further reductions in energy consumption, it concurrently leads to the end winding temperature exceeding its maximum limit of 120 °C. Analyzing Fig. 6.18, a noticeable trend emerges a rise in motor diameter is associated with a decrease in acceleration time. This trend can be explained by the increase in the peak torque and peak power of the motor. Following the same principle, an increase in the motor diameter results in a corresponding rise in the required voltage for the motor to maintain a constant speed. In instances where the DC voltage remains unchanged, the base speed of the motor concurrently decreases. In addition, an increased motor diameter results in a larger outer surface and improved cooling performance, thus, explaining the lower end winding and magnet temperatures. However, as the motor becomes overdesigned, the average efficiency of the motor is reduced.

Acceleration time can be effectively presented through a hyperbolic plot of motor torque and motor power, as illustrated in Fig. 6.19. As motor torque and power are fundamental parameters influencing acceleration, their combined representation in a hyperbolic plot allows for a clear understanding of how changes in torque and power affect

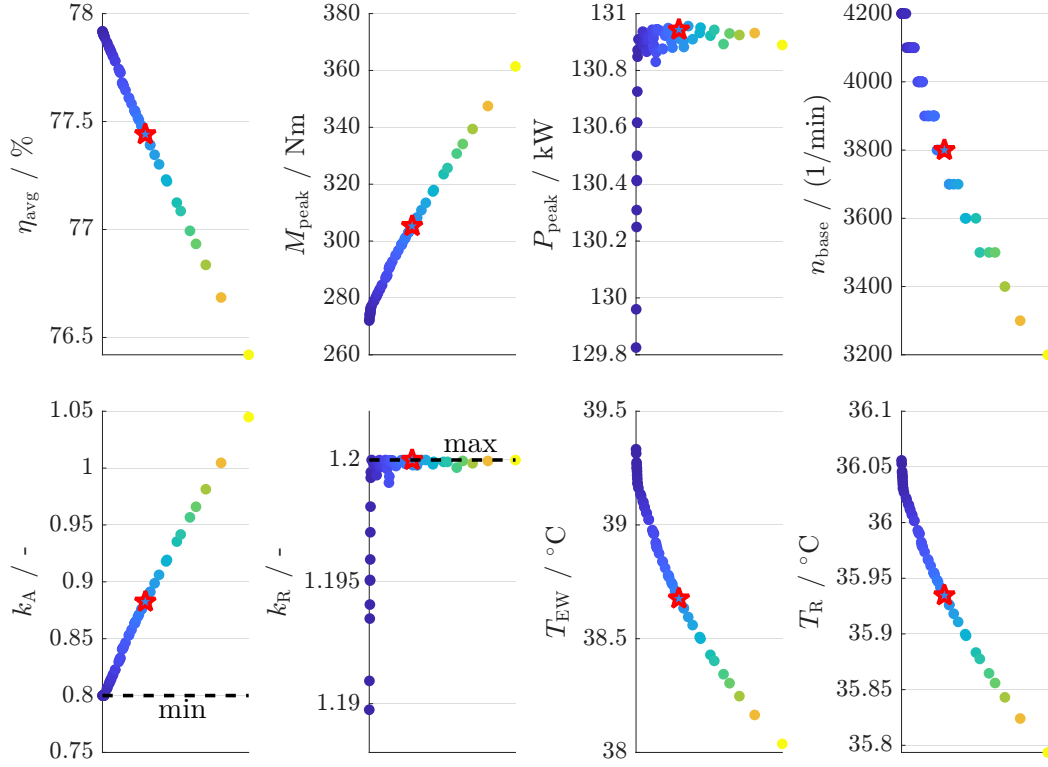


**Figure 6.17.** Supplementary plots of design variables and constraints for the Artemis urban cycle

acceleration time. In analyzing the figure, it becomes evident that there exists a direct correlation between motor torque/power and acceleration time. Increasing motor torque and power results in shorter acceleration times, while decreasing these parameters leads to longer acceleration times. Consider two driving scenarios: the Urban Cycle and the Highway Cycle. For the Urban Cycle, where frequent acceleration and deceleration are typical, a higher torque and power output are necessary to achieve satisfactory performance. With a torque of 306 Nm and power output of 130.9 kW, the acceleration time from 0 to 100 km/h is around 7.4 s. Conversely, for the Highway Cycle, characterized by sustained speeds and less frequent acceleration events, lower torque and power requirements suffice. In this scenario, the motor delivers a torque of 210 Nm and a power output of 115 kW. The acceleration time from 0 to 100 km/h is approximately 9.4 s.

The size optimization results of the PMSM for the "Urban Cycle" and "Highway Cycle" scenarios are shown in Table 6.3 and Table 6.4, respectively. The tables display the comparison between the reference and optimized motor energy consumption and acceleration time. As the results show, a shorter motor is preferred for both scenarios, because it reduces the total losses and improves the efficiency. For the "Urban Cycle" scenario, the energy consumption and the acceleration time of the optimum have improved by 0.53 % and 2.51 % compared to the reference case, respectively. Since the operating points of the urban cycle are within the base speed region of the PMSM, an increasing diameter improves the motor efficiency as well as the acceleration capability. Thus, a larger diameter motor is desired. Conversely, for the "Highway Cycle" scenario,

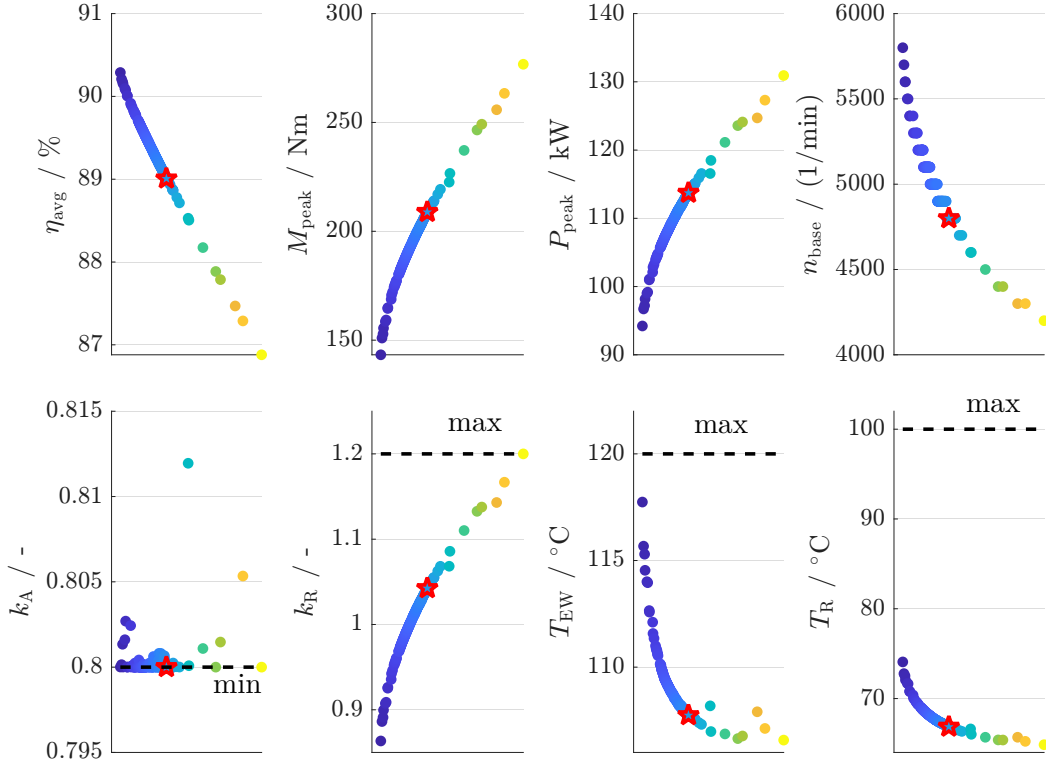


**Figure 6.18.** Supplementary plots of design variables and constraints for the Artemis highway cycle

the energy consumption increased by 2.84 %, whereas the acceleration time deteriorated by 1.29 %. This is because the operating points with a relatively large proportion of power are mainly in the high-speed region. Increasing the motor diameter improves acceleration performance but leads to an increase in losses (mainly AC copper losses and iron losses), while reducing the diameter reduces losses but decreases acceleration performance. Therefore, the optimal motor diameter is 1.04, which is close to the diameter of the reference motor.

**Table 6.3.** Optimization results of the PMSM for the "Urban Cycle" scenarios

Urban Cycle			
	Reference	Optimized	Improvement
Scaling factor	$k_A = 1$ $k_R = 1$	$k_A = 0.86$ $k_R = 1.20$	-
Energy consumption	0.7151 kWh	0.6997 kWh	0.53 %
0 – 100 km/h Acceleration time	9.28 s	7.41 s	2.51 %

The power share plot maps of both the reference and optimized motors for the urban

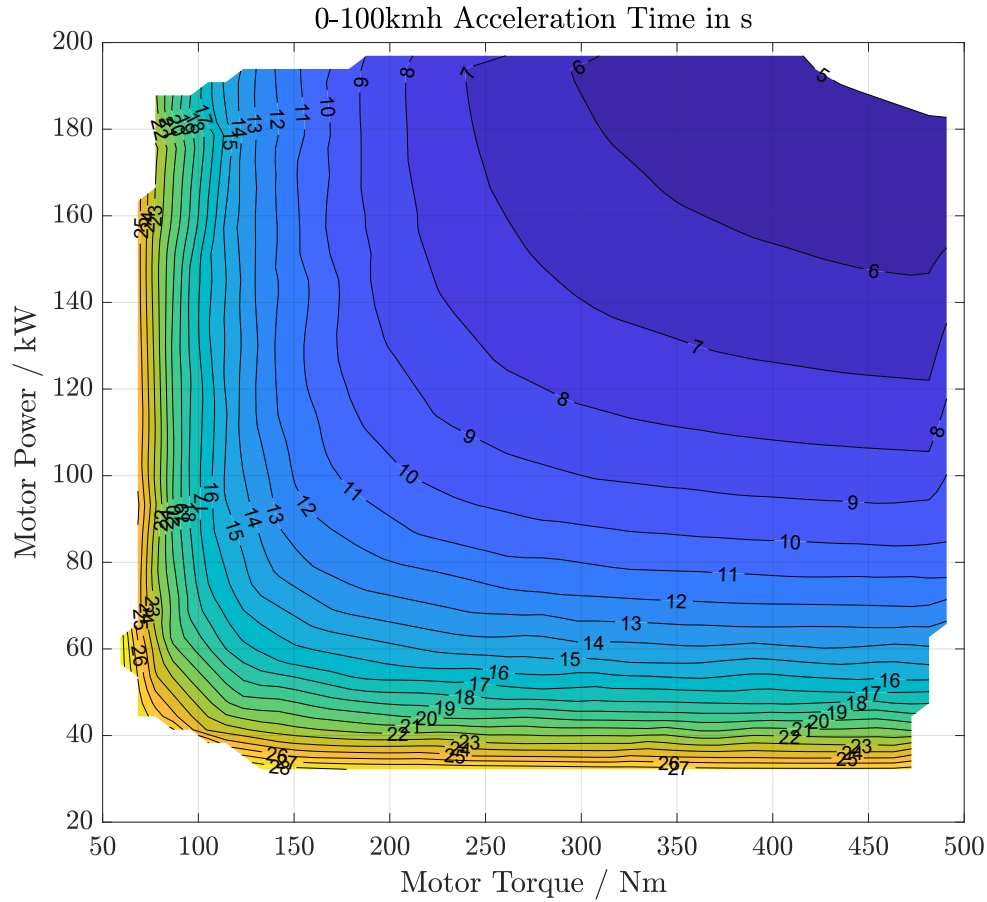


**Figure 6.19.** Relationship between acceleration time and motor peak torque and peak power

**Table 6.4.** Optimization results of the PMSM for the "Highway Cycle" scenarios

Highway Cycle			
	Reference	Optimized	Improvement
Scaling factor	$k_A = 1$ $k_R = 1$	$k_A = 0.8$ $k_R = 1.04$	-
Energy consumption	6.68 kWh	6.49 kWh	2.84 %
0 – 100 km/h Acceleration time	9.28 s	9.40 s	-1.29 %

cycle are depicted in Fig. 6.20. As indicated by the legend, the efficiency is represented by contours, while the operating points are depicted by colored clouds in the figures. A deeper red color indicates a higher frequency of operation in that particular region. Upon analysis of the power share plot, it becomes apparent that the operational points during

the urban cycle are predominantly concentrated in the low-speed and part-load regions. This concentration reflects the typical driving conditions encountered in urban scenarios, characterized by frequent stops, accelerations, and low to moderate speeds. Furthermore, the power share plot highlights the efficiency improvements achieved through motor optimization. By comparing the power distribution of the reference and optimized motors, the efficiency improvement resulting from scaling in this region is evident, with a noticeable increase in the number of operating points falling within higher efficiency contours compared to the reference motor. Moreover, the optimized motor demonstrates superior performance compared to the reference motor, particularly in terms of maximum torque and power output. This indicates that the optimized motor possesses greater capabilities for acceleration and climbing under urban driving conditions.

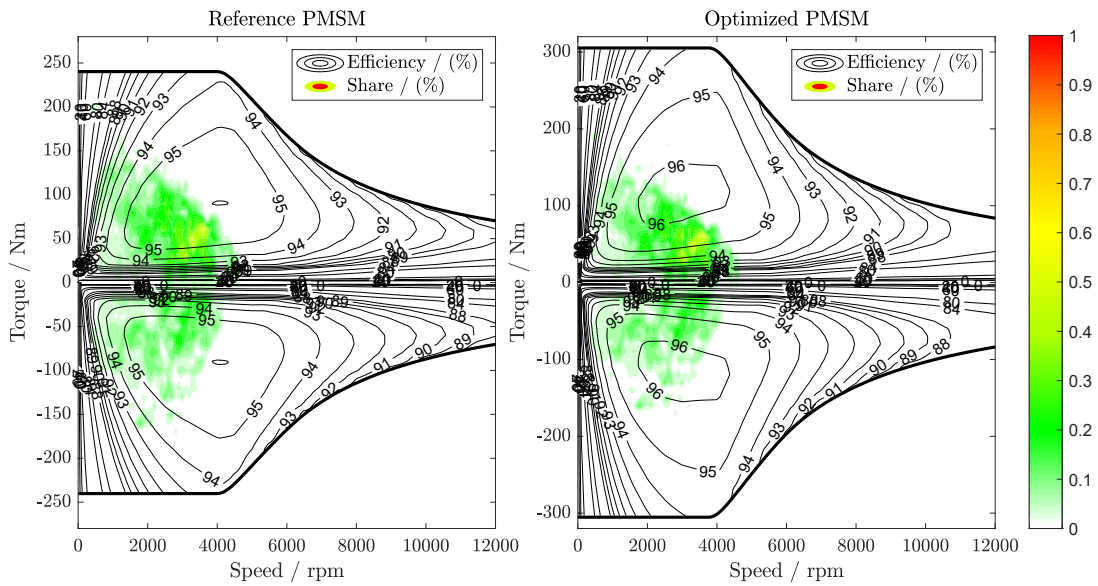


**Figure 6.20.** Power share plot maps of the reference and optimized motors for the urban cycle

In contrast to the urban driving cycle, where operational points are concentrated in the low-speed and part-load regions, highway driving cycles predominantly involve high-speed driving. This difference in operating conditions is reflected in the power share plot maps of both the reference and optimized motors during the highway cycle, as depicted in Fig. 6.21. Analyzing the power share plot, it becomes evident that the efficiency in the high-speed region has been notably improved in the optimized motor compared to the reference motor. A greater percentage of operational points fall within higher efficiency contours, indicating enhanced efficiency levels for the optimized motor across the high-speed region. This improvement in efficiency is a significant advantage, particularly for highway driving, where maintaining high efficiency at sustained speeds is crucial for overall fuel economy and vehicle performance. However, it's essential to note that while the overall efficiency of the optimized motor has improved, there is a trade-off in terms of energy consumption and acceleration performance. After optimization, the optimized motor exhibits a decline in maximum torque and power, which consequently affects acceleration performance. These reductions in torque, power, and acceleration may raise concerns among some users, particularly those accustomed to high-performance driving

experiences. Nevertheless, it's important to consider that highway driving scenarios typically do not have high requirements for acceleration performance. Instead, the focus is on maintaining steady speeds over extended periods, where efficiency becomes a primary concern. In this context, the observed improvements in efficiency within the high-speed region make the optimized motor a more suitable and efficient choice for highway driving applications.

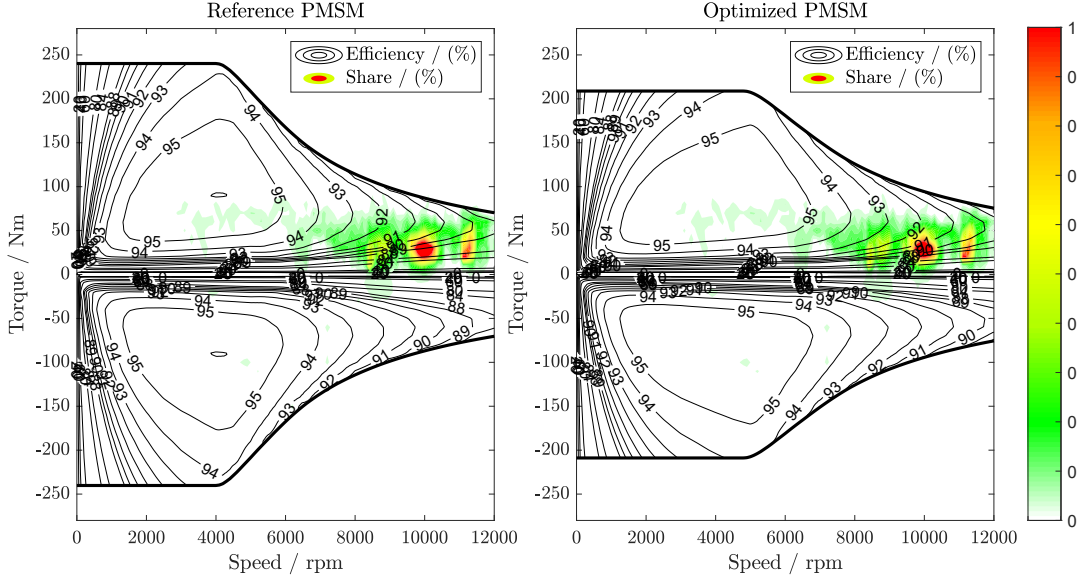


**Figure 6.21.** Power share plot maps of the reference and optimized motors for the highway cycle

Overall, the findings from the power share plot analysis indicate that the optimized motor exhibits higher efficiency within both the urban and highway driving scenarios compared to the reference motor. The trade-off in energy consumption and acceleration performance for the highway driving scenario also underscores the importance of tailoring motor performance to meet the specific requirements of different driving conditions, ultimately optimizing overall vehicle performance and energy efficiency.

## 6.4. Scope and Limitations of the Optimization

It is important to address this optimization study's deliberate scope. The decision to focus exclusively on the electric motor, while excluding the cooling system, was a choice driven by two primary considerations: to demonstrate the methodology's feasibility and to maintain manageable complexity.

First and foremost, the principal objective of this work was to showcase a specific optimization methodology. The core intent was to demonstrate the framework's capability to effectively integrate scaled electromagnetic and thermal simulations of the motor into a multi-objective optimization process. By doing so, we can clearly illustrate the direct impact of its geometric scaling on key performance indicators like energy efficiency, acceleration, and thermal behavior.

Secondly, from a practical standpoint, expanding the optimization to include the cooling system would introduce a significant number of additional variables and dimensions.

This would transform the problem into a far more complex, system-level challenge, exponentially increasing computational cost and making the results more challenging to interpret. Therefore, we adopted a pragmatic engineering approach: first, establish a baseline by quantifying the performance potential achievable through optimizing the core powertrain component—the motor itself. This initial analysis provides valuable insights into the most significant drivers of performance. Once the potential gains from the motor are fully understood, a more informed decision can be made regarding the necessity and potential benefits of expanding the optimization to a full system level, ensuring that any added complexity is justified by the pursuit of further, meaningful improvements.

This deliberate focus on the motor allows the study to leverage several key strengths. The primary strength of this optimization study is the use of axial and radial scaling factors as design variables. This simplifies a highly complex, multi-dimensional design problem into a computationally tractable one with just two variables. This method is highly effective for exploring general design trends and understanding the high-level impact on motor performance without the immense computational cost of a full geometric optimization. The inclusion of thermal constraints is also a critical strength, ensuring the resulting designs are physically viable and do not overheat under operational loads, a crucial consideration for real-world reliability.

Another significant advantage lies in its multi-objective optimization approach. Rather than seeking a single best design, the Pareto front provides a suite of non-dominated solutions, allowing to select a design that aligns with specific performance priorities.

However, the optimization study is not without its limitations. First, the optimization is constrained to only two scaling factors, creating a simplified design space. While efficient, this overlooks other crucial design parameters that significantly influence motor performance. Variables such as magnet layout, winding configuration, slot/tooth geometry, and lamination material were not considered. Optimizing these parameters could unlock further improvements beyond simple scaling.

Second, the analysis relies on a scaled model. While effective for trend analysis, the accuracy of the thermal and loss models under significant scaling could be a concern. For a final design, these Pareto-optimal points should be validated with higher-fidelity FEA to accurately capture localized thermal hotspots and complex loss mechanisms (like eddy current losses in magnets) that may not scale linearly.

# 7. Conclusion and Outlook

## 7.1. Conclusion

The objective of this dissertation is to develop a comprehensive methodology for the system-level design and optimization of a battery electric vehicle (BEV) powertrain. This is achieved by establishing a framework that integrates three core contributions: first, a detailed thermal model that extends beyond the electric machine to encompass the entire drivetrain; second, a novel scaling approach to efficiently adapt the motor's thermal and loss characteristics for different geometric designs; and third, the integration of these models into a complete BEV simulation environment. This integrated framework enables the rapid optimization of powertrain components, particularly motor geometry, to enhance vehicle efficiency and performance across various driving cycles while respecting thermal limitations.

The foundation of this work is a drivetrain thermal model that extends the traditional temperature analysis beyond the electrical machine (EM). This extension enables the consideration of temperature-related losses and thermal coupling between components. The model is based on the lumped parameter thermal network (LPTN) method, which is analogous to electrical circuit design and represents the dominant heat-flow mechanisms. To reduce parameter identification effort, the thermal modeling incorporates a-priori system knowledge that reveals the relationship between thermal parameters and operating status. Heat sources for the LPTN model are derived from loss maps measured on a test bench and validated with Ansys Motor-CAD, including a detailed loss distribution for the permanent magnet synchronous machine (PMSM). A global linear parameter-varying identification approach is applied to determine the LPTN model's parameters. Experimental validation using data from extended WLTC and US06 cycles, with varying coolant inlet temperatures and flow rates, confirms that all predicted temperatures are very close to measured values, with a maximum average temperature deviation of  $0.65^{\circ}\text{C}$ . The inverter junction experiences the largest temperature error at approximately  $7^{\circ}\text{C}$ , which is attributed to the limited bandwidth and slower transient response of the first-order thermal impedance model between the junction and the cooling plate.

To facilitate the rapid evaluation of different motor geometries within the optimization framework, a novel scaling approach is proposed. Based on axial and radial scaling factors, this approach allows for the convenient adaptation of motor losses and temperatures to new design requirements. It comprises two components: the scaling of losses and the scaling of the thermal model. The loss scaling method, derived from Poisson's equation, enables the direct proportional scaling of direct current (DC) copper, alternating current (AC) copper, iron, and magnet losses while maintaining a consistent magnetic flux density across all variations. A strong agreement between Motor-CAD and the scaling approach is demonstrated, with a maximum root mean square error (RMSE) of  $132.9\text{ W}$  for the total loss. For the thermal model, parameters are scaled based on the equivalent geometric relationships of motor components, assuming an identical convec-

tion coefficient for the same coolant conditions. Temperature validation of the scaling approach shows a maximum RMSE of less than  $3.92^{\circ}\text{C}$  and an average RMSE of  $1.42^{\circ}\text{C}$ . A sensitivity analysis reveals that axial scaling primarily influences the PMSM's peak torque with minimal impact on efficiency, whereas radial scaling significantly affects frequency-dependent losses, leading to a more pronounced alteration in temperature.

The thermal model and scaling approach are integrated into a holistic BEV model to enable system-level optimization for realistic urban and highway driving cycles. The BEV model is constructed using an extensive library of physical-based or map-based models to accurately represent system components and controllers. For the EM, the motor controller employs the maximum torque per ampere (MTPA) algorithm, and losses are calculated based on currents, speed, and temperature. Crucially, the BEV model incorporates a standard cooling system, implemented in Simscape, which accounts for the power consumption of the overall vehicle cooling system. This system, consisting of interconnected coolant and refrigerant circuits, maintains optimal temperatures for both the powertrain and the cabin. The consistency between the drivetrain component coolant outlet temperatures and the LPTN results confirms the model's accuracy, while the power levels of the cooling system actuators remain within acceptable ranges. This integration allows for a preliminary estimation of the LPTN's thermal overload capacity as part of the system-level optimization.

Applying this integrated BEV model, an optimization was performed at the vehicle system level using realistic technical data for an A-segment vehicle under both urban and highway driving cycles. The optimization results for both scenarios advocate for a shorter motor length, leading to reduced total losses and improved overall efficiency. For the urban cycle, the optimized configuration yields a 0.53% reduction in energy consumption and a 2.51% improvement in acceleration time compared to the reference case. In contrast, the highway cycle optimization results in a 2.84% increase in energy consumption and a 1.29% deterioration in acceleration time. This discrepancy highlights a critical design trade-off: reducing the motor diameter mitigates frequency-dependent AC copper and iron losses, but it consequently compromises the acceleration performance.

### 7.2. Outlook

Based on this work, several research avenues could be explored in the future. One such avenue involves the development of a machine learning-based scaling approach. This approach could automate the determination of the parameter scaling approach by learning from extensive datasets, finding the optimal variation pattern for the parameters. Additionally, extending the optimization framework to include gear ratio selection for 2-speed gearboxes holds promise. Incorporating gear ratio optimization could enhance overall system efficiency and performance, better aligning the powertrain with diverse driving scenarios. Furthermore, expanding the optimization criteria to encompass the total cost of the powertrain is another area of potential growth based on requirements as demanded by the project. This holistic approach would consider not only the motor but also other drivetrain components, such as the inverter and gearbox, resulting in a more informed decision for component selection. Finally, exploring alternative powertrain topologies, such as multiple motors or four-wheel-motor configurations, could yield improved performance under specific conditions or vehicle architectures.

# Bibliography

- [1] “Paris agreement,” Dec. 2015. [Online]. Available: <https://unfccc.int/resource/docs/2015/cop21/eng/l09r01.pdf>
- [2] L. Wang, V. Nian, H. Li, and J. Yuan, “Impacts of electric vehicle deployment on the electricity sector in a highly urbanised environment,” *Journal of Cleaner Production*, vol. 295, p. 126386, may 2021.
- [3] J. Andert, E. Köhler, J. Niehues, and G. Schürmann, “KSPG range extender,” *MTZ worldwide*, vol. 73, no. 5, pp. 12–18, 2012.
- [4] A. Wahl, C. Wellmann, B. Krautwig, P. Manns, B. Chen, C. Schernus, and J. Andert, “Efficiency increase through model predictive thermal control of electric vehicle powertrains,” *Energies*, vol. 15, no. 4, p. 1476, 2022.
- [5] G. D. Nunzio, I. B. Gharbia, and A. Sciarretta, “A time- and energy-optimal routing strategy for electric vehicles with charging constraints,” in *2020 IEEE 23rd International Conference on Intelligent Transportation Systems (ITSC)*, 2020, pp. 1–8.
- [6] C. Ngo, E. Solano-Araque, M. Aguado-Rojas, A. Sciarretta, B. Chen, and M. E. Baghdadi, “Real-time eco-driving for connected electric vehicles,” *IFAC-PapersOnLine*, vol. 54, no. 10, pp. 126–131, 2021.
- [7] S. Chakraborty, M. E. Baghdadi, J. Jaguemont, C. D. Cauwer, B. Chen, A. Wahl, P. Manns, C. Ngo, A. Sciarretta, and O. Hegazy, “Parameterized cloud-connected electro-thermal modelling of a battery electric vehicle,” in *2021 IEEE Vehicle Power and Propulsion Conference (VPPC)*, 2021.
- [8] K. Etzold, T. Fahrbach, S. Klein, R. Scheer, D. Guse, M. Klawitter, S. Pischinger, and J. Andert, “Function development with an electric-machine-in-the-loop setup: A case study,” *IEEE Transactions on Transportation Electrification*, vol. 5, no. 4, pp. 1419–1429, dec 2019.
- [9] I. Husain, B. Ozpineci, M. S. Islam, E. Gurpinar, G.-J. Su, W. Yu, S. Chowdhury, L. Xue, D. Rahman, and R. Sahu, “Electric drive technology trends, challenges, and opportunities for future electric vehicles,” *Proceedings of the IEEE*, vol. 109, no. 6, pp. 1039–1059, jun 2021.
- [10] M. Doppelbauer, *Grundlagen der Elektromobilität*. Springer Fachmedien Wiesbaden, 2020.
- [11] J. W. Kolar and U. Drogenik, “A general scheme for calculating switching- and conduction-losses of power semiconductors in numerical circuit simulations of power electronic systems; international power electronics conference; ; ipec-niigata 2005,” 2005. [Online]. Available: <https://api.semanticscholar.org/CorpusID:63065574>

- [12] J. Yang, Y. Che, L. Ran, and H. Jiang, "Evaluation of frequency and temperature dependence of power losses difference in parallel IGBTs," *IEEE Access*, vol. 8, pp. 104 074–104 084, 2020.
- [13] S. C. Das, G. Narayanan, and A. Tiwari, "Experimental study on the dependence of IGBT switching energy loss on DC link voltage," in *2014 IEEE International Conference on Power Electronics, Drives and Energy Systems (PEDES)*. IEEE, dec 2014.
- [14] A. Binder, *Elektrische Maschinen und Antriebe*. Springer Berlin Heidelberg, 2012.
- [15] D. Bauer, *Verlustanalyse bei elektrischen Maschinen für Elektro- und Hybridfahrzeuge zur Weiterverarbeitung in thermischen Netzwerkmodellen*. Springer Fachmedien Wiesbaden, 2019.
- [16] R. Wrobel, A. Mlot, and P. H. Mellor, "Contribution of end-winding proximity losses to temperature variation in electromagnetic devices," *IEEE Transactions on Industrial Electronics*, vol. 59, no. 2, pp. 848–857, feb 2012.
- [17] R. Wrobel, D. E. Salt, A. Griffo, N. Simpson, and P. H. Mellor, "Derivation and scaling of ac copper loss in thermal modeling of electrical machines," *IEEE Transactions on Industrial Electronics*, vol. 61, no. 8, pp. 4412–4420, 8 2014.
- [18] J. Schutzhold and W. Hofmann, "Analysis of the temperature dependence of losses in electrical machines," in *2013 IEEE Energy Conversion Congress and Exposition*. IEEE, sep 2013.
- [19] P. S. Ghahfarokhi, A. Podgornovs, A. Kallaste, A. J. M. Cardoso, A. Belahcen, and T. Vaimann, "The oil spray cooling system of automotive traction motors: The state of the art," *IEEE Transactions on Transportation Electrification*, vol. 9, no. 1, pp. 428–451, mar 2023.
- [20] M. Alatalo, S. T. Lundmark, and E. A. Grunditz, "Evaluation of three cooling concepts for an electric vehicle motor – 3d models," in *2020 International Conference on Electrical Machines (ICEM)*. IEEE, aug 2020.
- [21] ISO/TR14179-2, "Gears — thermal capacity; part 2:thermal load-carrying capacity," International Organization for Standardization, Tech. Rep., Aug. 2001. [Online]. Available: <https://nautos.de/7TE/search/item-detail/IX45759491>.
- [22] A. Christodoulis, "Prediction of power losses in an automotive gearbox incorporating a thermally coupled lubrication model," Ph.D. dissertation, 2017.
- [23] K. Michaelis, B.-R. Höhn, and M. Hinterstoifer, "Influence factors on gearbox power loss," *Industrial Lubrication and Tribology*, vol. 63, no. 1, pp. 46–55, feb 2011.
- [24] C. Changenet, X. Oviedo-Marlot, and P. Velez, "Power loss predictions in geared transmissions using thermal networks-applications to a six-speed manual gearbox," *Journal of Mechanical Design*, vol. 128, no. 3, pp. 618–625, aug 2005.
- [25] S. Group, *CR Seals handbook - Industrial shaft seals*, Jan. 2019.

- [26] F. B. Von Lukas Merkle, Matthias Baumann, *Improving a Gear Box Sealing System - Individual Test Design Based on Given Application Parameters and Failure Analysis*. ISGATEC GmbH, Mannheim, 2021, ch. Dichten - Dynamische Dichtsysteme, pp. 84–97.
- [27] C. W. I. Wulff, “Metamodellbasierte optimierung von betriebsstrategien im thermomanagement elektrischer fahrzeuge,” Ph.D. dissertation, RWTH Aachen University, 2020.
- [28] H. Winter and L. Wech, *Einflüsse auf den Wirkungsgrad von Kegelrad- und Hypoidgetrieben: Kegelradgetriebe, Kontakt, Konstruktion*. Ehningen: Expert Verlag, 1990.
- [29] D. Hemkemeyer, “Thermomanagement im elektrischen personenkraftwagen unter nutzung der abwärme des antriebs,” Ph.D. dissertation, RWTH Aachen University, 2017.
- [30] Frank P. Incropera, David P. Dewitt, Theodore L. Bergman, Adrienne S. Lavine, *Fundamentals of Heat and Mass Transfer 6th Edition*. R.R. Donnelley., 2006.
- [31] Frank Kreith, Raj M. Manglik, *Principles of Heat Transfer*. Cengage Learning, 2016.
- [32] D. Staton and A. Cavagnino, “Convection heat transfer and flow calculations suitable for analytical modelling of electric machines,” in *IECON 2006 - 32nd Annual Conference on IEEE Industrial Electronics*, 2006, pp. 4841–4846.
- [33] G. Bramerdorfer, J. A. Tapia, J. J. Pyrhonen, and A. Cavagnino, “Modern electrical machine design optimization: Techniques, trends, and best practices,” *IEEE Transactions on Industrial Electronics*, vol. 65, no. 10, pp. 7672–7684, oct 2018.
- [34] Carlos A. Coello Coello, Gary B. Lamont, David A. Van Veldhuizen, *Evolutionary Algorithms for Solving Multi-Objective Problems*. Springer US, 2007.
- [35] B. N. Cassimere and S. D. Sudhoff, “Population-based design of surface-mounted permanent-magnet synchronous machines,” *IEEE Transactions on Energy Conversion*, vol. 24, no. 2, pp. 338–346, jun 2009.
- [36] M. Mirjafari, S. Harb, and R. S. Balog, “Multiobjective optimization and topology selection for a module-integrated inverter,” *IEEE Transactions on Power Electronics*, vol. 30, no. 8, pp. 4219–4231, aug 2015.
- [37] S. G. Min, G. Bramerdorfer, and B. Sarlioglu, “Analytical modeling and optimization for electromagnetic performances of fractional-slot PM brushless machines,” *IEEE Transactions on Industrial Electronics*, vol. 65, no. 5, pp. 4017–4027, may 2018.
- [38] O. Wallscheid and J. Böcker, “Global identification of a low-order lumped-parameter thermal network for permanent magnet synchronous motors,” *IEEE Transactions on Energy Conversion*, vol. 31, no. 1, pp. 354–365, 3 2016.

- [39] Y. Duan and D. M. Ionel, “A review of recent developments in electrical machine design optimization methods with a permanent magnet synchronous motor benchmark study,” in *2011 IEEE Energy Conversion Congress and Exposition*. IEEE, sep 2011.
- [40] A. Fatemi, D. M. Ionel, N. A. O. Demerdash, and T. W. Nehl, “Fast multi-objective CMODE-type optimization of PM machines using multicore desktop computers,” *IEEE Transactions on Industry Applications*, vol. 52, no. 4, pp. 2941–2950, jul 2016.
- [41] M. Dorigo and T. Stützle, “The ant colony optimization metaheuristic: Algorithms, applications, and advances,” 2003. [Online]. Available: <https://api.semanticscholar.org/CorpusID:6315988>
- [42] M. Schlüter, J. A. Egea, and J. R. Banga, “Extended ant colony optimization for non-convex mixed integer nonlinear programming,” *Comput. Oper. Res.*, vol. 36, pp. 2217–2229, 2009. [Online]. Available: <https://api.semanticscholar.org/CorpusID:7425258>
- [43] M. Schlüter and M. Gerdts, “The oracle penalty method,” *Journal of Global Optimization*, vol. 47, no. 2, pp. 293–325, oct 2009.
- [44] M. Schlueter, C. H. Yam, T. Watanabe, and A. Oyama, “Parallelization impact on many-objective optimization for space trajectory design,” *International Journal of Machine Learning and Computing*, 2016. [Online]. Available: <https://api.semanticscholar.org/CorpusID:35429026>
- [45] S. D. Wilson, P. Stewart, and B. P. Taylor, “Methods of resistance estimation in permanent magnet synchronous motors for real-time thermal management,” *IEEE Transactions on Energy Conversion*, vol. 25, no. 3, pp. 698–707, sep 2010.
- [46] M. Ganchev, C. Kral, H. Oberguggenberger, and T. Wolbank, “Sensorless rotor temperature estimation of permanent magnet synchronous motor,” in *IECON 2011 - 37th Annual Conference of the IEEE Industrial Electronics Society*. IEEE, nov 2011.
- [47] D. E. G. Erazo, O. Wallscheid, and J. Bocker, “Improved fusion of permanent magnet temperature estimation techniques for synchronous motors using a kalman filter,” *IEEE Transactions on Industrial Electronics*, vol. 67, no. 3, pp. 1708–1717, mar 2020.
- [48] O. Wallscheid, T. Huber, W. Peters, and J. Bocker, “Real-time capable methods to determine the magnet temperature of permanent magnet synchronous motors — a review,” in *IECON 2014 - 40th Annual Conference of the IEEE Industrial Electronics Society*. IEEE, oct 2014.
- [49] A. Boglietti, A. Cavagnino, D. Staton, M. Shanel, M. Mueller, and C. Mejuto, “Evolution and modern approaches for thermal analysis of electrical machines,” *IEEE Transactions on Industrial Electronics*, vol. 56, no. 3, pp. 871–882, 2009.
- [50] T. Huber, W. Peters, and J. Böcker, “A low-order thermal model for monitoring critical temperatures in permanent magnet synchronous motors,” in *7th IET International Conference on Power Electronics, Machines and Drives*, 2014, pp. 1–6.

- [51] P. Mellor, D. Roberts, and D. Turner, “Lumped parameter thermal model for electrical machines of TEFC design,” *IEE Proceedings B Electric Power Applications*, vol. 138, no. 5, p. 205, 1991.
- [52] D. Kuehbacher, A. Kelleter, and D. Gerling, “An improved approach for transient thermal modeling using lumped parameter networks,” in *2013 International Electric Machines Drives Conference*. IEEE, may 2013.
- [53] F. Qi, A. Stippich, M. Guettler, M. Neubert, and R. W. D. Doncker, “Methodical considerations for setting up space-resolved lumped-parameter thermal models for electrical machines,” in *2014 17th International Conference on Electrical Machines and Systems (ICEMS)*. IEEE, oct 2014.
- [54] F. Qi, M. Schenk, and R. D. Doncker, “Discussing details of lumped parameter thermal modeling in electrical machines,” in *7th IET International Conference on Power Electronics, Machines and Drives (PEMD 2014)*. Institution of Engineering and Technology, 2014.
- [55] T. Huber, W. Peters, and J. Bocker, “Monitoring critical temperatures in permanent magnet synchronous motors using low-order thermal models,” in *2014 International Power Electronics Conference (IPEC-Hiroshima 2014 - ECCE ASIA)*. IEEE, may 2014.
- [56] W. Kirchgassner, O. Wallscheid, and J. Bocker, “Estimating electric motor temperatures with deep residual machine learning,” *IEEE Transactions on Power Electronics*, vol. 36, no. 7, pp. 7480–7488, jul 2021.
- [57] W. Kirchgassner, O. Wallscheid, and J. Bocker, “Data-driven permanent magnet temperature estimation in synchronous motors with supervised machine learning: A benchmark,” *IEEE Transactions on Energy Conversion*, vol. 36, no. 3, pp. 2059–2067, sep 2021.
- [58] S. Hochreiter and J. Schmidhuber, “Long short-term memory,” *Neural Comput.*, vol. 9, no. 8, p. 1735–1780, nov 1997. [Online]. Available: <https://doi.org/10.1162/neco.1997.9.8.1735>
- [59] O. Wallscheid, W. Kirchgassner, and J. Bocker, “Investigation of long short-term memory networks to temperature prediction for permanent magnet synchronous motors,” in *2017 International Joint Conference on Neural Networks (IJCNN)*. IEEE, may 2017.
- [60] V. K. Shaojie Bai, J. Zico Kolter, “Empirical evaluation of generic convolutional and recurrent networks for sequence modeling,” *arXiv1803.01271*, 2018.
- [61] G. Domingues, A. Reinap, and M. Alakula, “Design and cost optimization of electrified automotive powertrain.” IEEE, nov 2016.
- [62] A. Aroua, W. Lhomme, F. Verbelen, M. N. Ibrahim, A. Bouscayrol, P. Sergeant, and K. Stockman, “Impact of scaling laws of permanent magnet synchronous machines on the accuracy of energy consumption computation of electric vehicles,” *eTransportation*, vol. 18, p. 100269, Oct. 2023.

- [63] S. Kalt, J. Erhard, and M. Lienkamp, “Electric machine design tool for permanent magnet synchronous machines and induction machines,” *Machines*, vol. 8, no. 1, p. 15, Mar. 2020.
- [64] C. Gletter, A. Mayer, J. Kallo, T. Winsel, and O. Nelles, “A novel approach for development of neural network based electrical machine models for hev system-level design optimization,” in *Proceedings of the 5th International Conference on Vehicle Technology and Intelligent Transport Systems*. SCITEPRESS - Science and Technology Publications, 2019.
- [65] W. L. Soong, “Sizing of electrical machines,” 2008. [Online]. Available: <https://api.semanticscholar.org/CorpusID:6736188>
- [66] J. Bone, “Influence of rotor diameter and length on the rating of induction motors,” *IEE Journal on Electric Power Applications*, vol. 1, no. 1, pp. 2–6, feb 1978.
- [67] K. Binns, “The relationship between performance characteristics and size of permanent magnet motors.” IEEE, 1995.
- [68] Q. S. Gu and M. Stiebler, “Scaling and dimensioning of switched reluctance machines,” *European Transactions on Electrical Power*, vol. 7, no. 5, pp. 301–310, sep 2007.
- [69] S. Stipetic, D. Zarko, and M. Popescu, “Scaling laws for synchronous permanent magnet machines,” in *2015 Tenth International Conference on Ecological Vehicles and Renewable Energies (EVER)*, 2015, pp. 1–7.
- [70] S. Stipetic, D. Zarko, and M. Popescu, “Ultra-fast axial and radial scaling of synchronous permanent magnet machines,” *Institution of Engineering and Technology (IET)*, vol. 10, no. 7, pp. 658–666, 2016.
- [71] M. M. Nell, B. Groschup, and K. Hameyer, “Using scaled fe solutions for an efficient coupled electromagnetic–thermal induction machine model,” *COMPEL - The international journal for computation and mathematics in electrical and electronic engineering*, vol. 40, no. 2, pp. 267–279, Feb. 2021.
- [72] F. Pauli, A. Ruf, and K. Hameyer, “Thermal overload capability of permanent magnet synchronous motors employing scaling laws,” in *2018 XIII International Conference on Electrical Machines (ICEM)*, 2018, pp. 433–439.
- [73] M. Kuenzler, R. Pflueger, R. Lehmann, Q. Werner, and U. Schaefer, “Scalable thermal model of an electric machine for the thermal assessment in different electric vehicle use cases,” in *2020 International Symposium on Power Electronics, Electrical Drives, Automation and Motion (SPEEDAM)*, 2020, pp. 281–286.
- [74] N. Makowski and B. Helenbrook, “Scaling of permanent magnet machines with thermal effects,” in *2019 IEEE International Electric Machines & Drives Conference (IEMDC)*, 2019, pp. 2035–2041.
- [75] B. Chen, C. Wulff, K. Etzold, P. Manns, G. Birmes, J. Andert, and S. Pischinger, “A comprehensive thermal model for system-level electric drivetrain simulation with respect to heat exchange between components,” in *2020 19th IEEE Intersociety*

- 
- Conference on Thermal and Thermomechanical Phenomena in Electronic Systems (ITherm)*, 2020, pp. 558–567.
- [76] G. D. Demetriades, H. Z. de la Parra, E. Andersson, and H. Olsson, “A real-time thermal model of a permanent-magnet synchronous motor,” *IEEE Transactions on Power Electronics*, vol. 25, no. 2, pp. 463–474, feb 2010.
- [77] Y. A. Çengel, *Heat transfer*, ser. WCB/McGraw-Hill series in mechanical engineering. Boston, Mass. [u.a.]: WCB McGraw-Hill, 1998, literaturangaben.
- [78] R. Wu, H. Wang, K. B. Pedersen, K. Ma, P. Ghimire, F. Iannuzzo, and F. Blaabjerg, “A temperature-dependent thermal model of IGBT modules suitable for circuit-level simulations,” *IEEE Transactions on Industry Applications*, vol. 52, no. 4, pp. 3306–3314, jul 2016.
- [79] M. Kind, *Estimation of Liquid Cooled Heat Sink Performance at Different Operation Conditions*, SEMIKRON, 2015, accessed: Sep. 26, 2022. [Online]. Available: <https://www.semikron.com/dl/service-support/downloads/download/semikron-application-note-estimation-of-liquid-cooled-heat-sink-performance-at-different-operation-conditions-en-2015-10-16-rev-00.pdf>
- [80] C. Wulff, P. Manns, and S. Pischinger, “Optimum cooling circuit control for electric drivetrains for increased driving range,” in *28th Aachen Colloquium Automobile and Engine Technology*, Aachen, Germany, Oct. 2019, p. 1365–1377.
- [81] R. Wrobel, P. Mellor, M. Popescu, and D. Staton, “Power loss analysis in thermal design of permanent magnet machines – a review,” *IEEE Transactions on Industry Applications*, pp. 1–1, 2015.
- [82] *Hybrid Synchronous Motor HSM1-6.17.12 - C01*, BRUSA Elektronik AG, accessed: Sep. 26, 2022. [Online]. Available: <https://www.yumpu.com/la/document/view/104049/hybrid-synchronous-motor-hsm1-61712-c01>.
- [83] P. Mellor, R. Wrobel, and N. Simpson, “AC losses in high frequency electrical machine windings formed from large section conductors,” in *2014 IEEE Energy Conversion Congress and Exposition (ECCE)*. IEEE, sep 2014.
- [84] N. Denis, S. Odawara, and K. Fujisaki, “Attempt to evaluate the building factor of a stator core in inverter-fed permanent magnet synchronous motor,” *IEEE Transactions on Industrial Electronics*, vol. 64, no. 3, pp. 2424–2432, mar 2017.
- [85] P. Mellor, R. Wrobel, and N. McNeill, “Investigation of proximity losses in a high speed brushless permanent magnet motor,” in *Conference Record of the 2006 IEEE Industry Applications Conference Forty-First IAS Annual Meeting*. IEEE, oct 2006.
- [86] C. Du-Bar and O. Wallmark, “Eddy current losses in a hairpin winding for an automotive application,” in *2018 XIII International Conference on Electrical Machines (ICEM)*. IEEE, sep 2018.
- [87] J. Goss, P. Mellor, R. Wrobel, D. Staton, and M. Popescu, “The design of AC permanent magnet motors for electric vehicles: a computationally efficient model of the operational envelope,” in *6th IET International Conference on Power Electronics, Machines and Drives (PEMD 2012)*. IET, 2012.

- [88] G. K. GYIMAH, Z. ning GUO, P. HUANG, S. zhen JIANG, G. C. BARBER, G. xian LIU, and J. W. LIU, “Improvers of pressure-viscosity coefficients of two-phase liquid-solid lubricants,” *DEStech Transactions on Engineering and Technology Research*, no. amita, nov 2016.
- [89] M. Schlueter, J. A. Egea, and J. R. Banga, “Extended ant colony optimization for non-convex mixed integer nonlinear programming,” *Computers and Operations Research*, vol. 36, no. 7, pp. 2217–2229, 2009.
- [90] M. Schlueter, S. O. Erb, M. Gerdtts, S. Kemble, and J.-J. Rückmann, “Midaco on minlp space applications,” *Advances in Space Research*, vol. 51, no. 7, pp. 1116–1131, 2013.
- [91] E. Walter and L. Pronzato, *Identification of Parametric Models*. Springer, 1997.
- [92] M. Andresen, M. Schloh, G. Buticchi, and M. Liserre, “Computational light junction temperature estimator for active thermal control,” in *2016 IEEE Energy Conversion Congress and Exposition (ECCE)*. IEEE, sep 2016.
- [93] T. A. Polom, M. Andresen, M. Liserre, and R. D. Lorenz, “Experimentally extracting multiple spatial thermal models that accurately capture slow and fast properties of assembled power semiconductor converter systems,” in *2018 IEEE Energy Conversion Congress and Exposition (ECCE)*. IEEE, sep 2018.
- [94] R. W. D. Doncker, D. W. J. Pulle, and A. Veltman, *Advanced Electrical Drives*. Springer International Publishing, Aug. 2020. [Online]. Available: [https://www.ebook.de/de/product/39030233/rik\\_w\\_de\\_doncker\\_duco\\_w\\_j\\_pulle\\_andre\\_veltman\\_advanced\\_electrical\\_drives.html](https://www.ebook.de/de/product/39030233/rik_w_de_doncker_duco_w_j_pulle_andre_veltman_advanced_electrical_drives.html)
- [95] B. Chen, C. Monissen, M. Ayyildiz, G. Birmes, J. Andert, and S. Pischinger, “A study on scaling laws for thermal parameters of permanent magnet synchronous machines,” in *2021 24th International Conference on Electrical Machines and Systems (ICEMS)*, 2021, pp. 35–41.
- [96] B. Chen, C. Monissen, C. Wellmann, A. Wahl, M. Ayyildiz, R. Savelsberg, J. Andert, and S. Pischinger, “Thermal and loss modeling of scaled permanent magnet synchronous machines for automotive driving cycles,” *Proceedings of the Institution of Mechanical Engineers, Part D: Journal of Automobile Engineering*, Jun. 2024.
- [97] S. Stipetic, J. Goss, D. Zarko, and M. Popescu, “Calculation of efficiency maps using a scalable saturated model of synchronous permanent magnet machines,” *IEEE Transactions on Industry Applications*, vol. 54, no. 5, pp. 4257–4267, 2018.
- [98] K. Ramakrishnan, S. Stipetic, M. Gobbi, and G. Mastinu, “Optimal sizing of traction motors using scalable electric machine model,” *IEEE Transactions on Transportation Electrification*, vol. 4, no. 1, pp. 314–321, mar 2018.

# A. Appendix

## A.1. Loss Validation Between Motor-CAD and Measurements

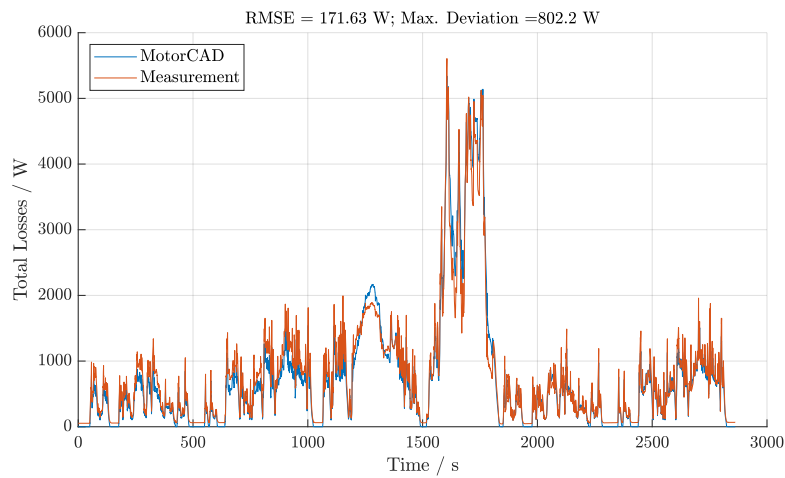


**Figure A.1.** Validation result of the total loss against worldwide harmonized light duty test cycle (WLTC) driving cycle at an ambient temperature of 20 °C

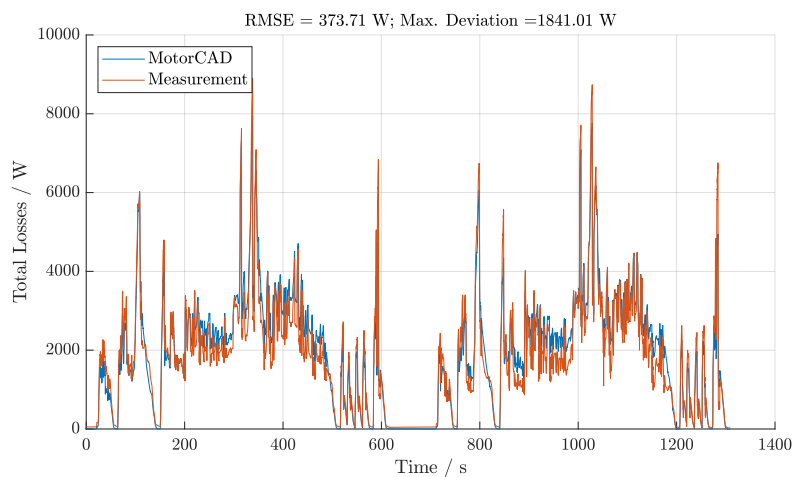


**Figure A.2.** Validation result of the total loss against US06 driving cycle at an ambient temperature of 20 °C

## A.2. Detailed Representation of Matrices in State Space Model of the Drivetrain LPTN

$$\mathbf{B} = \begin{bmatrix}
 0 & 0 & 0 & 0 & 0 & 0 & 0 \\
 \frac{1}{C_J} & 0 & 0 & 0 & 0 & 0 & 0 \\
 0 & 0 & 0 & 0 & 0 & 0 & 0 \\
 0 & 0 & 0 & 0 & 0 & \frac{1}{C_{COI}R_{CIN-COI}} & 0 \\
 0 & 0 & 0 & 0 & 0 & 0 & 0 \\
 0 & 0 & 0 & 0 & 0 & 0 & 0 \\
 0 & \frac{1}{C_S} & 0 & 0 & 0 & 0 & 0 \\
 0 & 0 & \frac{1}{C_{EW}} & 0 & 0 & 0 & 0 \\
 0 & 0 & 0 & \frac{1}{C_R} & 0 & 0 & 0 \\
 0 & 0 & 0 & 0 & \frac{1}{C_G} & 0 & 0 \\
 0 & 0 & 0 & 0 & 0 & 0 & 0 \\
 0 & 0 & 0 & 0 & 0 & 0 & 0 \\
 0 & 0 & 0 & 0 & 0 & 0 & \frac{1}{C_{ADC}R_{ADC-A}}
 \end{bmatrix}$$

$$\mathbf{C} = \begin{bmatrix}
 1 & 0 & 0 & 0 & 0 & 0 & 0 & 0 & 0 & 0 & 0 & 0 & 0 \\
 0 & 1 & 0 & 0 & 0 & 0 & 0 & 0 & 0 & 0 & 0 & 0 & 0 \\
 0 & 0 & 1 & 0 & 0 & 0 & 0 & 0 & 0 & 0 & 0 & 0 & 0 \\
 0 & 0 & 0 & 1 & 0 & 0 & 0 & 0 & 0 & 0 & 0 & 0 & 0 \\
 0 & 0 & 0 & 0 & 1 & 0 & 0 & 0 & 0 & 0 & 0 & 0 & 0 \\
 0 & 0 & 0 & 0 & 0 & 1 & 0 & 0 & 0 & 0 & 0 & 0 & 0 \\
 0 & 0 & 0 & 0 & 0 & 0 & 0 & 0 & 0 & 0 & 1 & 0 & 0 \\
 0 & 0 & 0 & 0 & 0 & 0 & 0 & 0 & 0 & 0 & 0 & 1 & 0 \\
 0 & 0 & 0 & 0 & 0 & 0 & 0 & 0 & 0 & 0 & 0 & 0 & 1
 \end{bmatrix}$$



### A.3. Parametrization and Validation of the LPTN for the Whole Drivetrain

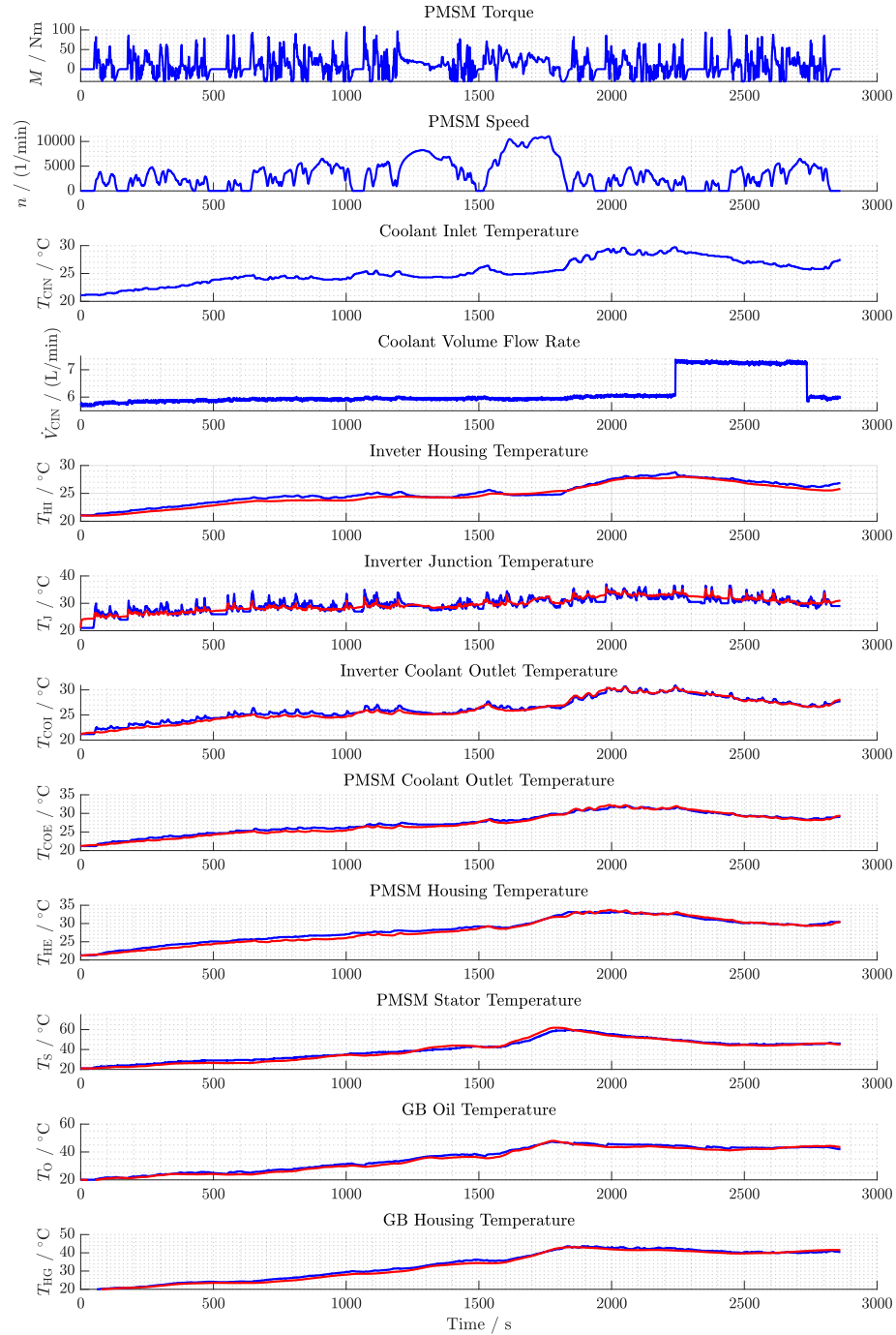


**Figure A.3.** Parametrization based on WLTC driving cycle with ambient temperature around 20 °C and varying coolant profiles (blue lines: measurement; red lines: simulation)

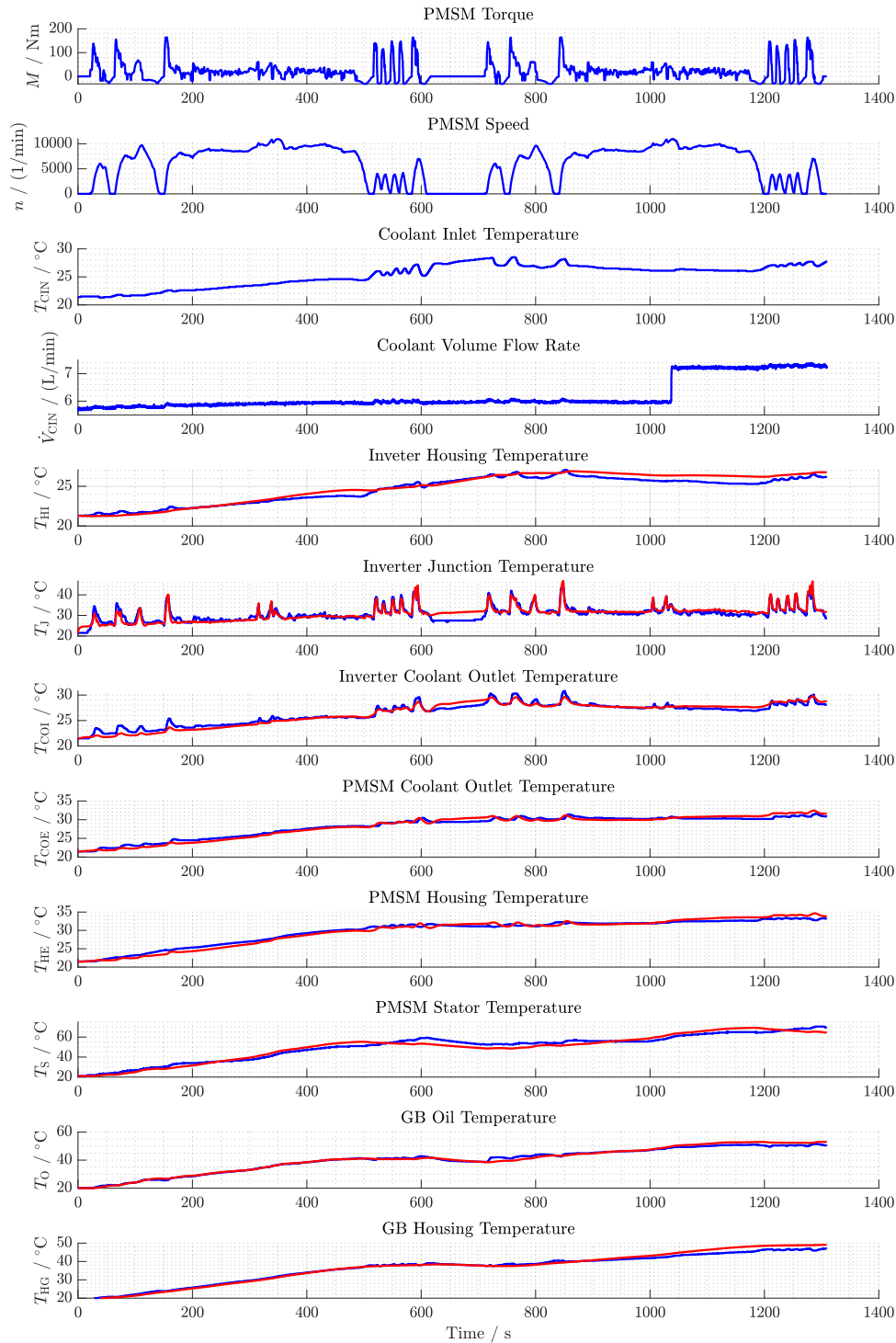


**Figure A.4.** Cross-Validation against US06 driving cycle with ambient temperature around 20 °C and varying coolant profiles (blue lines: measurement; red lines: simulation)

### A.4. Loss Validation of the Scaled PMSM

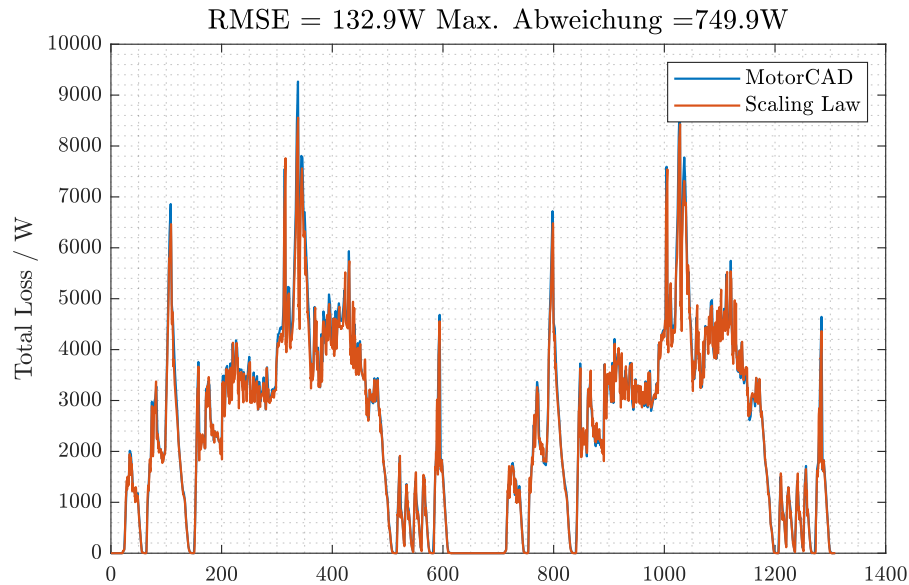


**Figure A.5.** Total losses validation for 1.2 radial scaling against the extended US06 cycle at the ambient temperature of 20 °C  
 Source: Chen et al. (2024). Reprinted with permission from SAGE Publications, Inc. doi:10.1177/09544070241254557

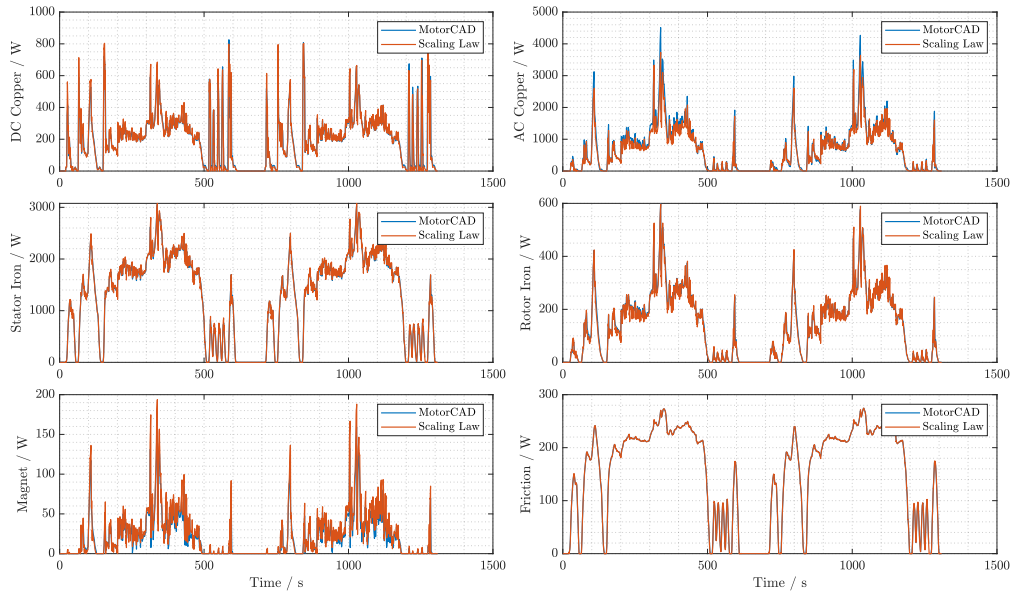


**Figure A.6.** Related losses validation for 1.2 radial scaling against the extended US06 cycle at the ambient temperature of 20 °C

**Table A.1.** RMSE deviation of total loss for WLTC cycle

WLTC Cycle RMSE / W		Axial Scaling				
		Factor 0.8	Factor 0.9	Factor 1	Factor 1.1	Factor 1.2
Radial Scaling	Factor 0.8	46	47	52	51	53
	Factor 0.9	55	55	56	57	59
	Factor 1	26	27	28	30	32
	Factor 1.1	22	23	25	27	29
	Factor 1.2	62	62	62	63	64

**Table A.2.** RMSE deviation of total loss for US06 cycle

US06 Cycle RMSE / W		Axial Scaling				
		Factor 0.8	Factor 0.9	Factor 1	Factor 1.1	Factor 1.2
Radial Scaling	Factor 0.8	115	153	182	211	242
	Factor 0.9	154	155	137	135	135
	Factor 1	86	77	78	80	82
	Factor 1.1	66	69	69	74	79
	Factor 1.2	129	127	125	126	128

### A.5. Cycle Profiles and Coolant Profiles for the Validation of the Reference PMSM

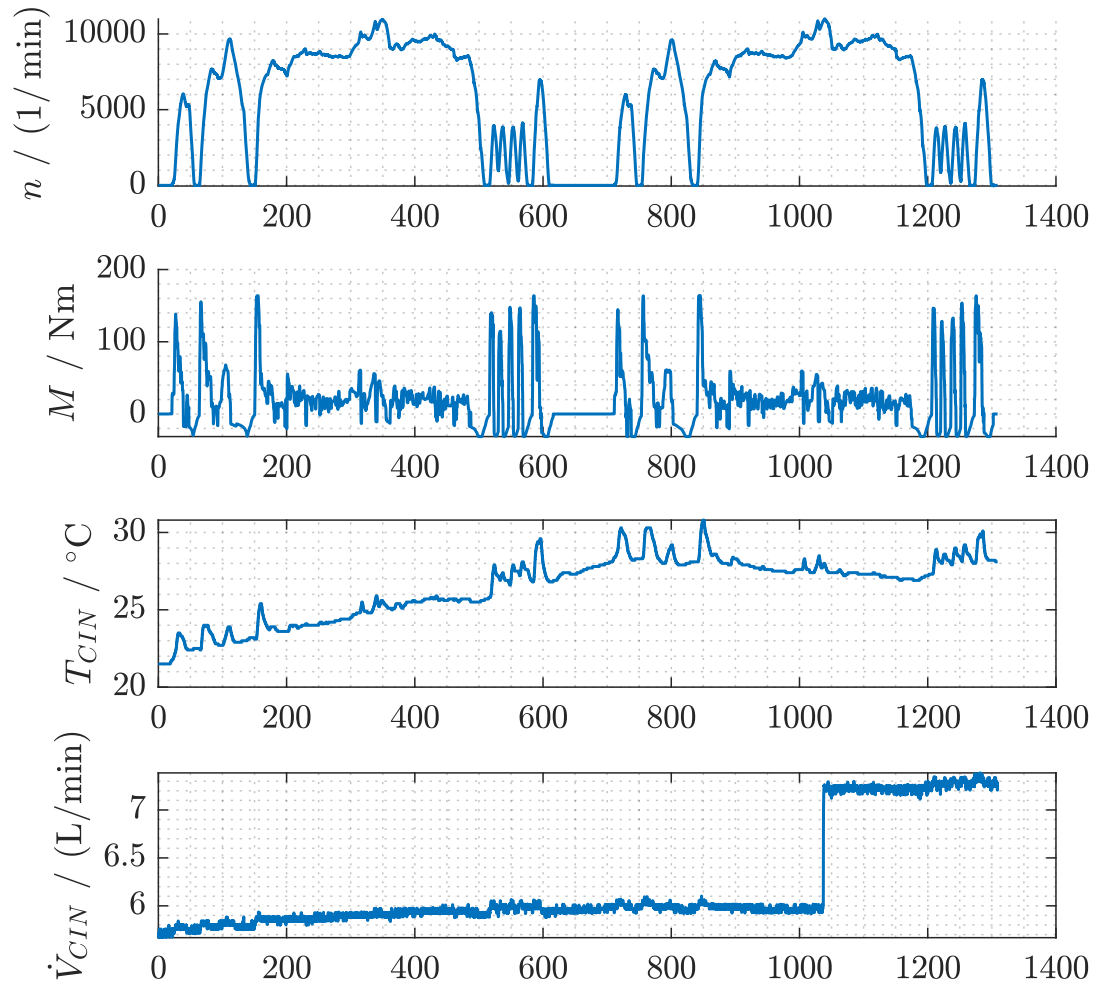


**Figure A.7.** Boundary condition for the extended US06 cycle at an ambient temperature of 20 °C

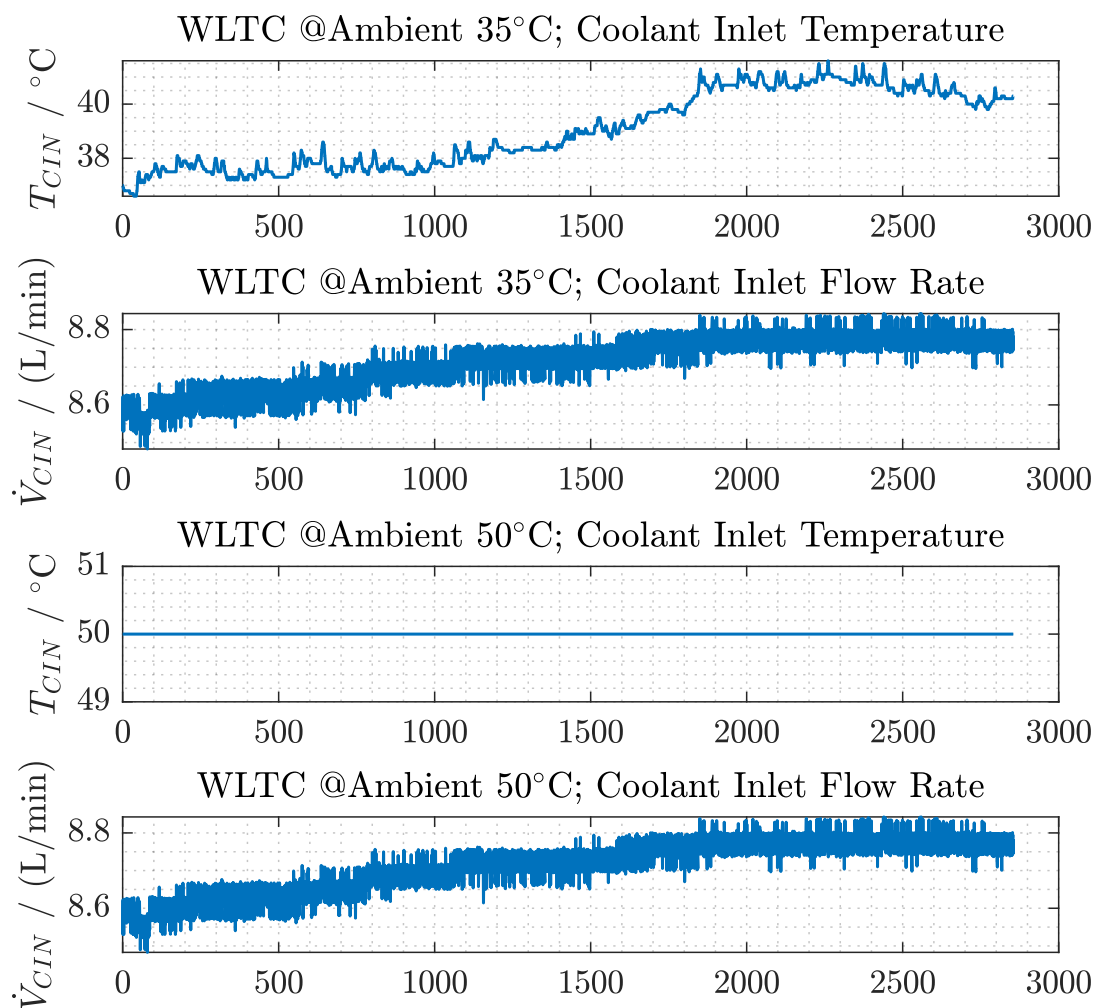


**Figure A.8.** Boundary condition for the extended WLTC cycle at an ambient temperature of 35°C and 50°C

### A.6. Temperature Validation of the Reference PMSM

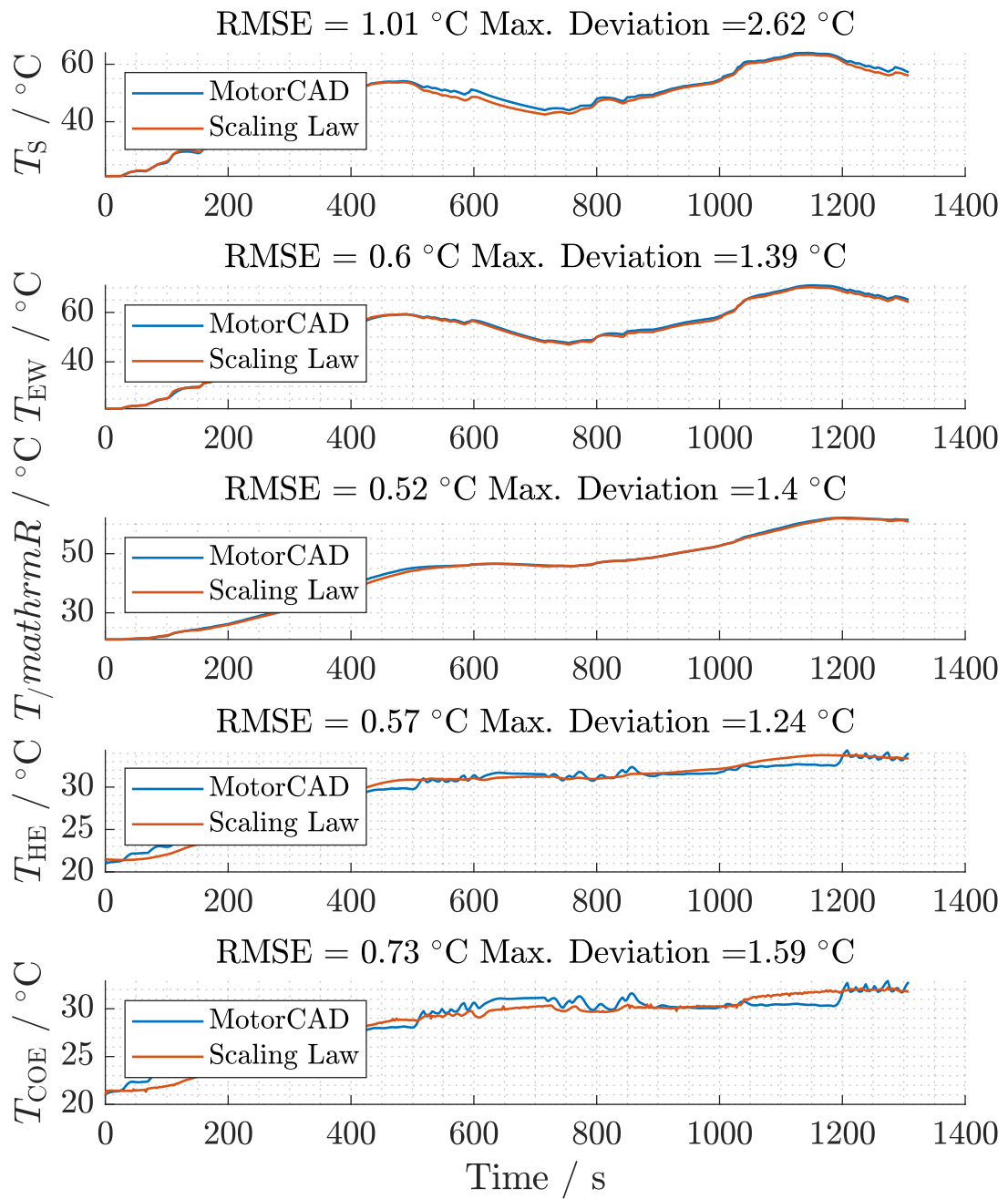


**Figure A.9.** Validation against the extended US06 cycle at an ambient temperature of 20  $^\circ\text{C}$

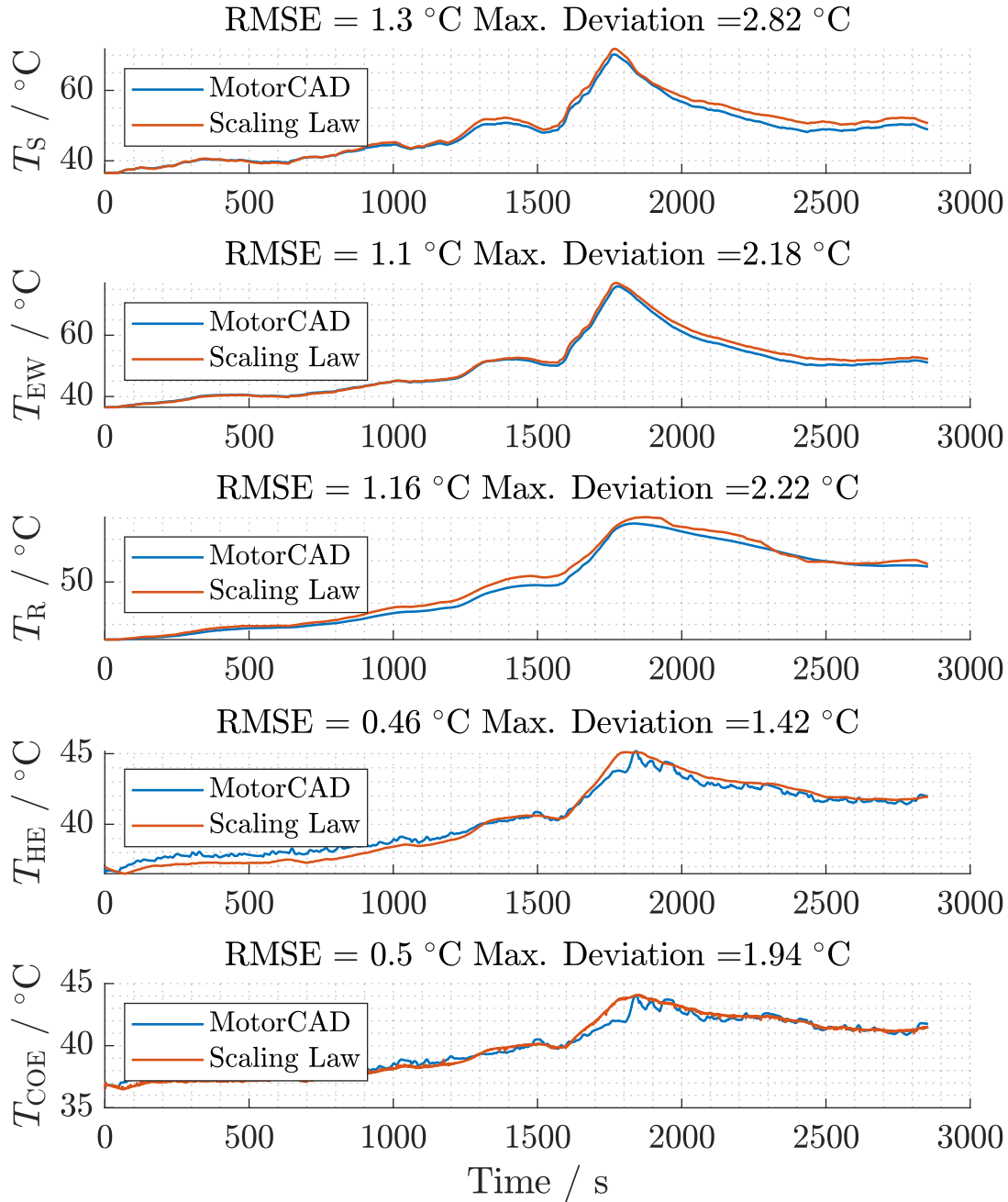


**Figure A.10.** Validation against the extended WLTC cycle at an ambient temperature of 35  $^\circ\text{C}$

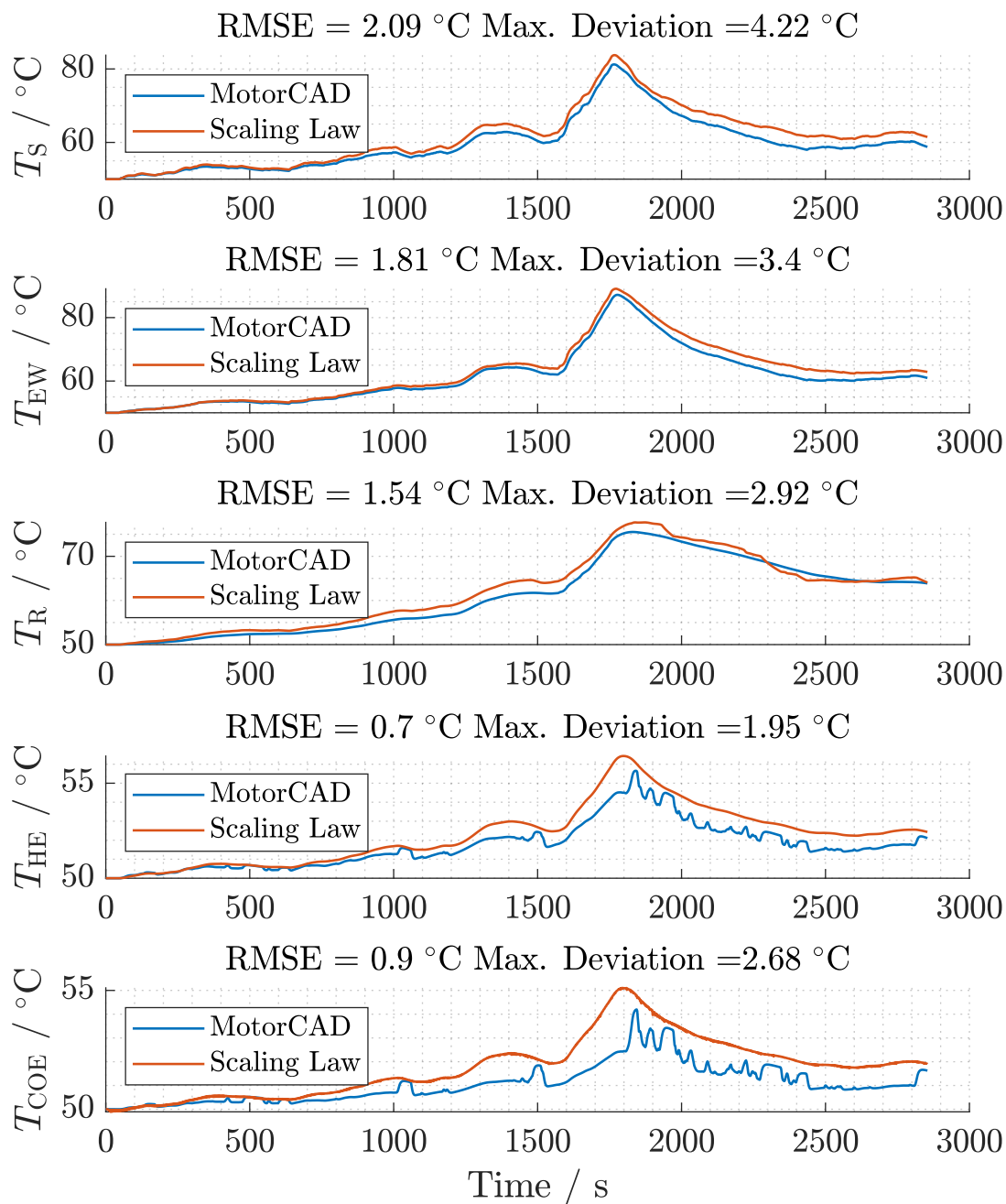


**Figure A.11.** Validation against the extended WLTC cycle at an ambient temperature of 50 °C

### A.7. Temperature Validation of the Scaled PMSM

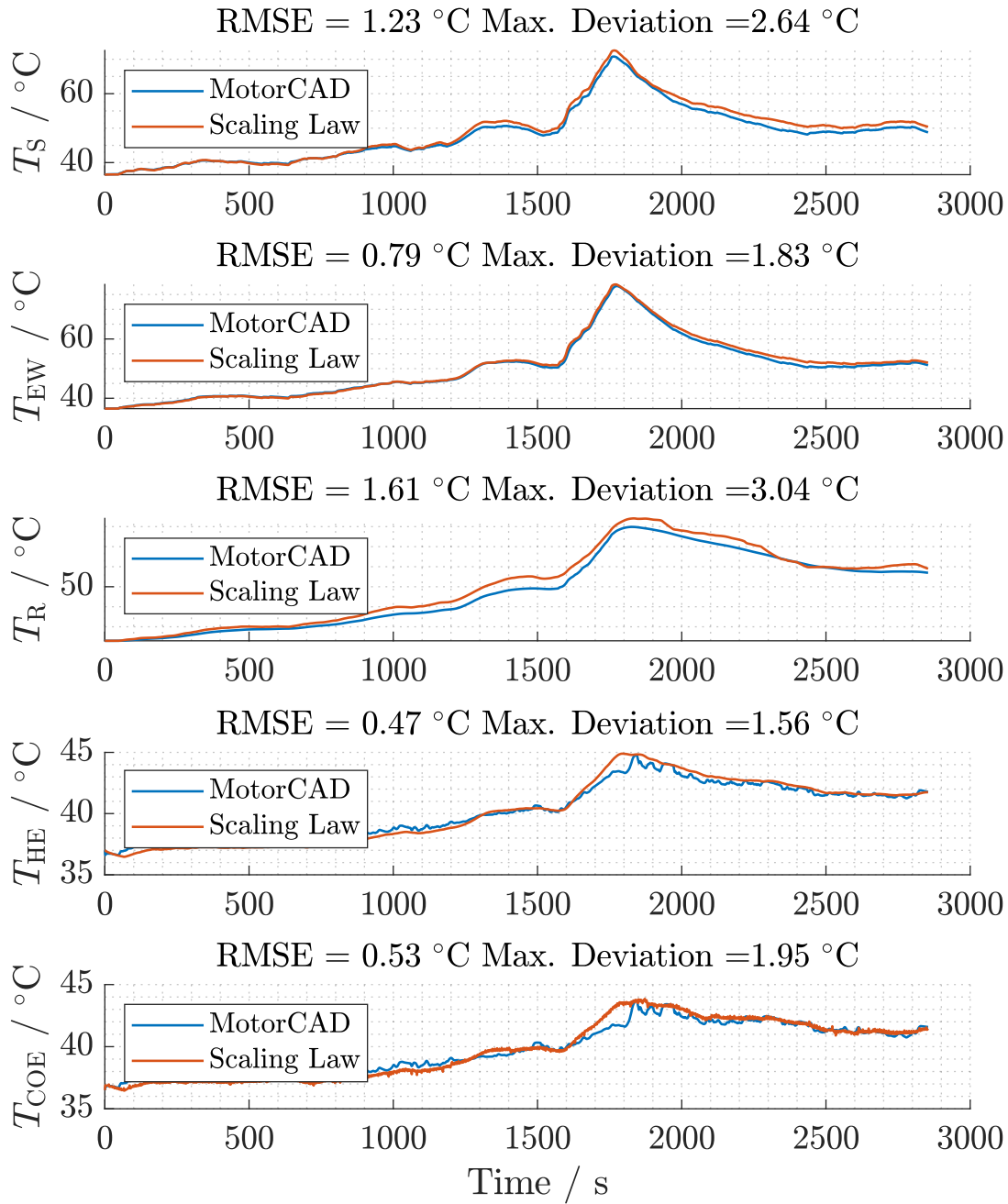


**Figure A.12.** Validation results of temperature estimation for 0.8 axial scaling against the extended WLTC cycle at an ambient temperature of 35 °C

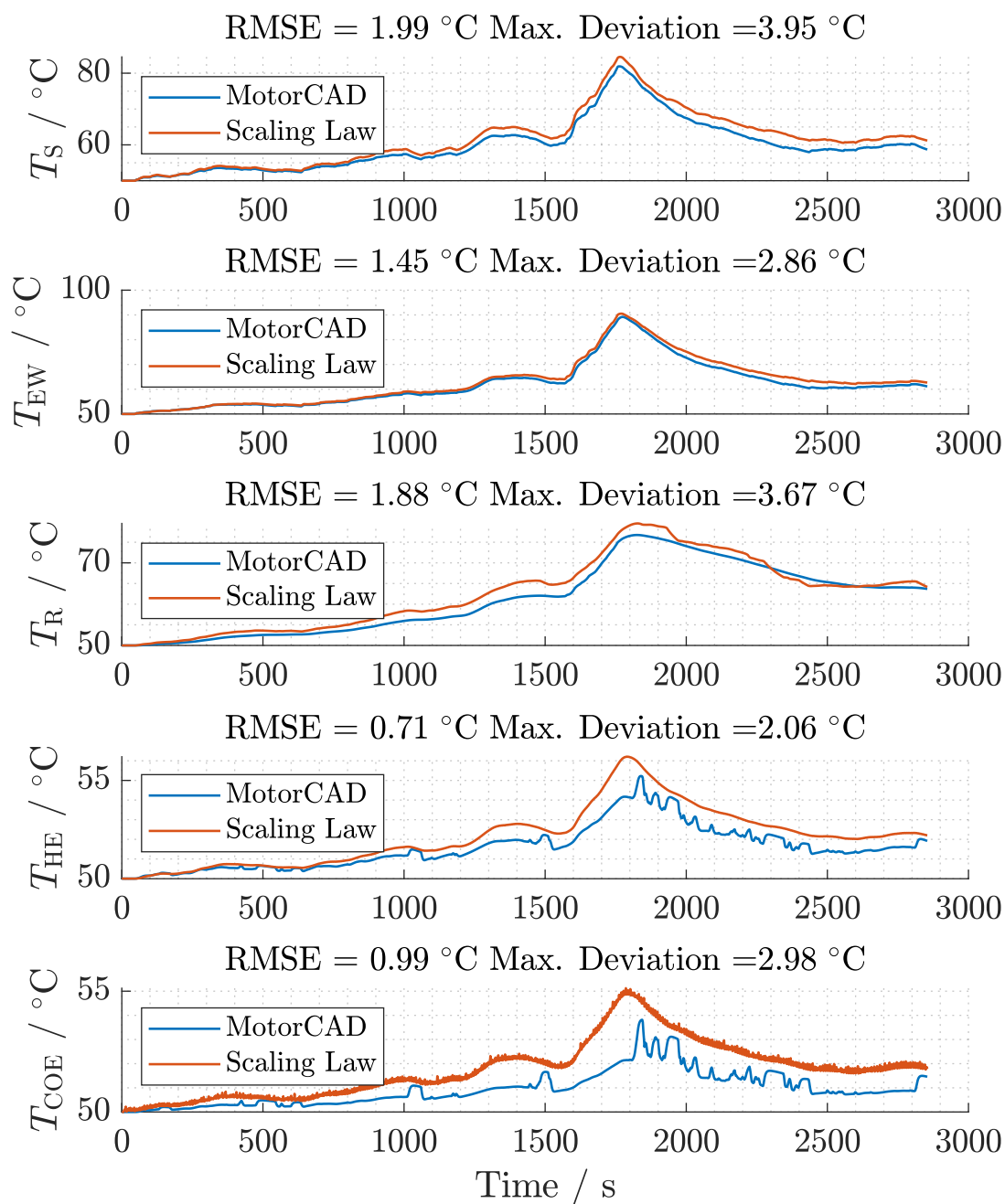


**Figure A.13.** Validation results of temperature estimation for 0.8 axial scaling against the extended WLTC cycle at an ambient temperature of 50  $^\circ\text{C}$

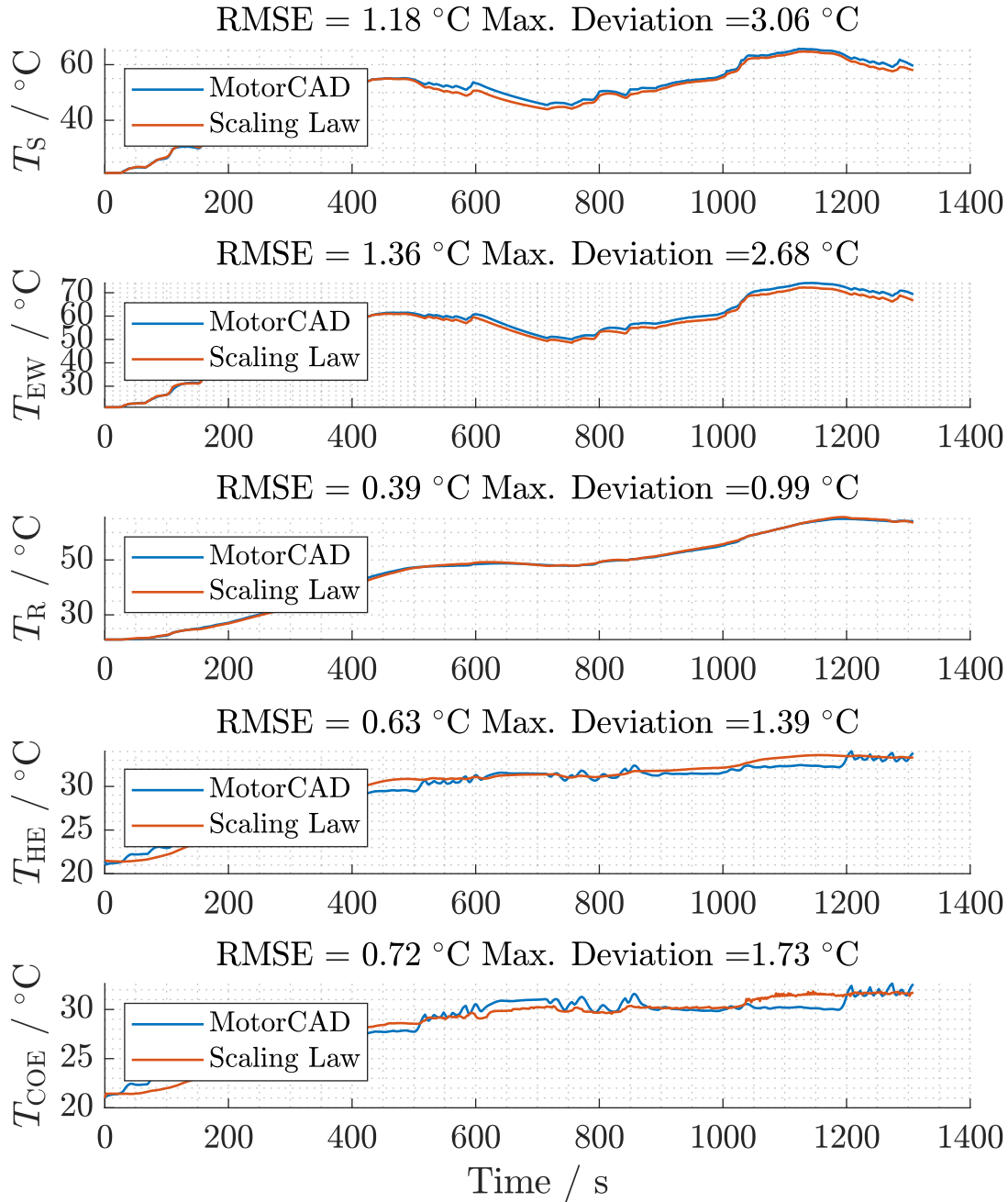


**Figure A.14.** Validation results of temperature estimation for 0.8 axial scaling against the US06 cycle at an ambient temperature of 20  $^\circ\text{C}$

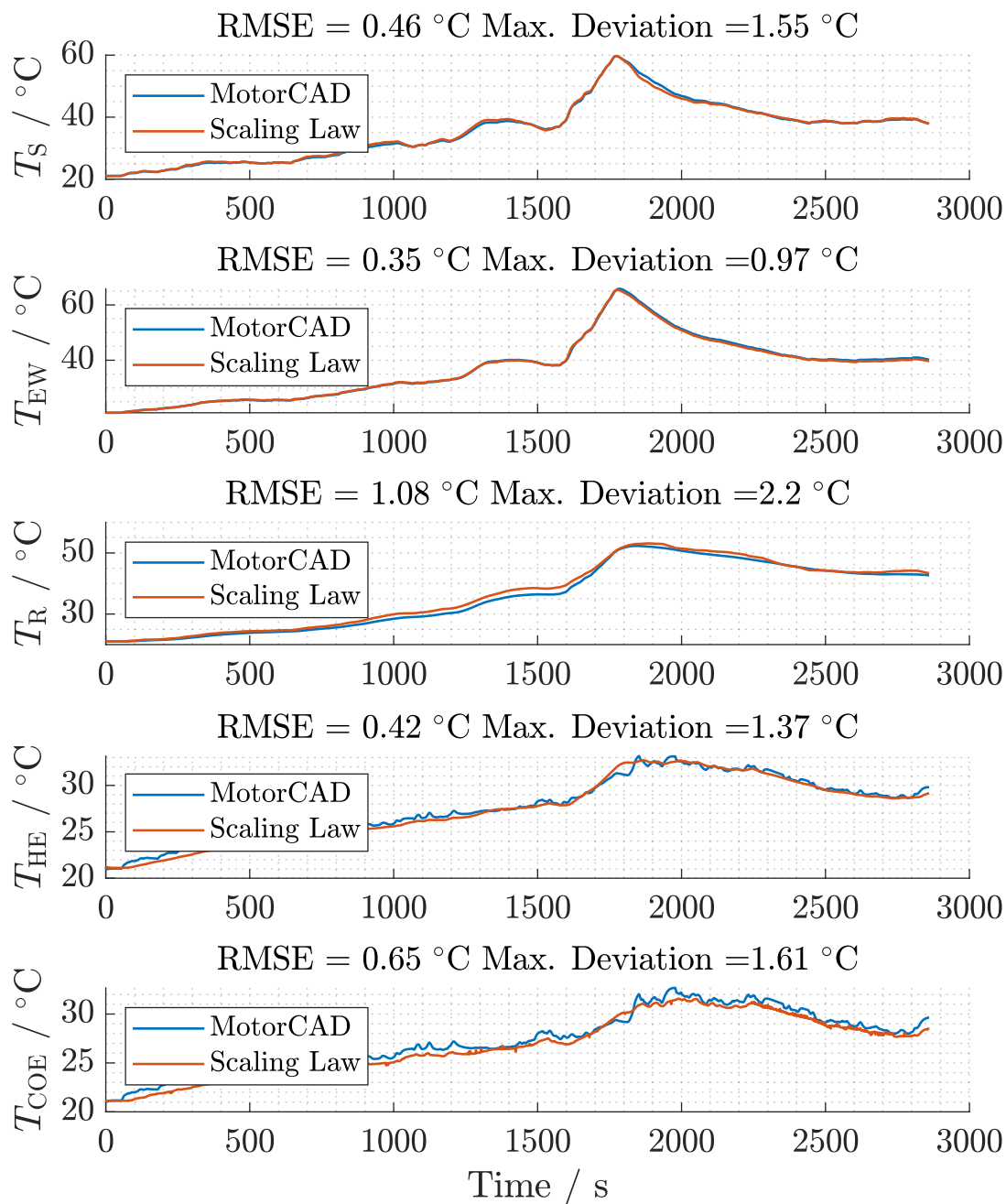


**Figure A.15.** Validation results of temperature estimation for 0.9 axial scaling against the extended WLTC cycle at an ambient temperature of 20 °C

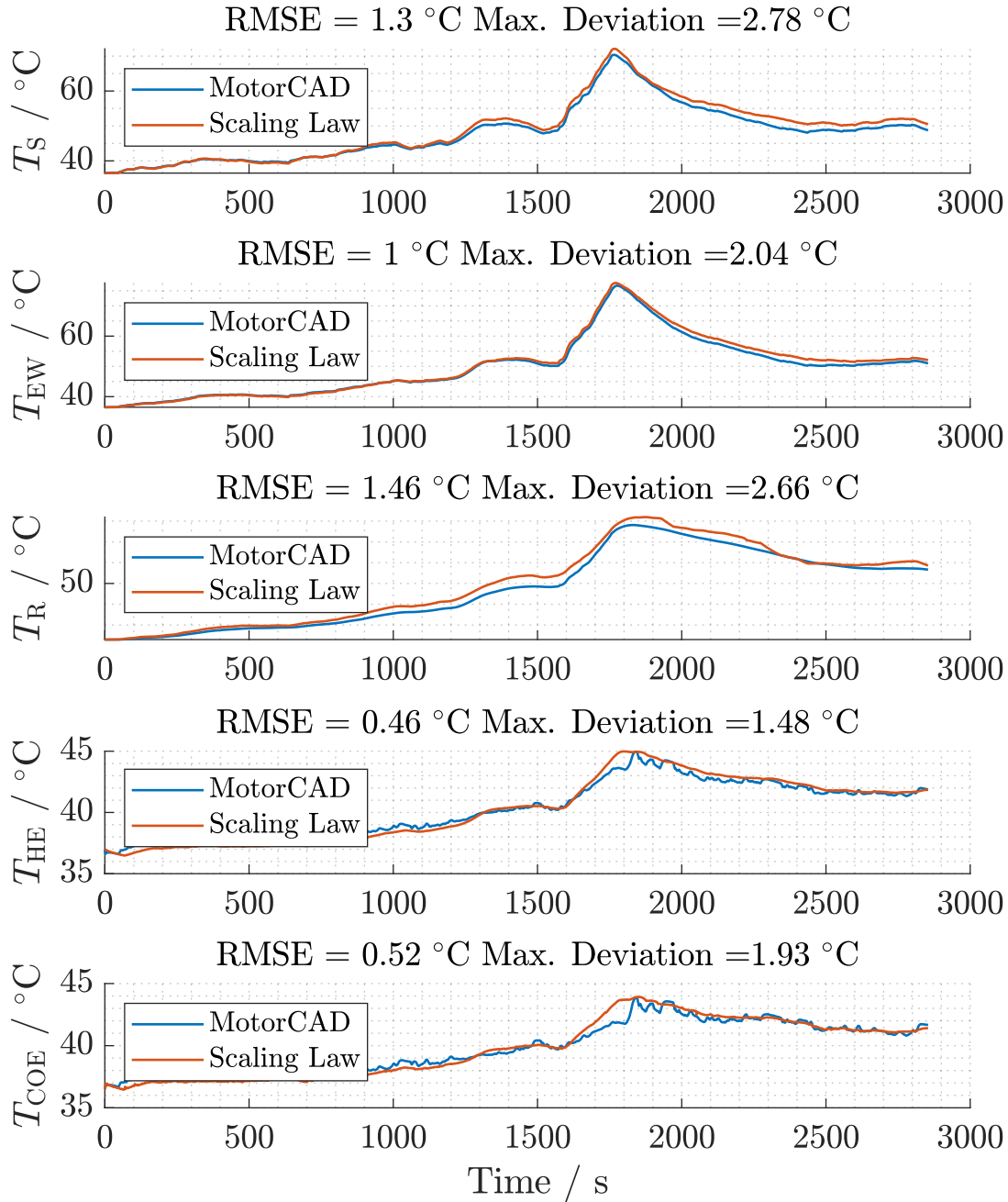


**Figure A.16.** Validation results of temperature estimation for 0.9 axial scaling against the extended WLTC cycle at an ambient temperature of 35 °C

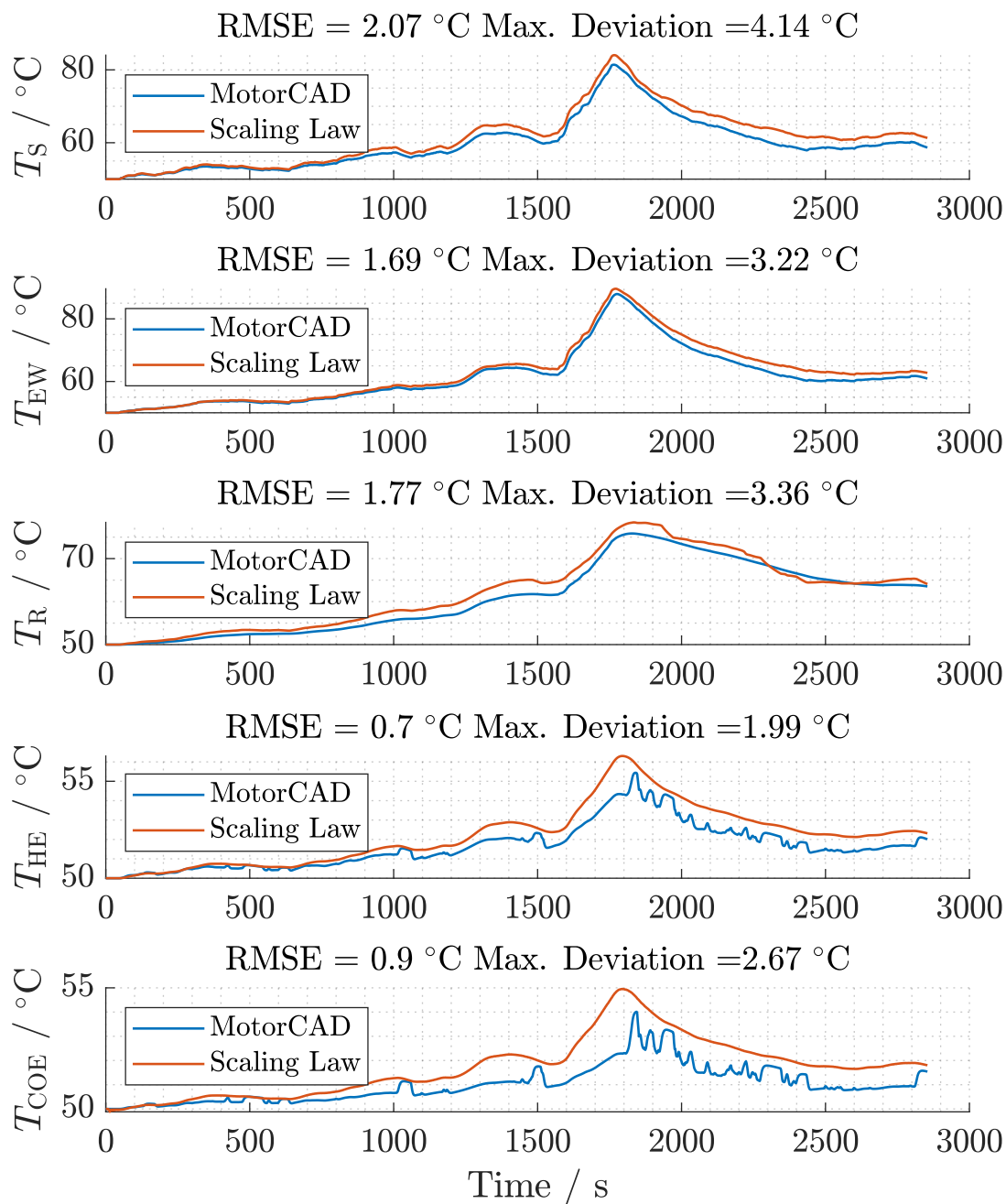


**Figure A.17.** Validation results of temperature estimation for 0.9 axial scaling against the extended WLTC cycle at an ambient temperature of 50 °C

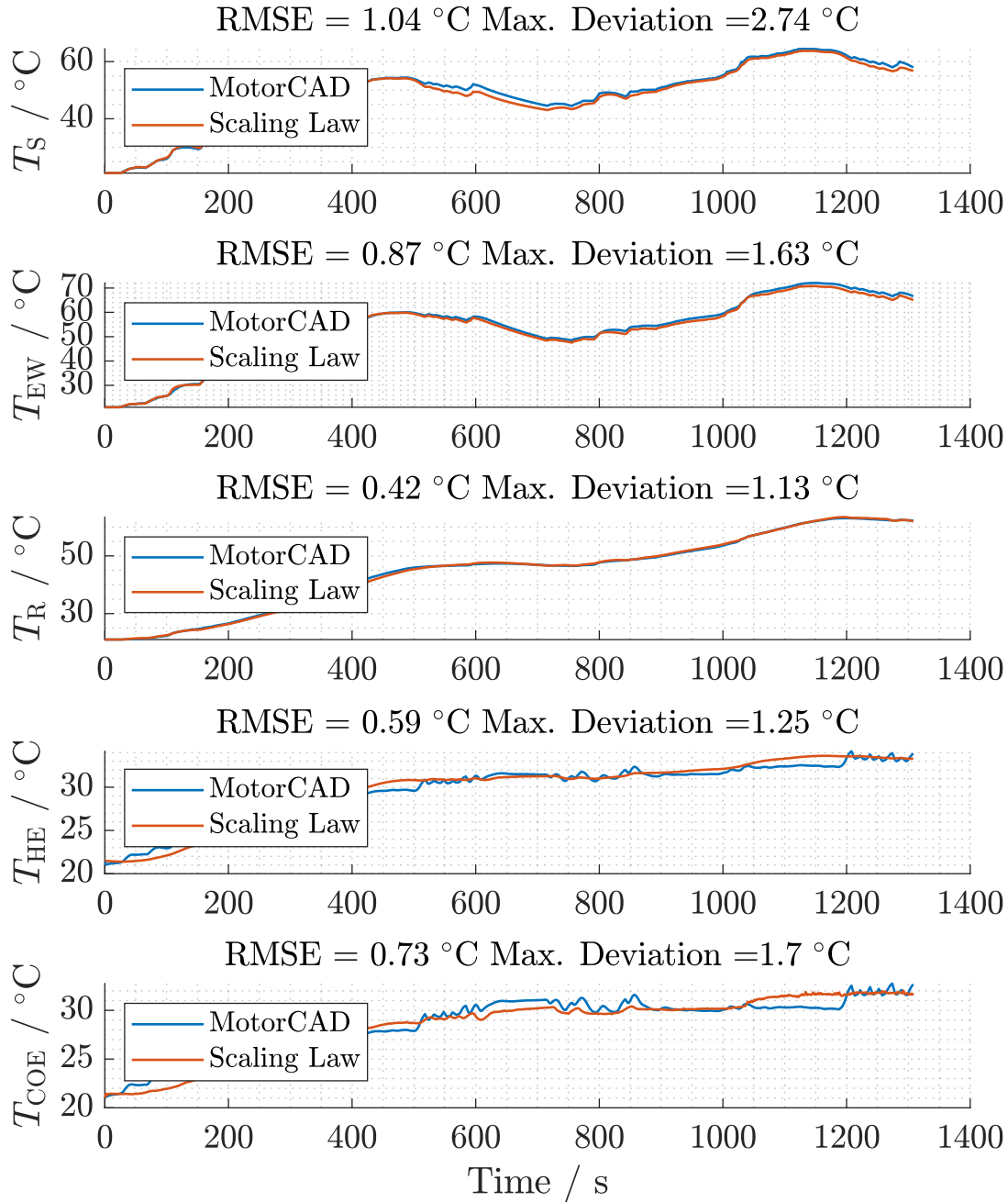


**Figure A.18.** Validation results of temperature estimation for 0.9 axial scaling against the US06 cycle at an ambient temperature of 20 °C

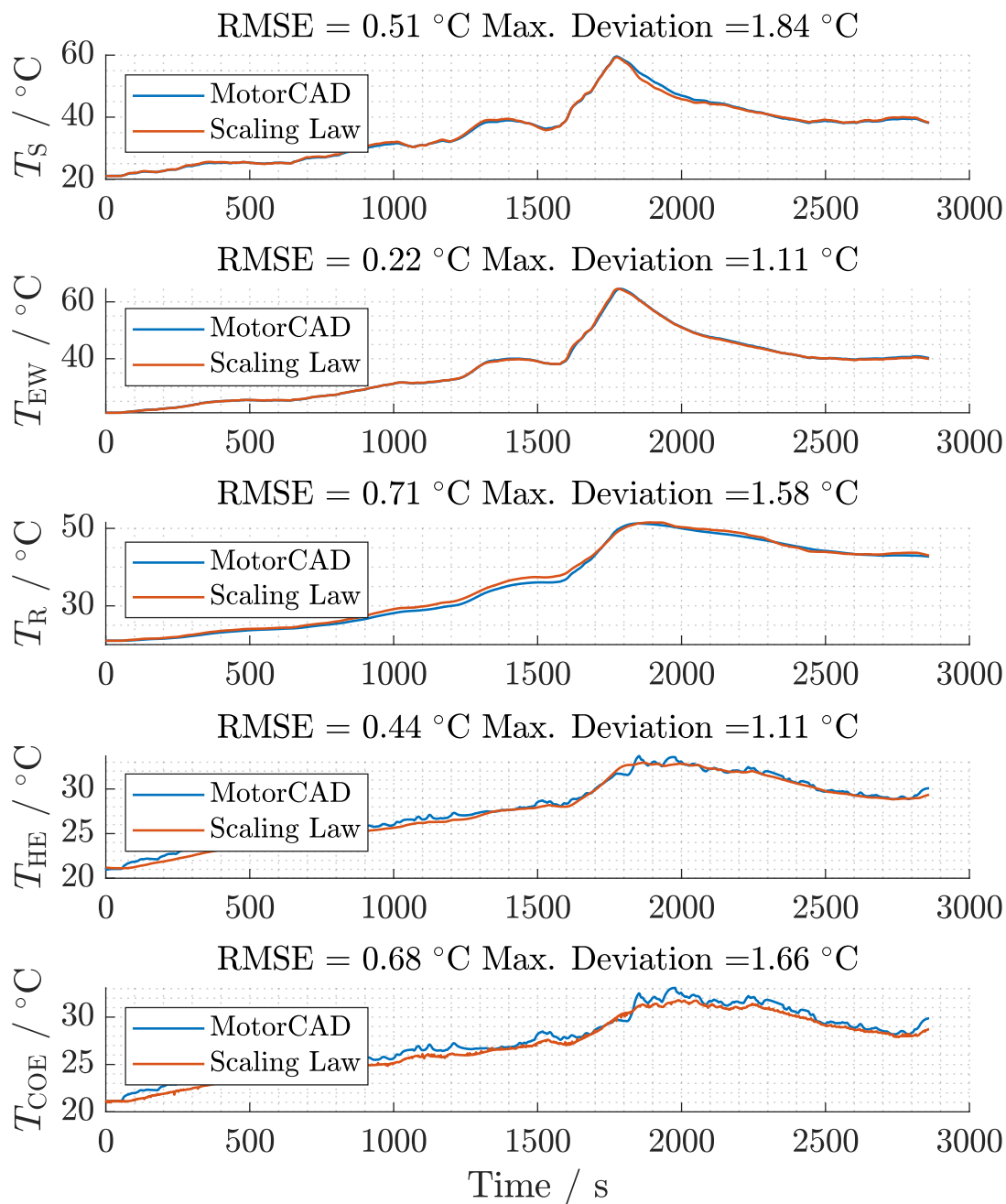


**Figure A.19.** Validation results of temperature estimation for 1.1 axial scaling against the extended WLTC cycle at an ambient temperature of 20 °C

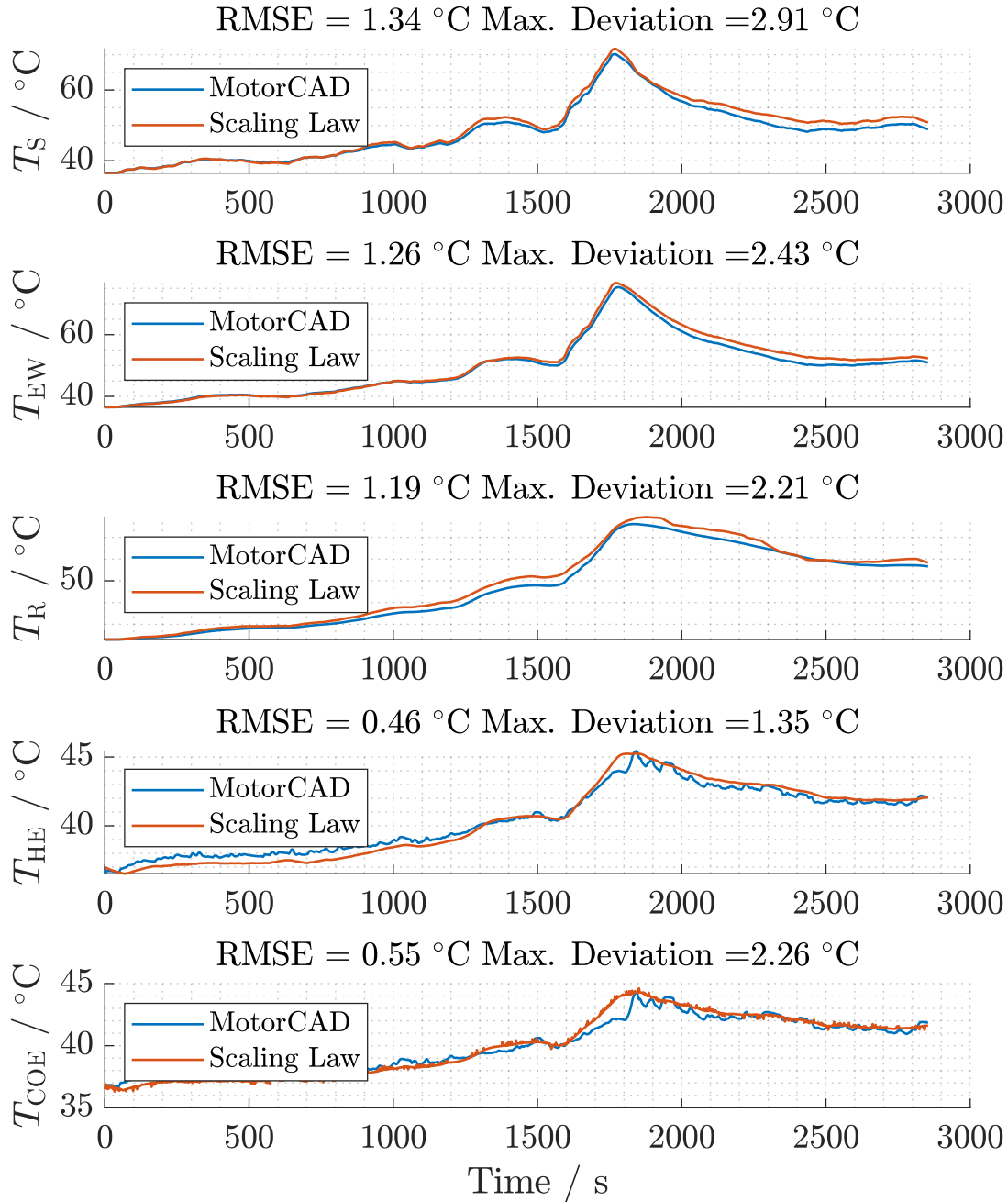


**Figure A.20.** Validation results of temperature estimation for 1.1 axial scaling against the extended WLTC cycle at an ambient temperature of 35  $^\circ\text{C}$

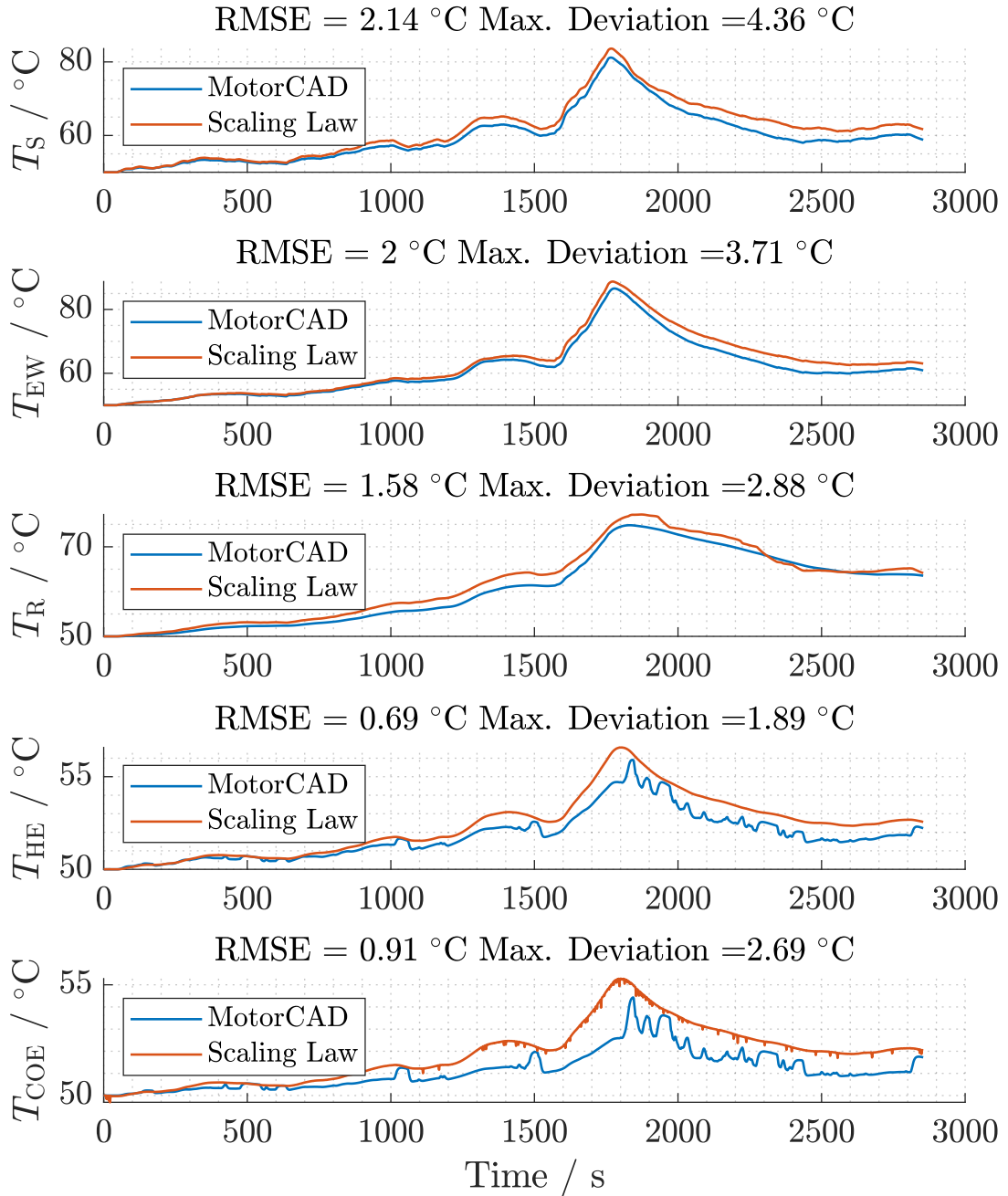


**Figure A.21.** Validation results of temperature estimation for 1.1 axial scaling against the extended WLTC cycle at an ambient temperature of 50 °C

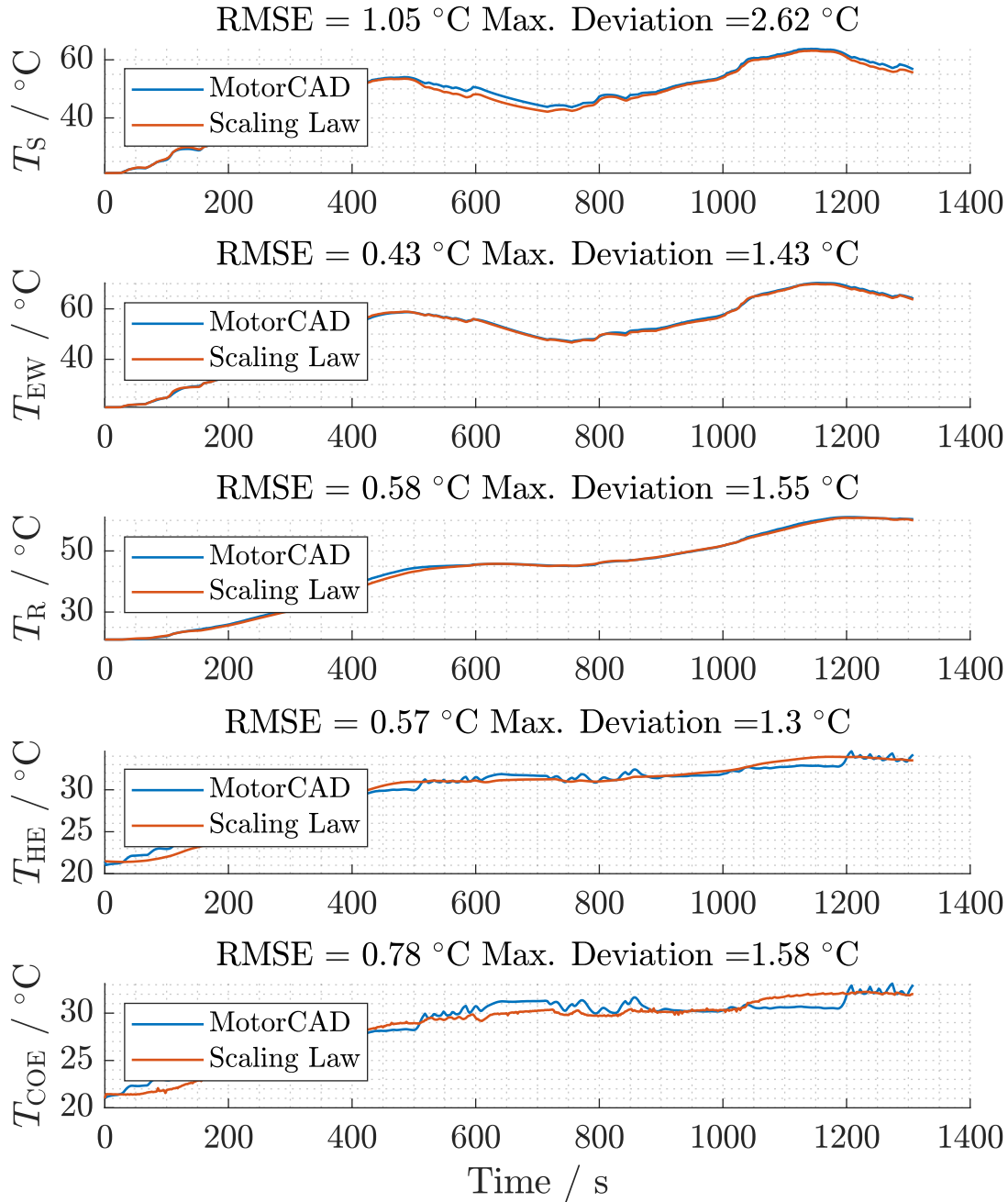


**Figure A.22.** Validation results of temperature estimation for 1.1 axial scaling against the US06 cycle at an ambient temperature of 20  $^\circ\text{C}$

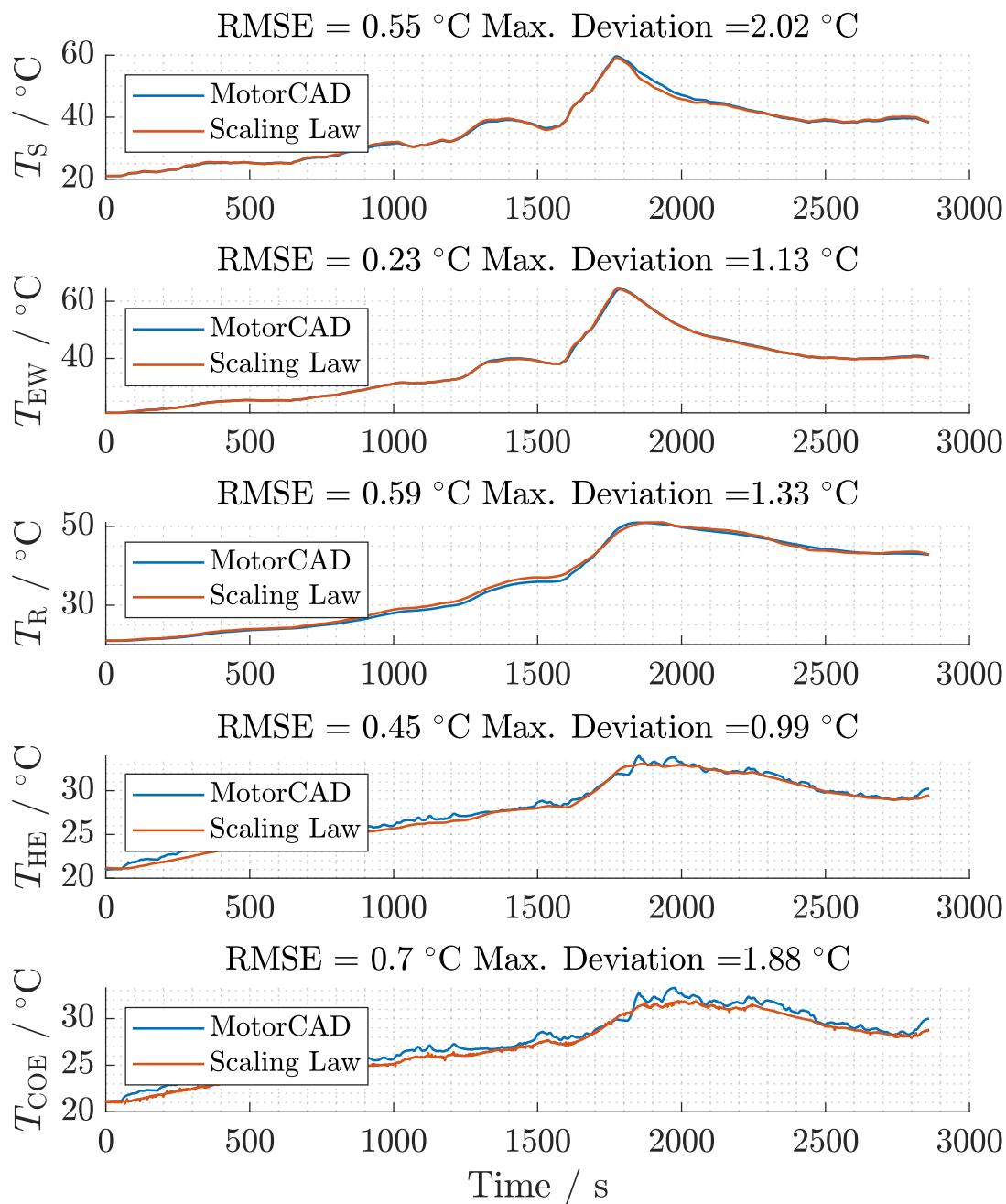


**Figure A.23.** Validation results of temperature estimation for 1.2 axial scaling against the extended WLTC cycle at an ambient temperature of 20 °C

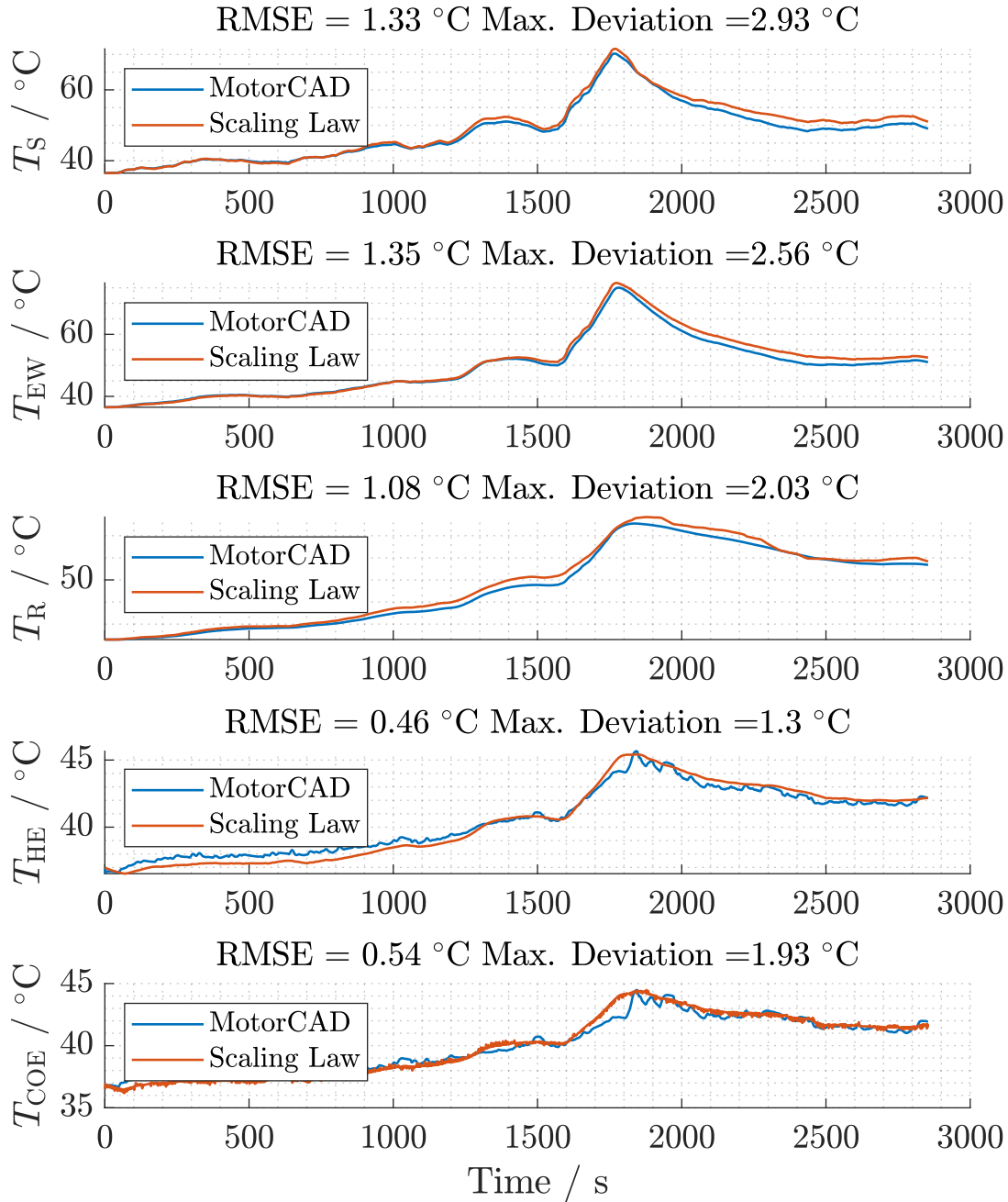


**Figure A.24.** Validation results of temperature estimation for 1.2 axial scaling against the extended WLTC cycle at an ambient temperature of 35 °C

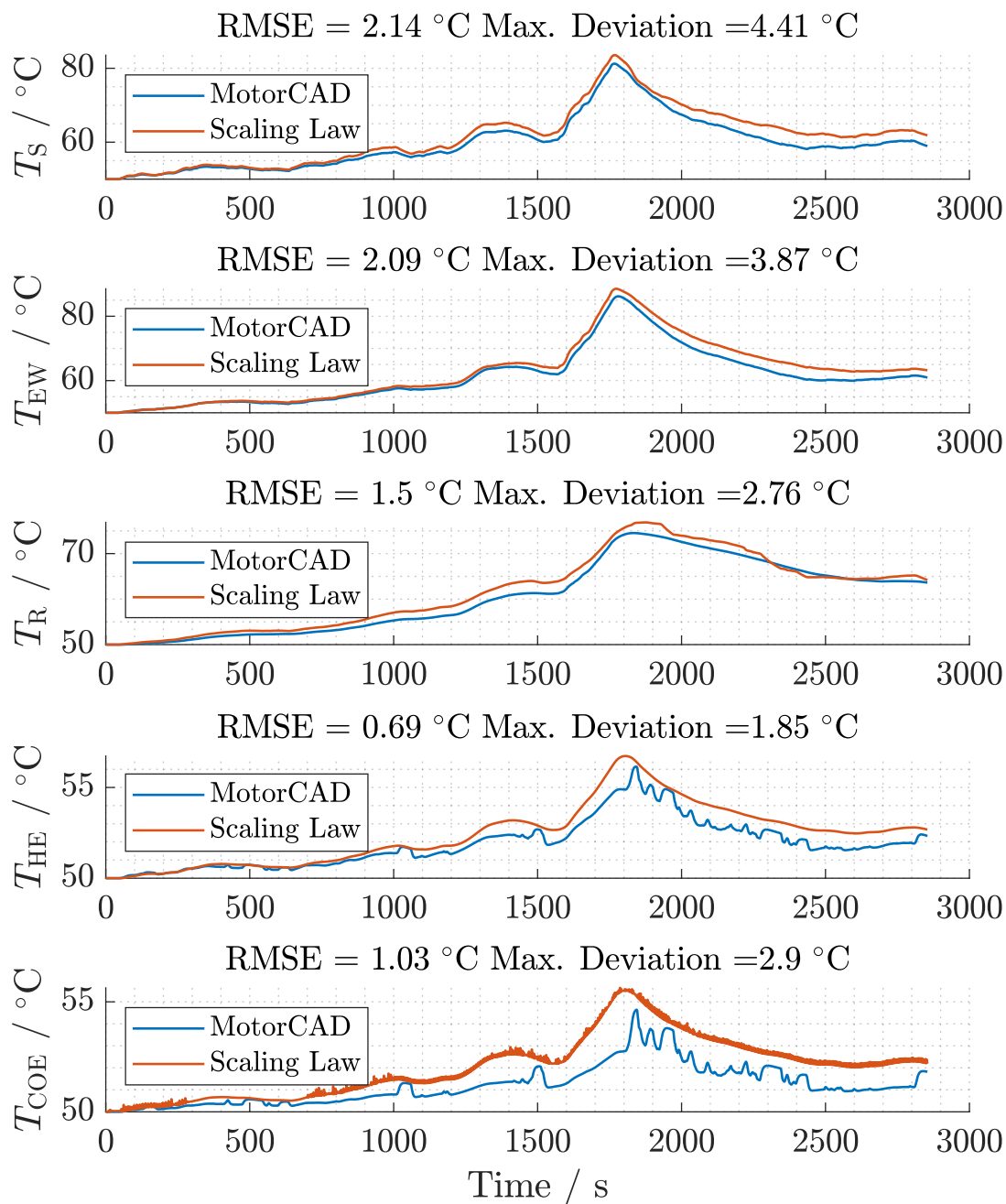


**Figure A.25.** Validation results of temperature estimation for 1.2 axial scaling against the extended WLTC cycle at an ambient temperature of 50  $^\circ\text{C}$

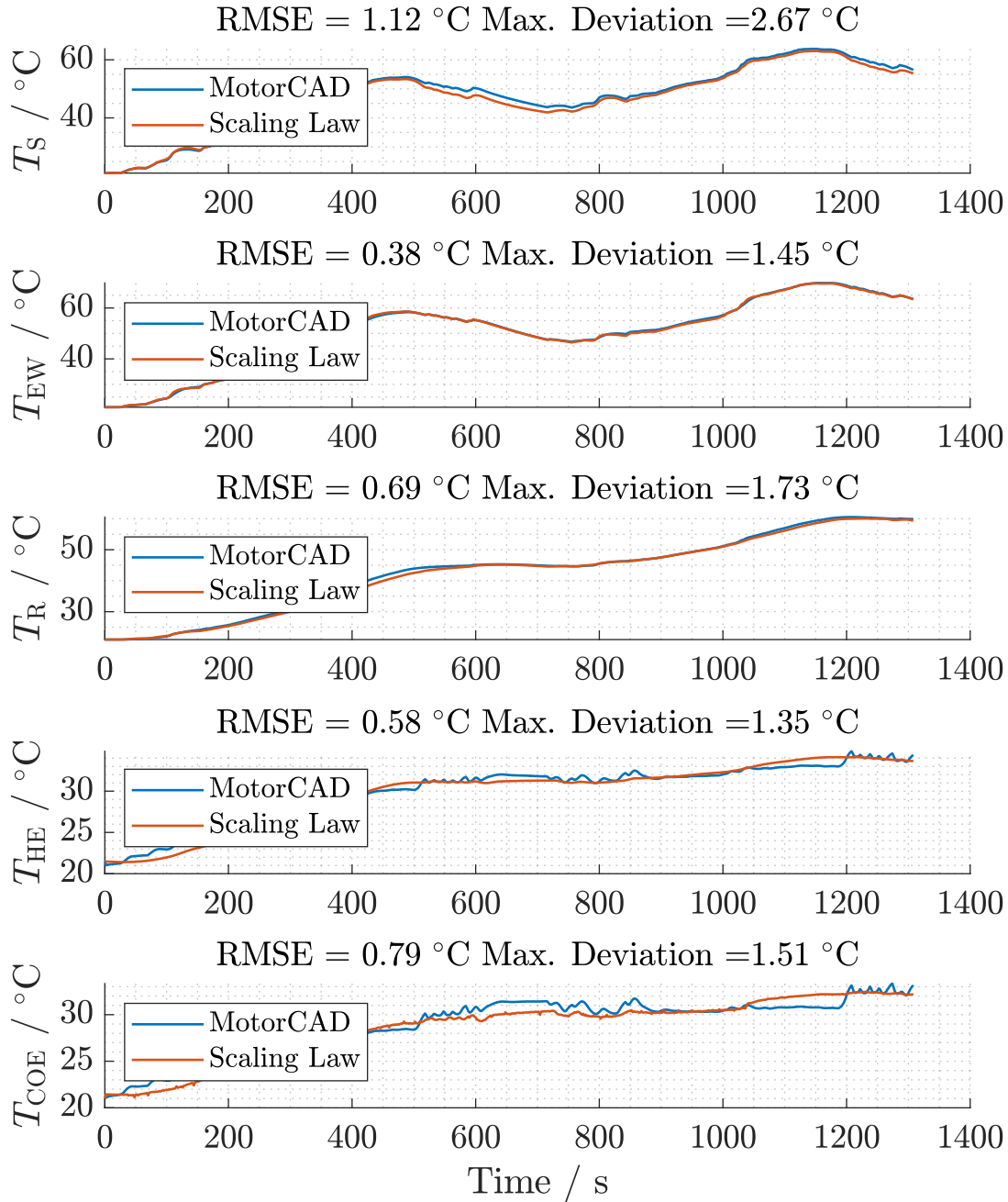


**Figure A.26.** Validation results of temperature estimation for 1.2 axial scaling against the US06 cycle at an ambient temperature of 20  $^\circ\text{C}$

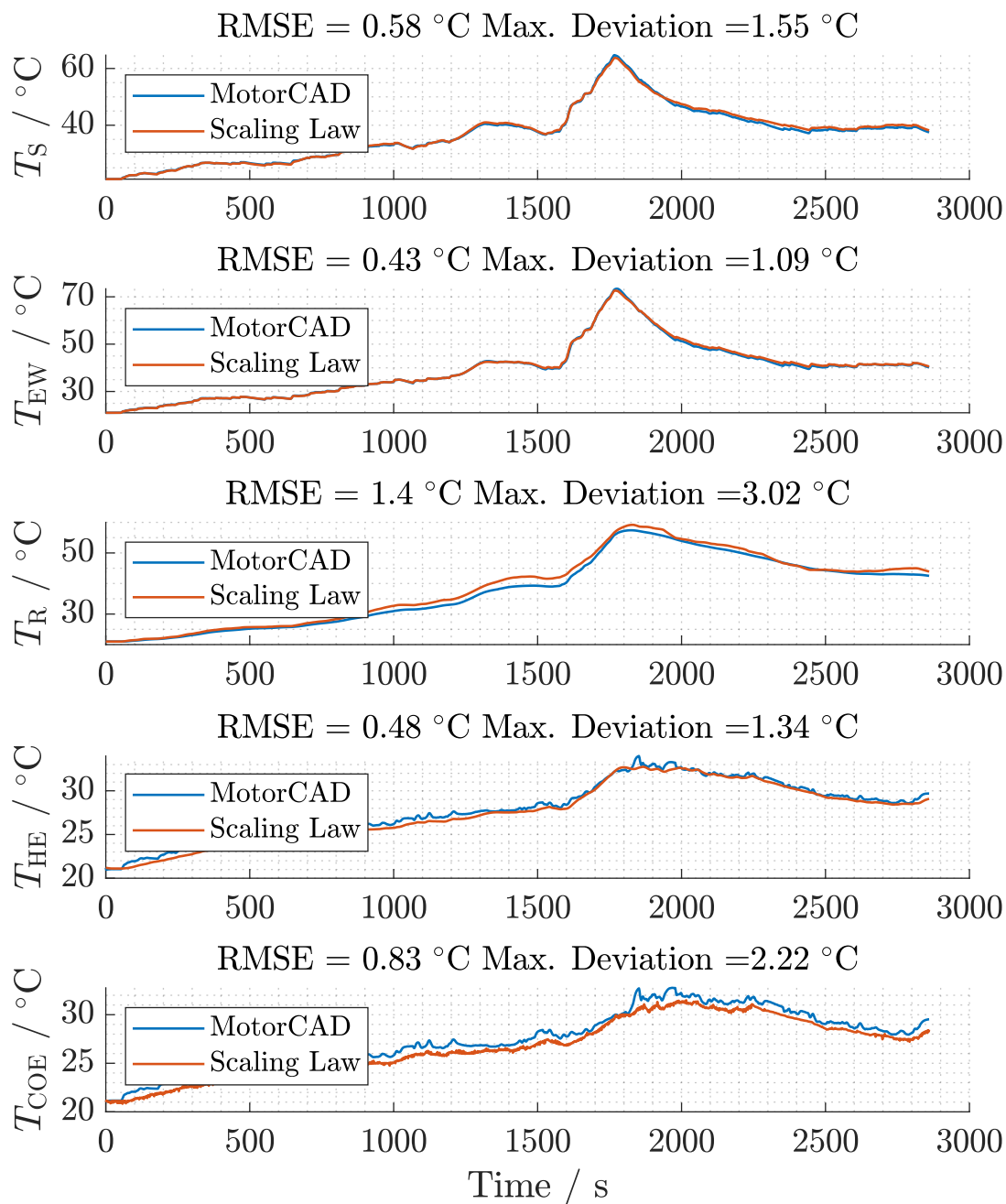


**Figure A.27.** Validation results of temperature estimation for 0.8 radial scaling against the extended WLTC cycle at an ambient temperature of 20 °C

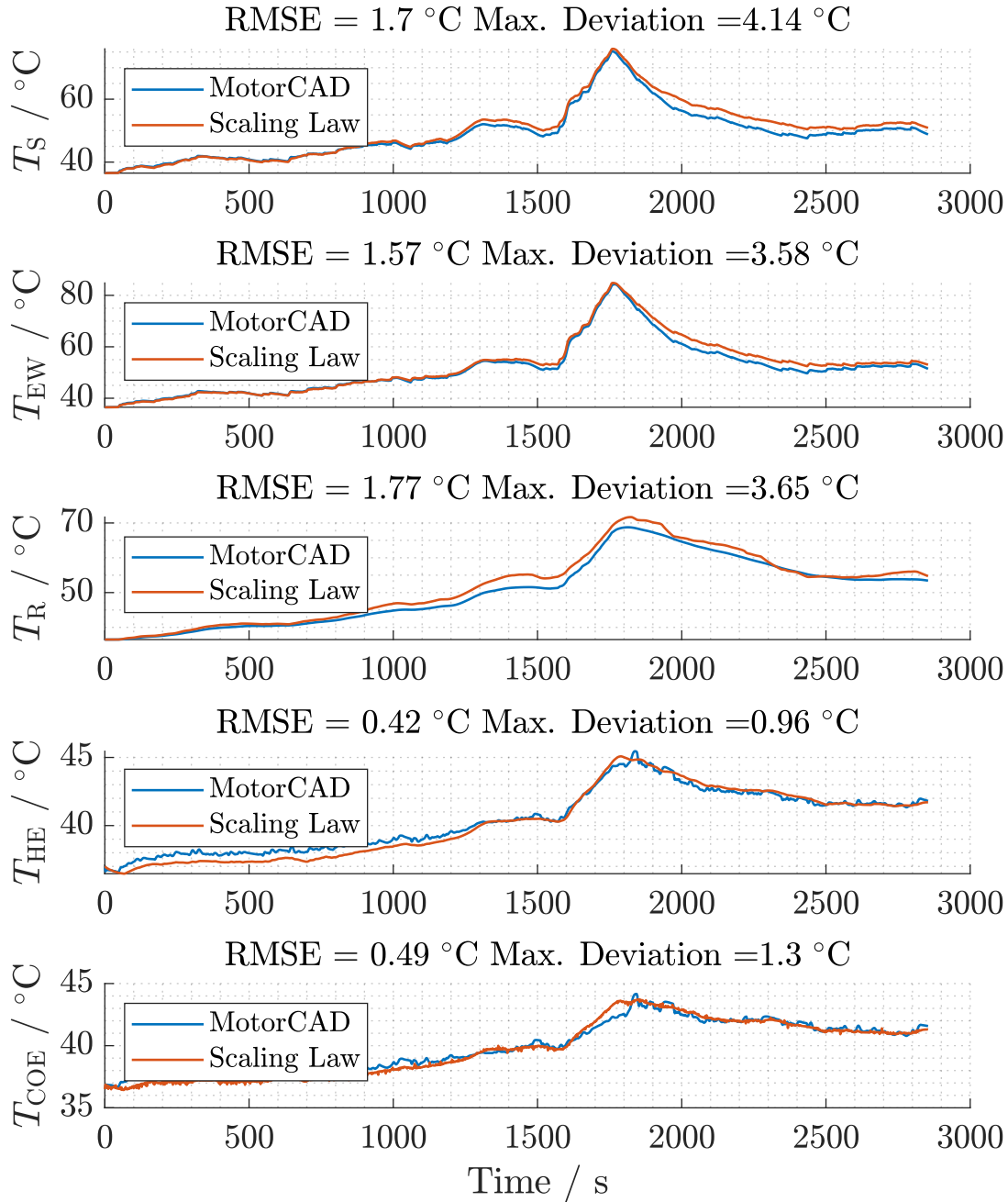


**Figure A.28.** Validation results of temperature estimation for 0.8 radial scaling against the extended WLTC cycle at an ambient temperature of 35  $^\circ\text{C}$

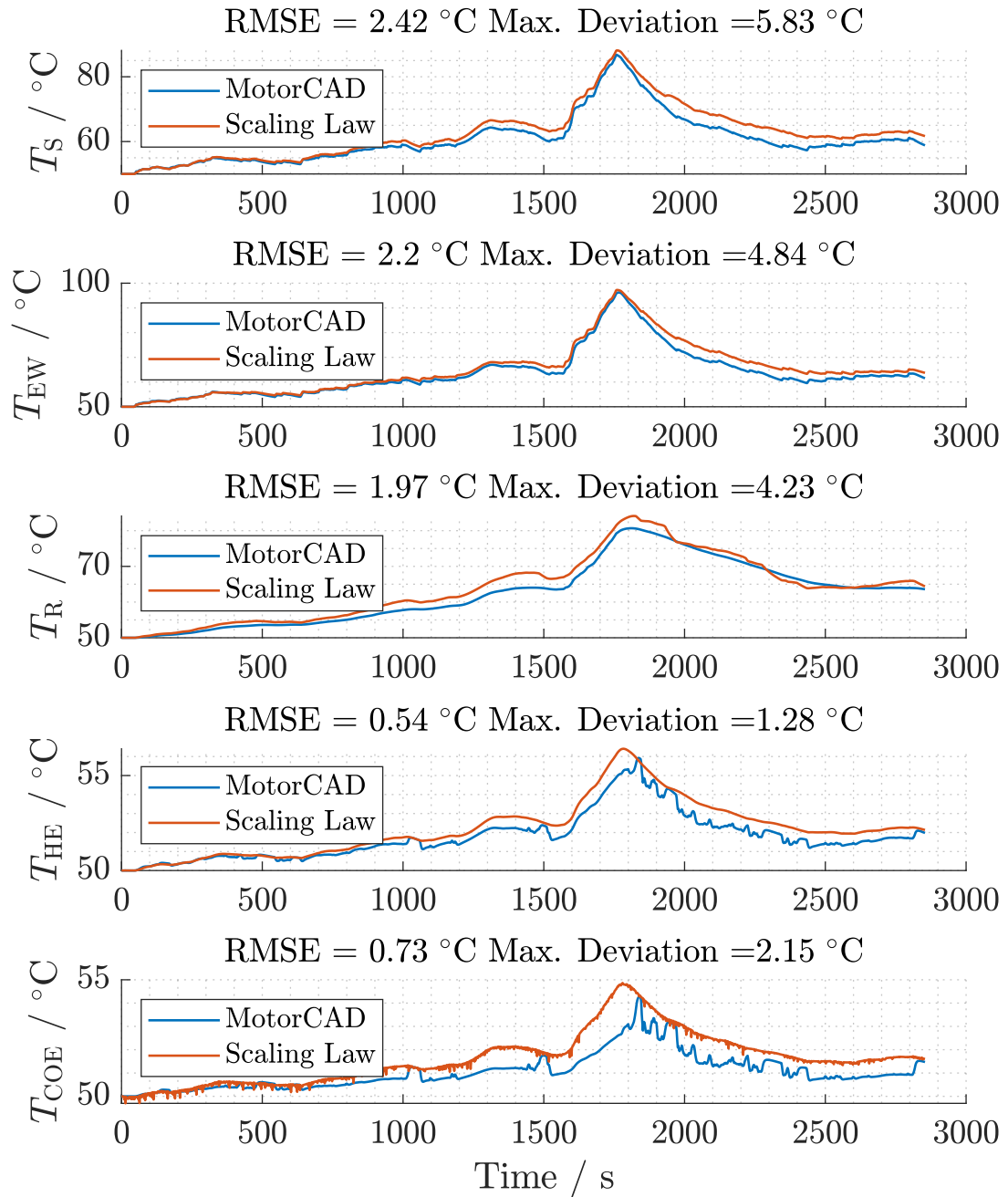


**Figure A.29.** Validation results of temperature estimation for 0.8 radial scaling against the extended WLTC cycle at an ambient temperature of 50  $^\circ\text{C}$

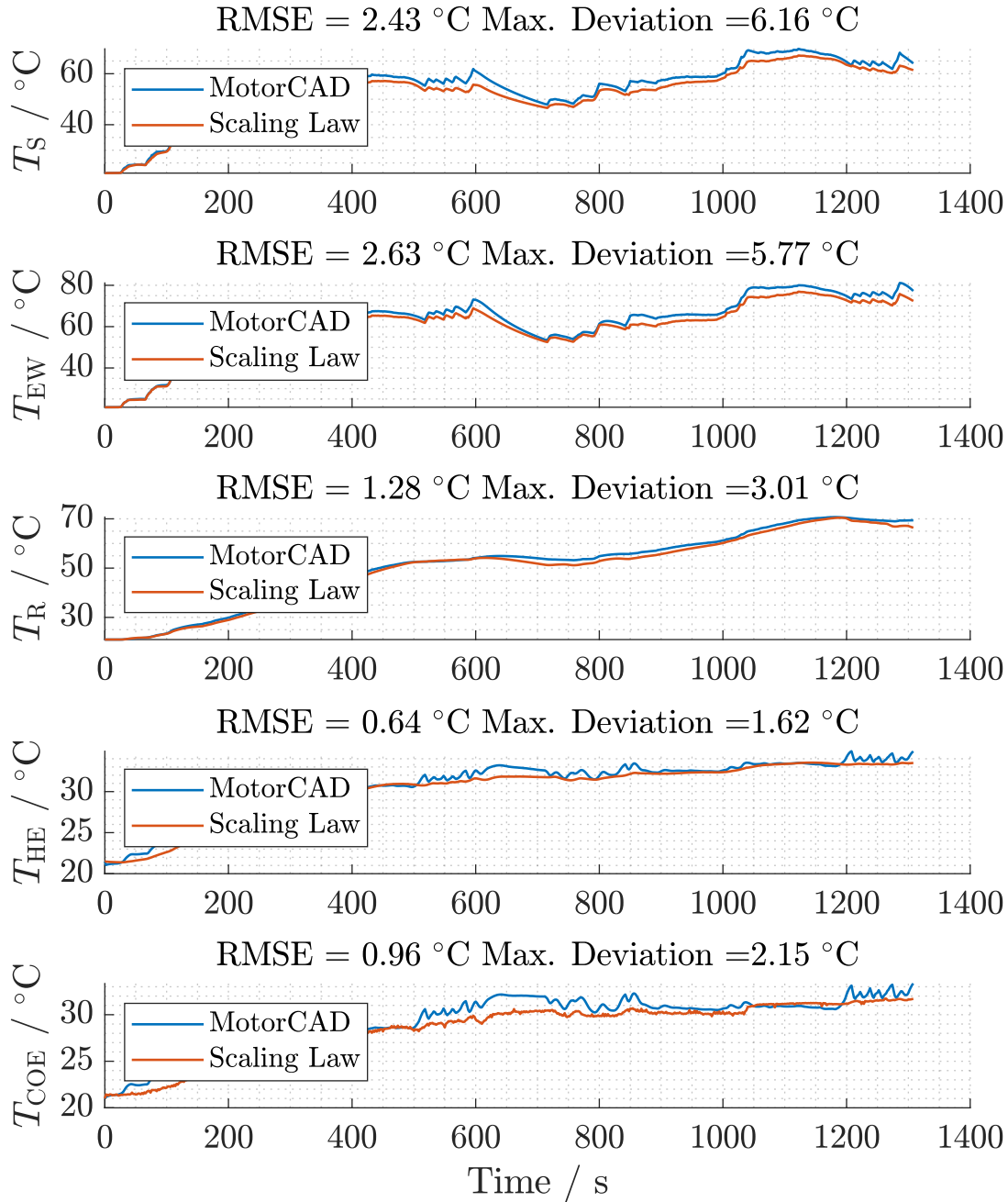


**Figure A.30.** Validation results of temperature estimation for 0.8 radial scaling against the US06 cycle at an ambient temperature of 20  $^\circ\text{C}$

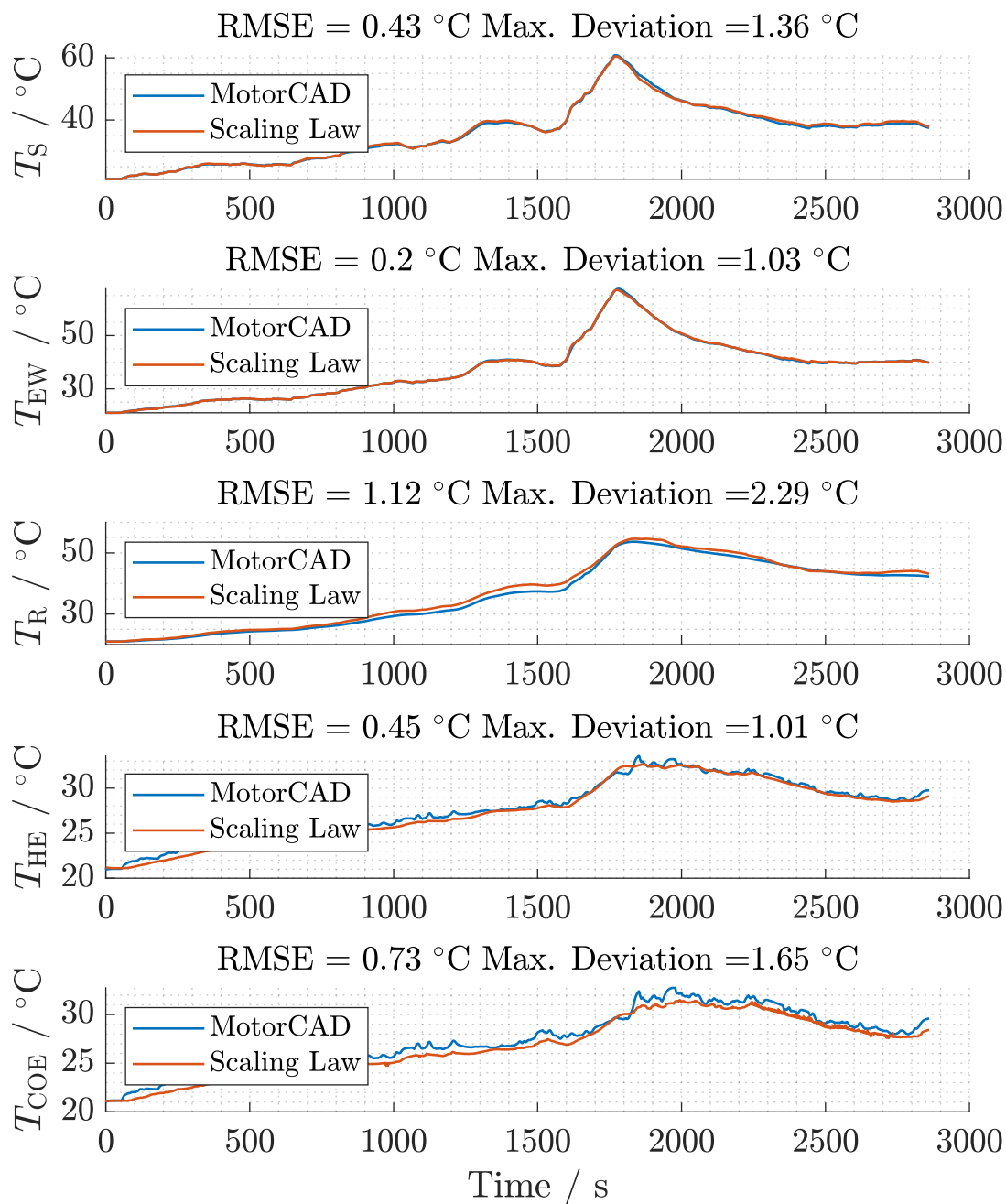


**Figure A.31.** Validation results of temperature estimation for 0.9 radial scaling against the extended WLTC cycle at an ambient temperature of 20 °C

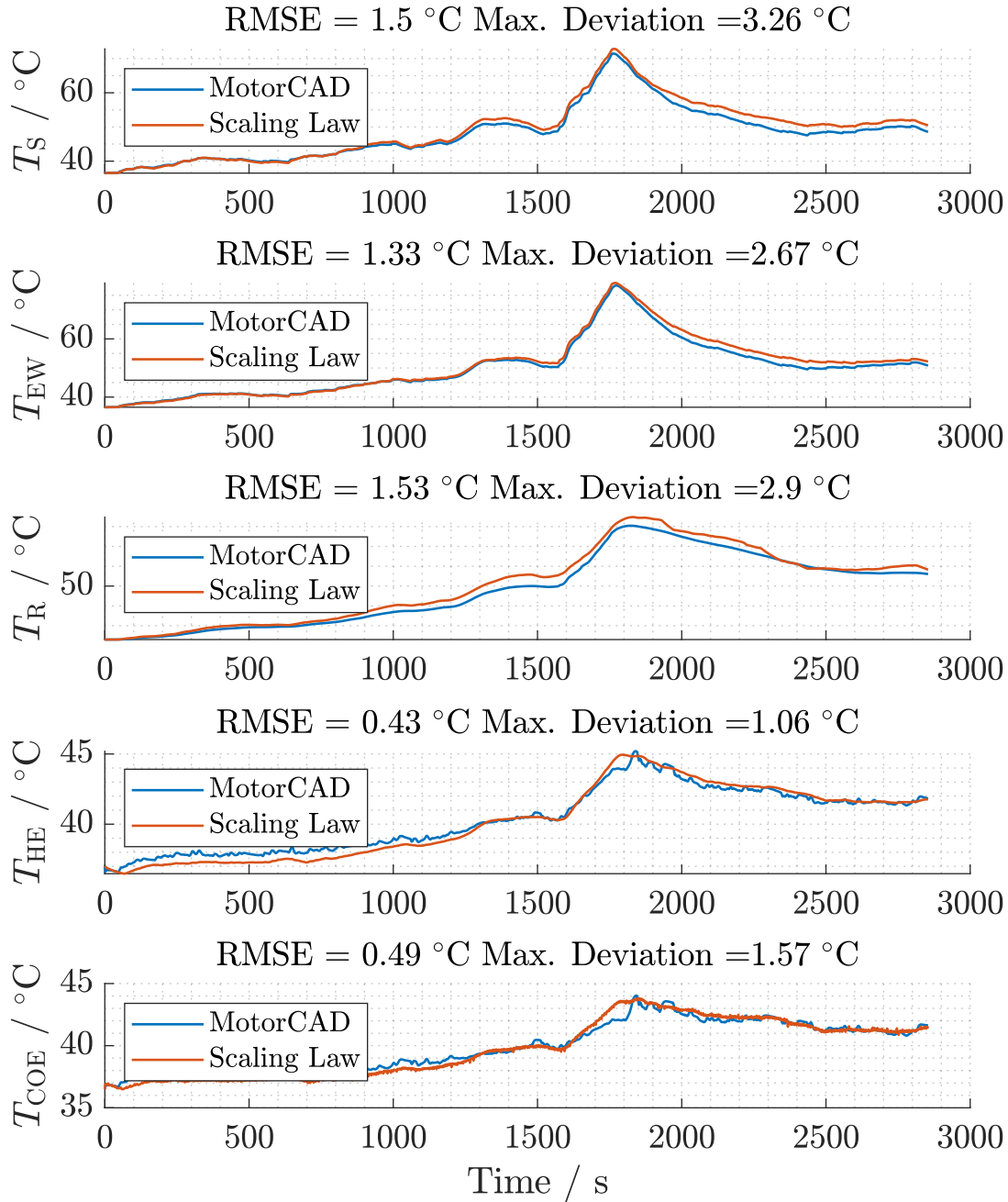


**Figure A.32.** Validation results of temperature estimation for 0.9 radial scaling against the extended WLTC cycle at an ambient temperature of 35 °C

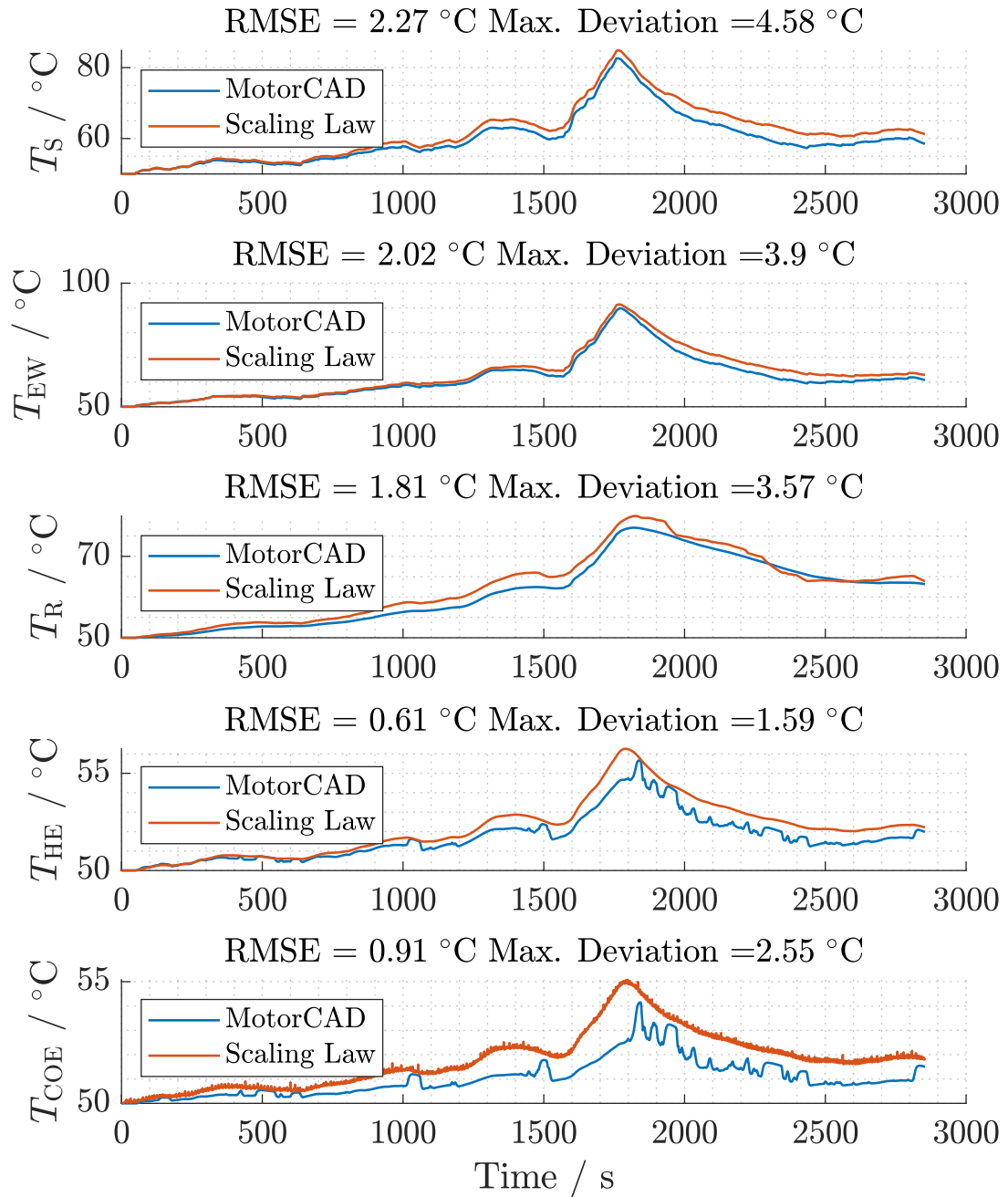


**Figure A.33.** Validation results of temperature estimation for 0.9 radial scaling against the extended WLTC cycle at an ambient temperature of 50  $^\circ\text{C}$

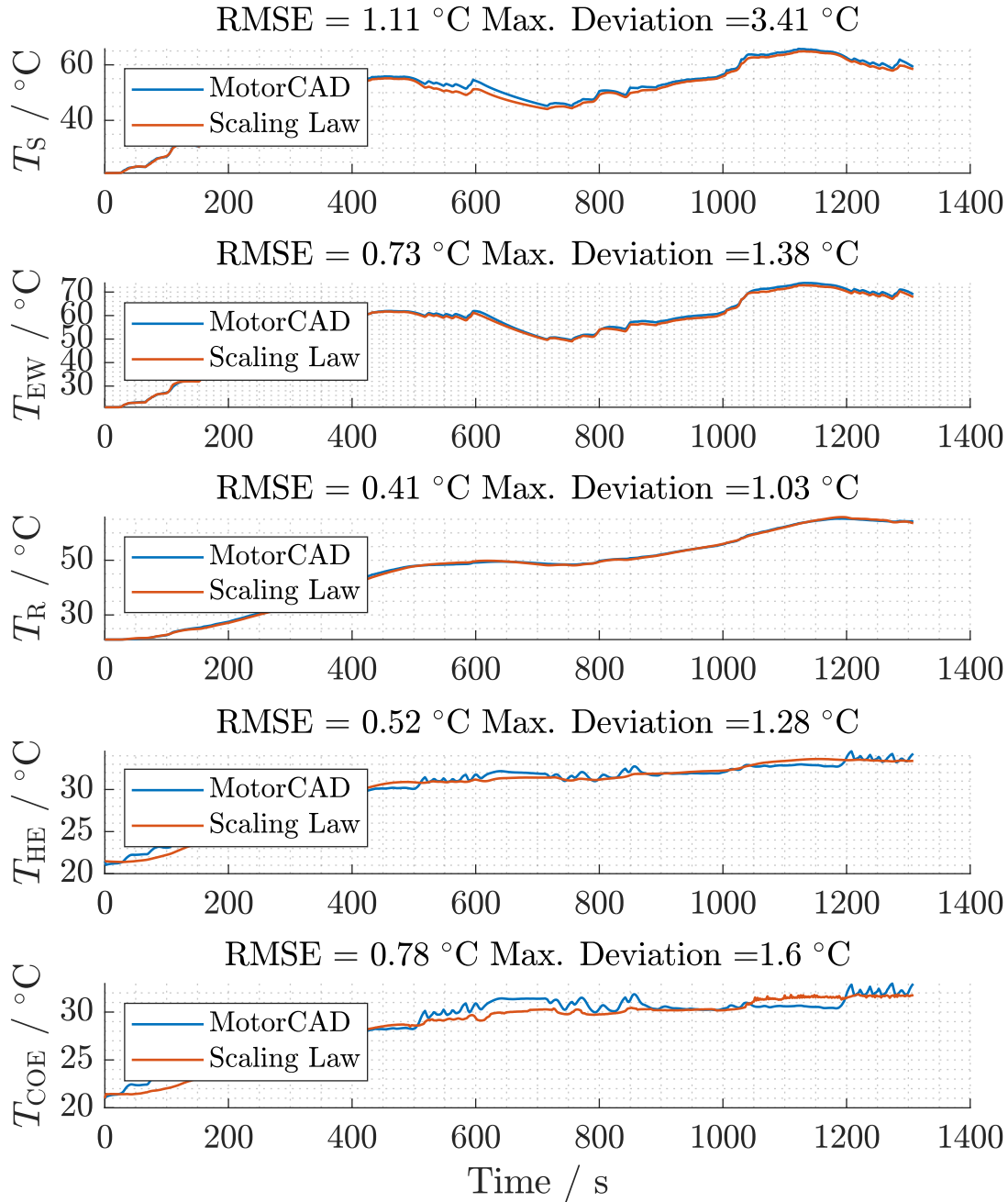


**Figure A.34.** Validation results of temperature estimation for 0.9 radial scaling against the US06 cycle at an ambient temperature of 20  $^\circ\text{C}$

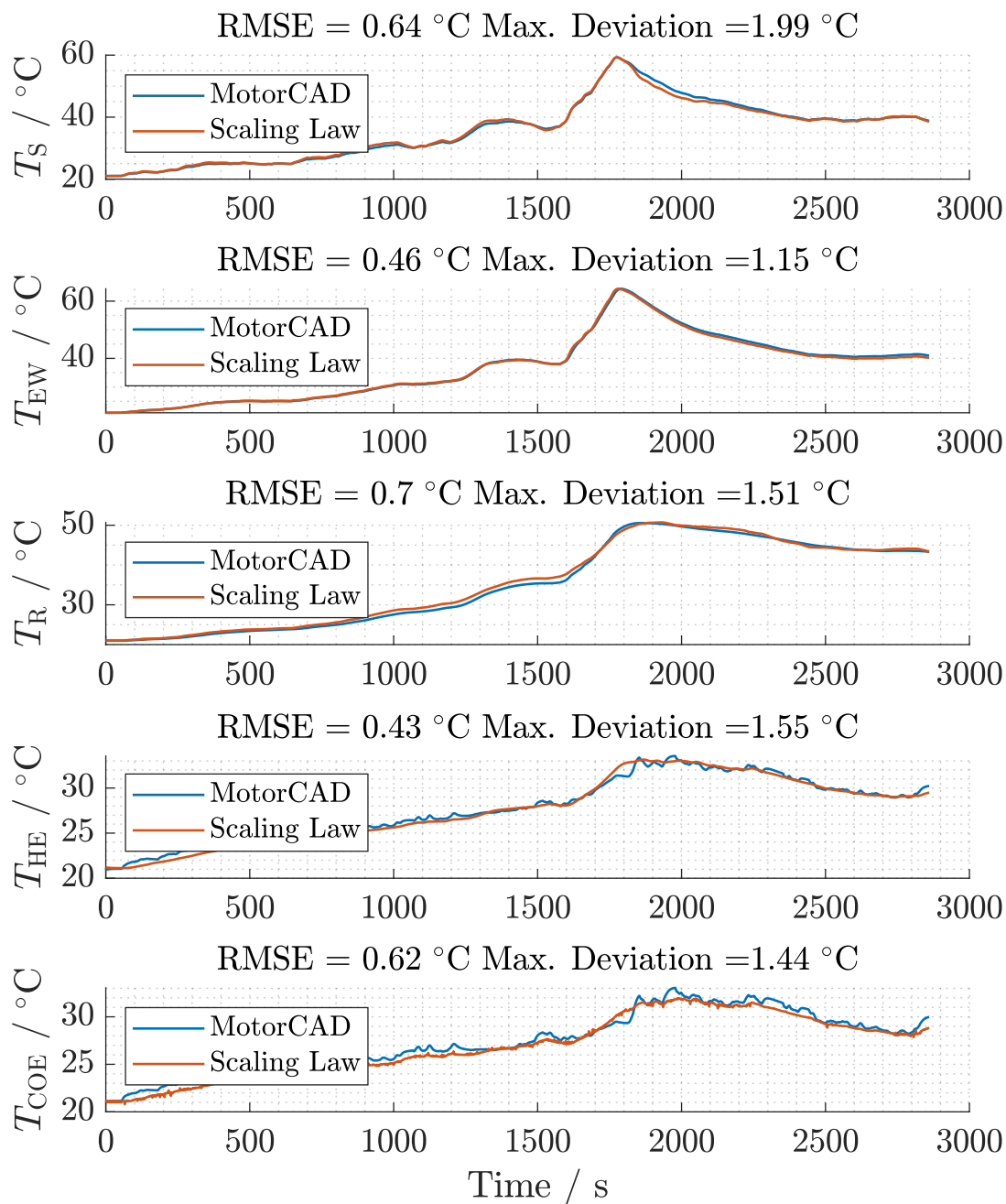


**Figure A.35.** Validation results of temperature estimation for 1.1 radial scaling against the extended WLTC cycle at an ambient temperature of  $20\text{ }^\circ\text{C}$

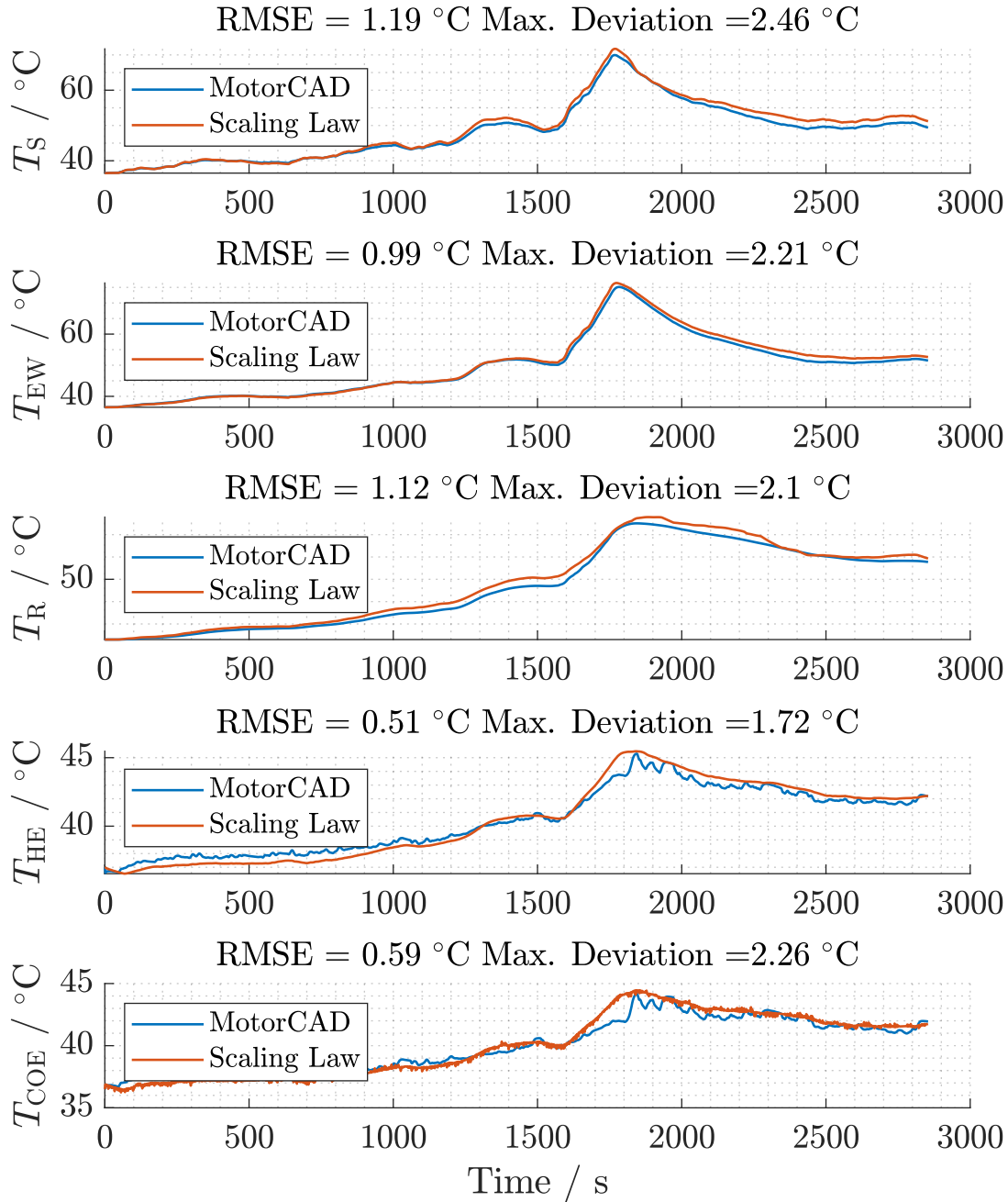


**Figure A.36.** Validation results of temperature estimation for 1.1 radial scaling against the extended WLTC cycle at an ambient temperature of 35 °C

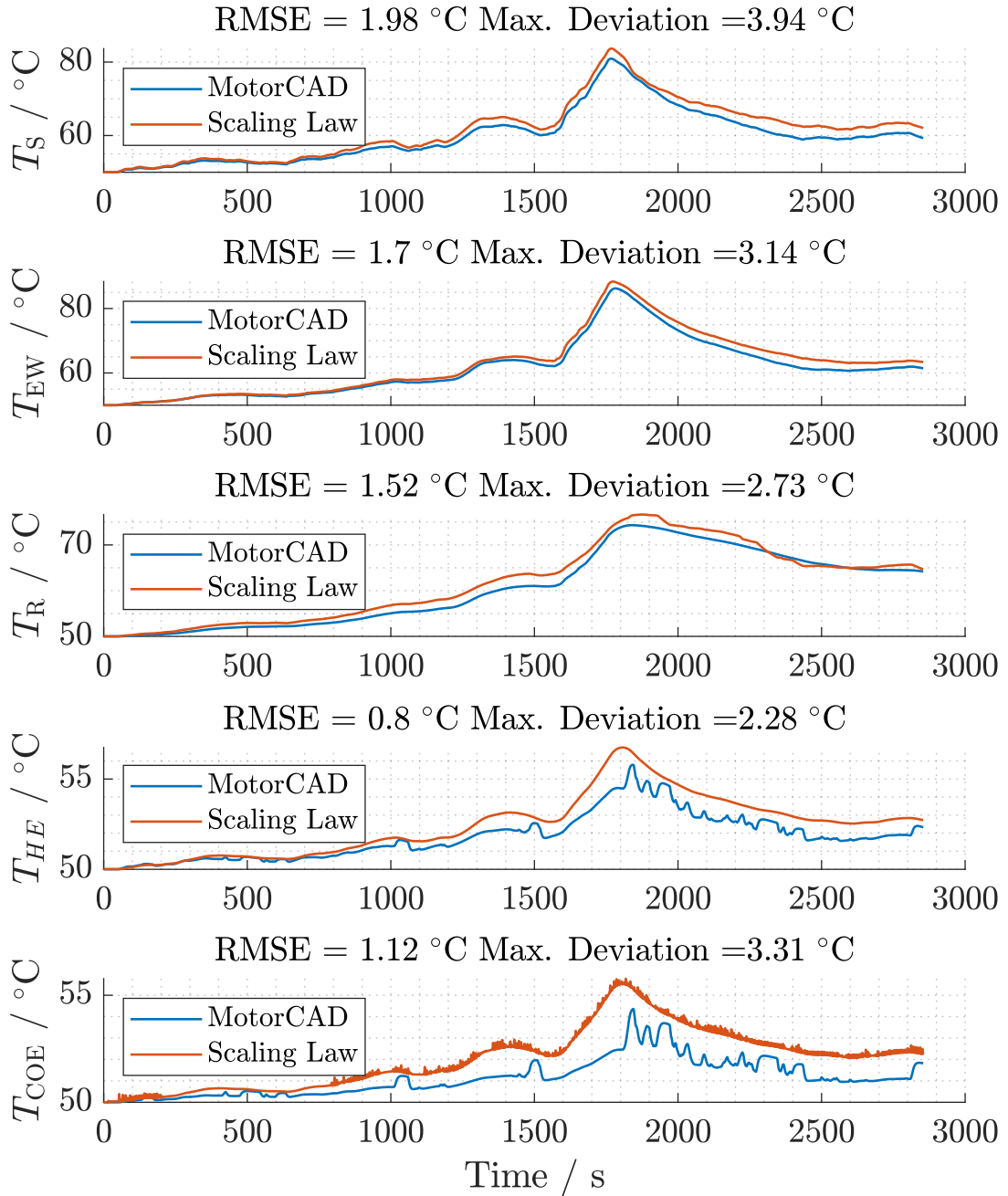


**Figure A.37.** Validation results of temperature estimation for 1.1 radial scaling against the extended WLTC cycle at an ambient temperature of 50 °C

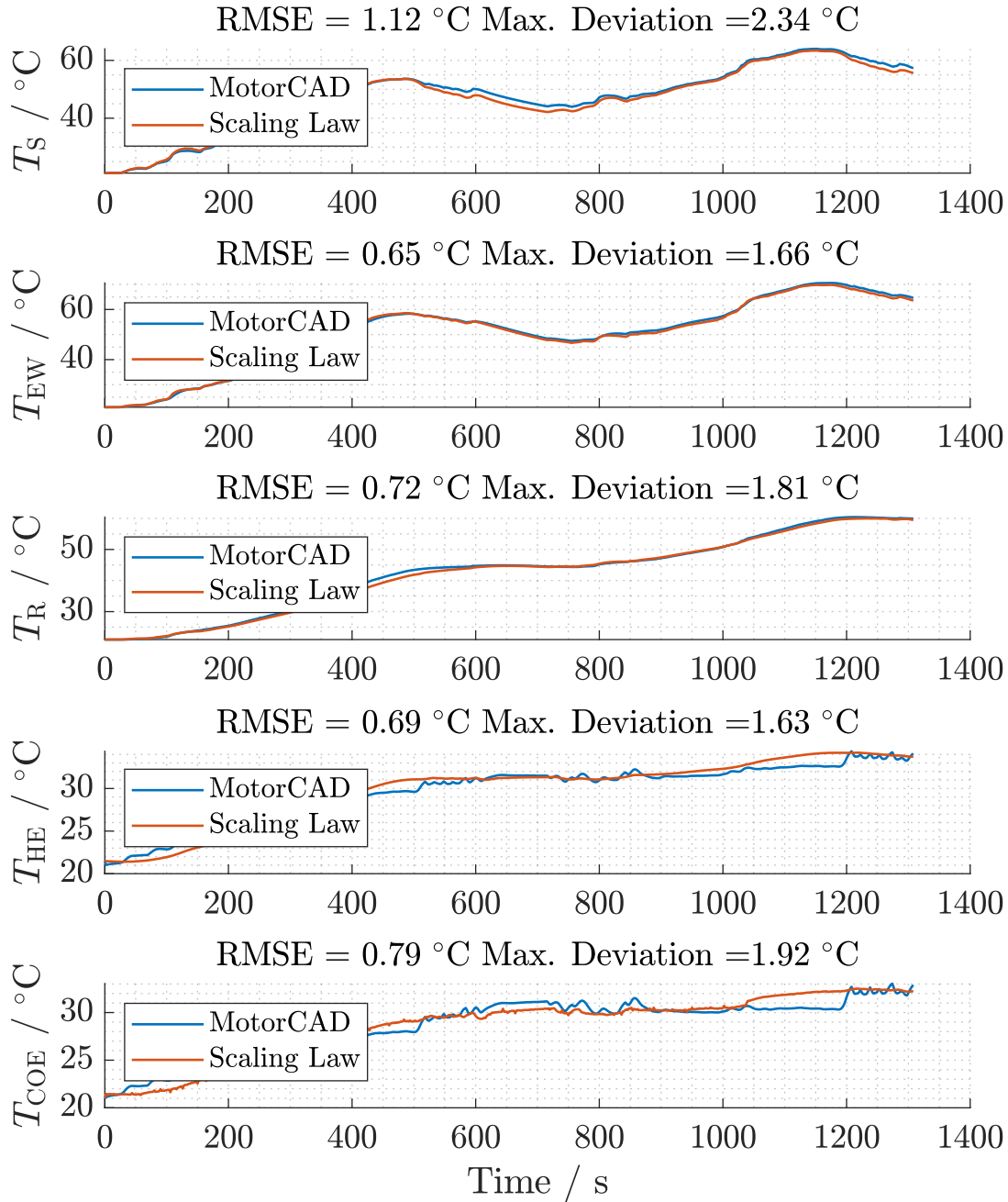


**Figure A.38.** Validation results of temperature estimation for 1.1 radial scaling against the US06 cycle at an ambient temperature of 20  $^\circ\text{C}$

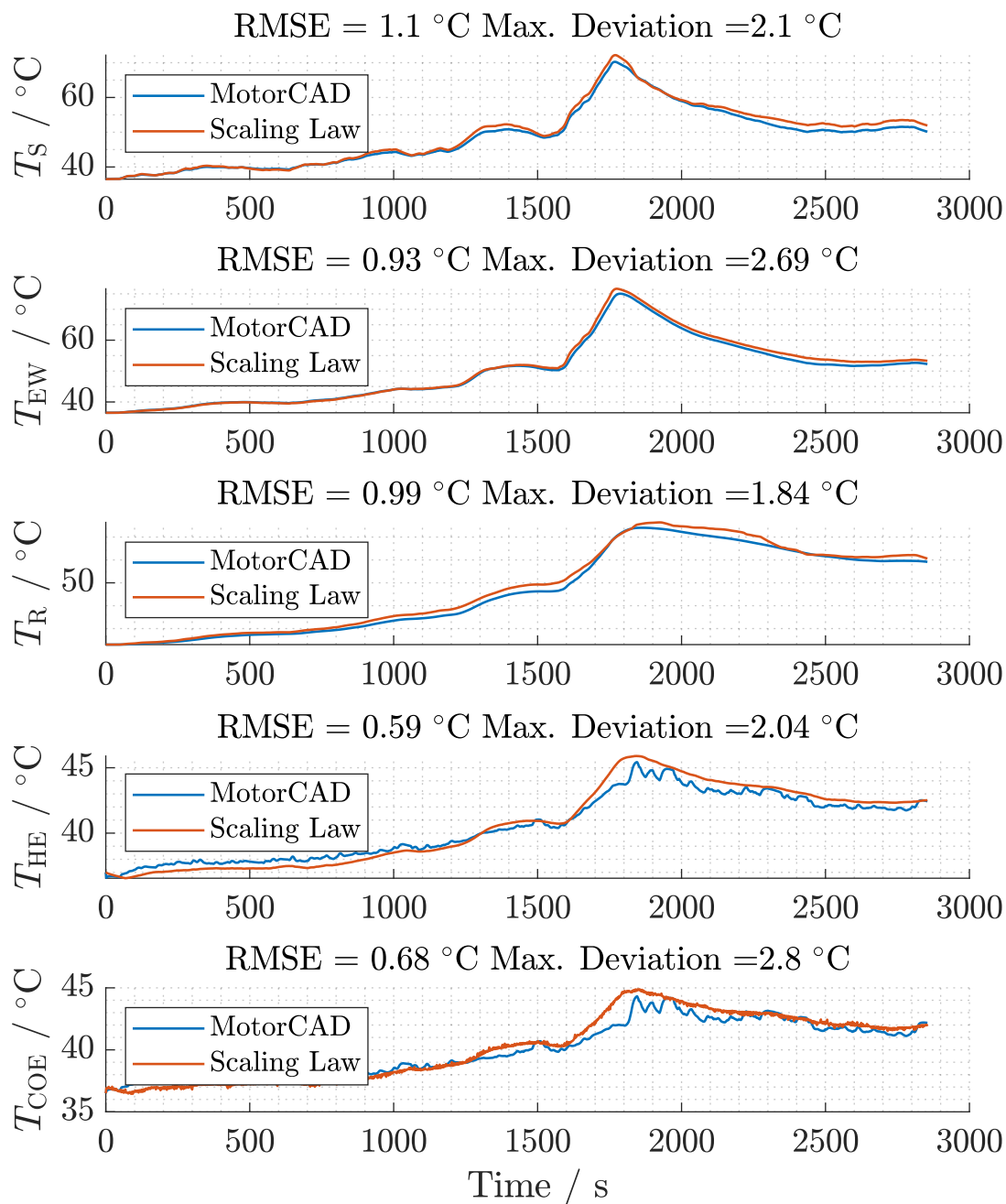


**Figure A.39.** Validation results of temperature estimation for 1.2 radial scaling against the extended WLTC cycle at an ambient temperature of 35  $^\circ\text{C}$

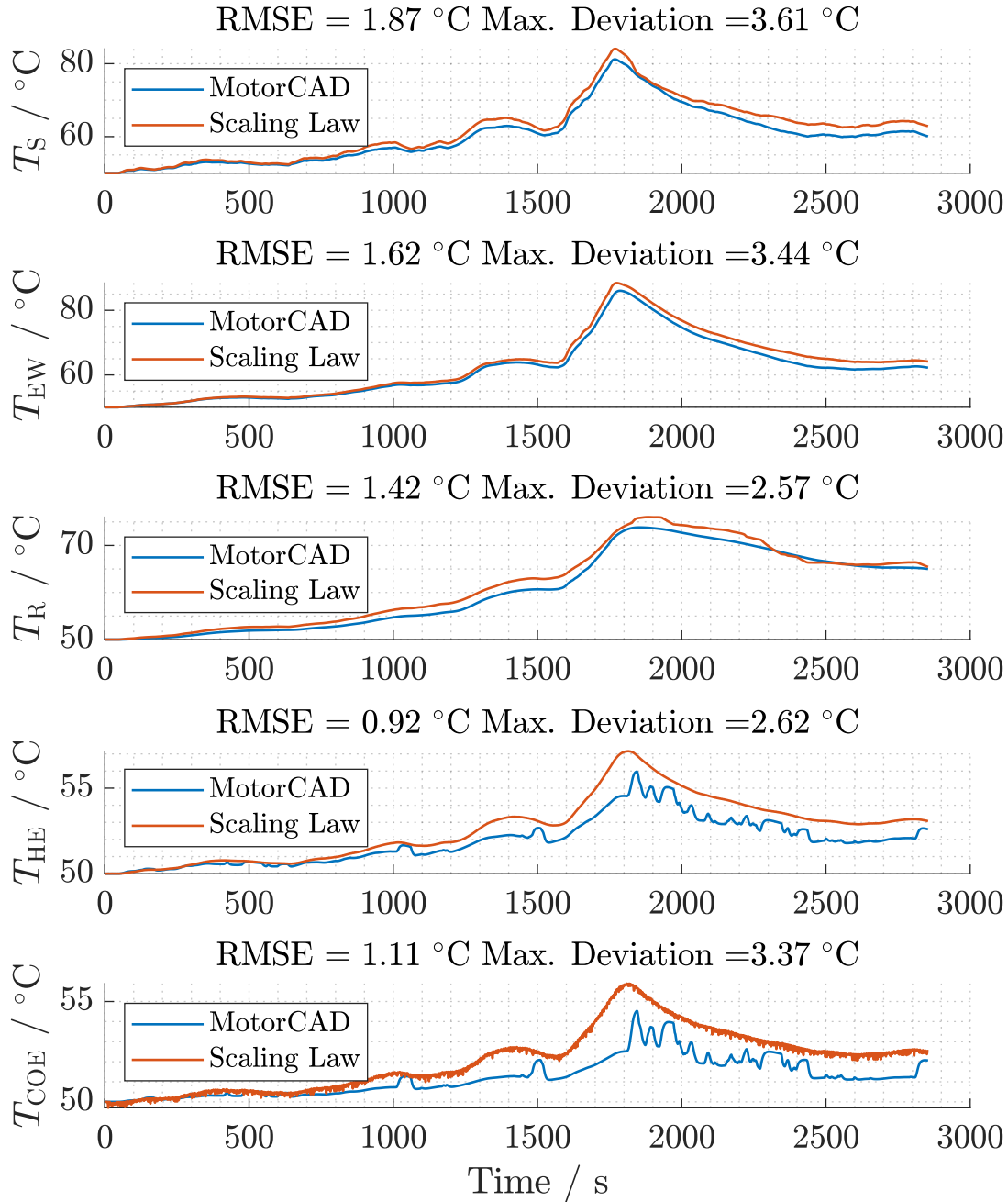


**Figure A.40.** Validation results of temperature estimation for 1.2 radial scaling against the extended WLTC cycle at an ambient temperature of 50 °C

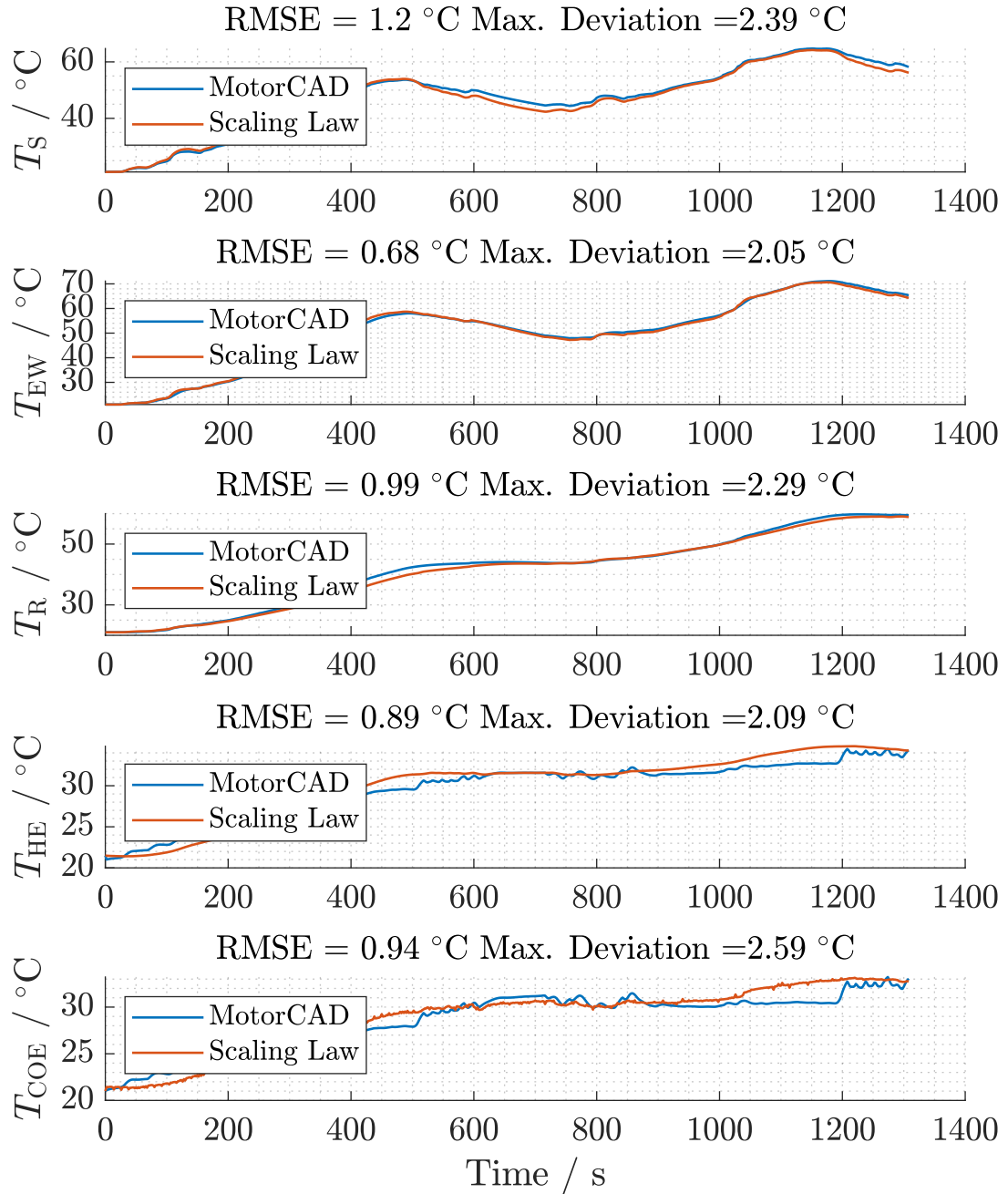


**Figure A.41.** Validation results of temperature estimation for 1.2 radial scaling against the US06 cycle at an ambient temperature of 20  $^\circ\text{C}$

# CURRICULUM VITAE

Bicheng Chen

## Personal Information

Date of birth: 29. January 1986  
Place of birth: Fujian, China  
Nationality: Chinese

## Education

10/2011–11/2013 Master of Science, Electrical Engineering at Technical University  
Kaiserslautern, Germany, Germany  
10/2008–09/2011 Bachelor of Science, Electrical Engineering at Technical University  
Kaiserslautern, Germany  
04/2008–07/2008 German Language Course at Technical University Kaiserslautern,  
Germany  
09/2005–01/2008 Bachelor of Science, Electrical Engineering at Fuzhou University,  
China

## Work Experience

04/2018–02/2024 Research Associate at Chair of Thermodynamics of Mobile Energy  
Conversion Systems (TME), RWTH Aachen University, Germany  
04/2018–02/2024 Project Engineer at FEV Europe GmbH, Germany  
09/2017–03/2018 Test Engineer at Betrandt AG, Wolfsburg, Germany  
07/2014–08/2017 Software Engineer at Motortech GmbH, Celle, Germany  
02/2012–10/2013 Student Worker at Chair of Control Systems, Technical Univer-  
sity Kaiserslautern, Germany  
09/2010–02/2011 Internship at Daimler AG, Stuttgart, Germany

